HSB
Hochschule Bremen
City University of Applied Sciences

Development of a Lunar Regolith Transport System Utilizing Compliant Mechanisms for a Regolith Based ISRU-Process

by

Tim Gumbold

A Master's Thesis submitted for the attainment of the academic degree
Master of Science in the Degree Program of

Aerospace Technologies

at the City University of Applied Sciences Bremen,
in the Faculty 5, School of Nature and Engineering,
Department of Mechanical Engineering

Matriculation Number: 5394122

First Examiner: Prof. Dr.-Ing. Sven Oppermann, Faculty 5, HsB

Second Examiner: Dr.-Ing. Paul Zabel, German Aerospace Center

June 15, 2026

Eidesstattliche Erklärung

Ich versichere, die von mir vorgelegte Arbeit selbstständig verfasst zu haben. Alle Stellen, die wörtlich oder sinngemäß aus veröffentlichten oder nicht veröffentlichten Arbeiten anderer entnommen sind, habe ich als entnommen kenntlich gemacht. Sämtliche Quellen und Hilfsmittel, die ich für die Arbeit benutzt habe, sind angegeben. Die Arbeit hat mit gleichem Inhalt bzw. in wesentlichen Teilen noch keiner anderen Prüfungsbehörde vorgelegen.

$Unterschrift:$ $Ort, Datum:$

Well, I'd like to visit the Moon
On a rocket ship high in the air
Yes, I'd like to visit the Moon
But I don't think I'd like to live there

—Jeff Moss, for Ernie

Zusammenfassung

Die Menschheit strebt eine Rückkehr zum Mond an. Die Nutzung vor Ort verfügbarer Ressourcen gewinnt zunehmend an Bedeutung. Diese Vorgehensweise ist als “In-Situ Resource Utilisation (ISRU)” bekannt. Das am häufigsten vorkommende Material, das für ISRU genutzt werden kann, ist der Mondregolith, der die Mondoberfläche bedeckt. In allen Schritten eines auf Regolith basierenden ISRU-Prozesses ist der Transport des Regoliths erforderlich. Der Mondregolith birgt zwar große Nutzungsmöglichkeiten, stellt jedoch auch ein hohes Risiko für jegliche auf der Oberfläche stationierte Hardware und Besatzung dar. Herkömmliche Mechanismen, die tribologische Paarungen beinhalten, sind in dieser stark abrasiven Umgebung von Natur aus anfällig für übermäßigen Verschleiß. Um dieses Problem in einer ISRU-Prozesskette zu lösen, entwickelt diese Studie ein Mondregolith-Transportsystem mit flexiblen Mechanismen. Diese Mechanismen erzielen Bewegung durch elastische Verformung, wodurch gleitende tribologische Paare vermieden werden und damit eine implizite Widerstandsfähigkeit gegenüber abrasiven Staubpartikeln gewährleistet wird.

Sechs Transportkonzepte wurden zusammengestellt und hinsichtlich ihrer Leistungs-, Umwelt- und Zuverlässigkeitsanforderungen bewertet. Das Sägezahnförderer-Konzept ging aus der Konzeptentwicklung als optimaler Mechanismus für den Transport von Regolith innerhalb einer Verarbeitungseinrichtung hervor, da es einen kontinuierlichen Materialfluss gewährleistet und sich an die bestehende Aufbereitungsarchitektur anpassen lässt. Um die extremen Temperaturen im Mondvakuum zu bewältigen, wurden Formgedächtnislegierungen für die Antriebstechnik ausgewählt. Ihre im Vergleich zu Konkurrenzlösungen immense volumetrische Energiedichte gleicht die inhärente Einschränkung niedriger Hubfrequenzen aus. Der Mechanismus wird durch nachgiebige Bieggelager geführt, um eine präzise Parallelbewegung zu gewährleisten und eine vollständige, implizite Staubwiderstandsfähigkeit zu erreichen.

Es wurde eine maßgeschneiderte zweidimensionale Systemsimulation programmiert und durch Versuche unter terrestrischen Bedingungen mit Quarzsand und Glasperlen validiert. Mithilfe eines Optimierers wurde die Simulation durch die Bestimmung von drei empirischen Parametern an die tatsächlichen Ergebnisse angepasst. Unter Verwendung dieses validierten Simulationswerkzeugs wurde ein Mehrzieloptimierer eingesetzt, um sowohl die spezifische Energie pro transportierter Masse als auch die Hubfrequenz unter Berücksichtigung der Einschränkungen des Aktuators zu minimieren. Die endgültige Konfiguration erreichte eine Förderleistung von 70,27 kg/h bei einer maximalen Fördersteigung von 40°, was die Mindestanforderung von 6 kg/h deutlich übertraf. Diese Studie zeigt, dass die Kombination aus nachgiebigen Mechanismen und Formgedächtnis-Aktuatoren eine

hochleistungsfähige Lösung für den Transport von Mondregolith bietet und einen zuverlässigen Langzeitbetrieb für zukünftige Einsätze auf der Mondoberfläche gewährleistet.

Abstract

As humanity looks to return to the Moon, the need for in-situ resource utilisation, that is, the use of materials present on the lunar surface, becomes increasingly important. The most abundant material usable for ISRU is the lunar regolith, covering the surface of the Moon. In all steps of a regolith-based ISRU process, regolith transport is required. While lunar regolith bears great possibilities for utilisation, it also poses a high risk to any hardware and crew stationed on the surface. Conventional mechanisms that incorporate sliding tribological pairs are inherently prone to excessive wear in this highly abrasive environment. To address this problem in an ISRU processing facility, this study develops a lunar regolith transport system that incorporates compliant mechanisms. These mechanisms achieve motion through elastic deformation, eliminating any sliding tribological pairs and thus providing implicit resilience to abrasive dust.

Six transport concepts were synthesised and evaluated against performance, environmental, and reliability requirements. The sawtooth conveyor concept emerged from the concept development as the optimal mechanism for intra-facility transport due to its flow continuity and adaptability to existing beneficiation architecture. To overcome the extreme temperatures of the lunar vacuum, Shape Memory Alloys were selected for actuation. Their immense volumetric energy density, as compared to competitive solutions, compensates for their inherent limitation of low actuation frequencies. The mechanism is guided by compliant flexure bearings to ensure precise parallel motion and achieve full implicit dust mitigation.

A custom two-dimensional system simulation was programmed and validated with tests under terrestrial conditions using quartz sand and glass beads. An optimiser was used to align the simulation to the real-world results by determining three empirical parameters. Utilising this validated simulation tool, a multi-objective genetic algorithm was employed to minimise both the specific energy per unit transported mass and the stroke frequency, accounting for the actuator's limitations. The final optimised lunar configuration successfully achieved a feed rate of 70.27 kg/h at a maximum transport slope of 40°, significantly exceeding the minimum requirement of 6 kg/h. This study demonstrates that pairing compliant mechanisms with SMA-actuators yields a highly capable lunar regolith transport solution, ensuring reliable long-term operation for future sustained operations on the lunar surface.

Contents

List of Figures

List of Tables

List of Abbreviations

ADLIF anti-symmetric double leaf-type isosceles-trapezoidal flexure joint

ANOVA Analysis of variance

AOR Angle of Repose

APA Amplified Piezoelectric Actuator

CAD Computer Aided Design

CM Compliant Mechanism

CNSA Chinese National Space Agency

COR Coefficient of Restitution

CV Coefficient of Variation

CPU Central Processing Unit

DEM Discrete Element Method

DLR German Aerospace Center

DPFB Double Parallelogram Flexure Bearing

ESA European Space Agency

EVA Extravehicular Activity

FFKM Perfluoroelastomer

GA Genetic Algorithm

IDM Implicit Dust Mitigation

ILRS International Lunar Research Station

ISRU In-Situ Resource Utilisation

ISS International Space Station

JWST James Webb Space Telescope

LDEF Long Duration Exposure Facility

LEO Low Earth Orbit

LIBS Laser-induced Breakdown Spectroscopy

LOP-G Lunar Orbital Platform-Gateway

LUNA LUNA Analog Facility

MAE Mean Absolute Error

MOF Main Optimisation Function

MSE Mean Squared Error

MTBF Mean Time Between Failures

MTTR Mean Time To Repair

NASA National Aeronautics and Space Administration

OC Operational Constraints

PEL Peaks of Eternal Light

PLA Polylactic Acid

POC Proof-of-concept

PSR Permanent Shadow Regions

PTFE Polytetrafluoroethylene

RAMS Reliability, Availability, Maintainability, Safety

SDOF Single Degree of Freedom

SMA Shape Memory Alloy

SPE Solar Particle Events

SPFB Single Parallelogram Flexure Bearing

SPOF Single Point of Failure

SRC Space Resources Challenge

SSA Specific Surface Area

SSE Sum of Squared Estimate of Errors

TRL Technology Readiness Level

UV Ultraviolet

List of Symbols

Latin Letters

Symbol	Description	Unit
a	Acceleration	$\mathrm{m/s^2}$
A_{particle}	Frontal area of the particle	$\mathrm{m^2}$
a_{actual}	Actual acceleration	$\mathrm{m/s^2}$
a_{conv}	Conveyor acceleration	$\mathrm{m/s^2}$
$\mathbf{a}_{\mathrm{conv}}$	Conveyor acceleration vector	$\mathrm{m/s^2}$
a_{eff}	Effective acceleration	$\mathrm{m/s^2}$
$\mathbf{a}_{\mathrm{eff}}$	Effective acceleration vector	$\mathrm{m/s^2}$
A_f	Austenitic finish temperature	K
A_{regolith}	Cross-sectional area of regolith fill	$\mathrm{m^2}$
A_{annulus}	Cross-sectional area of annulus	$\mathrm{m^2}$
A_{surface}	Surface area of wire	$\mathrm{m^2}$
a_{upstroke}	Upstroke acceleration	$\mathrm{m/s^2}$
b	Linear drag constant	kg/s
C_D	Drag coefficient	–
C_s	Stroke work coefficient	–
c	Cohesion	Pa
c_{loose}	Cohesion of loose material	Pa
c_1	Collision parameter	–
c_2	Collision parameter	–
c_3	Collision parameter	–
$c_{\mathrm{p,wire}}$	Specific heat capacity of wire	$\mathrm{J/(kg\,K)}$
d	Distance / Diameter	m
d_{avg}	Average particle distance	–
d_{wire}	Wire diameter	m
E_{conv}	Young's modulus of conveyor	Pa
$\mathbf{e}_n$	Normal vector	–
E_{particle}	Young's modulus of particle	Pa
$\dot{E}_{\mathrm{st}}$	Change in stored thermal energy	W
E^*	Effective Young's modulus	Pa

Symbol	Description	Unit
E_x	Centre of mass of particle distribution	–
f	Generic function	–
F_B	Buoyancy force	N
F_{bias}	Bias force	N
F_D	Atmospheric drag force	N
$F_{\text{D,quad}}$	Quadratic drag force	N
$F_{\text{D,stokes}}$	Stokes' drag force	N
F_G	Gravitational force	N
F_{kin}	Kinetic acceleration force	N
F_L	Lift force	N
f_{limit}	Stroke frequency limit	Hz
F_N	Normal force	N
f_{POC}	Stroke frequency in POC tests	Hz
F_{pot}	Potential energy force	N
F_{recovery}	Recovery force	N
f_{stroke}	Stroke frequency	Hz
f_{supply}	Supply frequency	Hz
g	Gravitational acceleration	m/s^2
g_{earth}	Terrestrial gravitational acceleration	m/s^2
g_{moon}	Lunar gravitational acceleration	m/s^2
$\mathbf{g}$	Gravitational acceleration vector	m/s^2
h	Pile height / Generic point index	m
h_{0-15}	Slope height for 0–15 cm depth	m
h_{30-60}	Slope height for 30–60 cm depth	m
i	Individual simulated particle index	–
I	Moment of inertia	kg m^2
j	Individual conveyor tooth index	–
$j_{\text{end,i}}$	Final resting tooth of particle i	–
k_{drag}	Empirical drag parameter	–
k_{elastic}	Elastic normal coefficient of restitution	–
k_{norm}	Normal coefficient of restitution	–
k_{plastic}	Plastic coefficient of restitution	–
k_{tang}	Tangential coefficient of restitution	–
$k_{\text{tang,sph}}$	Tangential coefficient of restitution for spheres	–
l	Generic length / Distance	m
L	Characteristic length	m
l_a	Tooth length (horizontal)	m

Symbol	Description	Unit
l_{adv}	Advancement wire length	m
$l_{\text{adv,hor}}$	Horizontal advancement distance	m
$l_{\text{adv,vert}}$	Vertical advancement distance	m
l_b	Tooth height (vertical)	m
l_c	Tooth pitch	m
l_{chain}	Chain length (Concept 6)	m
l_{conv}	Conveyor length	m
l_{element}	Rigid element length	m
$l_{\text{hinge,bent}}$	Bent hinge length	m
$l_{\text{hinge,straight}}$	Straight hinge length	m
l_{hor}	Horizontal transportation distance	m
l_{limit}	Particle distance limit	m
l_{SMA}	SMA contraction length	m
l_{stroke}	Stroke length	m
l_{t}	Plate thickness	m
l_{total}	Total sled length	m
l_{wall}	Sidewall height	m
l_{width}	Conveyor width	m
l_{wire}	Wire length	m
m	Mass	kg
m_{conv}	Conveyor mass	kg
$\dot{m}$	Average mass flow	kg/h
M_f	Martensitic finish temperature	K
$\dot{m}_{\text{limit}}$	Target mass flow limit	kg/h
m_{regolith}	Regolith mass	kg
$\dot{m}_{\text{regolith}}$	Regolith mass flow	kg/h
m_{sled}	Sled mass	kg
m^*	Effective mass	kg
$m_{\text{tooth,poc}}$	Tooth regolith mass in POC	kg
m_{total}	Total moved mass	kg
MAE	Mean absolute error	–
n	Number / Count	–
n_{adv}	Number of advancements	–
n_{bounce}	Number of bounce iterations	–
$n_{\text{inflection}}$	Number of inflection points	–
n_{launch}	Number of launched particles	–
n_{pop}	Population size	–

Symbol	Description	Unit
n_{teeth}	Number of teeth	–
n_{trough}	Number of wave troughs	–
$n_{\text{variables}}$	Number of optimization variables	–
n_{wire}	Number of actuation wires	–
P_0^*	Maximum contact pressure	Pa
p_1	Tooth profile point 1	–
p_2	Tooth profile point 2	–
p_3	Tooth profile point 3	–
p_4	Tooth profile point 4	–
P_{avg}	Average continuous power draw	W
$p_{\text{fill,2}}$	Regolith fill line intersection on second tooth	–
$\bar{P}_j$	Normalized particle mass ratio	–
p_{limit}	Limit stress / Contact pressure	Pa
p_{proj}	Projection point along ramp	–
$q_{\text{obj,1}}$	Optimization objective 1	–
$q_{\text{obj,2}}$	Optimization objective 2	–
Q_{rad}	Heat loss rate due to radiation	W
r	Catch radius / Generic radius	m
r_{hinge}	Hinge radius	m
r_{inner}	Inner radius of annulus	m
r_{outer}	Outer radius of annulus	m
r_{SMA}	SMA wire radius	m
r^*	Effective radius	m
Re	Reynolds number	–
s	Ramp length	m
s_{grav}	Gravity scaling factor	–
s_j	Standard deviation per test run	–
s_{scale}	Scale factor	–
SSE	Sum of squared errors	–
t	Time	s
T	Temperature	K
t_1	Intersection point 1	–
t_2	Intersection point 2	–
t_{adv}	Advancement time	s
t_{conv}	Conveyance duration	s
t_{cool}	Cooldown time	s
T_{cool}	Cooldown temperature	K

Symbol	Description	Unit
t_{down}	Downstroke time	s
T_{high}	High limit temperature	K
T_{hot}	Target heating temperature	K
t_i	Particle flight time	s
$\tilde{t}_i^{col}$	Collision flight time with drag	s
T_∞	Ambient temperature	K
T_{low}	Low limit temperature	K
t_{stroke}	Stroke time	s
t_{up}	Upstroke time	s
$\mathcal{U}$	Continuous uniform distribution	–
v	Velocity	m/s
v_0	Initial launch velocity	m/s
v_{actual}	Actual velocity	m/s
$\mathbf{v}^{\text{bounce}}$	Bounce velocity vector	m/s
v_{chain}	Chain transport direction velocity	m/s
v^{col}	Collision velocity	m/s
$v_{\text{max}}^{\text{col}}$	Maximum collision velocity	m/s
$\mathbf{v}_{i,\text{normal}}^{\text{col}}$	Normal velocity component at collision	m/s
$\mathbf{v}_{i,\text{tangent}}^{\text{col}}$	Tangential velocity component at collision	m/s
$\tilde{v}_{\text{col}}$	Collision velocity with drag	m/s
$\mathbf{v}^{\text{col}}$	Collision velocity vector	m/s
$v_{\text{contraction}}$	Contraction movement velocity	m/s
v_d	Downstroke velocity	m/s
v_{limit}	Limit velocity for plastic deformation	m/s
$v_{\text{norm}}^{\text{col}}$	Normal component of collision velocity	m/s
$\dot{V}_{\text{POC}}$	Volumetric flow rate in POC	m^3/s
$v_{\text{tang}}^{\text{col}}$	Tangential component of collision velocity	m/s
$\mathbf{v}$	Velocity vector	m/s
V_{wire}	Volume of the cylindrical wire	m^3
W_{bias}	Bias work	J
W_{heat}	Heating energy	J
$W_{\text{heat,adv}}$	Heating energy for advancement	J
$W_{\text{heat,conv}}$	Total heating energy for conveyance	J
$W_{\text{margin,SMA}}$	SMA margin work (recovery minus bias)	J
$w_{\text{pen},1}$	Stroke frequency objective penalty weight	–
$w_{\text{pen},2}$	Stroke frequency objective penalty weight	–
w_{penalty}	Penalty weight in optimization	–

Symbol	Description	Unit
$w_{\text{penalty,1}}$	Mass flow objective penalty weight	–
$w_{\text{penalty,2}}$	Specific energy objective penalty weight	–
W_{rad}	Total energy lost due to radiation	J
W_{recovery}	Recovery work	J
W_{spec}	Specific energy	J/kg
W_{total}	Total energy	J
W_{upstroke}	Energy per upstroke	J
w_v	Volumetric energy density	J/m^3
x	X-coordinate	m
$\bar{x}$	Average / Mean value	–
$\Delta\bar{x}$	Average bounce distance	m
x_{col}	Collision x-coordinate	m
$x_{\text{end,i}}$	Final x-coordinate	m
x_{hor}	Horizontal component	m
x_{launch}	Launch x-coordinate	m
x_{local}	Local x-coordinate	m
$\|\|x\|\|$	Magnitude of a vector	–
$\tilde{x}$	Horizontal position with drag	m
y	Y-coordinate	m
y_{base}	Base section y-coordinate	m
Y_{conveyor}	Yield strength of conveyor	Pa
y_{fill}	Fill line y-coordinate	m
y_{launch}	Launch y-coordinate	m
y_{local}	Local y-coordinate	m
Y_{particle}	Compressive strength of particle	Pa
y_{ramp}	Ramp section y-coordinate	m
$\tilde{y}$	Vertical position with drag	m
y_{traj}	Trajectory y-coordinate	m
z_{conv}	Generic coordinate of conveyor	m
z_{particle}	Generic coordinate of particle	m
z^*	Effective generic coordinate	m

Greek Letters

Symbol	Description	Unit
α	Conveyor angle	deg
β	Angle of apparent effective acceleration	deg
δ	Particle launch angle	deg
Δh	Lateral distance decrease	m
δ_i	Launch angle of individual particle	deg
Δl_{adv}	Total advancement distance	m
$\Delta l_{\text{adv,hor}}$	Horizontal advancement distance	m
$\Delta l_{\text{adv,vert}}$	Vertical advancement distance	m
Δl_{SMA}	SMA contraction distance	m
δ_{offset}	Launch angle offset	deg
ΔT	Temperature difference	K
ΔW_{pot}	Potential energy change per wave advancement	J
ϵ_{max}	Maximum actuation strain	–
ϵ_{wire}	Emissivity of SMA wire	–
γ	Weight density	N/m^3
λ	Randomization scaling factor	–
λ_i	Randomization factor for particle i	–
λ_{max}	Upper bound randomization factor	–
λ_{min}	Lower bound randomization factor	–
μ	Mass-specific linear drag / Dynamic viscosity	$\text{s}^{-1}/\text{Pa s}$
μ_{dynamic}	Dynamic viscosity	Pa s
μ_{friction}	Friction coefficient	–
μ_s	Coefficient of static friction	–
ν_{conv}	Poisson's ratio of conveyor	–
ν_{particle}	Poisson's ratio of particle	–
ω	Catch angle at the base intersection	deg
ϕ	Tooth angle / angle of internal friction	deg
ρ	Fluid density	kg/m^3
ρ_{alu}	Density of aluminium	kg/m^3
ρ_b	Bulk density	kg/m^3
ρ_{particle}	Density of particle	kg/m^3
$\rho_{\text{regolith,min}}$	Uncompressed regolith bulk density	kg/m^3
ρ_{wire}	Wire density	kg/m^3
$\rho_{\text{wire,l}}$	Wire linear density	kg/m
σ	Stefan–Boltzmann constant	$\text{W}/(\text{m}^2\,\text{K}^4)$
σ_f	SMA detwinning finish stress	Pa
σ_{max}	Maximum actuation stress	Pa

Symbol	Description	Unit
σ_{pooled}	Pooled standard deviation	–
σ_x	Spatial dispersion	–
τ	Pole pitch	m
θ	Angle of repose	deg
θ_{acc}	Angle of repose during acceleration	deg
θ_{static}	Static angle of repose	deg
ξ	Launch angle relative to conveyor	deg
$\xi_{\text{offset},2}$	Acceleration angle offset of conveyor	deg
ζ	Maximum actuation angle	deg

symbol list aktualisieren

1. Introduction

For the first time since the Apollo program ended in 1972, humanity is looking to resume crewed missions to the Moon. The Lunar Orbital Platform-Gateway (LOP-G) was proposed and developed to house astronauts for multi-week stays and to continue the international collaboration that culminated in the International Space Station (ISS). This program has been "paused" by the National Aeronautics and Space Administration (NASA) in favour of permanent infrastructure on the lunar surface for sustained operations [1]. This Moon base, to be created in collaboration with international partners [1], as well as the International Lunar Research Station (ILRS) proposed by the Chinese National Space Agency (CNSA) [2], marks the international dedication to long-term lunar surface activities.

The sustained lunar operations proposed by both NASA and CNSA cannot fully rely on terrestrial supplies, as is customary with stations in Low Earth Orbit (LEO) [3]. High transport expenses from Earth to the Moon dictate the use of local resources wherever possible [4]. Instead, the resources local to the Moon are used. This concept is called In-Situ Resource Utilisation (ISRU). The most abundant material on the Moon is lunar regolith, which covers the body's surface in a layer several meters thick [5, p. 286]. This conglomerate consists primarily of glass aggregates, rock fragments and other minerals. [5, p. 288]. At the lunar poles, however, Permanent Shadow Regions (PSR) are completely shielded by solar illumination, and thus may allow for significant water-ice deposits intermixed with the lunar regolith [6]. While dry regolith offers many possibilities for producing metals and other construction materials, as well as oxygen to support a human settlement, utilisation of icy regolith would enable in-situ fabrication of propellant and water [7]. For these reasons, the United States' Artemis program, as a successor to the Apollo missions and forerunner for sustained surface operations, chose the lunar south pole as the destination for humans to land [3].

An ISRU infrastructure typically comprises excavation, beneficiation, and utilisation steps. In all process steps, material transport between subsystems is required. In their second Space Resources Challenge (SRC) in 2025, focused on the excavation and beneficiation steps, the European Space Agency (ESA) challenged contestants to develop systems to gather lunar regolith simulant and perform size-based beneficiation, separating the collected material by grain size. The SRC concluded with a field test in the German Aerospace Centre's (DLR) LUNA Analog Facility (LUNA). In this field test, teams were tasked with collecting and beneficiating 15 kg of lunar regolith simulant in 2.5 h [8]. In the winning en-

try by Team BREMEN, a conveyor-belt-based regolith transport-and-dosing mechanism was used [9].

1.1 Problem Statement and Scope of Work

While lunar regolith is a major resource for ISRU, enabling the production of various products, it is also one of the greatest dangers to mechanisms operating on the Moon. Dust resilience is a primary design driver, as small, abrasive, and electrostatically charged regolith particles pose a high risk to conventional mechanical components such as bearings and motors (cf. Section 2.2.1). Furthermore, the extreme temperature fluctuations on the lunar South Pole prohibit the use of standard terrestrial systems.

This study builds on the SRC to increase the longevity of lunar regolith transport systems for ISRU by incorporating compliant mechanisms to achieve implicit dust mitigation. Team BREMEN's regolith transport-and-dosing mechanism serves as the reference for the system requirements developed in this work. This thesis shall answer the research question:

How can in-process regolith transportation be realised in the harsh lunar environment?

The primary objective of this work is the development of a lunar regolith transport system that fulfils the role described above and enables implicit dust mitigation through the utilisation of compliant mechanisms. Existing research on compliant mechanisms and techniques for regolith transport forms the foundation for the subsequent development of potential transportation concepts. In the scope of the concept development, the advantages and limitations of different concepts and actuation methods are discussed. Proof-of-concept tests are conducted on two of the synthesised concepts before one is further developed for application in the harsh lunar environment. A system simulation is created, culminating in a parameter optimisation utilising multi-objective genetic algorithms to maximise the concept's potential. The thesis concludes with a summary of the findings and an outlook on future work on the developed concepts and on lunar regolith transport.

2. Technical Background and State of the Art

This chapter provides a technical background to this study and discusses the state of the art of lunar regolith transport mechanisms and compliant mechanisms. Initially, the environmental boundary conditions on the lunar surface are explored in Section 2.1. Lunar regolith is investigated in Section 2.2, first taking a look at its physical properties, before examining existing concepts of transport mechanisms for granular materials, especially those proposed for lunar regolith transport. The state of the art in compliant mechanisms and their proposed use on the lunar surface is surveyed in Section 2.3. This chapter concludes with the definition of system requirements in Section 2.4, on the basis of which the concept development is performed in the next chapter.

2.1 Environmental Boundary Conditions for Lunar ISRU

The lunar surface is characterised by extreme environmental conditions, including extreme temperatures, high vacuum, unimpeded radiation and reduced gravity relative to Earth's. This section provides an overview of the environmental conditions in which the lunar regolith transport mechanism must function.

Extreme temperature gradients on the lunar surface impose strict thermal requirements on hardware. The temperature environment differs significantly across the lunar surface. While the equatorial regions are governed by intense variations due to the lunar day-night cycle, the polar regions exhibit intense local gradients. Regions of near-constant illumination, known as Peaks of Eternal Light (PEL), neighbour the contrasting Permanent Shadow Regionss. The Shackleton crater has been identified as a prime destination for ISRU efforts within the Artemis program [10] and is assumed to be the target in this study. Shackleton crater features a PSR in proximity to PELs, with large portions of the crater being permanently shielded from both Sun and Earth [11]. Bussey et al. identified the single point of maximum illumination in the lunar south pole region to be located near the rim of Shackleton crater, with an illumination fraction of 86 %. Average surface temperatures on the crater floor reach as low as 50 K (with minimum temperatures ca. 10 K lower), as illustrated in Figure 2.1. The neighbouring regions outside the PSR exhibit

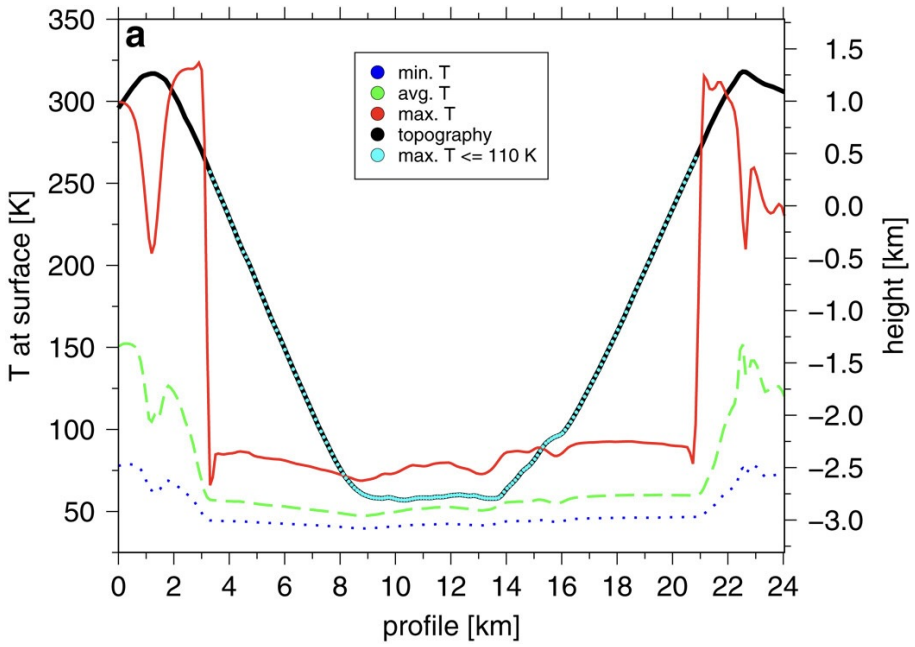

Figure 2.1: Shackleton crater surface temperatures, retrieved from Gläser et al. [6]

temperatures of up to 320 K [6]. For comparison, mid-latitude sites such as the Apollo 15 landing site exhibit daytime temperatures up to 374 K with night-time temperatures as low as 92 K [5, p. 34]. Temporal temperature fluctuations inside the PSRs are significantly lower, at ca. 25 K difference between the maximum and minimum temperatures inside Shackleton crater.

The Moon features a surface-boundary exosphere, representing a high-vacuum environment at a pressure of 3×10^{-15} bar. In these extremely low pressure environments, the pressure is replaced as a measurement by the number density; the number of particles per volume. The number density varies significantly during the day-night cycle from 10^6 particles/cm^3 during daytime to 2×10^5 particles/cm^3 during nighttime [12]. For this study, these changes are insignificant, and the lunar atmosphere is considered negligible. This low ambient pressure poses risks of cold welding for metals as well as outgassing for polymers [13, 14]. The lunar gravity is significantly lower than Earth's at approximately 1.62 m/s^2 (often cited as 1/6$^{\text{th}}$ of Earth's gravity). This may benefit transport systems by reducing the energy required to lift mass, though it also alters granular flow behaviour.

On Earth, chronic radiation stemming from solar wind, solar cosmic rays, and galactic cosmic rays is generally deflected by the magnetic field and atmosphere [15, p. 164]. The Moon, however, is not protected by Earth's magnetosphere and is thus subject to an intense radiation environment dominated by solar protons and galactic cosmic rays [16]. This radiation can have both instantaneous effects, primarily inhibiting the proper functioning of electronic devices due to single-ionising-particle interactions [16], and cumulative effects, such as increased polymer degradation [17]. Another effect of the lunar environment is the buildup of charge on the hardware and the triboelectric charging of the lunar

surface. This leads to adhesion between mechanisms and lunar soil, thereby increasing the dust load on moving parts [16].

The lunar surface is further exposed to a continuous influx of micrometeoroids, which have been examined for their potential danger to lunar infrastructure. For a base of similar dimensions to the International Space Station, located at the lunar south pole, the incident impact rate is estimated at ca. 15,000 impacts per year of particles in the range of 10×10^{-6} g to 10^{1} g [18]. This corresponds to an approximate flux of 1.5 particles/m^2 per year. While it is imperative that any components and the larger system remain unharmed by this influx, micrometeorites are not considered a significant danger. This evaluation must be revisited for application in long-distance transport.

The remoteness and inaccessibility of the proposed sites further constrain the design of ISRU infrastructure. The energy, and thus the expense, required for the transport from Earth to the lunar surface significantly exceeds the propulsive requirements for reaching LEO, rendering the terrestrial repair or resupply of failed mechanisms economically infeasible [4]. During the Artemis program, periods in which the facilities are uncrewed are expected to be in the range of 335 days [4], setting the requirement for self-sufficient systems that require no regular maintenance.

These environmental effects significantly complicate the use of conventional mechanisms for lunar regolith transport. Tribological pairs, as found in components such as electric motors and bearings, are inherently prone to high wear due to harsh, dusty environments. Abrasion of protective oxide layers, combined with direct metallic contact in these components, enables cold welding, which subsequently leads to increased friction and even mechanical seizure. The abrasive characteristics of lunar regolith will be discussed in more detail in Section 2.2.1. The limited applicability of polymers due to outgassing, extreme temperatures, and increased radiation-induced degradation limits the ability to shield components against the ingress of abrasive particles.

2.2 Properties and Handling of Lunar Regolith

While an important resource whose transport is the focus of this study, lunar regolith also poses a significant danger to any hardware and crew operating on the lunar surface. This section discusses the physical properties of lunar regolith and the resulting problems it poses. Subsequently, the state of the art of terrestrial transport mechanisms for granular material is examined, with a focus on systems proposed for lunar application and regolith transport. The section closes with remarks on the requirement for active or passive dust mitigation techniques in most transport systems and introduces the alternative of implicit dust mitigation.

2.2.1 Physical Properties of Lunar Regolith

The morphology of lunar regolith is characterised by its rugged surface and low sphericity. These properties can be quantified with the Specific Surface Area (SSA). According to Kring, a granular material with perfectly spherical particles, equivalent to lunar soil in particle size, would exhibit an SSA of $0.065\,\mathrm{m^2/g}$, nearly an order of magnitude less than the average value for lunar soil at $0.5\,\mathrm{m^2/g}$ [19]. The particle morphology is characterised by extreme angularity and re-entrant surfaces, which enable high cohesion through particle interlocking under pressure [20]. The cohesion of lunar regolith is highly dependent on its compression. The Lunar Sourcebook [5, pp. 492, 510] provides the reader with recommended values of cohesion, internal friction angle and bulk density for different depth ranges (and thus different compressions) of lunar regolith: To illustrate the signif-

Table 2.1: Soil mechanical parameters for lunar regolith at different depth ranges

Property	**Depth range [cm]**	**Value**
Cohesion c	0–15	$0.52\,\mathrm{kPa}$
Angle of internal friction ϕ	0–15	$42°$
Bulk density ρ_b	0–15	$1.50 \pm 0.05\,\mathrm{g/cm^3}$
Cohesion c	30–60	$3.0\,\mathrm{kPa}$
Angle of internal friction ϕ	30–60	$54°$
Bulk density ρ_b	30–60	$1.74 \pm 0.05\,\mathrm{g/cm^3}$

icant changes in cohesion due to compression, the maximum height of a vertical slope is calculated for these two lunar regolith levels. Using the soil mechanical properties from Table 2.1 with the gravitational acceleration on the Moon $g_{\mathrm{moon}} = 1.625\,\mathrm{m/s^2}$ results in vertical slope heights of $h_{0-15} = 1.92\,\mathrm{m}$ and $h_{30-60} = 13.06\,\mathrm{m}$ [21]. The cohesion of lunar regolith will be examined in more detail in Section 4.1.1.

Particle sizes measured in samples retrieved by the Apollo missions range from $10^{-3}\,\mathrm{mm}$ to $10^{1}\,\mathrm{mm}$, with a median of $7.2 \times 10^{-2}\,\mathrm{mm}$, commonly described as "either silty sand or sandy silt", according to Carrier [22, p. 1]. The fraction of particles with sizes under $20\,\mu\mathrm{m}$ is in the range of 10 % to 20 %. These small particle sizes pose a significant risk to mechanisms due to their penetrating ability.

In terrestrial tests of mechanisms for application on the Moon, regolith simulants are commonly used due to the scarcity of lunar samples. In ESA's SRC, the EAC-1A lunar regolith simulant was used, with particle sizes ranging from $<1\,\mu\mathrm{m}$ to $<2\,\mathrm{mm}$. Lunar regolith shows a similar composition; however, the extent of the lower-size fractions remains poorly characterised [23]. While the EAC-1A simulant only aims to represent the lunar soil, as defined by Heiken et al., that is the finer-grained fraction of the lunar regolith [5, p. 287], there is also a significant amount of larger components present in the lunar regolith, ranging up to a particle size of several millimetres [5, p. 478]. The system

developed in this study shall work not only with small particles of lunar soil but also with the larger particles present in lunar regolith.

Regolith is a complex mixture of rock fragments, mineral grains, breccias, impact/volcanic glasses, and agglutinates. The exact composition varies significantly with the exact sample site [5, p. 292]. The primary silicate minerals in lunar rocks are plagioclase feldspar, pyroxene and olivine [5, p. 122]. Lunar material is strictly anhydrous, completely lacking water-bearing minerals such as clays, micas, or amphiboles that are ubiquitous on Earth [5, p. 2]. Elemental iron (Fe^0) is found in the lunar regolith in significant doses, occurring primarily in very small particle sizes of <300 Å. These fine single-domain iron particles are commonly contained in agglutinates, fused particles produced by micrometeorite impacts. Mature soils, that is, components of the lunar regolith that have gone through extensive weathering by micrometeorites, contain up to 60 % agglutinates by volume [5, p. 296], increasing the bulk magnetic susceptibility of the lunar soil [24]. The iron-nickel alloy kamacite represents the most prevalent macro-scale metallic species, which is also highly ferromagnetic [5, p. 151].

Lunar regolith dust was identified in the Apollo program as a major concern for extended operation on the Moon. Eugene A. Cernan, commander of the Apollo 17 mission, referred to dust as "probably one of the most aggravating, restricting facets of lunar surface exploration" [25, p. 27-27]. Gaier summarised reports on dust from the Apollo missions in [26]. He notes that both clogging of mechanisms and severe abrasion proved problematic in all Apollo missions. The lunar regolith led to binding in several systems, such as the lunar equipment conveyor (a tether aiding sample loading) [27, p. 11-14], and the vacuum cleaner used to remove dust from the equipment [26]. Abrasion led to extensive wear, limiting visibility through gauges and visors and increasing the perceived wear on the Extravehicular Activity (EVA) suits by an order of magnitude, according to Pete Conrad, commander of the Apollo 12 mission [26]. The abundance of small particles in lunar regolith and the low gravitational acceleration result in large amounts of airborne dust during any surface activity. During the Apollo missions, dust coated any surfaces it contacted, with surface cleaning not always possible [28, pp. 9.19, 9.20].

2.2.2 Lunar Regolith Transport

This section gives an overview of the current state of the art of proposed lunar regolith transport mechanisms. Belt conveyors are widely employed in terrestrial industries, including high-purity environments such as the pharmaceutical sector [29], as well as in the mining sector, where they handle abrasive bulk materials [30]. These systems are highly versatile, capable of transporting both discrete unit loads and bulk materials. In a belt conveyor, a belt is tensioned by rollers that provide both structural support and

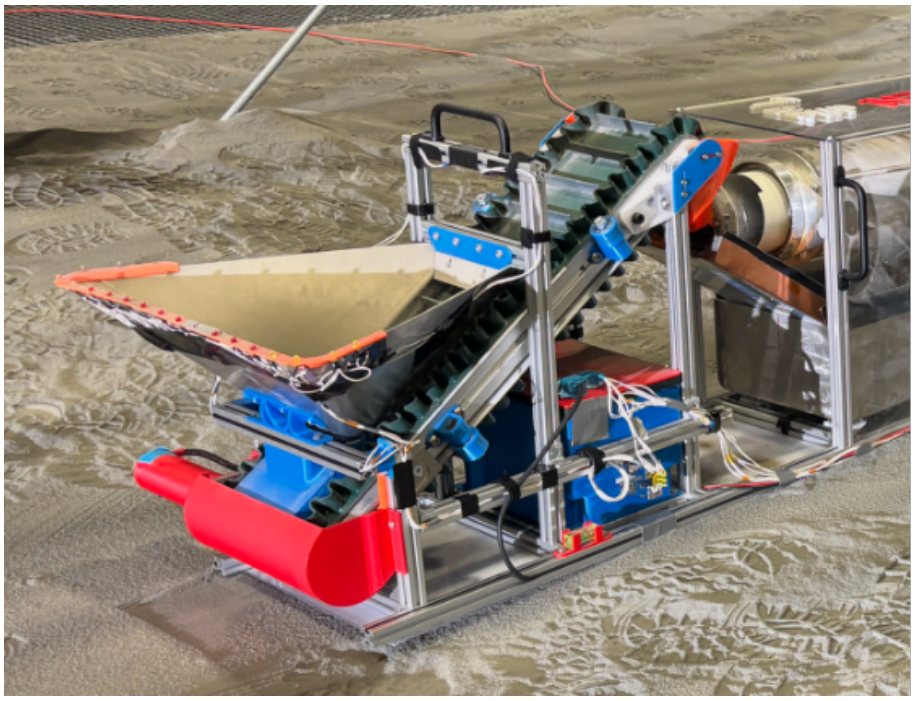

Figure 2.2: Belt conveyor used by Team BREMEN in the SRC as part of "Perry the Dosing Mechanism"

the driving force. For bulk material transport, the belt surface often features cleats for improved traction and corrugated sidewalls for material containment. Belt conveyors have been used in several regolith transport concepts in low Technology Readiness Level (TRL) development challenges. In ESA 's SRC, belt conveyors were used in concepts by Team BREMEN and Team FZI DUST [9, 31]. The transport-and-dosing mechanism used by Team BREMEN is shown in Figure 2.2. In the "Over the Dusty Moon Challenge", a belt conveyor was proposed for the horizontal transport subsystem by Team Spaceship [32].

Bucket elevators are similar to belt conveyors in that pulleys tension a flexible element and supply the driving force. In contrast to the belt conveyor, the flexible element is not the primary component that interfaces with the transported material. Instead, buckets carrying the bulk material are mounted on the flexible element. Since the flexible element is not directly in contact with the bulk material, chains and wire ropes may be used instead of belts. This concept has been proposed for use in a lunar ISRU process chain, though it suffers from the same problems as the belt conveyor in the use of bearings and a rotary motor. Additionally, linkages could bind due to dust if chains are used, as in the concept proposed by Kulinowski [33]. A bucket elevator was used as an excavator in the SRC by Team BREMEN (cf. Figure 2.3) [9].

Screw conveyors are commonly designed as a screw rotating inside a static tube or open trough, though variants with a screw fixed to a rotating tube are also used. In the concept utilising a static tube, ingress of regolith between the rotating screw and outer tube inherently results in high friction and poses a significant danger of binding. In systems

Figure 2.3: Bucket elevator used in the SRC for excavation by Team BREMEN, Photo: ©ESA

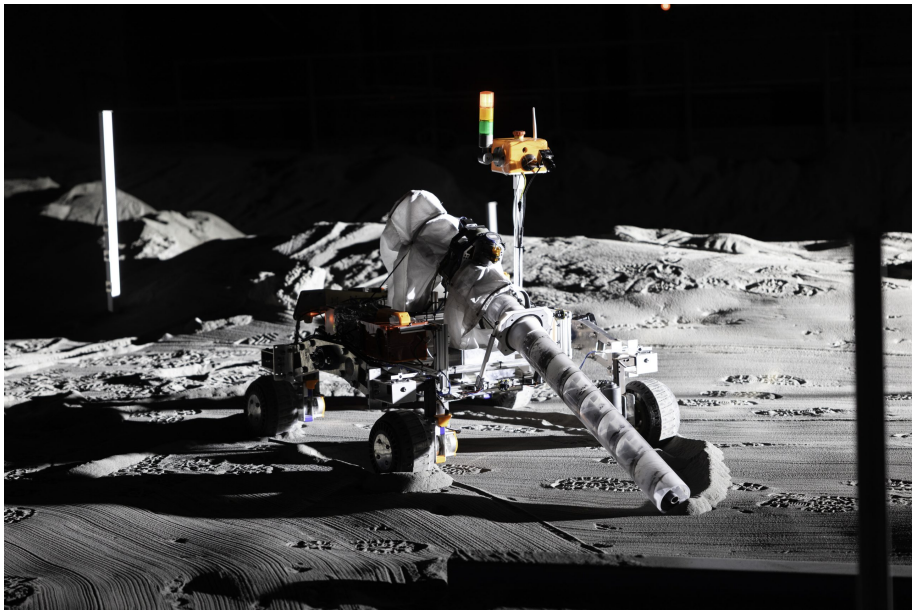

Figure 2.4: Screw conveyor used in the SRC for excavation by Team IPRL-API, Photo: ©ESA

proposed for lunar use, the variant connecting the screw and tube is common. This concept is proposed for both applications within an ISRU processing facility and for long-distance transport across the lunar surface [34]. An image of this concept in use during the SRC can be seen in Figure 2.4. The relative motion between the screw and tube is eliminated by their coupling. The transported material is enclosed during transport, reducing losses and dust generation. Both screw conveyor variants were used in several concepts in ESA 's SRC [9, 35–37]. In all concepts incorporating a screw conveyor, but Team BREMEN's, the rotating screw was used for excavation as well as transport of regolith.

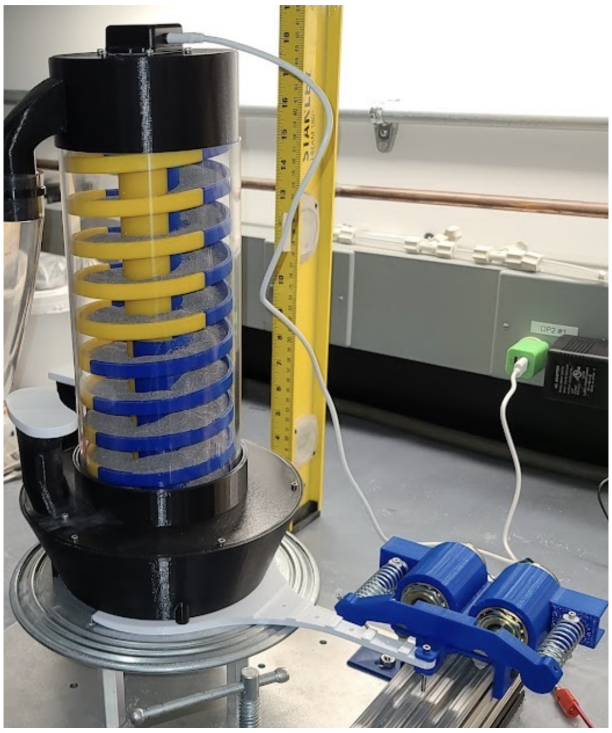

Figure 2.5: Prototype of a vibratory Spiral Conveyor as proposed by Olson et al. [38]

Vibratory conveyors are commonly used in industrial applications, including the food and mining industries [39]. They are often proposed for use on the Moon due to their minimal number of moving parts [40–42]. Kawamoto proposed using amplified piezoelectric actuators with vibratory conveyors for lunar regolith transport, thereby eliminating sliding tribological pairs. Piezoelectric actuators will be discussed in more detail in Section 3.1. The transport slope achievable with vibratory conveyors, however, is limited. Consequently, a variant of vibratory conveyors called spiral vibratory conveyors is commonly used for vertical transport, thereby avoiding slope limitations. The functioning principle of these conveyors has been tested under simulated lunar gravity [42]. A prototype of the tested system is shown in Figure 2.5. Vibratory conveyors will be elaborated on in Section 3.2.5.

The absence of atmosphere and low gravity enable ballistic transport. The high cohesion of compressed lunar regolith might enable the utilisation of such concepts with limited material losses. Ballistic transport has been proposed for long-distance transport [43,

p. 285], [44]. For the application within processing facilities, as discussed in this study, ballistic transport is deemed infeasible.

Taylor and Eimer proposed a magnetic excavation and conveying system. This concept utilises the ferromagnetic properties of the lunar regolith (as discussed in Section 2.2.1) to convey material magnetically. Here, a series of coils is staggered along a tube. Sequential powering of the coils moves the magnetic particles through the tube, similar in principle to a coil gun [45]. The extent of the magnetic fields beyond the tube allows for the introduction of material into the transport system from the lunar surface [46].

Most commonly proposed concepts, as well as solutions regularly used in terrestrial applications, feature tribological pairs as part of their design. In belt conveyors, bucket elevators, and screw conveyors, continuously rotating mechanisms necessitate the use of bearings and are driven by a rotary motor. In both components, regolith ingress poses a significant threat to increased friction and even binding of mechanisms, as discussed in Section 2.2.1. Consequently, regolith ingress must be prevented through active or passive dust mitigation. Active dust mitigation encompasses processes that actively exert a force to "clean" hardware [47]. As an example of active dust mitigation, electrodynamic dust shields transport dust particles off surfaces using electrodynamic forces generated by electrical traces on the hardware's surface. This technology has been tested and proposed for cleaning solar panels on lunar and Martian rovers [48]. Active dust mitigation significantly increases the complexity of these transportation concepts and requires additional energy. Passive dust mitigation offers a simpler, more efficient, but also more limited approach. These techniques aim to reduce dust load without actively exerting forces. This is commonly proposed with seals and coatings [47]. Vimukthi et al. examined the state of the art of passive dust-mitigation coatings and identified shortcomings, particularly regarding longevity under long-term abrasion by lunar regolith [49]. As an extension to the established approaches of active and passive dust mitigation, Budzyń et al. introduced the term Implicit Dust Mitigation. Unlike active and passive approaches, Implicit Dust Mitigation (IDM) does not aim to prevent dust from entering mechanisms or to remove it, but instead utilises mechanisms that are inherently resilient to the lunar regolith.

2.3 Compliant Mechanisms

This study proposes using Compliant Mechanisms (CMs) to create a regolith transport system that incorporates IDM. CMs achieve motion through elastic deformation, as opposed to relative movement between discrete parts connected by traditional kinematic pairs. As a result, CMs operate without sliding tribological pairs, thereby eliminating friction and the need for lubricants and seals. By removing the physical clearances and inter-element gaps necessary for rigid joints, backlash and wear-induced play are no con-

cern in CMs. The material's elastic deformation allows CMs to store and release energy, serving as integrated springs. Budzyń et al. initiated the research on the utilisation of

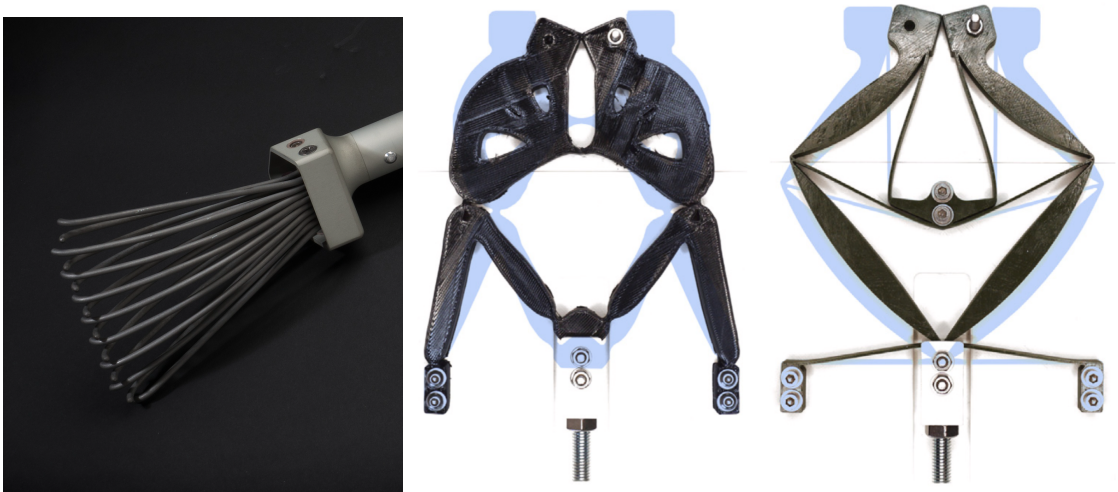

(a) Apollo tongs [50]

(b) Topology optimised compliant gripper [47]

(c) Analytically designed compliant gripper [47]

Figure 2.6: The tongs used on the Apollo missions, compared to the redesigned compliant mechanisms

Compliant Mechanisms for IDM with a case study on a compliant replacement for the "tongs" used in the Apollo missions [47, 51]. The tongs were a tool used for collecting small rocks with dimensions not exceeding 6 cm to 10 cm [51]. To achieve usability under the significant movement constraints imposed by the astronauts' rigid suits, the tongs featured a spring-loaded mechanism that automatically returned to its initial state after actuation [47]. The inherent characteristic of CMs to store elastic energy during bending allows for the incorporation of this spring-loading in the mechanism, without any additional components [47]. For this redesign, two foundational approaches of CMs were utilised: topology optimisation and analytical design [47]. The resultant geometries exhibit distinct morphological characteristics. The original tongs used in the Apollo missions are shown next to the two CM geometries created by Budzyń et al. in Figure 2.6.

CMs are commonly designed as combinations of rigid sections and compliant flexures. Both the topology-optimised geometry in Figure 2.6b and the analytically designed gripper in Figure 2.6c adopt this concept; the exact implementation varies. Carson and Wang categorised compliant flexures into four types: wire, blade, toroidal and notch [52]. In CMs that act only in-plane, such as the examples in Figure 2.6, the blade and notch flexures are used. The analytically designed gripper incorporated blade flexures, applicable for low-compression applications. In this application, the blade flexures are only loaded in tension. Notch flexures constrain all but a single rotational degree of freedom and are capable of compressive loading, as implemented in the topology optimised gripper. This comes, however, at the cost of a shorter stroke [52]. The wire and toroidal flexures can be seen as counterparts to the blade and notch in three-dimensional applications.

More advanced flexure types have been developed based on these foundational concepts. Cross-axis flexural pivots, cartwheel hinges, and more complex concepts, such as the anti-

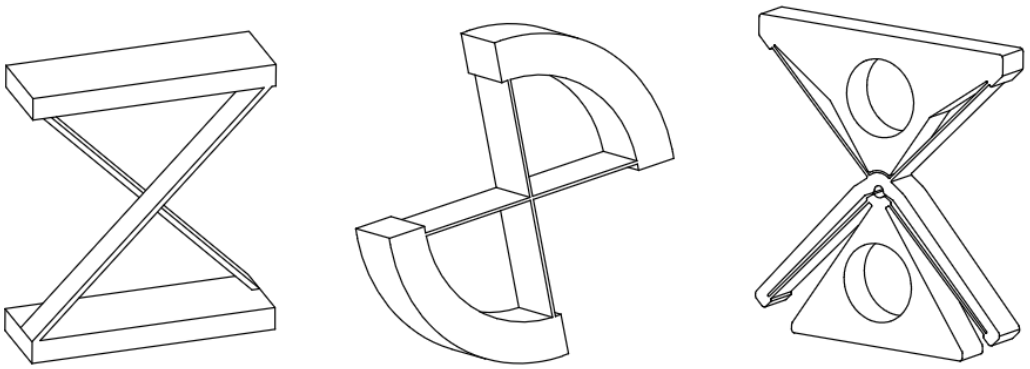

(a) Cross-axis flexural pivot (b) Cartwheel hinge (c) Anti-symmetric double leaf-type isosceles-trapezoidal flexure joint (ADLIF)

Figure 2.7: Complex flexure hinges based on blade flexures

symmetric double leaf-type isosceles-trapezoidal flexure joint (ADLIF), aim to achieve a trade-off between the low-constrained blade flexure and the low-stroke notch flexure [53]. These concepts are illustrated in Figure 2.7. It should be noted that concepts such as the ADLIF, which incorporate relative motion between different sections of the mechanism under low tolerances, might reintroduce regolith ingress problems.

Combining even foundational rigid sections and flexure types, highly specialised mechanisms can be formed. CMs based on notch flexures are commonly utilised with piezoelectric actuators to amplify their motion [54]. Conversely, CMs were used in the mirror positioning actuators of the James Webb Space Telescope (JWST). Here, the displacement produced by an electric motor is reduced for high-accuracy positioning of the mirror elements. The inherent absence of backlash in CMs offers a significant functional benefit in both contexts.

2.4 System Requirements

To determine the suitability of different concepts and evaluate their performance, requirements with attributed weights are defined. The weights are assigned based on the criticality of the requirement: **3** (Critical/Functional Necessity), **2** (High Importance), and **1** (Desirable). This section discusses the requirements, organised by the categories of performance requirements (Section 2.4.1), Reliability, Availability, Maintainability, Safety (RAMS) requirements (Section 2.4.2), environmental conditions (Section 2.4.3), and geometric and architectural constraints (Section 2.4.4). Table 2.2 shows all requirements with their corresponding ranges and weights.

In the subsequent Section 3.3, the concepts defined in Section 3.2 are evaluated based on these requirements and weights. Some requirements include quantitative target values and acceptance ranges, while others are purely qualitative.

Table 2.2: System Requirements Matrix derived from Section 2.4

ID	Requirement	Target Value	Weight	Source
1. Performance Requirements				
1.1	Feed Rate ($\dot{m}$)	6 (min) – 48 kg/h (target)	3	SRC rules
1.2	Material Loss	Minimised	2	SRC rules
1.3	System Mass (m)	10 (target)	3	SRC rules
1.4	Power Draw (P)	≤ 5 W	2	SRC rules
1.5	Dust Generation	Minimised	2	SRC rules
1.6.1/2	Hor./Vert. Transport	up to 1 m / 0.64 m	2	Team BREMEN
1.6.3	Conveyor Slope (θ)	0° to 40°	2	Team BREMEN
1.7	Flow Continuity	High	1	Team BREMEN
2. RAMS Requirements				
2.1	Reliability	High MTBF	3	Operational Constraints (OC)
2.2	Availability	High	3	Operational Constraints (OC)
2.3	Maintainability	Low MTTR	2	Operational Constraints (OC)
3. Environmental Conditions				
3.1	Ambient Pressure (p_0)	≈ 0 bar	3	Environment
3.2	Temperature Range (T)	50 K to 320 K	3	Environment
3.3	Radiation	High (Lunar environment)	3	Environment
3.4.1	Particle Size	1 µm to 3000 µm	2	Environment
3.4.2	Part. Composition	Lunar regolith comp.	2	Environment
3.5	Grav. Accel. (g)	1.625 m/s^2	3	Environment
3.6	Dust Resilience	High	3	Environment
4. Geometric and Architectural Constraints				
4.1	Interface Compatibility	To Benef. Inlet	2	Team BREMEN
4.2/3	Modularity / Scalability	Inter-connectable modules	2	Operational Constraints (OC)
4.4.1-3	Max. Dimension (LxWxH)	$1.5 \times 0.5 \times 1$m	1	Team Bremen / OC

2.4.1 Performance Requirements

The performance requirements are the metrics used to compare the concepts. The lunar regolith transport system is developed in this study for use in a scenario similar to ESA's SRC (cf. Section 1.1). The performance requirements thus primarily stem from the challenge's rules, specifically the regolith transport-and-dosing mechanism used by Team BREMEN.

The first performance requirement is the feed rate. It is assigned a weight of 3, as it directly dictates the throughput of the ISRU facility. The rules of the SRC define a target for the beneficiated regolith mass of 15 kg, which is to be achieved in the maximum test duration of 2.5 h. This results in a minimum feed rate of 6 kg/h under the assumption of continuous operation of the transport mechanism. Continuous operation is, however, unlikely in practice due to constraints imposed by other systems, such as the availability of material delivered by the excavation rover and the speed of the beneficiation mechanism. The winning concept thus used a higher feed rate of 48 kg/h. Based on these values, the transport system developed in this study shall achieve a minimum feed rate of 6 kg/h and a target of 48 kg/h.

The material loss requirement also stems from the SRC. A weight of 2 is assigned here. While a high material loss would significantly impede the system's performance, a small loss does not necessarily indicate that the concept is inadequate. This assessment is consistent with the evaluation of material loss in the SRC. Limited information is given in this regard; however, according to the final evaluation report, the material loss fraction of 13.7% in Team BREMEN's proposal is considered "moderate" [55]. The material losses of the lunar regolith transport mechanism shall be minimised, as any significant loss lowers the system's efficiency and effectiveness.

In the SRC, the mass of the complete concept, including excavation rover, regolith transport mechanism and beneficiation, was not to exceed 60 kg. The transport-and-dosing mechanism of the winning team had a mass of 10 kg. This mass is used as a target value for this system. To not exceed the total maximum mass of 60 kg, the transport system shall not exceed a mass of 15 kg. A mass of 10 kg is set as a design target. The system mass is a big factor in its feasibility for application on the Moon, due to the high transport costs, as established in Section 2.1, and is thus weighted at 3.

The total energy budget for the SRC was set to 300 W h for the entire system. This equates to a maximum average power draw of 120 W across all systems. Since the excavation rover required the bulk of this power for locomotion and excavation, the regolith dosing and transport mechanisms of the winning concept used only 1 W during operation. Following the benchmark set by Team BREMEN's system, the power draw of the transport system developed in this study shall not exceed 5 W. The energy budget is weighted at 2. In all

lunar endeavours, energy is a scarce good. Given the assumed application in the vicinity of PELs, however, this requirement is considered less critical than other requirements, such as system mass.

While there are no concrete metrics for dust generation in the SRC, it was still expected to be minimised. Dust generation was measured using dust meters positioned across the testing area to assess the impact of excavation, transport, and beneficiation. The dust generation of the transport system shall be minimised to reduce pollution of other systems in the vicinity. Due to the high impact on surrounding systems, the dust generation is weighted at 2.

The beneficiation architecture used by Team BREMEN in the SRC required a regolith dosing and transport mechanism to move regolith upward into the inlet of the beneficiation mechanism. In the challenge, a slope of $\approx 35°$ was necessary. Maximising the slope at a fixed target height minimises the system footprint. For other applications, an upward conveyance is not required. The system used in the SRC by Team BREMEN reached slope angles of up to 40°. The transport system developed in this study shall convey regolith at angles ranging from 0° to 40°.

The regolith transport system shall be adaptable for horizontal transport distances of up to 1 m, enabling flexible use. The vertical transportation distance results from the required slope and horizontal transportation distance at ≈ 0.64 m. The slope and transportation distance requirements are weighted at 2 to underline the importance of compatibility with existing systems.

The beneficiation mechanism used in the SRC was designed to achieve high continuity of material flow. However, the beneficiation system showed compatibility with rapid, intermittent regolith delivery. The material flow produced by the transport system shall nonetheless exhibit high uniformity to enable wide compatibility with different beneficiation systems. Non-compliance would, however, still result in a usable solution and is thus weighted at 1.

2.4.2 Reliability, Availability, Maintainability and Safety

The RAMS requirements consist of the four parts: reliability, availability, maintainability and safety [56, p. 50]. Reliability describes the ability of a system to perform a specified function without failure [56, p. 39]. It is expressed by the metric of Mean Time Between Failures (MTBF). Maintainability means the ability of a system to be repaired timely and

easily, should a failure occur [56, p. 32]. Its metric is the Mean Time To Repair (MTTR). The availability A is defined as a function of the reliability and maintainability [57]:

$$A = \frac{MTBF}{MTBF + MTTR} \tag{2.1}$$

If the reliability of a system is low, yet the maintainability is good, failures would be frequent, but repaired quickly. Conversely, should the reliability of a system be high, yet repairs be difficult and time-intensive, few failures occur, yet take a long time to fix. Ideally, a system demonstrates high reliability and maintainability, resulting in optimal availability. Due to the inaccessibility of infrastructure on the Moon, maintainability is inherently low, shifting the focus of the RAMS requirements to reliability. The reliability is thus weighted at 3, and the maintainability at 2. The availability weight reflects the high weights of both components at 3. Safety is secondary in this scenario, as no humans are assumed to be present during operation of the transport system. However, the safety requirement also includes minimising harm to other systems and the environment, so it must be taken into account [56, p. 40]. Within the scope of this study, the impact on the surroundings is limited to dust generation, as discussed in Section 2.4.1.

2.4.3 Environmental Conditions

The regolith transport system developed in this study shall operate on the lunar surface, necessitating compliance with the local environmental conditions, as discussed in Section 2.1.

All materials and mechanisms used in this system must be rated for high-vacuum environments. The transport system must be able to withstand extreme temperatures in the range of 50 K to 320 K, as are present in and around Shackleton crater (cf. Section 2.1). All mechanisms and materials must be rated for the lunar radiation environment. The transport system must be able to function under this reduced gravity. Compliance with the high-vacuum environment, extreme temperature ranges, ionising radiation, and reduced gravity is mission-critical and thus weighted at 3.

The regolith transport system shall be capable of handling particles in the range of 1 µm to 3 mm. Particles smaller or larger than that range shall not impede the system's function. Furthermore, the system shall be able to work with the mineralogical composition of the lunar regolith, especially ferromagnetic compounds. Non-compliance would impede the system's effectiveness but would likely not lead to mission failure. This requirement is thus weighted at 2.

As detailed in Section 2.2.1, dust was identified as a critical constraint for the implementation of sustained operations on the Moon. Dust resilience is thus considered mission-

critical at a weight of 3. The regolith transport system must be able to function under substantial dust load and exhibit Implicit Dust Mitigation.

2.4.4 Geometric and Architectural Constraints

The primary use case for the transport system is to transport regolith within an in-situ regolith processing facility (intra-facility). In this function, several different configurations might be required, demanding a high level of adaptability. To replace the transport-and-dosing mechanism used by Team BREMEN in the SRC, the transport system's output shall be compatible with the inlet of Team BREMEN's beneficiation mechanism. This inlet incorporates a vertically oriented circular cross-section of approximately 90 mm diameter, in which the material must be deposited. The transport system must therefore be capable of precise material deposition into the beneficiation aperture without mechanical interference.

To facilitate transport distances exceeding the baseline, the system shall feature a modular architecture. Multiple identical modules shall be connectable. To ensure this study is of value beyond the specified mission scenario, concepts developed here shall be scalable to other scenarios such as long-distance (extra-facility) horizontal transport or transport over significant inclines, for example, the transport of material from the PSR to the PEL of Shackleton crater. While not directly mission-critical, both requirements significantly enhance the value of the developed concept and are thus weighed at 2.

The maximum allowed outer dimensions are defined as 1.5 m × 0.5 m × 1 m (L×W×H). This represents an increase compared to the transport-and-dosing mechanism used in the SRC by Team BREMEN, which features outer dimensions of approximately 0.6 m × 0.3 m × 0.4 m. This adjustment is required due to the increased transportation distance requirements. These outer dimensions are to be considered as guidelines. Exact constraints are not defined. The outer dimensions are thus weighed at 1.

3. Concept Development

This chapter details the systematic development of various concepts for use as a lunar regolith transport mechanism, leading to the selection of one model for further development. It begins with the presentation of fundamental actuation principles in Section 3.1, which serve as a technical foundation for the synthesis of six concepts in Section 3.2. These concepts are theoretically evaluated against the requirements defined before in Section 2.4. The two most promising concepts are consequently selected for further investigation in a Proof-of-concept-validation in Section 3.4. Here, the feasibility of both concepts is empirically examined. Additionally, estimates of energy consumption are performed. One concept is ultimately decided on for further development and discussed in detail in Section 3.5.1.

3.1 Actuation Principles

This section aims to present actuation principles applicable to a regolith transport mechanism incorporating compliant mechanisms. A specific actuator choice is not made here, as this decision is highly dependent on the concept of which the actuator will be a part. While compliant mechanisms provide inherent dust mitigation, their benefits would be nullified by the use of conventional actuators, as are common in terrestrial applications (cf. Section 2.2.2). Notably, rotary motors require a rotating shaft interface in which sliding tribological pairs, such as bearings and seals, are unavoidable. Consequently, these interfaces remain vulnerable to dust, negating the resilience gained elsewhere in the system. In this section, actuation methods incorporating IDM using Shape Memory Alloys (SMAs), linear motors and piezoelectric actuators are explored.

Shape Memory Alloys

Shape Memory Alloys exhibit properties characteristic of these materials, including pseudoelasticity and the characteristic shape-memory effect. Both effects stem from unique phase-change characteristics that occur under significant thermal or mechanical stress. For the application as an actuator, the shape-memory effect is predominantly utilised. When heated above the austenitic finish temperature A_f, the crystal lattice transforms from a twinned martensitic state to an austenitic state. Upon cooling the material below the martensitic finish temperature M_f, this process is reversed, returning to the twinned

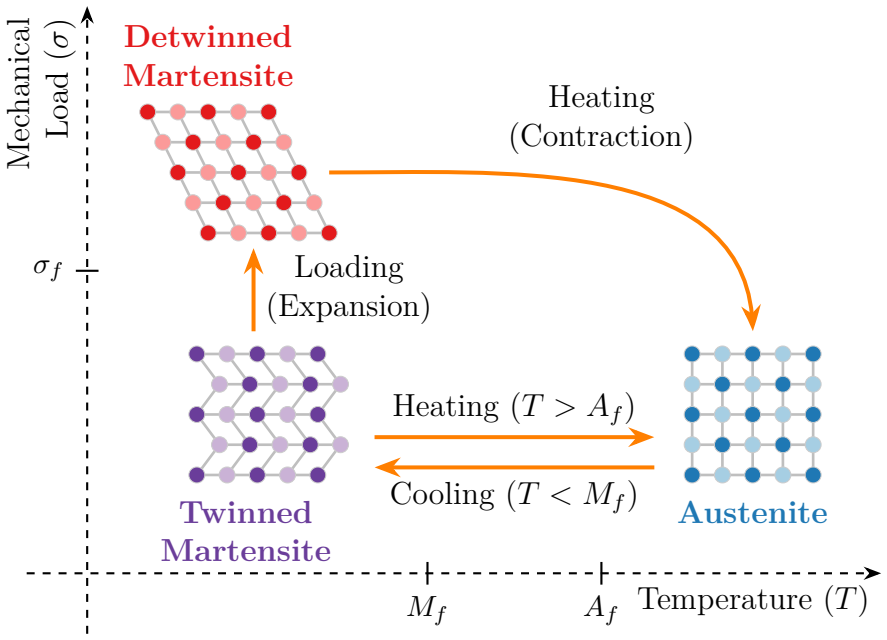

Figure 3.1: Phase changes in an SMA

martensitic state. This phase transformation produces negligible macroscopic strain. For use in an actuator, a mechanical load must be applied to the twinned martensitic phase to achieve stress above the "detwinning finish stress" σ_f. In this case, the martensite is "detwinned", resulting in significant deformation. Heating the material above its transformation temperature causes the detwinned martensite to revert to the austenitic state and thus to its initial form, thereby reversing the deformation induced by detwinning and resulting in significant contraction. Figure 3.1 illustrates the phase changes during heating/cooling and application of mechanical load.

SMA wires can be heated by passing a current through them. The magnitude of the current directly controls the temperature of the wire. Due to the direct correlation of temperature and wire stress, the current thus controls the force exerted by the actuator [58, p. 8]. SMA actuator can exert a high force in relation to its mass, reaching stresses of up to 650 MPa at a temperature of $A_f = 173\,^{\circ}\mathrm{C}$ [59]. For a wire with a diameter of 0.25 mm, this results in a force of 32 N at a linear density of 0.317 g/m. The force required to transition the material from its twinned martensitic state to its detwinned martensitic state is called the bias force. This force directly opposes the actuator force during heating, thereby reducing the actual usable load. A major limiting factor for the application of SMA actuators under lunar environmental conditions is the material's cooling. Under terrestrial conditions, convective and conductive heat transfer through the atmosphere enables effective cooling along the entire wire. The absence of an atmosphere on the Moon dictates the reliance on radiative and conductive cooling. To achieve high actuation frequencies, the heat dissipated from the actuator wires must be maximised. Introducing a contact surface along the length of the actuator would help in this regard; however,

it would introduce problems, including sliding tribological pairs and increased wear and friction. Conventionally, radiative heat transfer is limited in relation to convection and conduction, especially for low temperature processes, as the emission scales with the fourth power of the temperature [60, p. 27]. SMA-wires are thus likely only usable for low-frequency actuations.

Linear Electric Motor

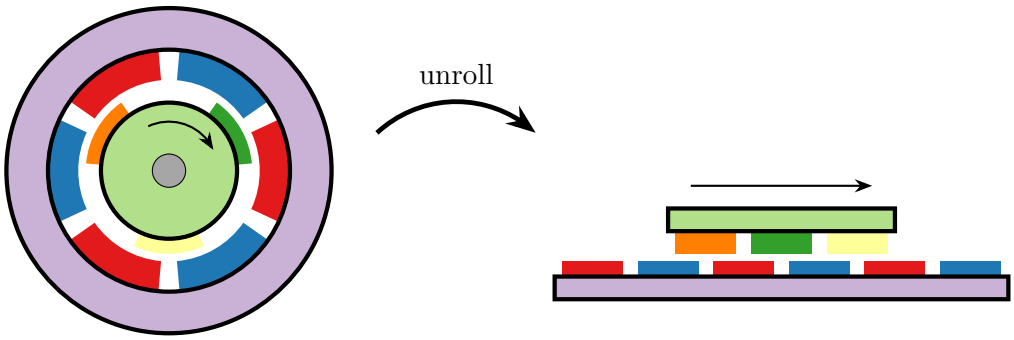

Figure 3.2: Structure of a linear electric motor

Linear electric motors follow the exact functioning principle of rotary electric motors. A linear electric motor may be conceptualised as an "unrolled" rotary motor [61, p. 297]. The stator of the rotary motor corresponds to the "primary" of the linear electric motor. The "secondary" of the linear motor stems from the rotary motor's rotor [62]. Figure 3.2 illustrates the structure of a linear motor as compared to a rotary motor. Energising the coils in the primary of a linear motor results in a linear travelling magnetic wave, as opposed to the rotating magnetic field in a rotary motor. This travelling field directly exerts a Lorentz force on the secondary, analogous to the force exerted on the rotor in a rotary motor. The roles of primary and secondary might be reversed, with the primary as the moving component and the secondary as the stationary one. The speed of the travelling field is determined by the pole pitch τ, that is, the distance between poles on the primary, and the supply frequency f_{supply} [61, p. 299]. Unlike other methods of linear electric actuation using rotary motors, this method generates force linearly, eliminating the need for conversion mechanisms from rotary to linear motion, such as lead screws, belts/chains, or gearboxes.

The application of linear electric motors as industrial actuators enables high-velocity, high-force actuation with high positioning accuracy. These motors commonly utilise plain bearings for guiding the moving primary [63, p. 14]. To eliminate sliding tribological pairs, linear guiding of the moving primary could be achieved using compliant guides, as described in Section 2.3. A major limitation of linear electric motors is their reliance on magnetic fields. As established in Section 2.2.1, lunar regolith contains ferromagnetic compounds and can even act ferromagnetic in bulk. During long-term use in a dusty lunar

regolith environment, these abrasive ferromagnetic compounds would likely accumulate on the magnets used in the linear motor. This could lead to increased friction, wear and even binding of the actuator, as well as presenting problems due to interference with the magnetic and electric fields. The application of linear electric motors would thus require additional active and/or passive dust mitigation techniques for long-term use on the lunar surface.

Piezoelectric Actuators

The piezoelectric effect describes the characteristic of some materials to generate an electric charge upon application of mechanical pressure. Piezoelectric actuators utilise the inverse of this piezoelectric effect. The application of an electric field to a piezoelectric crystal leads to a mechanical deformation of the crystal lattice. The deformation induced by this effect is extremely small, typically in the range of 0.1% of the material's total length. Commonly, multiple piezoelectric elements are stacked to increase their displacement. To further enhance this action for utilisation in the application as an actuator for a transport mechanism, the deformation can be mechanically amplified. Amplified Piezoelectric Actuators commonly employ compliant flexures for amplification [64, p. 266], making them inherently devoid of sliding tribological pairs, ideal for an application in a dusty lunar regolith environment. These mechanisms can reach forces on the order of several 10 N at displacements of up to several millimetres [54, 65]. The operating range of commercially available amplified piezoelectric actuators, however, is limited and does not comply with the lunar ambient temperature range [54, 65]. Studies investigating the behaviour of piezoelectric actuators at cryogenic temperatures indicate a significant decrease in stroke with decreasing temperature [66, 67]. Piezoelectric actuators are utilised in space applications, primarily for optics positioning due to their very high positioning resolution, stiffness, and compact footprint [68]. Furthermore, amplified piezoelectric actuators have been proposed as an actuation method for a vibratory conveyor for lunar regolith [40]. This concept will be examined in more detail in the following Sections 3.2 and 3.3.

3.2 Concept Synthesis

This section presents six concepts for lunar regolith transport systems that apply the working principles established in Section 3.1. Each concept employs compliant mechanisms designed to minimise or eliminate sliding tribological pairs. These pairs are ubiquitous in conventional conveyors used in terrestrial industry, as described in Section 2.2.2.

3.2.1 Concept 1: Bucket Escalator

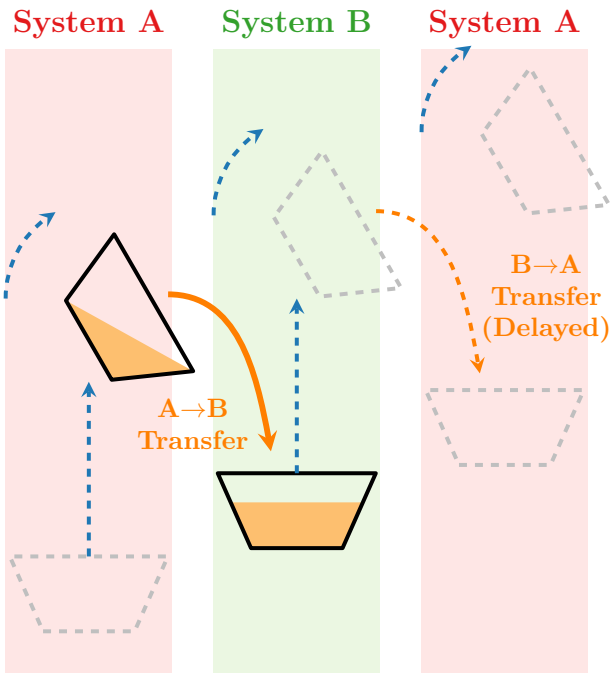

Figure 3.3: Bucket escalator sketch

The bucket escalator concept shares similarities with the continuous bucket elevator described in Section 2.2.2, in that the regolith is transported by moving buckets. The major difference between the two concepts lies in the buckets' range of motion. In the bucket elevator, the bulk material is loaded into a bucket at the system inlet and remains there until it exits the system. The buckets thus move the whole length of the conveyor. Since this large movement range is difficult to achieve with compliant guides, the bucket remains on a fixed, shorter track. It executes reciprocating strokes consisting of translatory and rotary motion on this limited track. Analogous to the continuous bucket elevator, material is loaded into the bucket at the bottom of its track and exits the container at the top end of its movement. In the escalator, the material is subsequently filled into the next bucket in line, which is currently at its lowest position. This process is illustrated in Figure 3.3. The material is transmitted repeatedly until it is discharged from the last bucket, having reached the full transport length of the conveyor. The tracks the buckets follow are defined by compliant mechanisms that combine linear and rotary guides. To move the buckets along their tracks, a high-stroke, potentially high-force actuation is required. This discrete motion of the bucket escalator inherently accommodates the weakness of a SMA actuator, requiring extended cool-off periods between strokes. The buckets could be connected into two interleaved movement systems, A and B, with buckets in a row alternating between the two systems. Both A and B perform the same motion, operating with a synchronised phase shift. This allows a lower actuator count and, consequently, lower mass and fewer redundant actuators.

3.2.2 Concept 2: Membrane Staircase

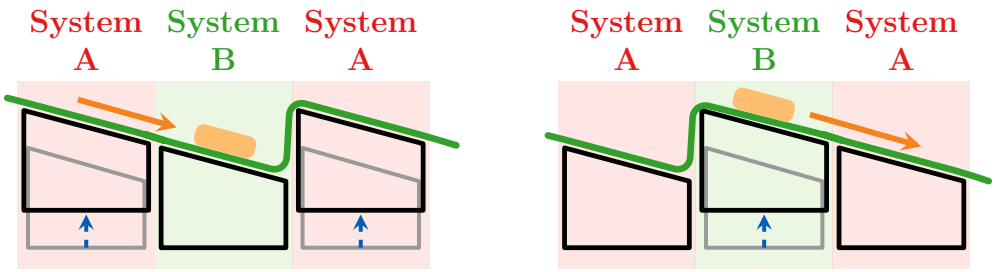

Figure 3.4: Membrane staircase sketch

Similar to Concept 1, Concept 2 also features components that execute reciprocating strokes on compliant guides, hereafter referred to as "wedges". In this case, the motion defined by the linear guides is constrained to a single translational degree of freedom of uniaxial vertical movement. The rigid actuation wedges lie beneath a continuous membrane spanning the entire system, which marks the interface with the transported material. Their motion pushes against the membrane, deforming it. The rigid wedges are sloped at their interface with the membrane. When a wedge pushes upward towards the membrane, the latter elastically deforms to conform to the underlying wedge contour. The membrane protects the intricate mechanics from the regolith, while still allowing the actuation wedges to interact with it. Material situated on the membrane above the wedge consequently translates along this induced slope onto the next wedge. This cycle repeats until the regolith is subsequently expelled from the end of the system. This system bears similarities to "step-feeders", which are regularly used for handling bulk parts [69]. However, step-feeder systems differ from this "Membrane Staircase" in that no membrane is employed to shield the mechanics from the transported goods, which is necessary in this application due to the highly abrasive nature of regolith. Analogous to Concept 1, the rigid actuation wedges may be arranged in an interleaved system performing alternating movement. Due to the similar movement as in Concept 1, the same actuation method is proposed.

3.2.3 Concept 3: Peristalsis

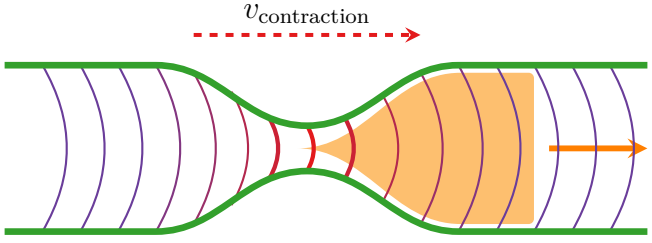

Figure 3.5: Peristalsis sketch

In contrast to Concepts 1 and 2, Concept 3 features no moving rigid components but instead relies directly on SMA-wire for conveyance. This biomimetic architecture draws inspiration from the biological gastrointestinal tract. Both the human colon and oesophagus work on the principle of peristalsis. A tube is filled with the material to be transported. By contracting the tube at a point and moving that contracted section along the tube, the material is steadily pushed forward. Figure 3.5 illustrates this working principle. The movement direction of the contracted region is indicated by $v_{\text{contraction}}$. For clarity, only the material inside the tube immediately influenced by the contraction region is shown. In the case of a regolith conveyor, the tube would consist of an elastic polymer, encircled by a helically or circumferentially wound SMA wire. This provides direct, fine control over the contraction of the entire circumference of the tube. In previous applications of the same principle, actuators indented the tube from the outside, leading to an uneven, inhomogeneous deformation of the tube [70].

3.2.4 Concept 4: Sawtooth Conveyor

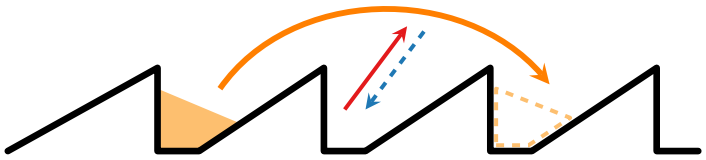

Figure 3.6: Sawtooth conveyor sketch

Concept 4 consists of a vibrating platform featuring an asymmetric sawtooth profile extending the width of the platform. This platform vibrates either in-plane or at an acute angle to the in-plane direction. The material is moved by the teeth of the sawtooth profile. A fast-forward stroke transmits energy to the regolith particles, launching them onto a ballistic trajectory that ends farther forward/upward on the platform, where the material is collected by a subsequent tooth. The fast upward stroke is depicted in Figure 3.6 by a red arrow. The downstroke does not have to be as fast, as no relative motion between the particles and the platform must be induced in this phase. It is illustrated in Figure 3.6 as a dotted blue arrow. Unlike previous concepts that exclusively use SMA actuators, this concept might benefit from other working principles, such as linear motors, that could also be applied here. Though piezoelectric actuators might also be possible for very small-scale applications, taking advantage of the very high frequency, the limited stroke likely proves inhibitive for this concept. For further concept development, SMA actuators are assumed. While the stroke frequency of this actuator principle is limited due to long cooldown times in the lunar vacuum, the high force/high stroke nature of this actuation caters well to the sawtooth conveyor concept. Additionally, SMA actuators show a signif-

icantly higher volumetric energy density than piezoelectric actuators, enabling a compact and light mechanism [71].

3.2.5 Concept 5: Vibratory Conveyor

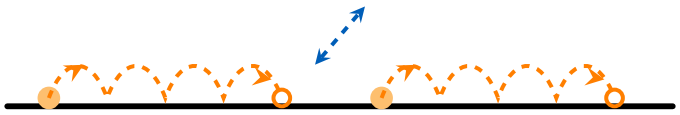

Figure 3.7: Vibratory conveyor sketch

The working principle is similar to the sawtooth conveyor; however, it utilises a strictly planar transportation deck, as illustrated in Figure 3.7. This concept requires an actuation direction oriented at an angle to the in-plane direction, providing both normal and tangential components. Similar to Concept 4, the vibrating platform applies a force to the particles, imparting a ballistic trajectory and conveying them along the platform with each stroke. In vibratory conveyors, the particles move on micro-ballistic trajectories, unlike the sawtooth conveyor, in which the particle trajectories are orders of magnitude larger. High vibration frequency then causes a high transport speed. The forward momentum transmitted to the particle relies solely on coulomb friction between the particle and the platform, as opposed to the direct mechanical engagement between the teeth and the particles featured in Concept 4 [72].

3.2.6 Concept 6: Wave Chain

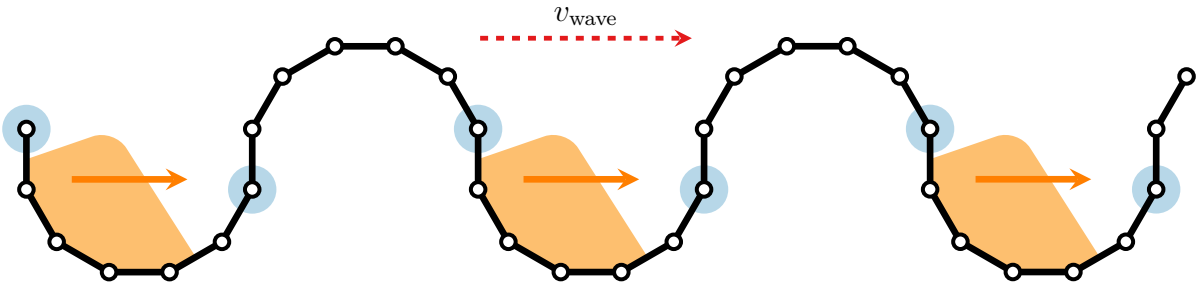

Figure 3.8: Wave chain sketch

Concept 6 consists of a chain of rigid members connected by Single Degree of Freedom (SDOF) hinges. The hinges employ compliant flexures, eliminating sliding tribological pairs and thus preventing the ingress of dust that would otherwise induce binding. Each hinge can be actuated bidirectionally from the resting straight position via SMA wires. The actuation of subsequent hinges forms the chain into a wave shape. The material to be transported is captured within the resulting troughs. By systematically reversing the actuation state of the hinges situated in the inflection points of the wave (marked hinges in Figure 3.8), it propagates in the transport direction denoted by v_{chain}.

3.3 Concept Evaluation

The concepts presented in Section 3.2 are assessed using an evaluation matrix. In this matrix, each concept is rated for its compliance with most requirements defined in Section 2.4. However, a quantitative comparison of the requirements for feed rate, mass, and power, as well as the safety component of the RAMS requirements, was omitted, as these parameters could not be reliably estimated within the scope of this preliminary evaluation. In the evaluation matrix, each concept received an integer rating ranging from -2 (very bad) to +2 (very good). The rating is multiplied by the requirement weights to form a weighted rating. These weighted ratings are summed up to form the aggregated ratings for each requirement category, as shown in Table 3.1. The complete evaluation matrix containing the ratings for all individual requirements is attached in Appendix A. For each concept, the corresponding weighted ratings are summed to obtain the total score. A relative score is defined as the division of the total score by the maximum achievable score. This maximum score is 110: the sum of all requirement weights multiplied by the best possible rating of 2. In this section, the evaluation of the concepts is explored, grouped by the requirement categories, and notable individual evaluations are discussed.

Table 3.1: Summary concept evaluation matrix

Evaluation Category	**C1**	**C2**	**C3**	**C4**	**C5**	**C6**
1. Performance	1	9	18	13	−2	10
2. RAMS	6	−11	−13	8	8	3
3. Environmental Conditions	18	−5	−3	22	30	29
4. System Architecture / Geometry	14	8	12	12	12	8
Total Score	**39**	**1**	**14**	**55**	**48**	**50**
Relative Score (%)	**35.45**	**0.91**	**12.73**	**50.00**	**43.64**	**45.45**

3.3.1 Performance

The evaluation of the performance requirements shows a large spread in ratings across the concepts from −4 to 24. Concept 1 and Concept 6 received a rating of −1 for the requirement of material loss, defined in Section 2.4.1. In both concepts, constraining the material to stay within the system poses significant mechanical challenges. In Concept 1, the material inherently falls from one bucket into another. This unconstrained motion would likely result in spillage. Since this action is repeated many times across the conveyor, these small amounts of material loss would accumulate over time. Constraining this movement is not feasible due to the large relative motion of the buckets. Concept 6 poses a problem with preventing the regolith from spilling out of the hinge sections. Two possibilities for the shielding are identified: A membrane connecting the two rigid

sections could constrain the material on the conveyor, while adapting to the changing angle between the sections. However, this presents significant material science challenges; maintaining the structural rigidity of membranes under lunar environmental conditions is difficult due to the high ionising radiation and high vacuum [73, pp. 20 -21], though it is an active area of research. Additionally, these membranes would be highly susceptible to degradation due to constant exposure to the highly abrasive lunar regolith [74]. The alter-

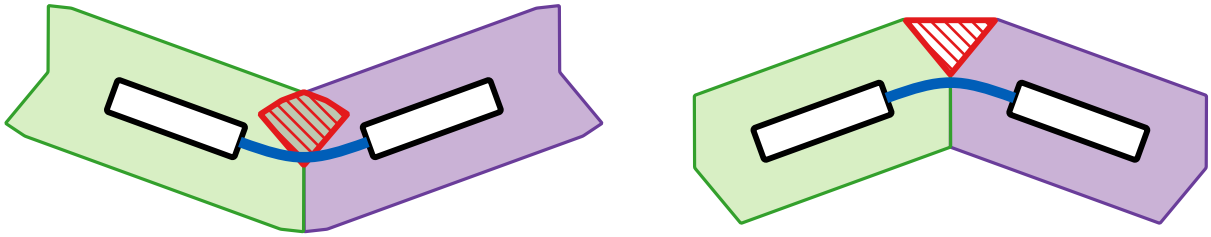

Figure 3.9: Rigid shielding problems of Concept 6

native for shielding the hinge sections consists of rigid walls that either overlap during the hinge's concave bending mode or do not cover the entire hinge section during its convex bending mode. In the case of overlapping walls, sliding tribological pairs form, leading to degradation and binding due to regolith ingress. The problem posed by rigid walls for Concept 6 is illustrated in Figure 3.9. The left example shows the walls in the case of an overlapping architecture, ensuring no gap opens between the walls during convex bending. In contrast, the right example shows the opposite, ensuring no overlap occurs during concave bending. In stark contrast, Concept 3 is rated at +2. By fully encapsulating the material during the whole conveyance process, material losses are effectively eliminated.

In Concepts 1, 4, and 5, regolith is significantly agitated by the conveyance process, which launches it on unconstrained ballistic trajectories. This would result in severe dust generation. Dust shielding would be required to prevent the contamination of other components and nearby systems. Because of this inherent complicating factor, these concepts receive a rating of -1 in the dust generation requirement, defined in Section 2.4.1.

The transportation slope requirement (cf. Section 2.4.1) is considered a knock-out criterion for Concept 5. This requirement is considered important to the success of a concept, at a weight of 2. Concept 5 does not meet the required value, as the transport slope of vibratory conveyors is inherently limited by the Coulomb friction between the granular material and the conveyor, as established in Section 3.2.5. Kawamoto examined the performance of a vibratory conveyor utilising piezoelectric actuators. In his tests, the flow rate decreased with increasing inclination, reaching 0 at an inclination of 24°, well below the required 40° [40].

The flow continuity for Concept 3 and Concept 6 is low because the material is delivered in large, distinct, infrequent batches. However, since the requirement of flow continuity is not considered as vital as the others, like the transportation slope at a weight of 1, these

limitations are not considered knock-out criteria. Concepts 1 and 2 also pose significant limitations regarding this requirement by conveying material in discrete portions, although continuity is marginally better due to the higher delivery frequency.

3.3.2 RAMS

None of the examined concepts fully satisfy the RAMS requirements, as defined in Section 2.4.2. Significant shortcomings in reliability are determined in Concepts 2 and 3. The membranes required for these concepts are prone to high wear, reducing their operational life. An overall more problematic area is the maintainability. Concept 3 does not fulfil the requirement. In this concept, the membrane is most likely to require replacement due to high abrasion, yet it is also the central part of the system. Replacement of this part would be equivalent to replacing most of the system. Concept 2 exhibits the same failure characteristic; the MTTR benefits from the lower integration of the membrane. In Concept 6, the parts experiencing the most wear, and thus most likely to require repair, are the hinges. These parts may be developed to be easily replaceable, but are inherently highly integrated due to the monolithic nature of compliant mechanisms. Restoring the system's functionality after replacing the hinges would undoubtedly result in significant downtime. Similar reasoning applies to Concept 1. Here, the buckets experience the most wear, while also being a main part of the system. Consequently, neither Concept 2 nor Concept 3 meets the availability requirement, as this requirement is derived from reliability and maintainability, both of which are subpar. As mentioned at the beginning of this section, the quantitative rating of the safety requirement is omitted in this evaluation. While some concepts might pose a higher risk to surrounding infrastructure in the event of a failure, for example, due to high kinetic energy, the magnitude of these effects cannot be determined in the scope of this evaluation.

3.3.3 Environmental Conditions

The Environmental Conditions exhibit the widest range among the six concepts across all requirement categories, ranging from an aggregated rating of -3 for Concept 3 to $+32$ for Concept 5. The environmental requirements pose a knock-out criterion for Concept 3. The required high-strength elastomeric membranes are not feasible in the lunar environment. The lunar conditions of high vacuum, strong radiation, and high temperatures all pose significant challenges for the application of polymers (and specifically elastomers). In many polymers, the low ambient pressure leads to outgassing, the sublimation of volatile components in the polymers. This effect is enhanced by high temperatures, as are present on the lunar surface [75] [6]. Both Ultraviolet (UV) radiation and ionising radiation severely

damage polymers. The energy of solar UV radiation is substantial enough to break polymer bonds. This can significantly influence material properties [75]. Ionising radiation, as produced by Solar Particle Events (SPE)s and galactic cosmic rays, ionises atoms in the polymer, changing its chemistry [5, p. 47] [75]. Even for materials that can withstand the challenging conditions of vacuum and radiation, the extreme temperatures on the lunar surface pose a limiting factor. The local temperatures exceed the usable temperatures even for space-grade elastomers. Table 3.2 shows the usable temperature gamut of selected common polymers for application in space. While polymers such as Kapton and

Table 3.2: Usable temperature ranges of selected space-grade polymers.

Material	**Use-case**	**Lower Bound**	**Upper Bound**	**Source**
Kapton (Polyimide)	Mechanical / Insulation	3 K	>500 K	[76]
PTFE	Bearings / Seals / Insulation	73 K	523 K	[77]
SSP2575 Silicone	Sealant	157 K	N/A[1]	[78]
FFKM	Sealing	228 K	523 K	[79]
RTV630	Apollo EVA Suit Gloves [26]	213 K	477 K	[80]

[1] N/A: Data not specified in the manufacturer's technical datasheet.

Polytetrafluoroethylene (PTFE) meet the thermal requirements, they are not elastomers and thus not applicable for this application. On the high-abrasion surfaces of the gloves and the soles of the Apollo program EVA suits, RTV630 silicon rubber was used. A similar limitation is apparent in Concept 2. While the membranes used might not need to be as elastic as in Concept 3, the same limitations regarding high vacuum, high-temperature range, and radiation persist. Concept 2 is thus rated at -1 in the requirements of ambient pressure, temperature range and radiation resilience.

Concepts 1 and 4 are rated at a medium 0 for applicability in high-vacuum and high-temperature environments. Both of these concepts likely require the use of SMA actuators. As discussed in Section 3.1, the absence of an atmosphere severely inhibits the cooling rate of the SMA actuators required to reset to their initial conditions. Additionally, the large temperature gradients on the Moon might interfere with the cooling and heating process. In areas with strong solar illumination, the actuators would need to be shielded to prevent excessive heating from the sun. Application in PSR would aid the operation of these actuators by increasing the cooling rate and eliminating solar heating issues. While Concept 6 also utilises SMA actuators, the actuation frequency is much lower, thereby reducing the cooling limitation imposed by the vacuum. Additionally, each actuator features an opposing part that operates in the opposite direction, aiding wire extension during cooling.

Concept 2 is less resilient to dust pollution than the other concepts. The rigid actuation wedges in this concept are positioned with minimal clearance between them, allowing the

membrane to follow their contours smoothly. While not in contact by design, this tight formation between the wedges may increase the risk of abrasion and binding from regolith ingress.

3.3.4 System Architecture

The first system architecture requirement is that the transport system be usable with the beneficiation system used by Team BREMEN in ESA's SRC. Concept 6 does not interface well with the beneficiation's inlet. The end of the chain inherently moves both laterally and vertically due to wave motion. Adaptation would likely require substantial reworking. Concept 3 fully meets the requirement. The circular cross-section of the peristaltic tube perfectly matches the circular inlet of the subsequent system.

The modularity rating is low for Concept 2. Connecting two modules would require either overlapping one membrane over the other or connecting both membranes. Since the membrane must be supported at every point by a wedge, overlapping two membranes is not straightforward. Without any adaptation of the underlying wedge structure, an unsupported section forms between two wedges, leading to unwanted deformation of the membrane. This deformed membrane would act as an accumulation point for regolith, impeding the material flow. By adapting the wedges, this problem can be eliminated. Shortened wedges at the interface could be connected to form a shared element between two subsequent modules. However, these specialised parts would reduce part standardisation and interchangeability. Connecting sequential membranes would result in serial reliability and significantly reduce maintainability, as the composite membrane would have to be replaced entirely in the event of damage. Concept 6 is rated at 0 for modularity, for the same reasons as for the beneficiation interface. Adaptation to another module is likely simpler, though, due to the identical architecture on both sides of the interface. Scalability of Concept 6 is assumed to be a significant advantage. The inherently sequential and self-repeating architecture of Concept 6 offers high flexibility in the number of elements connected to a chain, enabling versatile applications across different transport distances.

All concepts fully adhere to the geometric constraints with one exception. Concept 6 is inherently large in the height dimension. Two variables in the concept can be adjusted to reduce the height of the wave generated by the chain. Minimising the length of the rigid elements reduces the height for the same number of elements per wavelength. Analogously, increasing the actuation angle of the hinges does not decrease the height per element but reduces the number of rigid elements in a waveform. For illustration: if the elements at the inflection points shall be vertical in relation to the transport direction, at an actuation angle of 45°, two hinges are required, counting from a horizontal starting point,

while an actuation angle of 15° requires 6 hinges. However, these two methods come with severe consequences. Small rigid segments come at the cost of complicating hinge replacement and leaving less space for actuation mechanisms. Large actuation angles require longer actuator wires, necessitating larger rigid elements and negating the desired effect. Consequently, the wave height cannot be significantly reduced without sacrificing other important factors of the concept.

3.3.5 Final Theoretical Evaluation

The concepts emerging from the theoretical evaluation with the best ratings are:

1. Concept 4: 50.00 %
2. Concept 6: 45.45 %
3. Concept 5: 43.64 %

Concept 4 is by far the most promising, and is investigated further in the Proof-of-concept (POC)-tests in Section 3.4. Based on the total score alone, Concepts 6 and 5 follow at some distance with very similar ratings. Concept 5 is rated slightly worse than Concept 6. Additionally, it cannot meet the highly valued requirement for the transport slope and is therefore not considered further. Concept 6 shows promise as a novel concept. Although it poses challenges regarding material loss, flow continuity, geometric volume, and interface with the beneficiation system, a POC-test is conducted for this concept to further evaluate the feasibility and severity of these problems. While Concept 1 is not being investigated further within the scope of this thesis due to its relatively low rating, exploring this concept in another medium might prove valuable. Further development of Concepts 2 and 3 is not considered worthwhile for this application.

3.4 Proof-of-Concept Validation

The primary problems identified for Concepts 4 and 6 differ, and thus also do the POC validation tests performed for both concepts. For Concept 4, the question of whether the sawtooth conveyor can transport regolith is considered critical, while the actuation mechanism is treated as a lower-priority, lower-complexity problem. The opposite is true for Concept 6. Here, the actuation of a compliant hinge using an SMA actuator is the focus. The conveyance of regolith is considered straightforward once the chain's ability to form a moving wave is proven. The tests are described in Section 3.4.1 and Section 3.4.2, followed by a preliminary energy estimation for both concepts.

3.4.1 Proof-of-Concept of Concept 4

The validation of Concept 4 focuses on evaluating its feasibility across a range of geometric and kinematic parameters and different materials. This section will explore the test setup and methodology, then qualitatively examine the test results.

Test Setup and Procedure Concept 4

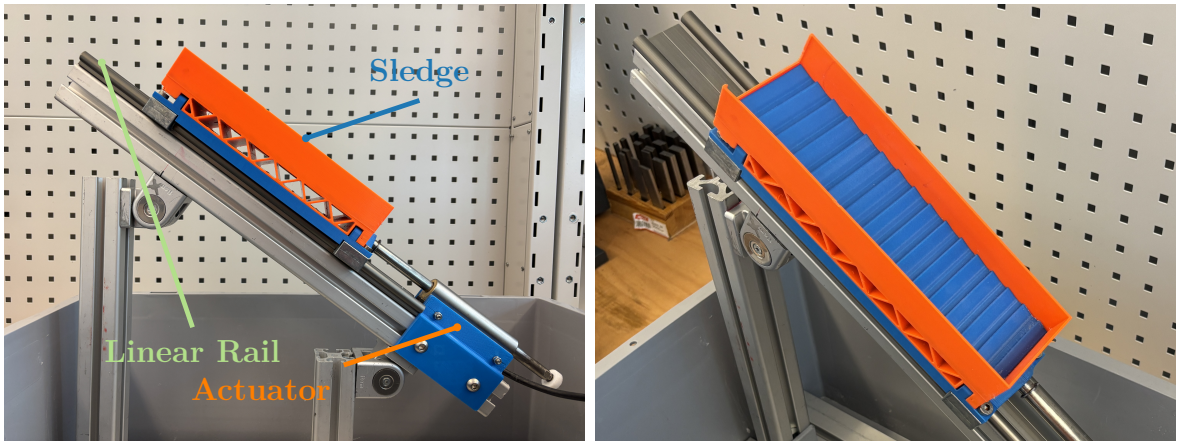

(a) Side view of the test setup for the POC-test of Concept 4

(b) Detail view of the sledge for the POC-test of Concept 4

Figure 3.10: Test setup for the POC-test of Concept 4

For the POC-tests of Concept 4, no compliant mechanisms were used, as the goal of these tests is the general feasibility of the sawtooth-conveyor concept, not the application of compliant mechanisms within this concept. Figure 3.10 shows this test's setup. A sledge is mounted on a linear rail with linear plain bearings. The angle of the linear rail is adjustable to test different conveyor angles. Within the sledge, a removable plate featuring a sawtooth profile is mounted to enable straightforward variation of the geometric parameters. Two sawtooth-plates were produced and used in these tests, whose geometric parameters are compared in Table 3.3. Henceforth, the sawtooth plates are referred to as "Profile 1" and "Profile 2". The sledge is actuated by a linear motor. Values for target positions (stroke

Table 3.3: Geometric Parameters for the POC-tests of Concept 4

Geometric Parameters	**Profile 1**	**Profile 2**
Tooth Pitch	20 mm	15 mm
Tooth Length	15 mm	10 mm
Tooth Height	5 mm	2.5 mm

length), maximum velocity and maximum acceleration are defined for the linear motor. The motor repeatedly executes a motion profile, targeting the maximum values. The actual

acceleration and velocities are governed by the force of the motor in combination with the sledge's weight and the stroke length, respectively. The maximum velocity and acceleration are set at an unreachable 100 m/s and 100 m/s^2 respectively. The actual velocity is thus controlled by the stroke length. At a stroke 10 mm, a velocity of $v_{\text{actual}} \approx 0.8$ m/s is reached. The actual acceleration is $a_{\text{actual}} \approx 54$ m/s^2. Figure 3.11 shows an extract of the periodic motion profile. In most tests, quartz sand is used as a proxy for lunar regolith.

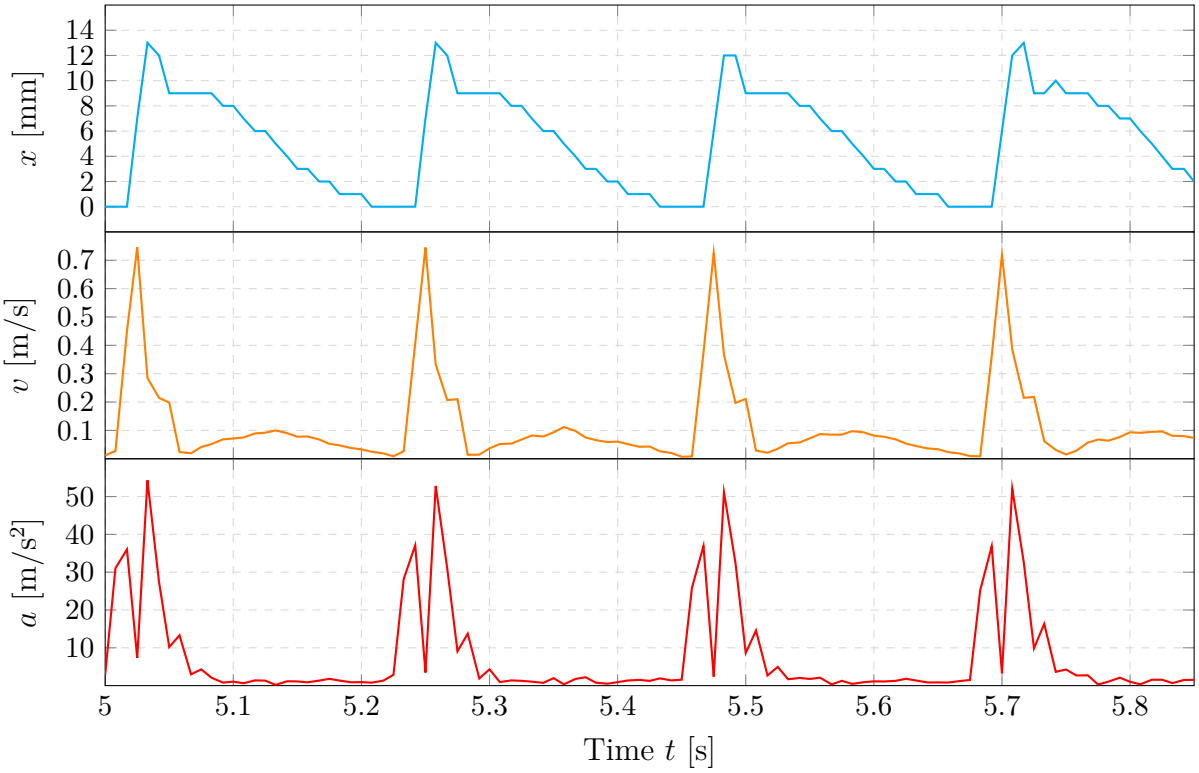

Figure 3.11: Motion profile for a 10 mm Stroke

Silica beads and steel nuts were used in two tests to assess the concept's compatibility with larger particles.

Test Results Concept 4

Table 3.4 shows the observations of the tests performed for Concept 4. A stroke of 20 mm resulted in the best particle conveyance. Although tests with a 10 mm stroke also efficiently transported material, the 20 mm stroke produced greater particle displacement per cycle, as particles moved across several teeth. To quantify this, tests using silica beads and steel nuts enabled single-particle tracking. However, the silica beads exhibited significant elastic rebound, preventing particle settlement before the next stroke and making behaviour less predictable. Therefore, tracking is performed using footage from the steel nuts test. Figure 3.12 shows the tracked displacement of three individual particles. These particles were chosen for their initial positions on the first tooth, which serve as analogues for subsequent positions in subsequent stages of the conveyor. Particles initially situated at the

Table 3.4: Qualitative Observations of Concept 4 POC Tests

Test Parameters			**Observations**	
Stroke	**Incline**	**Material**	**Profile 1**	**Profile 2**
10 mm	15°	Sand	Fast conveyance, slow settlement	–
10 mm	38°	Sand	Fast conveyance, fast settlement	–
20 mm	38°	Sand	*Very fast conveyance, high structural load, multi-pitch displacement*	
20 mm	38°	Steel Nuts	Very fast conveyance, high structural load, multi-pitch displacement	–
20 mm	38°	Silica Beads	Very fast conveyance, high structural load, multi-pitch displacement, high elastic rebound	–
8 mm	38°	Sand	*Slow conveyance, incomplete clearance, minimal advancement*	
5 mm	38°	Sand	No conveyance	–

conveyor's floor encounter different boundary conditions compared to those originating from any other position on the conveyor and thus are not considered representative. In this test, the investigated particles translated 4 or 5 teeth, which matches the qualitative observations from the tests involving quartz sand. Low stroke lengths performed significantly worse. At 8 mm, a significant fraction of the particles in a tooth do not clear the pitch to be caught by the subsequent tooth. There are no particles advancing more than one tooth per stroke. This limited conveyance is eliminated at a stroke of 5 mm. The energy transmitted to the particles here is not sufficient for them to advance to the next tooth.

The different geometric parameters did not result in a discernible difference. However, the geometry of Profile 1 and Profile 2 is similar. More exotic geometric parameters, in conjunction with varied motion parameters, might, however, change the conveyor's characteristics. The conveyor angle imposed little influence on the perceived conveyance. Particle behaviour at slopes of 15° and 38° was similar, with particle settlement at 38° accelerated, thereby increasing the achievable frequency. The concept showed no compatibility issues with larger particles, including silica beads and steel nuts. The volumetric flow rate was measured for a stroke of 10 mm at a slope of 38° at 1.15 cm^3/s. This corresponds to a mass flow rate of 5.8 kg/h, for the quartz sand's bulk density of 1400 kg/m^3, nearly meeting the minimum requirement of 6 kg/h, defined in Section 2.4.1, at a significantly smaller scale than the conveyor used in the SRC. Based on these tests, the sawtooth conveyor is considered a viable concept, demonstrating the feasibility of material conveyance by this mechanism.

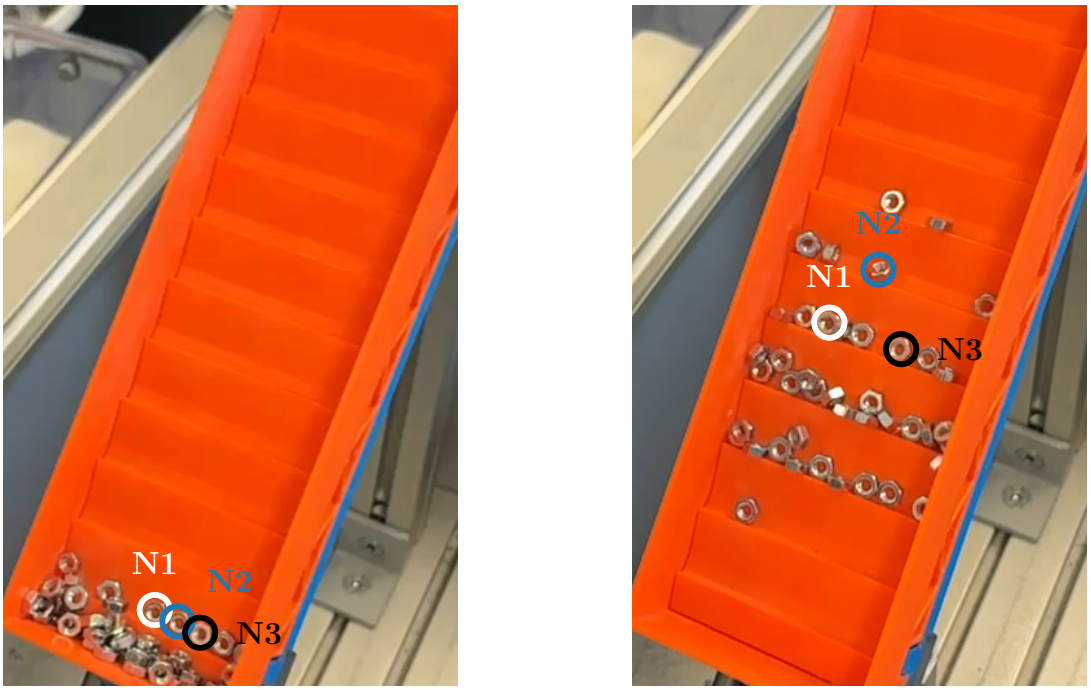

(a) Pre-test state (b) Distribution after the first stroke

Figure 3.12: Tracking individual particle displacement ($N1$–$N3$) for the 20 mm stroke test

3.4.2 Proof-of-Concept of Concept 6

The validation of Concept 6 followed an iterative approach, where the limitations identified in a preliminary single-hinge carrier informed the development of a refined multi-hinge system. The initially investigated single-hinge test carrier incorporates a "blade" flexure (cf. Section 2.3). Based on the learnings from this examination, the second test carrier features multiple "notch" flexures. Figure 3.13 shows the two test carriers used. In both assemblies, SMA-wire is fixed onto each segment. In the multi-hinge part, two screws are mounted on each side of each rigid element, allowing independent tightening of the wire sections. At the hinges, the wire is fed beneath two bars, ensuring a constant lever arm during concave bending. In convex bending, the wires conform to the bend, reducing tension in the outer wire during opposing actuation. The influence of supply current on the actuation force and angle was examined. It is worth noting that the exact values of these currents are of little significance for applications under lunar environmental conditions, given the absence of an atmosphere and the severe temperature range.

Phase I: Single-hinge Investigation

Tests with a single wire on one side of the hinge and two wires on opposing sides were performed using the single-hinge test carrier. A supply current to the wire of 0.5 A and 0.7 A was tested to investigate its influence on the actuation. Figure 3.14 shows the max-

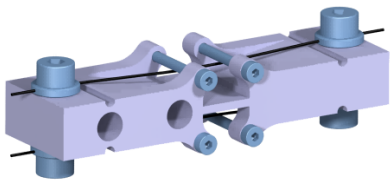

(a) Single-hinge test carrier

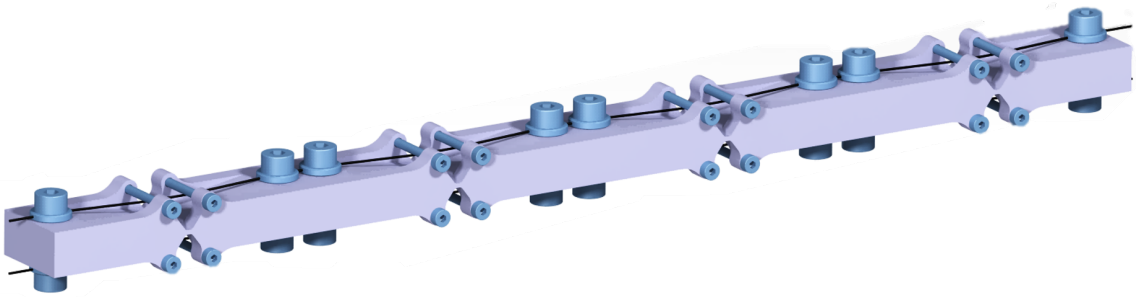

(b) Multi-hinge test carrier

Figure 3.13: Test carriers used in Concept 6's POC-tests

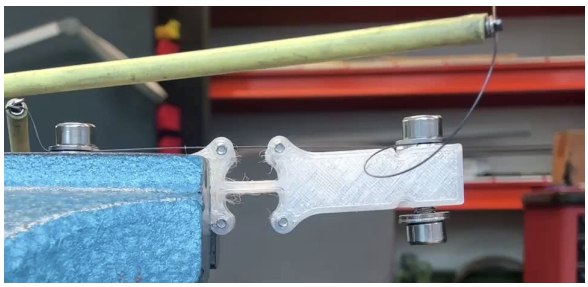

(a) 0.5 A, off

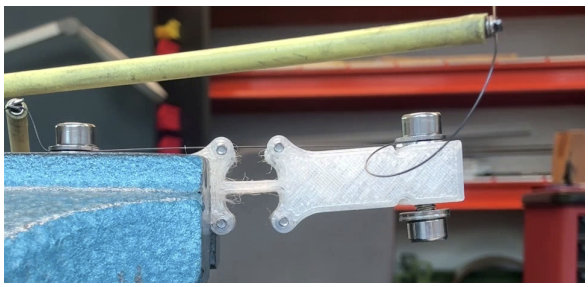

(b) 0.5 A, on

(c) 0.7 A, off

(d) 0.7 A, on

Figure 3.14: Comparison of different supply currents for hinge actuation

imum actuation angle for both cases as compared to their initial state. The lower current does not significantly actuate the hinge, whereas the 0.7 A test resulted in an approximate actuation angle of 13°.

Introduction of a second wire on the opposite side of the flexure allows for antagonistic actuation [81]. The tests with two wires showed asymmetric hinge extension at equal currents. Figure 3.15 clearly shows a significantly increased extension in the direction of the wire mounted with a slightly higher initial tension. The actuation against the determined primary extension direction is very low, indicating insufficient force generated by the SMA wire to overcome the tension of the opposing wire. During attachment of

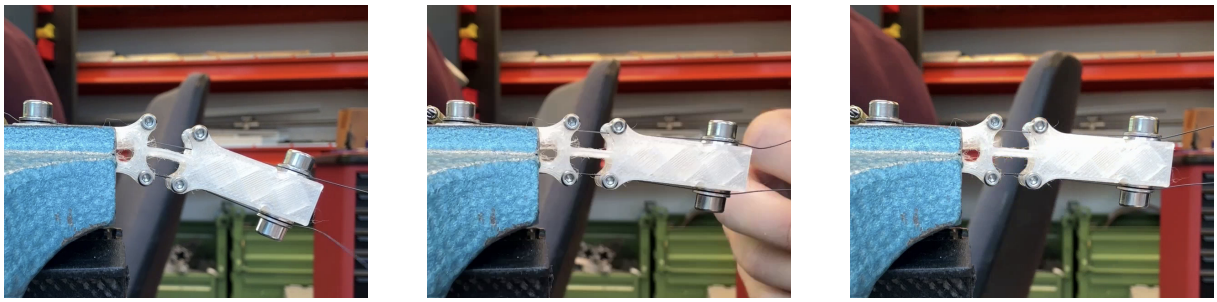

(a) downward actuation (b) no actuation (c) upward actuation

Figure 3.15: Comparison of actuation direction at 0.7 A

electrical contacts to the test carrier, low torsional loads were applied to the structure. This resulted in significant torsional deformation of the flexure, as shown in Figure 3.16. Furthermore, shear of the hinge, that is, lateral displacement normal to the plane of the blade flexure, is not fully constrained by this flexure either.

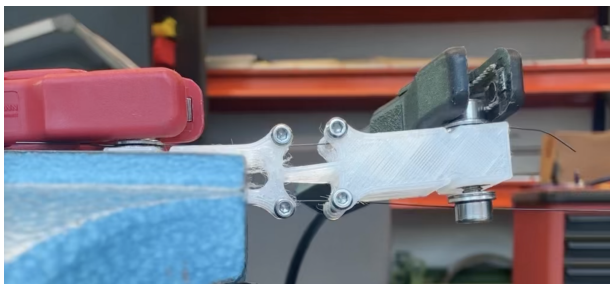

Figure 3.16: Torsional deformation of the blade flexure

Phase II: Multi-hinge Integration

While the single-hinge test carrier demonstrated the fundamental capability of the SMA wire to actuate a flexure, the observed torsional instability and shear displacement (cf. Figure 3.16) indicated that the “blade” geometry is insufficient for the loading conditions of a regolith conveyor. Consequently, a second iteration was developed, utilising several

"notch" flexures to provide higher SDOF constraint [52]. The following tests evaluate this refined geometry.

Higher supply currents of 1 A were investigated in lateral extension tests. Subsequently, tests with vertical actuation were performed to investigate the effects of gravity. Contrary to the limitations exposed by the single-hinge test, the supply current of 0.7 A did not produce asymmetric extension in the lateral multi-hinge tests. Both 0.7 A and 1 A resulted in high actuation angles, with the higher current reaching a slightly higher angle of 86°. The test carrier is shown at full extension in Figure 3.18b. After the actuation current is turned off, the test carrier returns to its initial state without requiring antagonistic actuation.

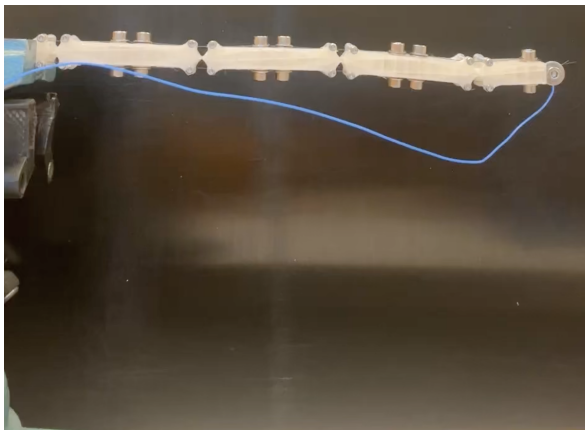

(a) Initial relaxed state

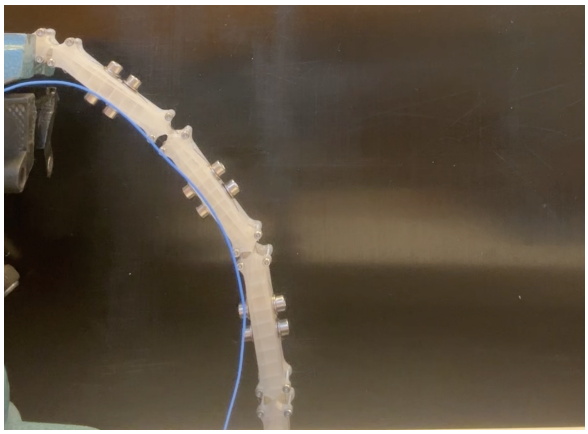

(b) Full actuation

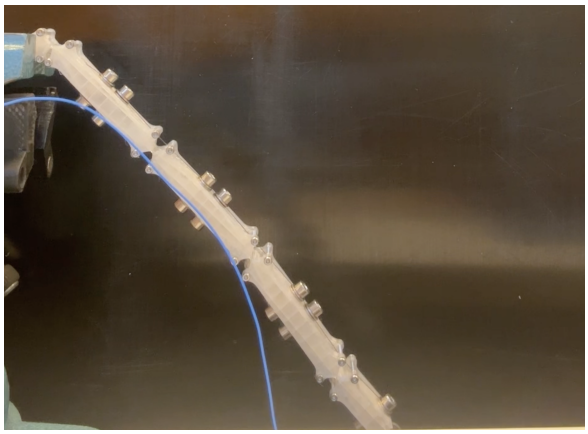

(c) Post-actuation relaxed state

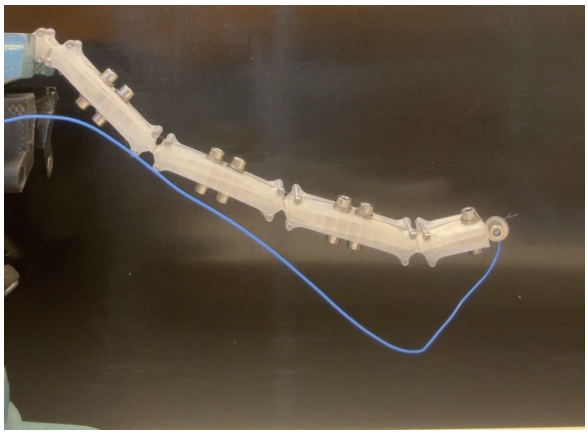

(d) Full opposite actuation

Figure 3.17: Extension states as a result of downward actuation

For the vertical actuation tests, the higher current of 1 A was used. The actuation speed of the downward actuation was significantly faster than that of the actuation in the lateral tests, while the actuation angle showed no significant difference. When the supply current was cut, the test carrier failed to return to its initial state. Instead, the first hinge overextended, exceeding the actuation angle, while the remaining hinges relaxed to their initial state. At opposite actuation, the first hinge stayed in the overextended state, while the remaining hinges performed the planned extension in the opposite direction. Figure 3.17

shows the initial relaxed state, full actuation, post-actuation relaxed state and full opposite actuation for this test. A symptom of the overextension in Figure 3.17c is the full contact of the SMA wire with the flexure. Due to this contact, the effective lever arm of the actuator on the hinge is minute, leading to a kinematic singularity. The return of this hinge to its initial state is thus almost completely reliant on the flexure's stiffness, which is insufficient with the gravitational force acting against this motion. While this behaviour is most apparent in this extreme case of overextension, the same principle applies to all actuations. The flexure's stiffness is thus an important design parameter for this concept. Loading with material and different gravitational acceleration on the Moon directly impacts this problem. In the case of further development, this effect must be investigated further under different environmental conditions. The full contact between the flexure and the wire poses an additional challenge due to the potential for a sliding tribological contact. In the full system, the surface of the chain would occasionally be loaded with lunar regolith, with the residue persisting permanently. Intrusion of abrasive material would significantly increase friction between the elements, posing a risk of impeding hinge motion and causing wear between the two materials, eventually leading to failure of the SMA wire and/or problems in the flexure.

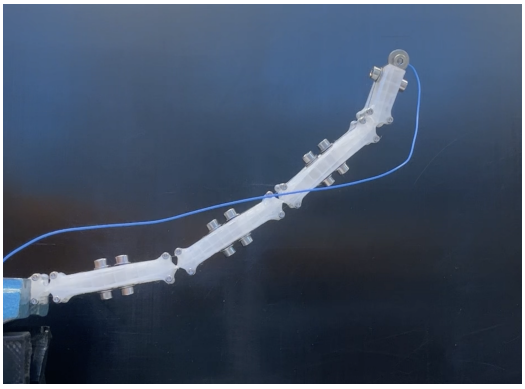

(a) Full upward actuation

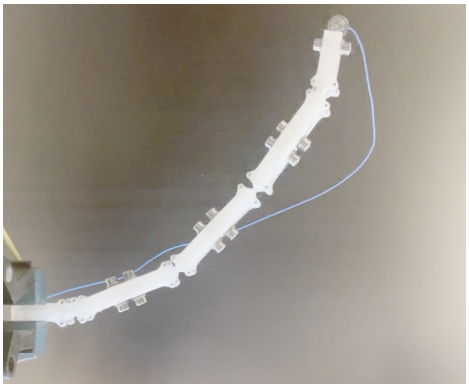

(b) Full lateral actuation

Figure 3.18: Comparison of upward and lateral actuation

At initial upward actuation, the test carrier behaved similarly to the lateral actuation. Extension is significantly slower than the speeds observed during downward or lateral actuation. The actuation angle is also significantly lower at 70°. A comparison between the test carrier in full lateral and upward extension is given in Figure 3.18. The test carrier returns to its initial state without antagonistic actuation, as previously demonstrated with lateral actuation.

The iterative validation of Concept 6 demonstrated the feasibility of SMA-actuated compliant hinges achieving an extension angle of $\approx 20°$ per hinge. The transition from a "blade" flexure to a "notch" flexure significantly improved the hinge's torsional and shear stiffness. However, the validation also showed limitations of this concept. A trade-off in supply voltage must be made for the specific wire and environmental conditions encoun-

tered to find the optimal balance between fast actuation at high angles and energy efficiency. Under gravitational acceleration, the hinges exhibited difficulty returning to their initial conditions, an effect that would need to be investigated further in the context of a waveform. Additionally, the pre-tension of the actuation wire significantly affects actuation performance. To conclude, the concept is considered feasible, with some challenges to be overcome in further development.

3.4.3 Energy Estimation

An energy estimation is conducted for both concepts investigated as part of the POC validation. The estimations aim to provide a comparison between the two concepts. The result is given as a specific energy, that is, the energy required per transported mass over the full conveyor distance. While the constant power draw is provided, it is not particularly significant without the context of the mass flow.

Energy for Concept 4

The energy requirements for Concept 4 are determined based on the force exerted during a single upstroke. For this estimation, the deceleration of the sledge at the end of the upstroke is idealised as instant. Due to the assumed actuation using SMA-wires, kinetic energy is assumed not to be recoverable in the deceleration. The force required for the upstroke consists of the acceleration force F_{kin}, the force to raise the sledge's potential energy F_{pot}, as well as an additional force required to return the SMA-actuators to their initial states. This component force is assumed to be provided by a pre-tensioned spring, likely incorporated in the flexure assembly guiding the sledge. The return force is calculated as the product of the number of springs n_{wire} and the force required for resetting a single wire F_{bias}. The energy required for actuation is calculated from the heating energy required for the SMA-actuators to contract. Application of the heating energy of a single wire to the complete wire set with n_{wire} yields the energy for a single upstroke W_{upstroke}. The average continuous power draw P_{avg} is subsequently determined utilising the stroke frequency f_{stroke}. The specific energy is ultimately calculated as a function of the mass flow $\dot{m}_{\text{regolith}}$ and P_{avg}.

Energy estimation commences with a mass estimate of the loaded sledge. As a conservative estimate, the mass of the full system's sledge is assumed to be equivalent to an 6061-T6 aluminium plate with a thickness of $l_{\text{t}} = 5\,\text{mm}$. The width of the sledge is assumed to be identical to the transport width of the conveyor belt used in Team BREMEN's transport

and dosing mechanism in ESA 's SRC at $l_{\text{width}} = 160\,\text{mm}$. The length of the sledge is calculated from the required horizontal transportation distance l_{hor}:

$$l_{\text{total}} = \frac{l_{\text{hor}}}{\cos\alpha} \tag{3.1}$$

At the maximum conveyor angle $\alpha = 40°$, the length of the sledge is $l_{\text{total}} = 1.3054\,\text{m}$. The sledge's mass is consequently calculated with the density of the aluminium of $\rho_{\text{alu}} = 2.7\,\text{g/cm}^3$:

$$m_{\text{sledge}} = (l_{\text{total}}\, l_{\text{width}}\, l_{\text{t}})\, \rho_{\text{alu}} \tag{3.2}$$

This results in a mass of $m_{\text{sledge}} = 2.82\,\text{kg}$. To calculate the regolith mass moved in a single stroke, a comparison to Profile 1 used in the POC-tests is drawn. In this setup, a single tooth held a sand mass of 2 g. This value is scaled up to the width of the full system and multiplied by the number of teeth, assuming an identical geometry to the POC-tests. For this, a scaling factor s_{scale} is introduced:

$$s_{\text{scale}} = \frac{l_{\text{width}}}{l_{\text{width,POC}}} \tag{3.3}$$

Both Profiles 1 and 2 are 70 mm wide. This results in a scaling factor of $s_{\text{scale}} = 2.286$ The total regolith mass in the full system is thus:

$$m_{\text{regolith}} = m_{\text{tooth,poc}}\, s_{\text{scale}}\, \frac{l_{\text{total}}}{l_c} \tag{3.4}$$

l_c is the tooth pitch of Profile 1, as defined in Table 3.3. This equates to a total regolith mass of $m_{\text{regolith}} = 0.2984\,\text{kg}$ and consequently a total moved mass of $m_{\text{total}} = m_{\text{sledge}} + m_{\text{regolith}} = 3.118\,\text{kg}$.

The acceleration of the sledge is scaled down to the lunar environment from that observed in the POC-tests. As shown in Figure 3.11, a maximum acceleration of $a_{\text{actual}} \approx 54\,\text{m/s}^2$ is reached in the POC-tests. As a worst case, this value is assumed to be constant throughout the entire acceleration. For this energy estimation, the sledge acceleration is scaled proportionally to the gravitational acceleration with the scaling factor $s_{\text{grav}} = g_{\text{moon}}/g_{\text{earth}} = 0.1656$. This results in an acceleration of $a_{\text{upstroke}} = 8.95\,\text{m/s}^2$. By multiplying the acceleration by the moved mass, the force required for this motion is obtained at $F_{\text{kin}} = 27.89\,\text{N}$. The moving mass is lifted during the upstroke, changing its potential energy. The force required for this change is calculated with:

$$F_{\text{pot}} = m_{\text{total}}\, g_{\text{moon}}\, \sin\alpha \tag{3.5}$$

When using SMA-wires for actuation, an inherent behavioural characteristic must be addressed. Two material properties govern the application of SMA actuators: When heated

beyond the transition temperature, the SMA wire transforms from its low-temperature martensitic state to its high-temperature austenitic state. During this transformation, the material contracts. The force applied by this contraction is called the "recovery force". For the nickel-titanium alloy wire with a diameter of 0.25 mm, as used in the POC-tests of Concept 6, this recovery force is estimated at $F_{\text{recovery}} \approx 10\,\text{N}$ (Value at $A_f = 100\,°\text{C}$ [59]). To return the wire to its initial martensitic state, a "bias force" must be applied. In the case of this wire, the bias force is estimated to $F_{\text{bias}} \approx 4.9\,\text{N}$ [82]. In Concept 4, this bias force would be exerted on the wire by the compliant linear guide, acting as a spring. Given sufficient pre-tension, the force of a spring can be assumed to be constant and equal to the bias force across its stroke. During the upstroke, the actuator must overcome this spring force in addition to the required acceleration force F_{kin}. The number of required wires $n_{\text{wire}} = 7$ to overcome this combined force is calculated with:

$$n_{\text{wire}} = \lceil \frac{F_{\text{kin}} + F_{\text{pot}}}{F_{\text{recovery}} - F_{\text{bias}}} \rceil \tag{3.6}$$

SMA wires exhibit contraction ratios of 3 % to 7 % [83]. For this estimation, an average value of 5 % is used. In each upstroke, the actuation wires must contract by a stroke length l_{stroke}. In this estimation, the stroke length most commonly used in the POC of $l_{\text{stroke}} = 10\,\text{mm}$ is assumed. This results in a wire length of $l_{\text{wire}} = 200\,\text{mm}$. The energy required to heat this wire to its contraction temperature is calculated with:

$$W_{\text{heat}} = c_{\text{p,wire}}\,\Delta T\,\rho_{\text{wire,l}}\,l_{\text{wire}} \tag{3.7}$$

The mass of the wire is included in this equation as the product of the wire length l_{wire} and the wire's linear density $\rho_{\text{wire,l}}$. The latter is calculated with:

$$\rho_{\text{wire,l}} = d_{\text{wire}}^2\,\frac{\pi}{4}\,\rho_{\text{wire}} \tag{3.8}$$

For the wire diameter of $d_{\text{wire}} = 0.25\,\text{mm}$ and a density of $\rho_{\text{wire}} = 6.45\,\text{g/cm}^3$, as were used in the POC-tests, the linear density equates to $\rho_{\text{wire,l}} = 0.317\,\text{g/m}$. ΔT is formed as the difference of the target temperature the wires are heated to $T_{\text{hot}} = 370\,\text{K}$ [84] and the worst case environmental temperature $T_\infty = 50\,\text{K}$, as defined in Section 2.4.3 and equates to $\Delta T = 320\,\text{K}$. The specific heat capacity is a material parameter of the wire at $c_{\text{p,wire}} = 320\,\text{J/kg K}$ [84]. With these values, the energy required to heat a single wire equates to $W_{\text{heat}} = 6.484\,\text{J}$. Applying this to the number of wires n_{wire} results in an energy per upstroke of $W_{\text{upstroke}} = 45.39\,\text{J}$. Radiative losses are neglected in this estimation because the wires' inherently short duration at high temperatures prevents them from radiating.

The volumetric flow rate was measured in the POC-tests at $\dot{V}_{\mathrm{POC}} = 1.15\,\mathrm{cm}^3/\mathrm{s}$. This flow rate was measured at a stroke frequency of $f_{\mathrm{POC}} = 4.4\,\mathrm{Hz}$. The flow rate of the full system is likely much lower due to the limitations of the SMA-actuators. In the scope of this preliminary estimation, the frequency reachable with this actuator system is not determinable. Instead, the mass flow requirement is used to determine the minimum required stroke frequency. The mass flow is calculated with:

$$\dot{m}_{\mathrm{regolith}} = \dot{V}_{\mathrm{POC}} \frac{f_{\mathrm{stroke}}}{f_{\mathrm{POC}}} s_{\mathrm{scale}} \rho_{\mathrm{regolith,min}} \tag{3.9}$$

with the uncompressed bulk density of lunar regolith $\rho_{\mathrm{regolith,min}}$. Carrier et al. found the minimum bulk density of lunar regolith at $\rho_{\mathrm{regolith,min}} = 0.89\,\mathrm{g}/\mathrm{cm}^3$. This is assumed to be the bulk density of the uncompressed material for this energy estimation. The volumetric flow rate from the POC tests $\dot{V}_{\mathrm{POC}}$ scaled by both the factor s_{scale}, as introduced in (3.3), as well as $f_{\mathrm{stroke}}/f_{\mathrm{POC}}$, a factor representing the change in stroke frequency. Under the boundary condition of the minimum required flow rate $\dot{m}_{\mathrm{regolith}} = 3\,\mathrm{kg/h}$, the frequency equates to $f_{\mathrm{stroke}} = 1.58\,\mathrm{Hz}$. By multiplying the energy per stroke W_{upstroke} by the stroke frequency f_{stroke}, the estimated average power draw of the system is calculated at $P_{\mathrm{avg}} = 71.62\,\mathrm{W}$. Dividing this average power draw by the mass flow rate, the total specific energy of Concept 4 is calculated:

$$W_{\mathrm{spec}} = \frac{P_{\mathrm{avg}}}{\dot{m}_{\mathrm{regolith}}} \tag{3.10}$$

The specific energy equates to $W_{\mathrm{spec}} = 85.94\,\mathrm{kJ/kg}$.

Energy for Concept 6

The energy estimation of Concept 6 follows a different approach than that of Concept 4. Here, the total specific energy is derived from the heating power required to raise and maintain the actuators' temperatures during the conveyance process. First, the mass of the transported regolith is determined. The work of raising the potential energy of the material is set in relation to the work exerted by a single wire during actuation. The required number of wires follows from this relation. The energy required to heat the wires to the temperature at which they transform from martensite to austenite is then used to determine the total heating energy for a full-wave cycle of 1 m. Radiation losses of the wires are determined for the duration of the conveyance. Ultimately, average continuous power draw and specific energy are determined for comparison to Concept 4. Estimating the mass of the moved regolith requires quantifying the volume the material occupies. Figure 3.19 shows the cross-sectional area assumed to be occupied by regolith. It is defined as an annulus section constrained by the chain and the inner radius of the sidewalls. In this case, the height of the sidewalls l_{wall} is assumed to be equal to the length of one

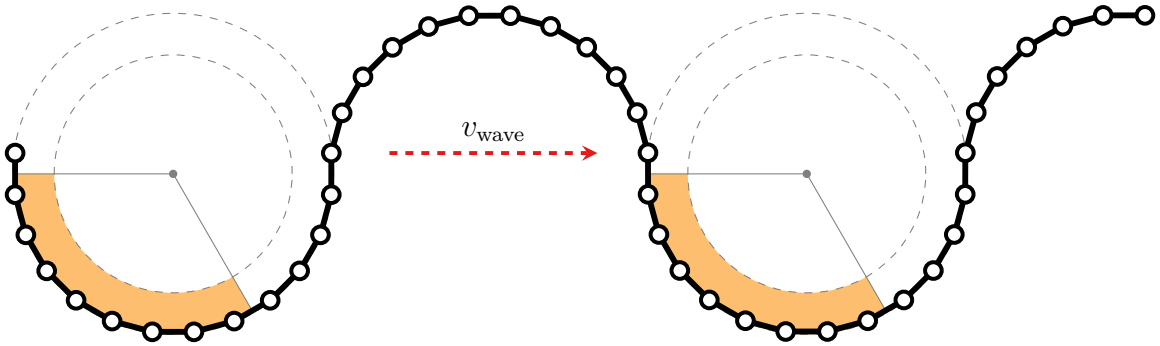

Figure 3.19: Cross-sectional area assumed to be occupied by regolith

rigid element $l_{\text{element}} = 30\,\text{mm}$. The regolith is assumed to fill 1/3 of the full annulus. At an assumed maximum actuation angle of $\zeta = 15°$, the outer radius of this annulus is $r_{\text{outer}} = 114\,\text{mm}$, and the inner radius consequently $r_{\text{inner}} = 84\,\text{mm}$. The area of the annulus section thus equates to $A_{\text{annulus}} = 6.2 \cdot 10^{-3}\,\text{m}^2$. The total regolith mass on the conveyor is calculated with:

$$m_{\text{regolith}} = A_{\text{annulus}}\, l_{\text{width}}\, \rho_{\text{regolith,min}}\, n_{\text{trough}} \tag{3.11}$$

The width of the conveyor l_{width} and the bulk density of the regolith $\rho_{\text{regolith,min}}$ are equal to the values used for Concept 4, as defined in Section 3.4.3. n_{trough} denotes the number of wave troughs in which regolith is conveyed. It has been geometrically determined from the parameters of l_{element} and ζ. For this simplified estimation, the mass of regolith is proportional to the integer amount of complete troughs on the conveyor and equates to $m_{\text{regolith}} = 1.77\,\text{kg}$.

The chain-wave moves in discrete steps, henceforth called “wave advancements”. Each step consists of the inversion of the curvatures of the compliant hinges located at the inflection points, as described in Section 3.2.6. The distance between each inflection is necessary for both calculating the change in potential the regolith experiences and the advancement velocity, and, consequently, the mass flow. This delta is defined as:

$$\Delta l_{\text{adv}} = l_{\text{element}}\, \sin(2\,\zeta) \tag{3.12}$$

ζ is defined as the maximum actuation angle. The total change in angle from one actuation direction to the opposite is equal to twice the maximum actuation angle. Multiplying the sine of this angle by the length of the element results in the total advancement distance in the movement direction. For the change in potential energy, the regolith’s vertical

displacement is required. The value for the vertical and horizontal displacement for each wave advancement is calculated with:

$$\Delta l_{\text{adv,hor}} = \Delta l_{\text{adv}} \sin\alpha \tag{3.13}$$

$$\Delta l_{\text{adv,vert}} = \Delta l_{\text{adv}} \cos\alpha \tag{3.14}$$

$$\tag{3.15}$$

Calculating the change in potential energy for each wave advancement with:

$$\Delta W_{\text{pot}} = m_{\text{regolith}}\, g_{\text{moon}}\, \Delta l_{\text{adv,vert}} \tag{3.16}$$

yields $\Delta W_{\text{pot}} = 27.8\,\text{mJ}$. This value is set in relation to the work [...] by a single SMA-actuator wire to determine the required number of wires. This work is defined as:

$$W_{\text{margin,SMA}} = W_{\text{recovery}} - W_{\text{bias}} \tag{3.17}$$

W_{recovery} and W_{bias} represents the application of the characteristic forces F_{recovery} and F_{bias}, which were defined in Section 3.4.3 along the contraction of the wire Δl_{SMA}. This contraction is defined by the hinge geometry. For this estimation, the hinge geometry used in the POC-tests is assumed. Figure 3.20 shows the hinge geometry in its initial state and in its fully actuated state.

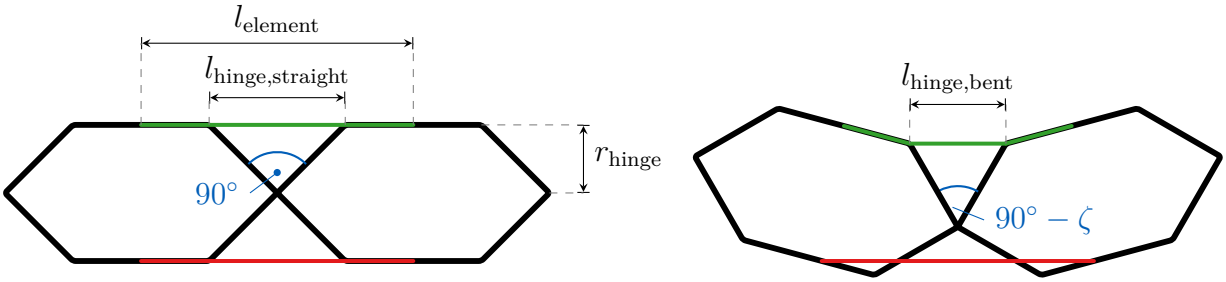

Figure 3.20: Hinge geometry

The actuation angle in Figure 3.20 is exaggerated for clarity. As illustrated in Figure 3.15a, and expanded on in Section 3.4.2, the SMA-wire on the convex side of the hinge (indicated in red in Figure 3.20) conforms to the inside of the hinge. Consequently, any tension arising from the antagonistic actuation is neglected. The variables $l_{\text{hinge,straight}} = 10\,\text{mm}$, $r_{\text{hinge}} = 5\,\text{mm}$ are used. The contraction is equal to the difference between $l_{\text{hinge,straight}}$ and $l_{\text{hinge,bent}}$. This difference is calculated from the hinge geometry with:

$$\Delta l_{\text{SMA}} = l_{\text{hinge,straight}} - 2\, r_{\text{SMA}}\, \sqrt{2}\, \sin(\frac{90° - \zeta}{2}) \tag{3.18}$$

SMA wires exhibit contraction ratios of 3 % to 7 % [83]. The wire spans the length of one element. The contraction length of $\Delta l_{\text{SMA}} = 1.391\,\text{mm}$ thus corresponds to a contraction

ratio of 4.64, the actuation angle of $\zeta = 15°$ is thus considered realistic under the given hinge geometry. Applying F_{recovery} and F_{bias} over the contraction Δl_{SMA}, recovery and bias work are calculated to $W_{\text{recovery}} = 13.91\,\text{mW}$ and $W_{\text{bias}} = 6.83\,\text{mW}$. The number of wire required to perform ΔW_{pot} equates to $n_{\text{wire}} = 4$ and is calculated with:

$$n_{\text{wire}} = \left\lceil \frac{\Delta W_{\text{pot}}}{W_{\text{recovery}} - W_{\text{bias}}} \right\rceil \tag{3.19}$$

The heating energy is now calculated for a single wire, before being applied to the complete set of wires. (3.7) introduced the calculation of the energy required to heat a single wire of specified length l_{wire}. The heating energy calculation for Concept 6 is split into the initial heating required to transform the wire from its straight state to its waveform and the energy required to advance the wave. For continuous operation, the singular event of initial heating is considered negligible.

For each wave advancement, the actuation direction of the hinges located at the inflection points is reversed. This requires heating of the antagonistic wire. The actuation wire for a single hinge is assumed to be equal in length to a rigid element, resulting in a total advancement wire length of:

$$l_{\text{adv}} = n_{\text{inflection}}\, l_{\text{element}} \tag{3.20}$$

The number of inflection points $n_{\text{inflection}} = 6$ is derived from geometric modelling in Computer Aided Design (CAD). The heating energy for wave advancement is calculated with (3.7) at $W_{\text{heat,adv}} = 5.84\,\text{J}$. In this estimation, the energy $W_{\text{heat,conv}}$ to convey the regolith over the full distance l_{total} is calculated. For this, the advancement energy must be multiplied by the number of advancements required for this full transport and the number of wires defined in (3.19):

$$W_{\text{heat,conv}} = W_{\text{heat,adv}}\, n_{\text{adv}} \tag{3.21}$$

with the number of advancements being the quotient of the total length l_{total} and the horizontal advancement displacement $\Delta l_{\text{adv,hor}}$, rounded up to the nearest integer. This equates to $n_{\text{adv}} = 88$. The total heating energy across all wires for the full transport is thus calculated to $W_{\text{heat,conv}} = 3.081\,\text{kJ}$.

During the whole conveyance process, a wire length equivalent to $n_{\text{wire}}\, l_{\text{chain}}$ is heated to the target temperature T_{hot}. In this estimation, conductive cooling at the contact points of the wires is considered negligible; only radiation losses are taken into account. The heat loss rate due to radiative cooling is calculated as a function of the temperature difference between the radiating body and the environment at [60, p. 33]:

$$Q_{\text{rad}} = \epsilon_{\text{wire}} \cdot \sigma \cdot (T_{\text{hot}}^4 - T_{\infty}^4) \cdot A_{\text{surface}} \tag{3.22}$$

This equation assumes a view factor of 1, corresponding to the radiating body having a direct line of sight to open space in all directions. While this is likely not the case for the wires in this concept, the exact view factor is not known, so the worst-case is assumed. The emissivity of the SMA-wire at T_{hot} is $\epsilon_{\text{wire}} \approx 0.17$ [85]. The Stefan-Boltzmann-constant is a universal constant at $\sigma = 5.670 \times 10^{-8}\,\text{W}/(\text{m}^2\,\text{K}^4)$. The combined surface area of the wires A_{surface} is calculated with:

$$A_{\text{surface}} = n_{\text{wire}}\, l_{\text{chain}}\, \pi\, d_{\text{wire}} \tag{3.23}$$

with $d_{\text{wire}} = 0.25\,\text{mm}$ being the diameter of one actuation wire. The surface area of the wire ends is neglected. This results in a heat flow due to radiation of $Q_{\text{rad}} = 0.298\,\text{W}$. This heat flow is applied over the whole duration of the conveyance $t_{\text{conv}} = 880\,\text{s}$. t_{conv} is calculated as the product of the number of advancements n_{adv} and the time per advancement t_{adv}. For this, the time for full extension measured in the POC-tests was used at t_{adv} $approx 10\,\text{s}$. The total energy lost due to radiation can be calculated to $W_{\text{rad}} = 1.573\,\text{kJ}$.

Together with the heating energy, this results in a total energy for one metre of horizontal conveyance at a slope of 40° of $W_{\text{total}} = 4.654\,\text{kJ}$. For comparison with Concept 4 in Section 3.5.1, the specific energy as a function of the transported mass W_{spec}, the average continuous power draw P_{avg}, and the mass flow $\dot{m}_{\text{regolith}}$ are calculated:

$$W_{\text{spec}} = \frac{W_{\text{total}}}{m_{\text{regolith}}} \approx 1.751\,\text{kJ/kg} \tag{3.24}$$

$$P_{\text{avg}} = \frac{W_{\text{total}}}{t_{\text{conv}}} \approx 5.289\,\text{W} \tag{3.25}$$

$$\dot{m}_{\text{regolith}} = \frac{m_{\text{regolith}}}{t_{\text{conv}}} \approx 10.87\,\text{kg/h} \tag{3.26}$$

3.5 Final Concept

Following the POC validation, a final concept is selected in Section 3.5.1 from the previously evaluated candidates, namely Concept 4 and Concept 6. Consequently, the selected concept is detailed in Section 3.5, including the final selection of an actuation method and a preliminary conceptualisation of the compliant guiding mechanism.

3.5.1 Concept Decision

The selection between Concept 4 and Concept 6 is evaluated through a synthesis of theoretical compliance (cf. Section 3.3), Proof-of-concept tests, and analytical energy es-

timations. Table 3.5 shows a summary of the trade-off between Concept 4 and Concept 6.

Table 3.5: Trade-off between Concept 4 and Concept 6

Concept 4		**Concept 6**	
Pro	**Con**	**Pro**	**Con**
More continuous conveyance	High specific energy	Low specific energy	Highly non-continuous conveyance
Insensitivity to load variations		High mass flow	Large dimensions
Enhanced subsystem interfacing		High conveying distance due to high scalability	Susceptibility to material loss
			Overextension problems
			Problems with tribological pairs
			Problems with Interfacing to other subsystems
			SPOF

The energy estimates showed that Concept 6 is two orders of magnitude more efficient than Concept 4 (cf. Section 3.4.3). While this represents a significant performance deficit, mission-critical requirements for reliability, long-term feasibility, and robustness in a dust-contaminated environment outweigh concerns about energy efficiency. In the POC-tests, Concept 6 showed high sensitivity to loading and gravitational acceleration. In the vertical actuation tests, the multi-hinge test carrier failed to revert to its initial condition. While this effect is expected to be less pronounced under lunar gravitational acceleration, the introduction of loading during the conveyance of the material may counteract the positive effects of the reduced gravity. The reciprocating motion of Concept 4 avoids these complex kinematic problems.

Concept 6 is designed as a series of hinge/actuator subsystems. The conveyor's reliance on a large number of complex subsystems exposes a SPOF. The failure of one subsystem would lead to the complete dysfunction of the whole system. A major factor contributing to the hinges' reliability was revealed in the POC-tests. During overextension, the SMA-wire on the convex side of the extension contacted the compliant hinge, forming a tribological pair. In operation as a conveyor, these contact areas would likely become contaminated with lunar regolith, posing a significant risk of high wear to both the hinge

and the actuation wire. Concept 4, on the other hand, features the possibility of introducing redundancy by including additional SMA-wires, in addition to those required for actuation. A Single Point of Failure (SPOF) in Concept 4 is present in the failure of the sledge itself, which does not exhibit the same complexity and wear characteristics as the hinge subsystems in Concept 6. As identified in Section 3.3.4, Concept 4 features better adaptability to the beneficiation subsystem. While the output of Concept 4 inherently shows oscillation, making adaptation to the static inlet of the beneficiation subsystem a challenge. The relatively low displacement of the sledge is, however, much better compensable than the highly dynamic wave geometry of Concept 6, which exhibits significant displacement, both laterally and vertically.

Concept 6 exhibits superior scalability, enhancing feasibility for long-distance transport. Conversely, extending Concept 4 for such applications necessitates a modular approach, as increasing the sledge length would introduce significant manufacturing and maintainability challenges. The mass flow calculated in Section 3.4.3 is higher for Concept 6 than it is for Concept 4. While Concept 4 nearly met the required minimum mass flow in the POC-tests, the lower actuation frequency, despite unchanged sawtooth geometry, significantly reduced its performance. While Concept 6 shows promising mass flow, its continuity is very low. The transport of material in the wave troughs inherently leads to highly discretised delivery. The problems with losses, as identified in Section 3.3.1, are another major disadvantage of Concept 6 and would need to be addressed to enable its application.

Consequently, Concept 4 is chosen as the superior concept for further development in this study. While Concept 6 showed significant advantages to Concept 4 in the energy requirements, Concept 4 is much more suitable for application in a local ISRU process chain. The higher flow continuity, adaptability to the beneficiation subsystem, the possibility for redundancy, and expected longevity in dusty environments show clear advantages over Concept 6 for this application. However, the high scalability, improved efficiency, and higher mass flow of Concept 6 make it well-suited for an application as a long-distance transport mechanism, for example, transporting regolith out of a lunar crater. While Concept 6 still shows significant problems that need to be overcome, notably material losses and SPOF-architecture, and is considered unsuitable for the local application, it is proposed for further research in this long-distance application.

Further development will focus on overcoming the limitations of specific energy and mass flow, as identified in Section 3.4.3. The following section defines the mechanical architecture of Concept 4, establishing the foundation required for system simulation and optimisation in Chapter 4.

3.5.2 System Specification

This section discusses the system's qualitative architecture, particularly the selection of actuation principles and compliant kinematics. Exact quantitative dimensioning is not performed within this study. Instead, the focus lies on simulation and optimisation in the following Chapter 4 and Chapter 5, thereby defining boundaries for a future, more elaborate design.

As discussed in Section 3.1, implementation of linear motors would require additional active or passive dust mitigation techniques, and is thus not examined further; only piezoelectric and SMA actuators remain under consideration for this application. To evaluate the suitability of both actuation methods, the performance of SMA and piezoelectric actuation is compared utilising performance maps compiled by Huber et al. [71].

The volumetric energy density of an actuator is calculated with:

$$w_{\mathrm{v}} = C_s \, \sigma_{\max} \, \epsilon_{\max} \tag{3.27}$$

Here, C_s is the actuator's stroke work coefficient, $\sigma_{\max}$ is the maximum actuation stress, and $\epsilon_{\max}$ is the maximum actuation strain. The relevant properties for the piezoelectric and SMA actuators are summarised in Table 3.6.

Table 3.6: Comparison of mechanical actuator characteristics based on Huber et al. [71]

Parameter	**SMA**	**Piezoelectric (High-Strain)**
C_s	0.3 – 0.6	≈ 0.5
$\sigma_{\max}$ in MPa	100 – 700	4 – 9
$\epsilon_{\max}$	7×10^{-3} – 7×10^{-2}	5×10^{-5} – 2×10^{-4}
w_{v} in J/m^3	2.1×10^{5} – 2.9×10^{7}	1×10^{2} – 9×10^{2}

The power density of piezoelectric actuators is higher than that of SMA-based concepts at $5 \times 10^{8}\,\mathrm{W/m^3}$ and $1 \times 10^{8}\,\mathrm{W/m^3}$ respectively. Due to the significantly higher actuation frequency, however, the energy density of SMA-actuators exceeds piezoelectric methods by several orders of magnitude. The POC-tests demonstrated a required actuation force of 60 N for the sawtooth assembly. In the full-size system for lunar application, this force is expected to be higher due to the increased system size. As established in Section 2.4.1, the system mass has a high impact on the feasibility of a concept. Consequently, actuation utilising SMAs is selected for further investigation in this study due to its significantly higher energy density. However, the primary limitation of SMA-actuators, the limited stroke frequency, must be acknowledged. The thermal cycling and cooling limitations in the lunar vacuum environment, discussed in Section 3.1, dictate a low actuation frequency.

The linear rail and plain bearings used in the POC-tests are replaced with CMs for application on the Moon. In the previous tests, the sawtooth profile was guided to follow a strictly linear motion, constraining all but one degree of freedom. Constraining all rotational degrees of freedom of the sawtooth conveyor is paramount to ensuring that the forces acting on the particles across the conveyor are homogeneous; constraining all but one translational degree of freedom is not necessary. In CMs, parallelogram-based flexures are utilised to constrain a body to a parallel motion. The simplest form is a Single Parallelogram Flexure Bearing (SPFB), consisting of two rigid elements and two flexures. Figure 3.21 shows a SPFB in its initial state as well as at significant deformation. As

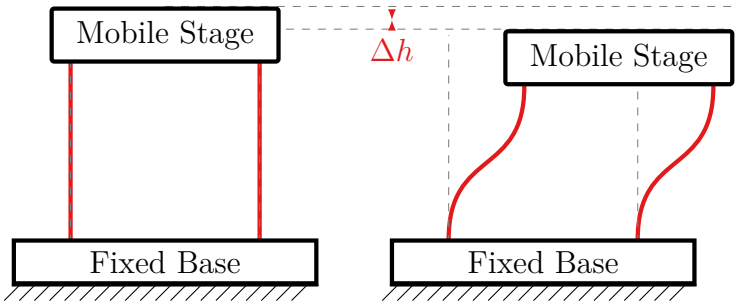

Figure 3.21: Single Parallelogram Flexure Bearing

shown in Figure 3.21, the vertical distance between the fixed base and mobile stage decreases significantly (by Δh) at horizontal deformation, resulting in a parallel, but not linear motion of the mobile stage. To achieve strictly linear motion, two SPFBs are combined to form a Double Parallelogram Flexure Bearing (DPFB), which counteract their respective vertical deformations. The deflection of a DPFB is illustrated in Figure 3.22. The intermediate stage follows the same motion as the mobile stage in the SPFB; the vertical motion of the lower mobile stage is counteracted by the second SPFB, which acts in parallel with the initial mechanism. The constraint to a strictly linear motion,

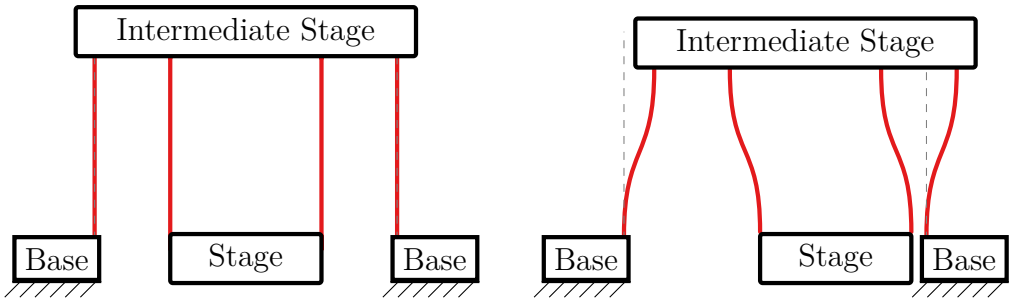

Figure 3.22: Double Parallelogram Flexure Bearing

as is achievable with DPFBs, is not necessarily required for the final application. While constraining the sawtooth profile to a parallel motion is imperative, the vertical displacement inherent to the SPFB is assumed not to influence the effectiveness of this concept negatively.

The illustrations in Figure 3.21 and Figure 3.22 assume the use of simple, distributed compliance blade flexures, as introduced in Section 2.3. In compliant mechanism design, a distinction is made between distributed and lumped compliance mechanisms [86]. Distributed compliance describes the above assumed and illustrated architecture. Lumped compliance replaces most of the flexure blades with rigid elements, retaining only the outermost section for compliance. In this case, the contracted blade flexures may also be replaced by notch flexures, enabling higher compressive loading (cf. Section 2.3). Figure 3.23 illustrates the principle of lumped compliance on the example of the SPFB, equivalent to the mechanism introduced in Figure 3.21. The shorter flexure length in

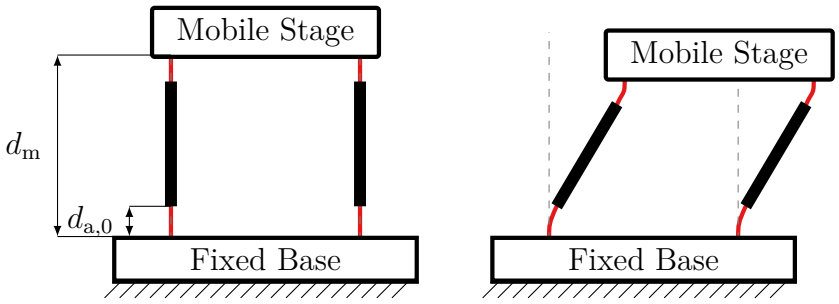

Figure 3.23: Lumped compliance mechanism

lumped compliance mechanisms results in higher stiffness in both axial loading (compression and tension) and the horizontal (in-plane) direction. At the same stress level in the flexures, shorter flexures have a reduced range of motion [86].

In distributed compliance mechanisms, displacement-dependent elastokinematic effects are significant. The axial stiffness of the mechanism decreases significantly during horizontal deflection. The magnitude of these effects in lumped compliance mechanisms is negligible in relation to distributed compliance mechanisms; their axial stiffness is thus effectively independent of the horizontal deflection [86]. Distributed compliance mechanisms also exhibit a greater tendency toward load stiffening. This effect describes the increase in stiffness in the horizontal direction under axial tensile loads. A decrease in flexure length $d_{\mathrm{a},0}$ relative to the complete module length (d_m) toward lumped compliance reduces this effect [86]. Distributed compliance mechanisms exhibit a lower horizontal stiffness than lumped compliance mechanisms. This effect represents a significant constraint in this application involving SMA-actuators. As discussed in Section 3.1, SMA-actuators require a bias force to transform from their twinned martensitic state to the extended de-twinned martensitic state. This force is to be provided by the inherent elastic return force of the compliant mechanism. The required force could, however, likely be reached with both architectures, given adequate dimensioning.

A detailed design of the compliant guiding mechanism is not performed in this study. Depending on the required bias force, axial load, and stroke distance, either or both lumped- and distributed-compliance mechanisms may be applicable. The progression from the

conceptual architecture of Concept 4 to a subsequent system design requires defining these key system parameters. The parameters are subsequently derived from a system simulation and parameter optimisation, taking into account the inherent limitations of SMA-actuation and the sawtooth-conveyor concept. SMA-actuators are limited to low frequencies due to the required cooldown time of the wires. The simulation and optimisation thus aim to find parameters to minimise this actuation frequency. The energy estimates for Concept 4 and Concept 6 revealed high specific energy as a primary disadvantage of the sawtooth conveyor. This aspect will also be addressed in the optimisation. The resulting geometrical and kinetic parameters lay a foundation for further dimensioning and development. From the simulation, loads acting on the sledge and supporting structure will become apparent, enabling their future in-depth design.

4. System Simulation

A system simulation is performed to enable in-depth evaluation and to define critical system parameters for further development of the sawtooth conveyor concept. In Section 4.1, physical foundations used in the system simulation are explained. Section 4.2 will first discuss the simulation function itself, before the simulation is verified in comparison with a validation test in Section 4.3, making use of a fitment optimiser to align the simulation to the test results. The simplification and limitations accepted by the simulation are summarised in Section 4.4.

4.1 Physical Foundations

This section discusses physical foundations for the simulation function in Section 4.2: The Angle of Repose (AOR) is an important property for calculating the lunar regolith's behaviour on the sawtooth conveyor. Its calculation and the specific characteristics of lunar regolith are reviewed in Section 4.1.1. In all collisions between particles and the conveyor, some kinetic energy of the particle is lost to heat and plastic deformation. This energy loss is described by the Coefficient of Restitution (COR). The definition of the COR is discussed in Section 4.1.2. For the validation campaign (cf. Section 4.3), the simulation must be adapted to operate under terrestrial conditions, since the tests will be performed at standard gravitational acceleration and at sea level. For this, a drag model simulating the influence of atmospheric drag on the particle is established in Section 4.1.3.

4.1.1 Angle of Repose

When poured onto a surface under gravity and allowed to spread uninterrupted, a granular material will form a conical pile with a specific slope angle known as the AOR. The AOR depends on a multitude of material properties, including, but not limited to [87]:

- geometrical properties of the particles (particle roundness, sphericity, roughness)
- particle size
- friction coefficients
- coefficient of restitution
- moisture content

Figure 4.1: Angle of Repose (AOR) of table salt on a felt hat

If a granular material is cohesive, that is, if significant inter-particle attractive forces are present, the AOR of that material is dependent both on the height of the pile examined and on the gravitational acceleration the material is experiencing. To determine the AOR of lunar regolith under terrestrial and lunar conditions, the cohesion-behaviour of the material must be examined. The AOR of a cohesive material θ is calculated with

$$\frac{\gamma\, h}{2\, c} = \frac{2\, \sin(\theta)\, \cos(\phi)}{1 - \cos(\theta - \phi)} \tag{4.1}$$

with h being the height of the pile, and c being the cohesion of the examined material. The weight density γ is defined by the bulk density ρ_b multiplied by the gravitational acceleration g. The angle ϕ denotes the angle of internal friction of the material. The AOR is defined here as the angle between the horizontal and the slope of the pile, as illustrated in Figure 4.1. As such, it decreases with increasing gravitational acceleration. As explored in Section 2.2.1, the cohesion of lunar regolith is highly dependent on its compression.

The AOR of lunar regolith under Earth gravity has been measured at 58°, using samples returned by the Apollo 14 mission [88]. Here, the regolith was dropped onto a brass sphere from a very low altitude, resulting in an uncompacted mass. This AOR can be used in (4.1) to calculate the apparent cohesion of the regolith for this level of compression. From Figure 1 in Calle's experiment, the pile height is estimated to be 2 cm [88]. The bulk density of uncompressed regolith is given by Carrier et al. at $0.89\,\mathrm{g\,cm^2}$ [89]. The resulting cohesion of $c_{loose} \approx 2.7\,\mathrm{Pa}$ pales in comparison to the common values in Table 2.1 and is thus deemed negligible. In this thesis, the lunar regolith will be treated as cohesionless, unless stated otherwise. At very low gravitational accelerations and very low pile heights, however, even the small cohesion of 2.7 Pa could have significant effects. This is accepted

as a simplification in the simulation. The AOR for a cohesionless soil, such as sand or gravel [87], is calculated with

$$\theta = \arctan \mu_s \tag{4.2}$$

with μ_s being the coefficient of static friction between the particles in the material. As can be seen from this equation, the AOR of cohesionless soils is independent of the magnitude of the gravitational acceleration. The measured AOR of lunar regolith can thus be applied for all gravitational accelerations under the condition that the lunar regolith is not compressed. The measured angle (58°) is very high compared to other granular materials [88]. As a comparison, Ottawa sand, which is a standard testing sand [92], has an AOR of 28°.

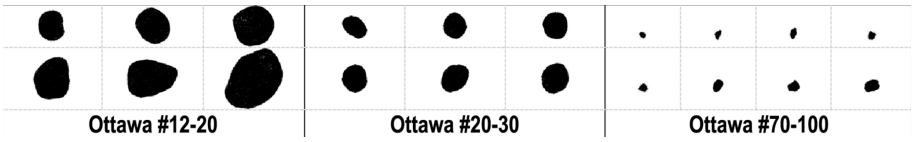

(a) Particle morphology of Ottawa sand, used with permission from SNCSC from Linzhu and Iskander (2022) [90]

(b) Particle morphology of selected scoriaceous particles of lunar regolith samples, reproduced from Heywood (1971) [91]

Figure 4.2: Comparison of particle morphology of Ottawa sand and lunar regolith

The AOR of purely cohesionless materials is equal to the internal friction angle ϕ, which is given by Nedderman [21, p. 39]. Lunar regolith's high AOR stems from its extremely rough and irregular particle surfaces [20]. This contrasts sharply with Ottawa sand. While the sand is highly spherical with a roundness index of 0.9 [93], lunar regolith possesses a significantly lower roundness of just 0.21 to 0.22 [5]. A comparison of the particle shape of selected lunar regolith particles and Ottawa sand particles can be seen in Figure 4.2.

4.1.2 Restitution Coefficients

The Coefficient of Restitution (COR) is often assumed to be constant, dependent only on the material properties of the two materials colliding [94, p. 142]. Furthermore, splitting the COR into a normal and a tangential component is often neglected, only considering the component normal to the surface [94, p. 146]. These assumptions may not hold in all cases and thus must be examined. First, the normal COR will be examined, followed by the tangential coefficient.

The normal COR remains constant only if the collision velocity does not exceed the critical yield velocity, where plastic deformation begins [95]. To determine if a velocity-dependent COR is required for this simulation, the threshold for plastic deformation must be calculated. For this examination, the conveyor material is assumed to be aluminium 6061-T6. The material properties of lunar regolith are highly heterogeneous due to the wide range of materials present. Overall values for the Young's modulus, Poisson's ratio, and compressive strength of regolith are thus unavailable. For this calculation, the properties of basalt are used as an analogue for the lunar regolith. It is used as a substitute for regolith in structural lunar regolith simulants like JSC-1 [96]. Basalt's properties are highly dependent on the exact species and location of the material. The average of the applicable values is used for this estimation. The material properties used are listed in Table 4.1

Table 4.1: Assumed material properties of the Al 6061-T6 conveyor and the basalt regolith analogue

Material	**Property**	**Symbol**	**Units**	**Range**	**Avg.**	**Source**
Al 6061-T6	Young's Modulus	E_{conv}	GPa	–	68.9	[97]
	Poisson's Ratio	ν_{conv}	–	–	0.33	[97]
	Yield Strength	Y_{conveyor}	MPa	–	276	[97]
Basalt Analogue	Young's Modulus	E_{particle}	GPa	60 – 100	80	[98]
	Poisson's Ratio	ν_{particle}	–	0.1 – 0.35	0.225	[99]
	Comp. Strength	Y_{particle}	MPa	110 – 338	224	[98]
	Density	ρ_{particle}	g/cm^3	2.7 – 3.0	2.85	[98]

First, the maximum contact pressure P_0^* at the collision of a sphere with a half-space is calculated. According to Johnson, P_0^* can be obtained with [100, p. 361]:

$$P_0^* = \frac{3}{2\pi}\left(\frac{4\,E^*}{3\,r^{*\,3/4}}\right)^{4/5}\left(\frac{5}{4}m^*\left(v^{\text{col}}\right)^2\right)^{1/5} \tag{4.3}$$

where v^{col} is the collision velocity. This equation contains the effective Young's modulus E^*. This value combines the Young's modulus and Poisson's ratio of both collision parties:

$$\frac{1}{E^*} = \frac{1-\nu_{\text{conv}}^2}{E_{\text{conv}}} + \frac{1-\nu_{\text{particle}}^2}{E_{\text{particle}}} \tag{4.4}$$

The values r^* and m^* are similarly defined as

$$\frac{1}{z^*} = \frac{1}{z_{\text{particle}}} + \frac{1}{z_{\text{conv}}}, \text{for z} \in \{r, m\} \tag{4.5}$$

For both components, the conveyor's term is zero, as the collision surface of the conveyor is always flat, represented by its radius $r_{\text{conv}} = \infty$. The conveyor's mass m_{conv} is also assumed to be infinite in relation to the particle's mass.

The highest velocity reached by a particle is the initial launch velocity, which is contained in the optimisation at $v_0 < 2\,\mathrm{m/s}$. An exception to this rule occurs when a particle's launch point within the regolith fill area is higher than its impact point, and it encounters no collisions along the way, as this could cause the particle to be slightly accelerated beyond its launch velocity by gravity. As this possible additional acceleration distance is minimal (cf. Section 4.2.1), the launch velocity is used as the maximum collision velocity $v_{\mathrm{max}}^{\mathrm{col}}$.

According to Johnson [100, p. 361], plastic deformation sets in if the contact pressure exceeds the limit value p_{limit} defined as

$$p_{\mathrm{limit}} = \begin{cases} 1.6\,Y_{\mathrm{conveyor}} & \text{, for the conveyor} \\ 1\,Y_{\mathrm{particle}} & \text{, for the particle} \end{cases} \tag{4.6}$$

While both the yield strength of the conveyor's aluminium and the particle's compressive strength are noted here with Y, they do not actually act exactly in the same way. Exceeding the aluminium's yield strength leads to plastic deformation. Basalt (or lunar regolith) particles are very brittle. Exceeding the compression strength of the particle does not lead to plastic deformation, but instead initially to fracturing of asperities and small corners, to eventually shattering of the particle [101].

Rearranging (4.3) for the velocity, with P_0^* set to the limit stress p_{limit}, the limit velocity for plastic deformation to occur is obtained:

$$v_{\mathrm{limit}} = \frac{\pi^2 p_{\mathrm{limit}}^{5/2}}{\sqrt{40\rho_{\mathrm{particle}}}(E^*)^2} \tag{4.7}$$

Using the estimated values defined earlier, this results in a limit velocity of $v_{\mathrm{limit}} = 0.0135\,\mathrm{m/s}$, much less than the maximum collision velocity of $v_{\mathrm{max}}^{\mathrm{col}}$. In his book, Johnson states that the limit velocity is often very low, mentioning a velocity of $0.14\,\mathrm{m/s}$ for the collision between a hard steel and a medium hard steel [100, p. 361]. While Johnson's value is roughly an order of magnitude higher than that for the collision discussed in this section, this is considered realistic given the much weaker mechanical properties of the basalt particle and the aluminium conveyor relative to steel. Plastic deformation sets in at very low normal collision velocities, requiring the implementation of velocity-dependent calculation of the normal COR. For collision velocities exceeding the limit velocity, Johnson estimates the COR to scale proportionally with $v^{\mathrm{col}^{-1/4}}$ [100, p. 363]. Together with the boundary condition of

$$k_{\mathrm{plastic}}(v_{\mathrm{limit}}) = k_{\mathrm{elastic}} \tag{4.8}$$

With k_{plastic} being the COR with plastic deformation as a function of the normal collision velocity and k_{elastic} being the constant COR of an elastic collision, k_{plastic} is calculated for the plastic deformation regime with:

$$k_{\text{plastic}} = k_{\text{elastic}} \left(\frac{v_{\text{limit}}}{v^{\text{col}}} \right)^{1/4} \tag{4.9}$$

The tangential coefficient of restitution is not dependent on the impact velocity, but on the impact angle. The coefficient k_{tang} is constant for varying impact velocities, as long as they collide with the surface at the same angle. For grazing impacts with an impact angle that approaches 0, k_{tang} approaches 1, leading to almost all of the particle's horizontal velocity being preserved. The opposite occurs for impact angles approaching 1. Here, the coefficient approaches 0 [94, p. 144]. Wedel et al. describe an equation for the tangential COR between two non-spherical particles [102]:

$$k_{\text{tang}} = 1 - \frac{k_{\text{norm}} + 1}{1 + c_1} \left[\mu_{\text{friction}} + c_2 \right] \frac{v_{\text{norm}}^{\text{col}}}{v_{\text{tang}}^{\text{col}}} \tag{4.10}$$

For k_{norm}, either k_{elastic} or k_{plastic} are used, depending on the normal velocity. μ_{friction} is the friction coefficient between the particles. The dependence on the impact angle is evident in the division of the normal and tangential velocity components. That leaves the factors c_1 and c_2. These factors are parameters that incorporate particle shape and angular velocity relative to the collision direction. When performing Discrete Element Method (DEM) simulations that model complex particle interactions, these parameters can be used to describe particle behaviour accurately. For this calculation, however, two simplifications are applied. First, this equation will be adapted to the collision of a single particle with a wall, rather than two particles. Second, the particles are assumed to be spherical, as is the case for the particles used in the validation tests (cf. Section 4.3). As per Wedel, spherical particles lead to the simplified equation [102]:

$$k_{\text{tang,sph}} = 1 - \frac{\mu_{\text{friction}} \left(k_{\text{norm}} + 1 \right)}{c_3^{-1}} \frac{v_{\text{norm}}^{\text{col}}}{v_{\text{tang}}^{\text{col}}} \tag{4.11}$$

Here, a new coefficient c_3 replaces c_1 and c_2. c_3 is defined as:

$$c_3 = 1 + m^* \left(I_2^{-1} \, r_2^2 + I_1^{-1} \, r_1^2 \right) \tag{4.12}$$

I is the moment of inertia for each collision particle. Just like previously defined in (4.5), m^* is the effective mass, combining the masses of both particles. In the particle-wall collision, radius, mass and moment of inertia of the wall are considered infinite, leaving

m as the particle's mass, and removing the second particle's term from the equation. The definition of c_3 gets simplified further to:

$$c_3 = 1 + m\,(I_1^{-1}\,r_1^2) \tag{4.13}$$

With the moment of inertia of a solid sphere of $I = 0.4\,m\,r^2$, the coefficient simplifies to a constant $c_3 = 3.5$. In the system simulation, this final simplified tangent COR will be used:

$$k_{\text{tang}} = 1 - 3.5\,\mu_{\text{friction}}\,(k_{\text{norm}} + 1)\,\frac{v_{\text{norm}}^{\text{col}}}{v_{\text{tang}}^{\text{col}}} \tag{4.14}$$

A limitation of this approach to calculating k_{tang} becomes apparent at high impact angles. This equation can yield very large negative values for the tangential COR. As this is not a realistic behaviour for the spherical particles simulated here, the results are cut off at $k_{\text{tang}} = 0$ [102]. The values for k_{elastic} and μ_{friction} are not theoretically determinable in the scope of this thesis. Still, they are instead used as parameters to tune the simulation to more closely resemble the test results in the fitment optimiser in Section 4.3.5.

4.1.3 Drag Calculation

The atmospheric drag on particles can be described by two analytical models for different Reynolds-number ranges. Linear (Stokes') drag is highly accurate for very low Reynolds numbers of up to $Re = 1$. In this regime, flow remains fully laminar, leading to a linear relationship between velocity and drag force. For significantly higher Reynolds numbers, starting at $Re = 1000$, the drag force scales with the square of the velocity, while a drag coefficient C_D remains constant with changes in velocity:

$$\mathbf{F}_{D,\text{quad}} = -\frac{1}{2}\,\rho\,\mathbf{v}\,|\mathbf{v}|\,C_D\,A_{\text{particle}} \tag{4.15}$$

$$\mathbf{F}_{D,\text{stokes}} = -6\,\pi\,\mu_{\text{dynamic}}\,r\,\mathbf{v} \tag{4.16}$$

The quadratic drag includes the fluid density ρ, the particle velocity vector $\mathbf{v}$, the drag coefficient C_D and the frontal area of the particle A_{particle}. In the Stokes drag equation, the particle size is represented by its radius r, while the fluid properties are represented by the dynamic viscosity μ_{dynamic}. The maximum Reynolds number Re is determined to evaluate which drag model is applicable for this particle simulation:

$$Re = \frac{\rho\,|\mathbf{v}|\,L}{\mu_{\text{dynamic}}} \tag{4.17}$$

This equation introduces a characteristic length L. For spherical particles, this length is the particles' diameter, here, 0.2 mm [103, p. 143]. The maximum particle velocity is assumed to be the launch velocity, capped in the optimiser at 2 m/s. With the fluid

parameters in a standard atmosphere at sea level [104], the maximum Reynolds number at launch velocity equates to $Re \approx 27.4$. During the simulation, the particles reach very low velocities, approaching 0 as they come to rest, resulting in Reynolds numbers $Re < 1$. Therefore, at high velocities, the particle motion lies in a transition region, significantly above the Stokes drag regime yet well below the quadratic drag regime. Many empirical models have been developed to approximate the drag coefficient C_D of a spherical particle in this transition region for use in the quadratic drag equation [103, p. 360]. A notable example is the Schiller-Naumann correlation [103, p. 111]:

$$C_D = \frac{24}{Re}\left(1 + 0.15\, Re^{0.687}\right) \tag{4.18}$$

Quadratic drag equations cannot be solved analytically for a particle following a two-dimensional projectile trajectory, as is the case in this particle simulation [105, p. 57], and thus must be solved numerically. Inoptimisermizer used to improve the sawtooth conveyor parameters, extensive population sizes across successive generations render the computational overhead of a numerical solution inhibitive. Instead, an adapted linear drag model based on Stokes' drag is used as a linear fit to the non-linear drag force within the particles' velocity range. In a benchmark comparing quadratic drag calculations using the Schiller-Naumann correlation and a linear drag model, the linear model was, on average, two orders of magnitude faster than the Schiller-Naumann correlation. The benchmark is attached in Appendix D. The linear drag model allows the particles' equations of motion to be solved as a system of decoupled first-order linear differential equations, enabling the performance advantage over the quadratic drag model.

In many equations applying Stokes' drag, the constants from (4.16) are combined to a parameter b, such that

$$\mathbf{F}_{D,\text{stokes}} = b\, v \tag{4.19}$$

Further equations are simplified by replacing the parameter b with the drag parameter k_{drag} via the expression:

$$k_{\text{drag}} = \frac{b}{m} \tag{4.20}$$

This parameter is empirically determined using the validation tests in Section 4.3 to adjust the linear drag model for higher Reynolds numbers and aerodynamic effects not directly accounted for in the simulation, such as wake effects within the particle cloud.

This model enables fast simulation, enabling comprehensive optimisations. However, it might increase susceptibility to overfitting, since the physical accuracy of this linear model is limited in the Reynolds regimes in which the simulation operates. For a more physically accurate simulation, a non-linear drag equation is required. A direct implementation of the quadratic equations would sacrifice simulation speed; however, measures can be taken

to optimise the calculations. The C_D values may be calculated for the relevant range of Reynolds numbers before the simulation is run. These values are then saved in a lookup table, which is accessed from within the simulation. However, this approach introduces discretisation errors that the higher-accuracy drag calculation may not justify. This trade-off must be evaluated for further development of this simulation, which is beyond the scope of this thesis.

4.2 Simulation Function

In this section, the simulation function and its underlying mathematics are described. This custom-developed function is significantly simplified compared to more sophisticated solutions such as DEM analysis. Most notably, a major limitation of this method is the lack of particle collisions. Furthermore, the number of simulated particles is far less than the number of particles in the real-world system. Here, the trajectories of individual particles are tracked as a proxy for the behaviour of the complex granular material. While these properties limit the realism of the simulation, they also allow the program to run much faster than more comprehensive software, such as a DEM analysis, enabling numerous iterations in the optimisation in Chapter 5.

Figure 4.3 shows the simulation functions structure. It is split into 3 blocks: The main calculation function initialises the variables needed for the simulation, handles geometry parameters, and distributes the particle launch points before entering the bounce loop. After the bounce loop, the particle distribution at the end of the simulation and the average particle distance are calculated. In the bounce loop, the particles are simulated. Every iteration of this loop represents the flight path of all particles from one collision with the conveyor to the next. The particle trajectories and their intersections with the conveyor are calculated by the intersection calculation function, which is called from within the bounce loop. Upon being called, this function calculates the intersections between all passed particles and the sawtooth sections, discarding false positives along the way.

The following index conventions are used throughout this section to describe the geometry and physics of the simulation mathematically: the index j denotes the specific conveyor tooth ($j \in \{1, 2, \ldots, n_{\text{teeth}}\}$), and the index i denotes the individual simulated particle ($i \in \{1, 2, \ldots, n_{\text{launch}}\}$).

4.2.1 Main Calculation Function

At the beginning of the main calculation function, geometric parameters, simulation parameters, motion parameters and calculation settings are initialised. Geometric param-

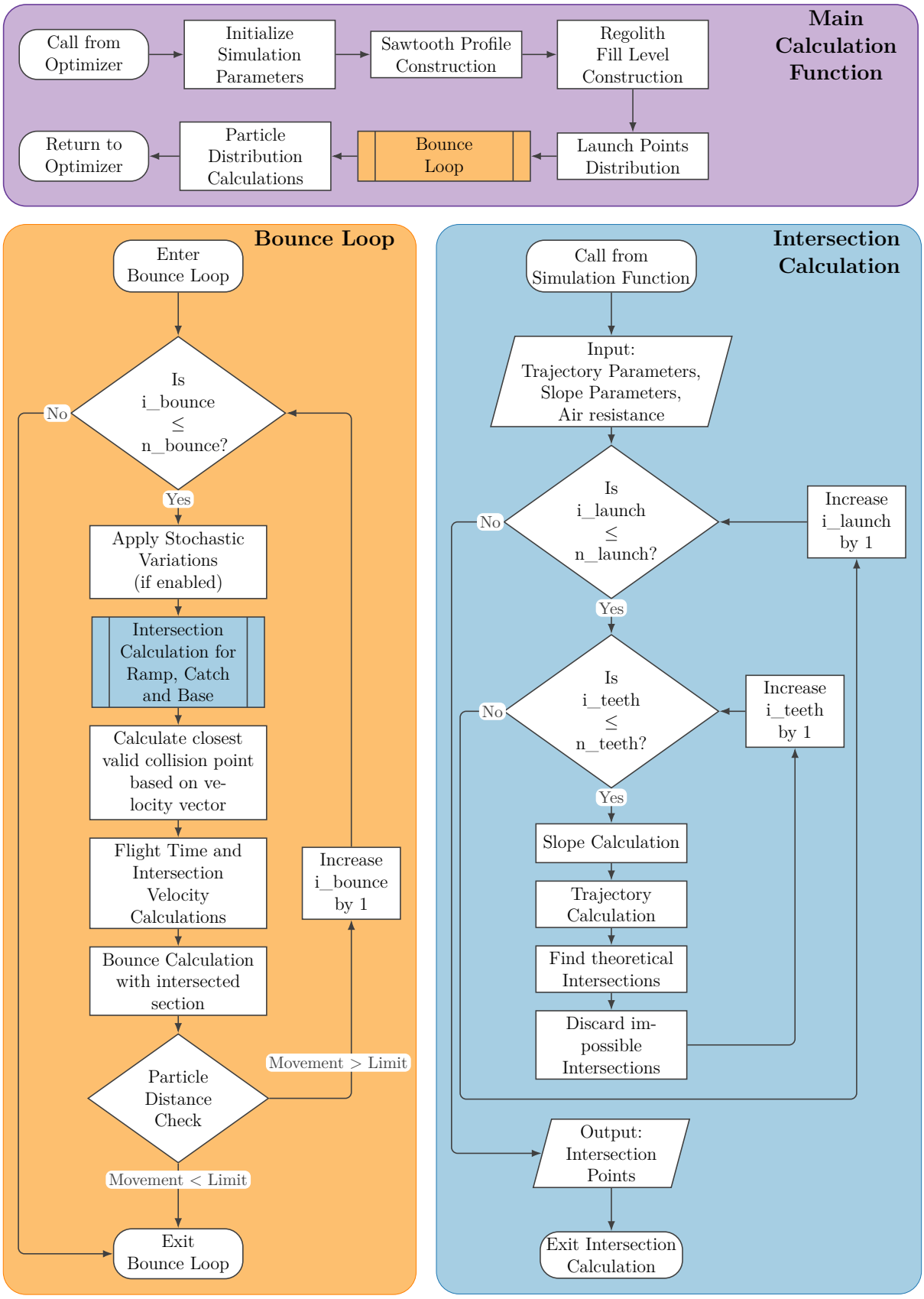

Figure 4.3: Flowchart of the system simulation

eters define the sawtooth profile. This includes the number of teeth n_{teeth}, as this value is needed for profile definition. Motion parameters consist of the initial particle velocity v_0, acceleration a and the angle of the initial particle velocity relative to the conveyor ξ. The number of particles n_{launch} and the number of bounce iterations n_{bounce} complete the simulation parameters.

Depending on the desired conditions, different calculation settings can be selected: the gravitational acceleration g applied to the particles can be switched between Earth gravity and lunar gravity. The application of atmospheric drag can be toggled between terrestrial conditions at sea level and vacuum. For the angle of repose of the simulated material, the values for glass beads and lunar regolith are selectable. The application of randomisation to launch velocities and angles is also toggleable.

4.2.2 Geometry Definition

Figure 4.4 shows the definition of the sawtooth profile based on the geometric parameters. Each tooth consists of 3 sections: the ramp, the catch, and the base. These sections are required for the intersection calculation discussed in Section 4.2.5. The sections are defined by 4 points: p_1 to p_4, with the first tooth's p_1 as the conveyor's base point at the origin. The conveyor is generated iteratively, comprising n_{teeth} teeth. Each tooth corresponds to a set of points p_1 to p_4. The conveyor sits at an angle α. In Figure 4.4, the profile is shown rotated to match the local coordinates of the points. The absolute horizontal x_{hor} is depicted with the conveyor angle α.

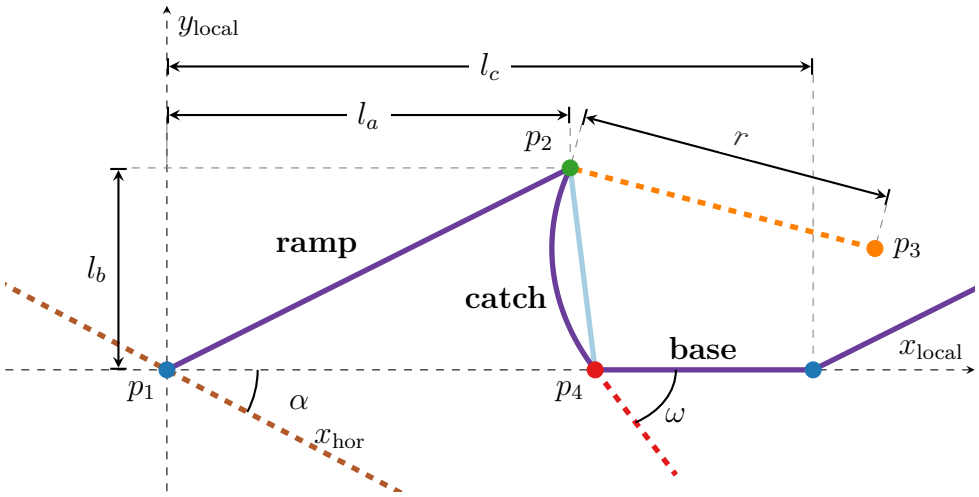

Figure 4.4: Definition of the sawtooth profile geometry

The position of the subsequent tooth's base point $p_{1,j+1}$ is calculated by rotating the local tooth pitch l_c into the global coordinate system by applying α. This results in the

horizontal and vertical components of l_c being added to the coordinates of the starting point $p_{1,j}$:

$$\begin{pmatrix} x_{1,j+1} \\ y_{1,j+1} \end{pmatrix} = \begin{pmatrix} x_{1,j} \\ y_{1,j} \end{pmatrix} + l_c \begin{pmatrix} \cos\alpha \\ \sin\alpha \end{pmatrix} \tag{4.21}$$

The ramp section is defined by two points p_1 and p_2. Figure 4.4 shows the points marked in the context of one tooth. p_2 is the peak point of the tooth, from where the catch section starts.

The local horizontal and vertical distances between p_1 and p_2 are denoted by l_a and l_b, respectively. p_2 is constructed very similarly to $p_{1,j+1}$. In this case, the ramp length s is rotated by both the conveyor angle and an additional tooth angle ϕ. The ramp length s is defined as the hypotenuse of the triangle with legs l_a and l_b.

$$\begin{pmatrix} x_{2,j+1} \\ y_{2,j+1} \end{pmatrix} = \begin{pmatrix} x_{1,j} \\ y_{1,j} \end{pmatrix} + s \begin{pmatrix} \cos(\alpha+\phi) \\ \sin(\alpha+\phi) \end{pmatrix}, \text{with } s = \sqrt{l_a^2 + l_b^2} \tag{4.22}$$

ϕ is derived from the tooth length l_a and the tooth height l_b with

$$\phi = \arctan\left(\frac{l_b}{l_a}\right) \tag{4.23}$$

For the profile definition and regolith fill definition (cf. Section 4.2.3), the catch section is handled as an arc intersection p_2 and p_4 (point marked "p_4" in Figure 4.4) with its centre at p_3 (point marked "p_3" in Figure 4.4). In Section 4.2.5, collisions between the particles and the sawtooth profile will be calculated. For these applications, the catch is simplified to a straight line between p_2 and p_4 instead. This simplified collision boundary is depicted in Figure 4.4 as a straight line connecting p_2 and p_4. To define the catch section, p_3 and p_4 will first be calculated in local coordinates relative to the conveyor and the start of the tooth, before being transformed into the global coordinate system.

p_3's local y-coordinate y_3^{local} is defined by the local vertical distance between p_3 and p_4:

$$y_3^{\text{local}} = r\cos\omega \tag{4.24}$$

r is the radius of the catch-arc. ω is the angle between the arc and the conveyor's base at its intersection point with the base at p_4. The local vertical distance between p_3 and p_4 can be described very similarly by replacing $\cos\omega$ in (4.24) with $\sin\omega$. However, since

x_4^{local} is not defined yet, x_3^{local} is instead derived from p_2. The local coordinates of p_2 are gained by transforming the global coordinates of p_2 back into the local coordinate system:

$$\begin{pmatrix} x_2^{\text{local}} \\ y_2^{\text{local}} \end{pmatrix} = \begin{pmatrix} \cos\alpha & \sin\alpha \\ -\sin\alpha & \cos\alpha \end{pmatrix} \begin{pmatrix} x_{2,1} \\ y_{2,1} \end{pmatrix} \tag{4.25}$$

x_3^{local} is then calculated with the Pythagorean theorem:

$$x_3^{\text{local}} = x_2^{\text{local}} + \sqrt{r^2 - (y_2^{\text{local}} - y_3^{\text{local}})^2} \tag{4.26}$$

An equation analogous to (4.24) is utilized to calculate x_4^{local}:

$$x_4^{\text{local}} = x_3^{\text{local}} - r\sin\omega \tag{4.27}$$

The base is congruent with the local x-axis; consequently, its y-coordinate is 0. Since p_4 marks the intersection between the catch and the base, $y_4^{\text{local}} = 0$. With p_3^{local} and p_4^{local} established, these local coordinates can now be converted into the global coordinates by applying the inverse transformation used for finding p_2^{local}:

$$\begin{pmatrix} x_{h,j} \\ y_{h,j} \end{pmatrix} = \begin{pmatrix} x_{1,j} \\ y_{1,j} \end{pmatrix} + \begin{pmatrix} \cos\alpha & -\sin\alpha \\ \sin\alpha & \cos\alpha \end{pmatrix} \begin{pmatrix} x_h^{\text{local}} \\ y_h^{\text{local}} \end{pmatrix}, \quad \text{for } h \in \{3, 4\} \tag{4.28}$$

4.2.3 Regolith Fill Area

The next step in preparing the simulation is to define the area the particles inhabit, henceforth referred to as the "regolith fill area". This regolith fill area is situated between the first and second tooth, as seen in Figure 4.5. The particle launch points will be distributed within this area. The cross-sectional area will also be used in Chapter 5 to calculate the mass of regolith moved per stroke. The regolith fill area is bound by the sawtooth profile, consisting of the first catch section, the base section between the first and second tooth, as well as the second tooth's ramp section. However, as shown in Figure 4.5, the regolith is not fully constrained by the sawtooth geometry but instead forms an open interface with the environment at the surface. The angle of this surface depends on the acceleration the regolith experiences and thus must be calculated to determine the regolith fill area.

As discussed in Section 4.1.1, the lunar regolith is treated as cohesionless. In the accelerated reference frame of the conveyor, the AOR θ_{acc} is thus dependent only on the static angle of repose of the material as well as the angle of the apparent acceleration the material is experiencing. This effective acceleration vector is composed of the conveyor's acceleration, the direction of that acceleration and the gravitational acceleration.

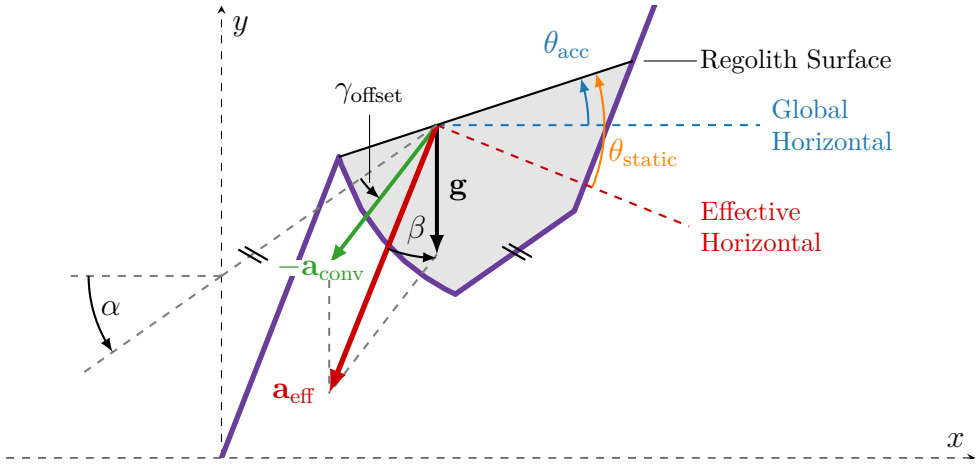

Figure 4.5: Forces acting on the regolith during acceleration

Figure 4.5 shows the values involved in the calculation of the regolith's AOR during acceleration. For this calculation, an effective gravity vector $\mathbf{a}_{\text{eff}}$ is established from which the dynamic AOR θ_{acc} can be derived. During the upstroke of the conveyor, two accelerations are acting on the regolith: the gravitational acceleration g and the conveyor's acceleration a. The Cartesian components of these accelerations are as follows:

$$\mathbf{g} = \begin{pmatrix} 0 \\ -g \end{pmatrix} \tag{4.29}$$

$$\mathbf{a}_{\text{conv}} = \begin{pmatrix} -a \cdot \cos(\alpha + \xi_{\text{offset},2}) \\ -a \cdot \sin(\alpha + \xi_{\text{offset},2}) \end{pmatrix} \tag{4.30}$$

The gravitational acceleration g acts vertically downward, so the horizontal component is 0. The conveyor's acceleration a is acting at the conveyor angle α with an additional offset $\xi_{\text{offset},2}$, as the conveyor may accelerate at an angle relative to its base. The resultant effective acceleration vector $\mathbf{a}_{\text{eff}}$ is thus defined as:

$$\mathbf{a}_{\text{eff}} = \begin{pmatrix} -a \cdot \cos(\alpha + \xi_{\text{offset},2}) \\ -a \cdot \sin(\alpha + \xi_{\text{offset},2}) - g \end{pmatrix} \tag{4.31}$$

From this vector, the angle at which the effective acceleration is acting, β, can be calculated:

$$\beta = \arctan\left(\frac{y_{\text{eff}}}{x_{\text{eff}}}\right) \tag{4.32}$$

Since the regolith is assumed to act as a cohesionless material, the magnitude of the effective acceleration has no effect on the actual AOR during acceleration. It is only dependent on the direction of the effective acceleration. The angle between the effective horizontal during acceleration and the regolith surface is always θ_{static}, the static AOR of

regolith. Subtracting the angle of the effective acceleration β from the static AOR results in the global AOR under acceleration:

$$\theta_{\text{acc}} = \theta_{\text{static}} - \beta \tag{4.33}$$

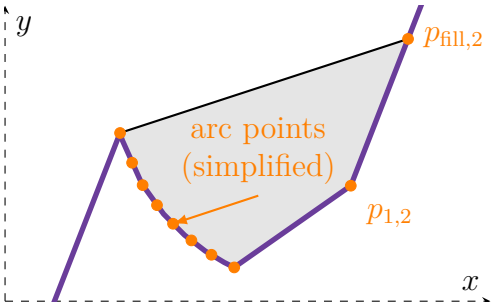

Figure 4.6: Regolith fill area during acceleration

In this simulation, the regolith fill area is represented as a polygon defined by a set of points along the sawtooth profile. The points defining the polygon are depicted in Figure 4.6. In the catch section, an array of 1000 points along the arc is established to create a smooth profile. In Figure 4.6, this vector is shown in a simplified form with only 8 points. From the top of the catch section, the regolith fill-line defined by the accelerated AOR calculated in (4.33) extends towards the second tooth. The intersection between the fill-line and the conveyor $p_{\text{fill},2}$ defines the next point of the polygon. Depending on the magnitude and direction of the conveyor's acceleration, this fill line might not reach the ramp of the second tooth, but instead intersect with the base section before that. If the fill-line reaches the ramp of the second tooth, the starting point of that tooth $p_{1,2}$ marks the last point defining the regolith fill area polygon. Since the intersection point $p_{\text{fill},2}$ may fall on either the ramp section of the second tooth or the base section, the intersection points between the fill-level equation and both of these sections must be considered:

$$y_{\text{fill}}(x) = y_{2,1} + \tan(\theta_{\text{acc}})(x - x_{2,1}) \tag{4.34}$$

$$y_{\text{ramp}}(x) = y_{1,2} + \tan(\alpha + \phi)(x - x_{1,2}) \tag{4.35}$$

$$y_{\text{base}}(x) = y_{1,1} + \tan(\alpha)(x - x_{1,1}) \tag{4.36}$$

Solving for the intersection of the fill-line equation with both of the other equations yields two mathematically valid x-coordinates. In the case of the fill-line actually colliding with the ramp section of the second tooth, the intersection x-coordinate will inherently be smaller than the x-coordinate of the theoretical base intersection. By choosing the point with the smallest x-coordinate, the physically viable intersection point is isolated, and the polygon can be constructed. This approach only works for sufficiently large accelerations. An acceleration magnitude that is too low will cause the regolith fill-level line to extend over the top of the second tooth. A more advanced mechanism enabling the spilling of

regolith into the second tooth would be required for low accelerations. In this simulation, accelerations of that magnitude will not be considered.

The particle launch points are distributed within the polygon representing the regolith fill area. The points are generated using the Halton sequence. The Halton-sequence generates a set of deterministic yet low-discrepancy points [106, pp. 441-443]. Compared to a pseudorandom number generator like the one underlying MATLAB 's `rand()` function, the generated points are much more evenly spread. A comparison of the two methods can be seen in Figure 4.7. The points are generated using MATLAB 's built-in `haltonset()`

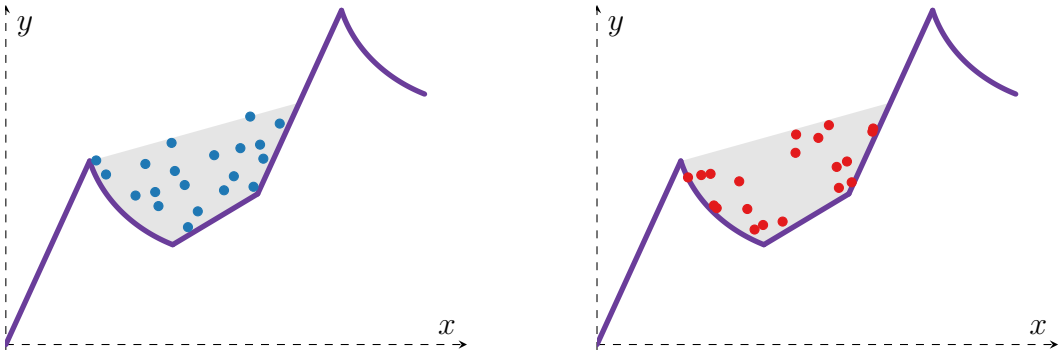

(a) Distribution of 20 points using a Halton sequence

(b) Distribution of 20 points using pseudorandom number generation

Figure 4.7: Comparison of initial launch point distributions within the regolith fill.

function, out of which the first 2000 points are sampled, excluding the set's first point. The first entry of the Halton sequence is always 0. Since the sequence never reaches 1, this extreme point is never balanced, leading to a bias towards the origin [107]. The points generated by the Halton sequence are distributed between 0 and 1 in both x and y coordinates. These points shall populate the regolith fill area. First, the values are scaled to fit within a bounding box that surrounds the regolith fill area.

$$\begin{pmatrix} x_{\text{halton,box}} \\ y_{\text{halton,box}} \end{pmatrix} = \begin{pmatrix} x_{\text{min,box}} \\ y_{\text{min,box}} \end{pmatrix} + \left(\begin{pmatrix} x_{\text{max,box}} \\ y_{\text{max,box}} \end{pmatrix} - \begin{pmatrix} x_{\text{min,box}} \\ y_{\text{min,box}} \end{pmatrix} \cdot \begin{pmatrix} x_{\text{halton}} \\ y_{\text{halton}} \end{pmatrix} \right) \tag{4.37}$$

The bounds of this box are defined by the extremities of the polygon that makes up the regolith fill area. Now, the values that actually lie inside the polygon are isolated with the MATLAB function `inpolygon()`. All of these values are valid as particle launch points. The first n_{launch} values of this set of valid values are chosen to act as launch points for the simulated particles.

4.2.4 Bounce Loop

The particle launch points are used in the bounce loop to calculate the particles' trajectories and intersections with the conveyor structure. The loop terminates once every

particle has come to rest or the maximum defined number of bounces n_{bounce} is reached. At the beginning of the bounce loop, stochastic variations are optionally applied to the particle launch velocities and angles. First, an array of randomisation factors λ_i is created using MATLAB 's built-in pseudorandom number generator `rand()`. The random values are evenly distributed between previously defined upper and lower bounds.

$$\lambda_i \sim \mathcal{U}(\lambda_{\min}, \lambda_{\max}) \quad \text{for } i = 1, 2, \ldots, (2 \cdot n_{\text{launch}}) \tag{4.38}$$

As (4.38) shows, the array created is twice as long as the number of simulated particles n_{launch}. Since two separate properties are being randomised, the double-length array ensures the use of an individual pseudorandom number for every randomised value. Otherwise, the launch velocity and angle for a particle would be changed by the same factor. In the next step, the particle launch angles are multiplied by the factors from the first half of the randomisation array; subsequently, the values from the second half of the randomisation array are applied to the launch velocities. The randomisation array is regenerated on every iteration of the bounce loop, providing the particles with new factors for each bounce. The seed of the pseudorandom number generator is set at the beginning of the main calculation function. Here, randomisation for the simulation is repeatable to ensure comparability between separate simulation runs.

From within the bounce loop, the intersection calculation function is called for the ramp, catch and base sections of the conveyor. In the first iteration of the bounce loop, the intersection function for the catch section calculates intersections only for catch sections starting from the second tooth. Since the launch point distribution is generated based on the actual catch curve, while the intersection calculation relies on a simplified catch geometry represented by a line connecting p_1 and p_2 (cf. Figure 4.4). All launch points generated between the catch arc and the simplified catch line would collide with the catch line, preventing their trajectory from being properly computed. Consequently, the catch line of the first tooth is ignored for the first bounce iteration, that is, until the first collision of each particle with the conveyor. This prevents any particles from falsely being caught in front of the first catch line upon launch. To calculate the intersections with the ramp sections, the start and end points of all teeth are passed to the intersection calculation function. The base intersection calculation does not require multiple sections, as the base section for the whole conveyor can be expressed as a single line between $p_{1,1}$, that is, the first point of the first tooth, and $p_{4,end}$, that is, the last point of the last tooth. The computational procedure of the intersection calculation function is discussed in Section 4.2.5.

The intersection calculation function returns all possible intersection points between each particle and each sawtooth section. Since every call of the intersection function only handles one type of sawtooth section (catch, ramp, base), there still might be intersection

points that do not translate to physically valid collisions; the trajectory of a particle might intersect multiple sawtooth sections, putting one intersection point in the "shadow" of another section. This behaviour is captured by accepting only the first intersection along the flight path of each particle. First, the x-coordinates of all computed intersection points are saved into one array, and all of the y-coordinates are saved into another array. These arrays are of the size $n_{\text{launch}} \times 3$. The flight direction is determined by examining the sign of the horizontal launch velocity:

$$v_{x,i}^{\text{launch}} = v_i^{\text{launch}} \cos(\delta_i) \tag{4.39}$$

If the sign of $v_{x,i}^{\text{launch}}$ is positive, the intersection with the smallest x-coordinate is selected; conversely, for a negative sign, the largest x-coordinate is selected. During this process, the row (the intersected section) is saved. This is used to assign the correct y-coordinate out of the corresponding array. Additionally, this index allows identifying which section the particle collided with. This information will be used when calculating the direction in which the particle bounces off the conveyor.

To determine the particle behaviour when it bounces off the conveyor, the incident velocity, including the speed and angle of incidence, is required. The computation for this is split between applying and not applying atmospheric drag to the particle; this discussion starts with the former. Figure 4.8 shows a free body diagram of a particle, depicting the forces

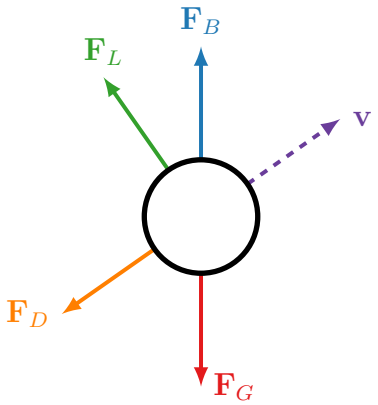

Figure 4.8: Particle during movement through the atmosphere

acting on the particle, to illustrate the difference between a particle moving through a vacuum and a particle experiencing atmospheric effects. For non-spinning symmetrical particles, the lift-force $\mathbf{F}_L$ is 0, and thus not considered in this simplified simulation [108]. The buoyancy force $\mathbf{F}_B$ is negligible due to the large density of the particle in relation to the fluid density. When moving through a vacuum, the only force acting on the particle is $\mathbf{F}_G$, always acting straight down. In the atmosphere, an additional drag force $\mathbf{F}_D$ is acting on the particle, always acting opposite to the movement direction depicted by $\mathbf{v}$. The particle flight time t_i is required to calculate the incident velocities. Since the

horizontal velocity of the particle $v_{x,i}$ is constant in vacuum and the horizontal distance is known, the flight time is calculated as a division of the two:

$$t_i = \frac{x_i^{\text{col}} - x_i^{\text{launch}}}{v_{x,i}} \tag{4.40}$$

The incidence velocity is split into horizontal and vertical components. As established, the horizontal component is equal to the horizontal component of the particles' launch velocity: $v_{x,i}^{\text{col}} = v_{x,i}^{\text{launch}}$. The vertical component is calculated as the vertical component of the launch velocity with the gravitational acceleration applied over the flight time:

$$v_{y,i}^{\text{col}} = v_i^{\text{launch}} \sin\delta_i - g\, t_i \tag{4.41}$$

Calculating these components under atmospheric drag requires linear drag equations. First, the flight time will be derived from the horizontal position equation [109, p. 227]:

$$\tilde{x}_i(t) = v_{x,i}^{\text{launch}} \frac{m}{b} \left(1 - e^{-b\,t/m}\right) \tag{4.42}$$

In this equation, m is the mass of the particle and b is a medium-specific constant. In the following calculations, the expression b/m will be noted as k_{drag}. k_{drag} is defined as a empirical drag parameter in Section 4.1.3. By isolating $e^{-k_{\text{drag}}\,t}$ from (4.42) and taking the natural logarithm of both sides, the equation for the flight time is:

$$\tilde{t}_i^{\,\text{col}} = \frac{1}{k_{\text{drag}}} \ln\left(1 - \frac{k_{\text{drag}}(x_i - x_{0,i})}{v_{x,i}^{\text{launch}}}\right) \tag{4.43}$$

The horizontal component of the collision velocity is the horizontal component of the launch velocity multiplied by a factor for the atmospheric drag [109, p. 227]:

$$\tilde{v}_{x,i}^{\text{col}} = v_{x,i}^{\text{launch}}\, e^{-k_{\text{drag}} \cdot t_i} \tag{4.44}$$

The vertical component is calculated with [109, p. 227]:

$$\tilde{v}_{y,i}^{\text{col}} = -\frac{g}{k_{\text{drag}}} + \left(\frac{g}{k_{\text{drag}}} + v_{y,i}^{\text{launch}}\right) e^{-k_{\text{drag}} \cdot t_i} \tag{4.45}$$

From the horizontal and vertical velocity components, the incident velocity vector $\mathbf{v}^{\,\text{col}}$ is formed as

$$\mathbf{v}_i^{\text{col}} = \begin{cases} \begin{pmatrix} v_{x,i}^{\text{col}} \\ v_{y,i}^{\text{col}} \end{pmatrix} & \text{if aerodynamic drag is neglected} \\ \begin{pmatrix} \tilde{v}_{x,i}^{\text{col}} \\ \tilde{v}_{y,i}^{\text{col}} \end{pmatrix} & \text{if aerodynamic drag is considered} \end{cases} \tag{4.46}$$

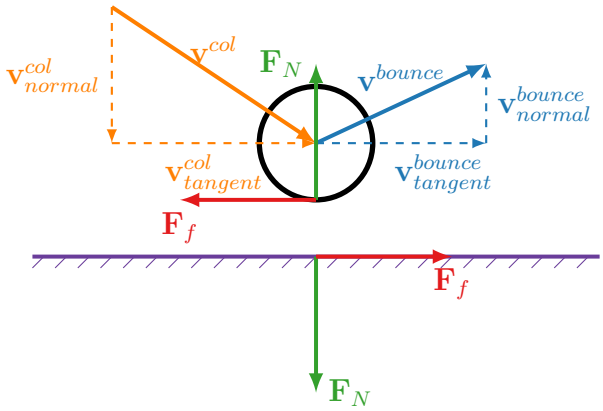

Figure 4.9: Free-body diagram of a particle at collision with a surface

Figure 4.9 illustrates the forces acting on the particle during the collision, as well as the particle's velocity components. The forces depicted in Figure 4.8 are still acting on this particle, as it is moving, but are not shown in this diagram for clarity. The incident velocity vector is mirrored on the normals of the sawtooth sections the particles are colliding with, resulting in the rebound velocity vector. First, the vertical and horizontal components of the incidence velocities are converted to normal and tangential components in relation to the collision surface.

$$\mathbf{v}^{\text{col}}_{i,\text{normal}} = (\mathbf{v}^{\text{col}}_{i} \cdot \mathbf{e}_{\text{n}})\, \mathbf{e}_{\text{n}} \tag{4.47}$$

$$\mathbf{v}^{\text{col}}_{i,\text{tangent}} = \mathbf{v}^{\text{col}}_{i} - \mathbf{v}^{\text{col}}_{i,\text{normal}} \tag{4.48}$$

$\mathbf{e}_{\text{n}}$ denotes the normal vector of intersected sawtooth section. The normal force F_N exerted on the particle by the surface changes its movement direction. By inverting the normal component of the vector, the incident velocity is effectively reflected along the surface normal. A real collision can never be perfectly elastic, as some energy will always be lost to deformation and thermal energy. The dimensionless coefficient for the energy lost during the collision is the COR. For a single collision, the COR can have a different effect on the normal and tangential velocity components due to particle rotation and friction. The COR is split into a normal and tangential component, as discussed in Section 4.1.2, allowing for a differentiated consideration of the effects influencing the rebound velocities. For velocities exceeding the limit velocity v_{limit}, as defined in (4.7), the plastic COR k_{plastic} is used for the normal COR k_{norm}. For velocities below v_{limit}, k_{elastic} is used. The tangential COR k_{tang}, defined in (4.14), is used regardless of collision velocity and is dependent on the collision angle, as initially shown in (4.11). These coefficients are applied to the normal and tangential component velocities to calculate the rebound velocity vector $\mathbf{v}^{\text{bounce}}$:

$$\mathbf{v}^{\text{bounce}}_{i} = k_{\text{tang}}\, \mathbf{v}^{\text{col}}_{i,\text{tangent}} - k_{\text{norm}}\, \mathbf{v}^{\text{col}}_{i,\text{normal}} \tag{4.49}$$

For the next bounce iteration, the rebound velocity vector is converted into the velocity magnitude and the new launch angle.

The bounce loop has two break conditions. At the beginning of the main calculation function, the maximum number of bounce iterations, n_{bounce}, was defined. Once the bounce loop reaches this bound, it terminates. The second break condition is the average bounce distance:

$$\Delta\bar{x} = \frac{1}{n_{\text{launch}}} \sum_{i=1}^{n_{\text{launch}}} \left| x_i^{\text{col}} - x_i^{\text{launch}} \right| \tag{4.50}$$

Here, the average of the absolute difference between the collision point and launch point for all particles of the last bounce iteration is taken and compared to a limit value l_{limit}. The loop terminates if $\Delta\bar{x} < l_{\text{limit}}$.

4.2.5 Intersection Calculation

First, the linear function of the examined sawtooth section is defined. Since the start point p_A and end point p_B of the section are known, the line is trivially established using the standard two-point form:

$$f_s(x) = \frac{y_B - y_A}{x_B - x_A}(x - x_A) + y_A \tag{4.51}$$

The trajectory of each particle is calculated to find the collision point of a particle with the examined section. For this, the vertical position as a function of the horizontal position is required. This calculation is once again split into a computation with and without drag. When not applying atmospheric drag, the particles follow a standard parabolic trajectory:

$$y_i^{\text{traj}}(x) = y_i^{\text{launch}} + (x - x_i^{\text{launch}}) \tan\delta_i - \frac{g}{2(v_{x,i}^{\text{launch}})^2}(x - x_i^{\text{launch}})^2 \tag{4.52}$$

A few basic trajectory parameters are used in this equation: y_i^{traj} is the vertical position of the particle as a function of the horizontal position. It follows from the launch parameters of height y_i^{launch}, horizontal position x_i^{launch}, horizontal velocity component $v_{x,i}^{\text{launch}}$ and angle δ_i. x is the momentary horizontal position. This equation stems from the time-derived position equations $y(t)$ and $x(t)$.

Applying atmospheric drag to the particle complicates the computation. While the regolith particles move through vacuum on the Moon, validation tests on Earth are performed in the atmosphere with glass beads, necessitating the application of atmospheric drag. The atmospheric particle trajectories are calculated according to Stokes' law. The basis of the drag-inclusive calculations is the horizontal and vertical positions as functions

of time $\tilde{x}(t)$ and $\tilde{y}(t)$, just like before in the drag-less calculations. The equations for these, including Stokes' drag, are:

$$\tilde{x} = v_{x,i}^{\text{launch}} \frac{1}{k_{\text{drag}}} \left(1 - e^{-k_{\text{drag}}\, t}\right) \tag{4.53}$$

$$r\tilde{y} = -\frac{g}{k_{\text{drag}}}\, t + \left(\frac{g}{k_{\text{drag}}^2} + \frac{v_{y,i}^{\text{launch}}}{k_{\text{drag}}}\right) \left(1 - e^{-k_{\text{drag}}\, t}\right) \tag{4.54}$$

The empirical drag parameter k_{drag} has been introduced in (4.43). Rearranging (4.53) and inserting it into (4.54), the equation for the vertical position as a function of the horizontal position $\tilde{y}(\tilde{x})$ is found:

$$\tilde{y}(\tilde{x}) = y_0 + \frac{g}{k_{\text{drag}}^2} \ln\left(1 - \frac{k_{\text{drag}}\,(\tilde{x} - x_0)}{v_{x,i}^{\text{launch}}}\right) + \left(g\, \frac{1}{k_{\text{drag}}\, v_{x,i}^{\text{launch}}} + \tan\delta\right) (\tilde{x} - x_0) \tag{4.55}$$

Subsequently, the intersections of the sawtooth section's linear equation and the trajectory function $y(x)$ or $\tilde{y}(x)$ are computed. This results in all mathematically valid intersections between the line coincident with the examined sawtooth section and the trajectory function. However, not all mathematically valid intersections are physically possible, leading to the following cases having to be ignored by the intersection calculation function:

1. Intersection point lies behind launch point in direction of travel
2. Intersection point lies outside of the examined section
3. Intersection point is identical to launch point

These cases can be elegantly caught by exploiting how the intersection points are calculated in MATLAB. This is done with the `fzero()` function. The function finds the roots of the difference of the two functions defined earlier. It requires an x-interval and looks for roots (or intersections in this case) inside this interval. Catching the first case requires examining the horizontal component of the launch velocity. If its sign is positive (the particle is flying to the right), the x-interval is clamped at the lower end at the particle's horizontal launch position. The opposite occurs if the sign is negative: the interval is clamped by the launch point at the upper end. Elimination of case 2 is done by clamping the examination window at the start point and end point of the examined section. Should the launch point lie within the section, it replaces either the start point or the end point in this function, depending on the flight direction.

Lastly, case 3 is dealt with by applying a small buffer when clamping the x-interval at the launch point, resulting in $x = x_{\text{launch}} \pm 1 \cdot 10^{-6}\,\text{mm}$ being invalid. This could lead to a problem in the very rare case where a particle bounces off nearly perfectly vertical, causing it to land back in the invalid range. Thus, nearly perfectly vertical bounces are disregarded should they occur. The coordinates for these cases are replaced with "`NaN`", so as not to interfere with future calculations. Vertical bounces are determined by checking

if the horizontal component is zero with a tolerance of $\pm 1 \cdot 10^{-6}$ mm/s. Any intersections beyond the x-interval will also be disregarded. The resulting valid intersection points for all examined particles are then given back to the main calculation function for further use in the bounce loop.

4.2.6 Performance Metrics

The simulation concludes with the calculation of performance metrics for comparing different sawtooth conveyor configurations. In this basic simulation, the comparison metrics are the final particle distribution and the average particle distance. These will be compared to test results of the same initial configuration in Section 4.3. The final particle distribution shows the percentage of particles that end up in each tooth after the bounce loop ends. The final horizontal position of each particle is discretised to the number of the tooth it comes to rest in, using:

$$j_{\text{end},i} = \left\lfloor \frac{x_{\text{end},i} - x_{2,1}}{l_c \cos \alpha} \right\rfloor + 1 \tag{4.56}$$

If a particle ends up on the ramp section of tooth i, it counts as ending up in tooth $i-1$, as that is where it would have ended up had it moved farther. That means that in terms of the final distribution, the horizontal starting coordinate of each tooth is offset by the length of a ramp section. This offset is accounted for by the numerator in (4.56). This value is divided by the horizontal length of a tooth $l_c \cos \alpha$ to express the particle distance as a fraction of the tooth length. The floor function is applied to the quotient, and an offset of 1 is added to get the correct tooth. For the average particle distance, the final particle distance of each particle is summed up and divided by the number of particles n_{launch}:

$$d_{\text{avg}} = \frac{1}{n_{\text{launch}}} \sum_{i=1}^{n_{\text{launch}}} x_i \tag{4.57}$$

4.3 Validation Campaign

As part of the validation campaign for the analytical simulation, three test series are performed. The test series differs in the granular material used and the applied motion profile. Each test series consists of ten test runs using the same procedure. The simulation inherently follows a Lagrangian approach of tracking all individual particles to find their intersections with the conveyor, and finally arrive at a resting spot [110, p. 71]. Extraction of the analytical particle trajectories is computationally straightforward. Following individual particles in a test, however, is unrealistic given their size and number, as well as

the complex interactions among them. Instead, the particle distribution across the teeth of the conveyor is evaluated once all particles have settled. This approach is similar to the fluid-mechanic concept of an Eulerian specification [110, p. 71]. For both simulation and test, the percentage of particles launched that end up in each tooth after one stroke is determined. In the simulation, the particles are counted, while in the test, the mass of particles in each tooth is measured. This section will describe the test setup of the validation campaign in Section 4.3.1 and the test procedure in Section 4.3.2. The test results will initially be compared among the test series in Section 4.3.3. To best represent the real-world behaviour of the conveyor, the simulation is aligned with the validation test results in Section 4.3.4. Subsequently, a comparison is drawn between the test results and adapted simulation outcomes in Section 4.3.5. The section concludes with a discussion of the validation campaign's limitations in Section 4.3.6.

4.3.1 Test Setup

The test setup for all three test series is identical to the POC-tests in Section 3.4, as depicted in Figure 3.10, except for the exact motion profile and material used. The parameters varied across the three test series are summarised in Table 4.2. The sawtooth

Table 4.2: Experimental parameters in the validation campaign

Parameter	**Series 1**	**Series 2**	**Series 3**
Material	Quartz sand	Quartz sand	Glass beads
Motion Profile	Single cycle POC-test profile	Delayed motion profile	Delayed motion profile

profile introduced in the POC-tests as Profile 1 is used across the three test series. In Section 4.2.2, the geometric and motion variables were introduced. The parameters used in the validation campaign are listed in Table 4.3. The first test series features a motion

Table 4.3: Sawtooth geometric and kinematic parameters for the validation tests

l_c [mm]	l_a [mm]	l_b [mm]	r [mm]	ω [°]	δ_{offset} [°]	v_0 [m/s]	a_{conv} [m/s^2]
20	15	5	5	60	0	1.0	60

profile identical to the one used in the POC tests in Section 3.4. In the POC-tests, this motion profile was repeated to evaluate the concept's ability to convey material across the conveyor. In this validation test, the motion profile is only executed once per test run. The motion profile of the second and third test series is modified to incorporate a delayed and decelerated downstroke. Figure 4.10 shows the initial states of the test series

(a) Series 1 and 2: Quartz sand

(b) Series 3: Glass beads

Figure 4.10: Initial states of the validation test series

performed in the validation campaign. In Series 1 and 2, WF 34 quartz sand was used as a substitute for lunar regolith. In Series 3, the quartz sand is replaced by glass beads.

4.3.2 Test Procedure

Initial conditions involved loading the first tooth of the sawtooth profile with ca. 2 g of particles. In the third test, the exact mass of the loaded particles was recorded, allowing the calculation of a recovery rate for each test run. Due to the scale's inaccuracy, this value was omitted from the first two tests. After loading, the sawtooth sledge was percussively agitated to promote particle settlement and provide a consistent initial state across test runs. Subsequently, the motion profile defined in the actuator control software (cf. Section 3.4) was executed once. The particles have been distributed over the first teeth of the conveyor. In all test runs, teeth 1-4 were populated by particles. Following the execution of the motion profile, the sawtooth conveyor is removed from the actuator and the weighing procedure is performed:

1. The sledge is weighed without disturbing the particles spread across the teeth.
2. The material filling the furthest tooth is removed with pressurised air. During this operation, the remaining teeth are shielded from the air to prevent disturbance of the particles.
3. Repeat this procedure until the empty sledge is weighed.

The particle distribution results are normalised to the recovered mass, minimising the influence of the losses on the final distributions. This test run is repeated 10 times for each test. The particle distributions are averaged for comparison with the simulation.

4.3.3 Test Result Comparison

For comparing the results of the three tests, please note that in the first two tests, a scale with an accuracy of 100 mg was used, while the scale in the third test had an accuracy of 10 mg. The complete test results are attached in Appendix B. Table 4.4 shows key statistical metrics of the three validation tests upon which the three tests can be compared. The centre of mass E_x is the average distance the particles travelled in the

Table 4.4: Validation test result metrics

	Centre of Mass $[E_x]$	**Spatial Dispersion** $[\sigma_x]$	**Run Repeatability** $[\sigma_{\text{pooled}}$ %$]$	**Recovery Rate** [%]
Test 1	2.14	0.96	0.26	–
Test 2	2.09	0.99	0.60	–
Test 3	1.85	0.87	0.11	97.7

test. This value is given as a tooth fraction, with 1 meaning the average distance between teeth in the sawtooth profile. The centre of mass is calculated with:

$$E_x = \sum_{j=1}^{n} j \cdot \bar{P}_j \tag{4.58}$$

where j denotes the individual tooth, n is the number of examined teeth (4 for the three validation tests), and $\bar{P}_j$ is the normalised particle mass ratio in the individual tooth. The spatial dispersion σ_x, or standard deviation of the spatial particle distribution, is a metric of how much the particles are spread across the teeth. It is calculated with:

$$\sigma_x = \sqrt{\sum_{j=1}^{n} \bar{P}_j \cdot (j - E_x)^2} \tag{4.59}$$

A concentration of all particles on one tooth would result in a spatial dispersion of 0, an equal spread across all 4 populated teeth would result in a σ_x of 1.118. Experimental repeatability is calculated by determining the standard deviation s_j across all 10 test runs. These deviations are pooled to obtain a single value that describes the repeatability of each test.

$$\sigma_{\text{pooled}} = \sqrt{\frac{1}{n} \sum_{j=1}^{n} s_j^2} \tag{4.60}$$

A lower σ_{pooled} corresponds to a higher repeatability. As mentioned before, the recovery rate is only available for the third validation test and represents the ratio of input mass

to retrieved mass. Figure 4.11 shows the particle distributions for each test. Both the

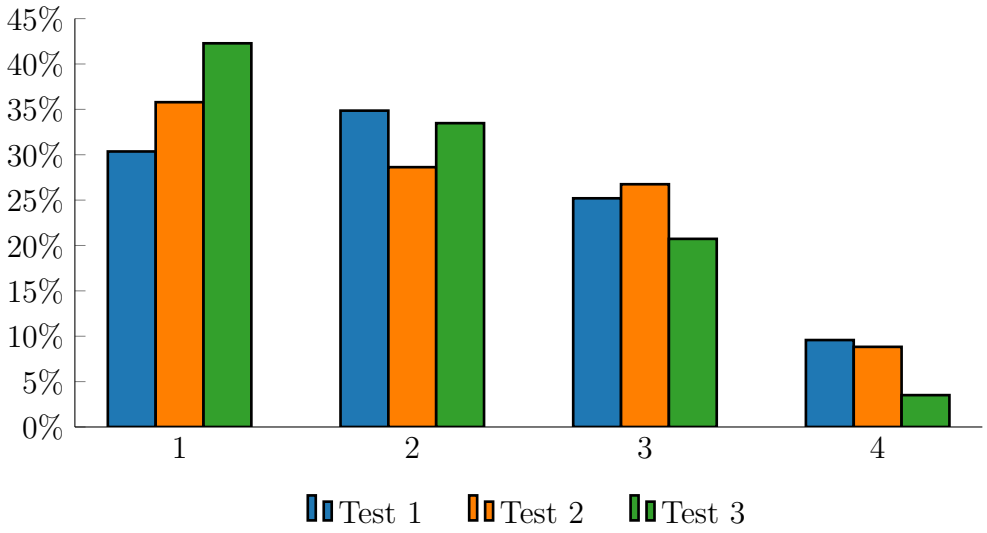

Figure 4.11: Average particle distribution for the 3 validation tests

statistical metrics and the direct examination of the particle distribution show the effect of the modified motion profile in the second test. While the centre of mass in the second test is not much lower than in the first test, the particle distribution clearly shows a shift from the second tooth being the most populated in test 1 to the first tooth having the most particles in the second test. Notably, the amounts in the last tooth are nearly identical. Test 3 shows the least spatial dispersion and best repeatability. However, the centre of mass is the lowest of all three tests. All of these effects can be attributed to the more concise particle distribution of the glass beads. The larger particles present in the quartz sand are less inhibited by aerodynamic drag due to their higher ballistic coefficient. The mass (and thus inertia) of a particle increases with the cube of the radius. In contrast, the surface area (and thus atmospheric drag) only increases with the square of the radius. The higher run repeatability could also be attributed to the more accurate measuring device, resulting in fewer rounding errors.

For the metrics of centre of mass, spatial dispersion, and run repeatability, the statistical significance of the difference between using quartz sand and glass beads is evaluated. Statistical significance is rejected if the p-value exceeds the significance level of 0.05. Table 4.5 shows the p-values for the three tests performed to investigate the third test's statistical significance. For the centre of mass and spatial dispersion, Welch's t-test is performed. It calculates the p-value for the null hypothesis that the expected values of two datasets are identical. For the run repeatability, a two-sample F-test is performed. It calculates the p-value for the null hypothesis that the variances of two data sets are identical. While the values given in Table 4.4 are given as an average (or pooled value) over the 10 test runs, the datasets used in these significance tests make use of the data from

all test runs to determine the significance. The full datasets and test code are attached in Appendix B and Appendix D.

Table 4.5: Statistical significance Tests 2 - 3

	Centre of Mass $[E_x]$	**Spatial Dispersion** $[\sigma_x]$	**Run Repeatability** $[\sigma_{\text{pooled}}\ \%]$
p-Value	0.0023	0.0081	0.00033

For all metrics, the p-values are well below the significance level, indicating very high statistical significance between test 2 and test 3.

4.3.4 Alignment of Simulation to Validation Tests

In the simulation function, three parameters were identified as not being theoretically determinable in the scope of this thesis. These factors are the elastic normal coefficient of restitution k_{elastic}, the friction coefficient μ_{friction}, and the empirical drag parameter k_{drag}. A "fitment optimiser" is utilised to determine these parameters, align the simulation with the test results, and bridge the gap between the lunar-focused approach used in the simulation and the terrestrial validation tests. Its flowchart is shown in Figure 4.12. The optimisation metric is the particle distribution across the conveyor's teeth. In the optimiser, a Genetic Algorithm (GA) is employed, using MATLAB 's `ga()` function. As opposed to other optimisation algorithms like MATLAB 's `fminsearch()` or `patternsearch()`, the GA is more adept at finding a global optimum to a function, given sufficient population and generations [111, p. 9], though convergence on the global optimum is not guaranteed. This section will describe the operation of a GA before applying this to this specific application as a fitment optimiser.

A genetic algorithm works by first generating an initial population of individuals. The number of individuals is controlled by the corresponding "population size" parameter n_{pop}. An individual is the result of a function, given a set of input parameters, or "features". The specific combination of features passed to the function is a "chromosome" [111, p. 21]. The features are restricted by bounds. Each value has an upper and a lower limit. In more complex algorithms, such as the one employed in Chapter 5, additional constraints may be applied to the features. In this initial population, the features assigned to individuals may be purely random (or pseudorandom due to computational constraints) or defined by a population function [111, p. 9]. The initial population marks generation 0. In each generation, the performance of each individual is evaluated with a fitness function [111, p. 10]. The fitness function calculates a single fitness value from the corresponding chromosome. This fitness value is being optimised in the algorithm. The next generation consists of the offspring of the last generation's individuals. This offspring is created with three

core principles: selection, crossover and mutation. Selection dictates that primarily high-performance individuals (those with a high fitness score) are allowed to reproduce. The next generation is thus mainly composed of these high-fitness individuals, with low performers less likely to reproduce [111, p. 16].

The exact chromosomes of the offspring are determined by two mechanisms: crossing over and mutation. Each offspring has two or more parents. Crossover dictates that the chromosomes of the parents are combined for the offspring to inherit [111, p. 16]. The features may, however, also change independently of the parents, by mutation. The mutation is defined by a mutation function that computes a mutation probability. This probability may change throughout the simulation, and dictates how often features change randomly in the offspring [111, p. 16]. This process of reproducing the fittest individuals into offspring is repeated over many generations, ideally leading the population to converge on the global optimum. Tuning the population size, mutation probability, and crossover function can increase the efficiency and effectiveness of optimisation. Adversely, choosing the wrong parameters may lead to problems in the optimisation. A too low population size could, for example, lead to an effect called "genetic drift", which describes a random convergence of an algorithm on one solution over another, with the convergence being stemmed in stochastic errors as opposed to fitness [111, p. 185].

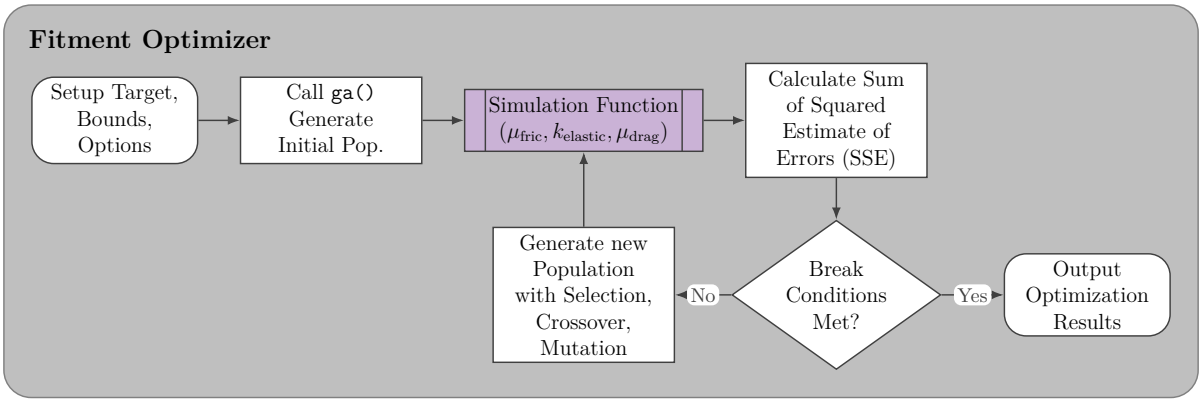

Figure 4.12: Flowchart of the fitment optimiser

In the context of the fitment optimiser, the population consists of individual simulations, as described in Section 4.2. The chromosomes passed to these individuals consist of the undetermined parameters k_{elastic}, μ_{friction}, and k_{drag}. The parameters for the restitution calculation are adjusted within bounds of 0.01 - 1. As described in Section 4.1.2, only positive coefficients are examined in this simulation. The physical upper bound of a restitution coefficient is 1. Higher values than 1 are theoretically possible due to the conversion of rotational kinetic energy into translational kinetic energy. However, since the accumulation of rotational velocity is not tracked in the simplified simulation function, the restitution coefficients are capped at 1. Typical values for the friction coefficient μ_{friction} range from 0.3 to 0.7, with some metal-to-metal contact exceeding 1, and low-friction materials like

PTFE reaching 0.01. The sawtooth profile used in the validation tests is made out of Polylactic Acid (PLA). The friction coefficient between glass and PLA is not accessible in the scope of this study. For a glass-metal contact, the value is expected to lie in the range of 0.5 - 0.7; the coefficient for a polystyrene-polystyrene pairing is the highest of the polymer combinations mentioned by Ober et al. at 0.8 [112, p. 158]. Based on these values, a coefficient of friction greater than 1 would be considered unrealistic and is not included in the optimisation. The drag parameter k_{drag} is set in a range from $0.1 - 15$.

The fitness function is based on the particle distribution. Instead of maximising a fitness, MATLAB 's `ga()` function aims to minimise a cost value. The simulation function outputs an array of particle ratios across the teeth (the particle distribution), while the optimiser requires a single scalar cost value. Consequently, the discrepancies between the particle distribution in the validation test and the simulation results must be combined into a single value. This can be done with the SSE or Mean Absolute Error (MAE). The MAE takes the average of the sum of absolute differences between simulation and test results:

$$\text{MAE} = \frac{1}{n} \sum_{\text{j=1}}^{n} (|\bar{P}_{j,\text{sim}} - \bar{P}_{j,\text{test}}|) \tag{4.61}$$

The SSE is calculated by squaring the differences before creating the sum. Dividing the result by the number of samples n would result in the Mean Squared Error (MSE).

$$\text{SSE} = \sum_{\text{j=1}}^{n} (\bar{P}_{j,\text{sim}} - \bar{P}_{j,\text{test}})^2 \tag{4.62}$$

$\bar{P}_{j,\text{test}}$ is identical to the value used first in (4.58), with $\bar{P}_{j,\text{sim}}$ being its equivalent from the simulation. In this fitment optimiser, the SSE is used because it disproportionately penalises large discrepancies. Using MAE equally penalises a single massive error and multiple smaller errors under the condition that their magnitude is equal. In the simulation, a single massive error in a single tooth would likely indicate a foundational flaw. In contrast, multiple smaller errors across the teeth may be attributed to stochastic noise, such as particle interactions or inhomogeneous atmospheric resistance. The population size is set to $n_{\text{pop}} = 500$. The population is distributed by the standard `gacreationuniform`, a random distribution [113]. During optimiser development, smaller population sizes were used, resulting in high dependence on initial conditions and failure to converge on the global optimum. The mutation and crossover functions are also set to the standard values of MATLAB 's `ga()` function. The mutation is calculated with the function `mutationgaussian`. Here, a random number from a Gaussian distribution with mean 0 is added to every feature of every individual. The distribution from which these summands are taken is defined by the parameters `shrink` and `scale`, and changes throughout the simulation. While the standard deviation of the distribution is large in the initial generation, leading to a high mutation probability, it shrinks to 0 in the last generation, reducing the mutation proba-

bility as the optimisation converges on a solution [113]. MATLAB 's `crossoverscattered` calculates the crossover from parents to offspring. It chooses the properties taken from each parent at random and inherits them to the offspring [113]. The following stopping criteria may stop the optimisation [113]: During the runs of the fitment optimiser, either the limit of `MaxGenerations` at $100 \times n_{\text{variables}}$, with $n_{\text{variables}} = 3$, was reached, or `MaxStallGenerations` stopped the optimiser at stall generations [114]. Stall generations occur when the best individual of a generation does not show significantly better fitness than the best individual in the previous generation.

4.3.5 Comparison of Simulation and Validation Tests

The optimised simulation results are compared with the validation test results for both the second and the third test. In Section 4.1.2, the restitution coefficients are calculated as a function of collision speed and angle. These angle and speed-dependent coefficients are hereinafter referred to as variable coefficients. Both the simulations with constant coefficients and variable coefficients are fitted to the test results to determine the impact of this sophistication. Figure 4.13 shows all comparison cases. In Test 3, the variable coefficients

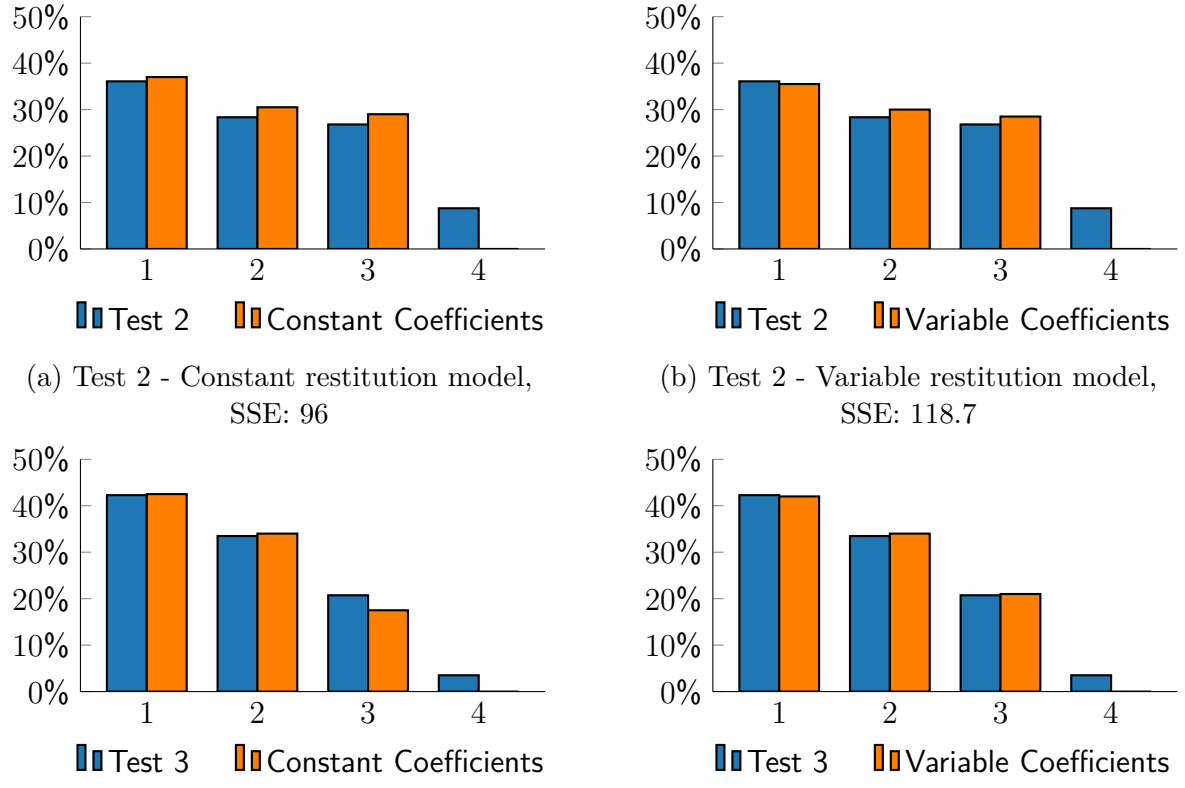

(a) Test 2 - Constant restitution model, SSE: 96

(b) Test 2 - Variable restitution model, SSE: 118.7

(c) Test 3 - Constant restitution model, SSE: 29.3

(d) Test 3 - Variable restitution model, SSE: 13.8

Figure 4.13: Average Particle Distribution for the Validation Tests

are aligning to the test results much better than the constant coefficients, with the SSE

for the former being less than half of the latter. However, both of these cases are very accurate compared to the simulations aligned with Test 2. This leads to the conclusion that the use of glass beads in the validation tests has a substantial effect on the comparability between the test and the simulation. In Test 2, there is also a large difference between the constant and variable coefficients. While the difference between the error-values for both cases is absolutely larger than in Test 3, the relative discrepancy is lower, with the SSE in Figure 4.13a being approximately 3/4 the magnitude of Figure 4.13b. Conversely, in Test 2, the constant restitution coefficients align much better with the test results than the variable coefficients. This might indicate that implementing variable restitution coefficients has a minor effect, or even is detrimental to the simulation's accuracy. Since the simulation errors for Test 2 are immense compared to Test 3, the validity of these conclusions is in doubt. The simulation performed with variable restitution coefficients adapted to Test 3 yielded the highest accuracy among the four models compared. Consequently, this configuration is adopted as the baseline model for the remainder of this study. The determined best-fit values are: $k_{\text{elastic}} = 0.854$, $\mu_{\text{friction}} = 0.133$, and $k_{\text{drag}} = 5.347$. Figure 4.14 shows a detailed view of the comparison depicted in Figure 4.13d, including

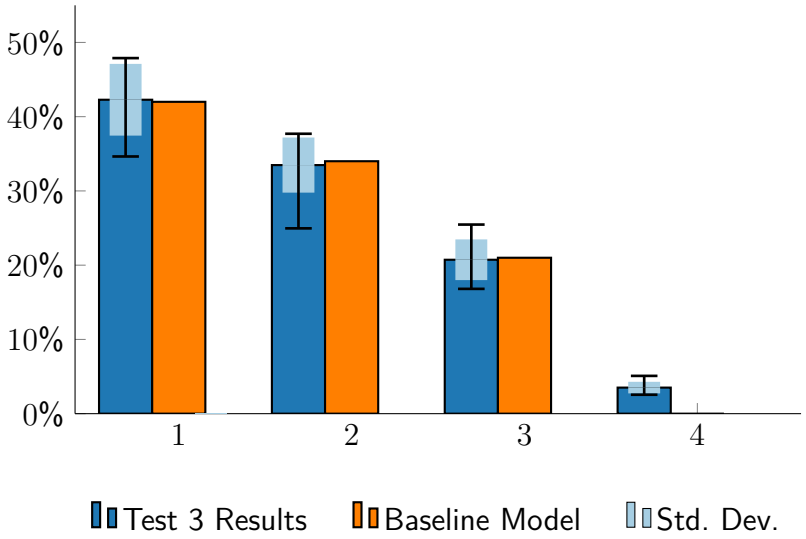

Figure 4.14: Detailed comparison of Test 3 results and baseline model

standard deviation depicted as light blue bars, as well as the minimum and maximum values as error bars for each tooth across all test runs of Test 3. The simulation matches the test nearly perfectly for teeth 1-3, falling within the experimental standard deviation bounds. The results of tooth 4 represent an outlier, performing significantly outside the expected range. This problem is not singular to this specific model, but is common to all cases depicted in Figure 4.13. None of the simulations rendered particles in tooth 4, despite the Test 2 results showing an even higher particle fraction in tooth 4 than in Test 3. This under-representation of spatial dispersion in the simulations is attributed to simplifications made to enable simulation optimisation. The simplifications and limitations of the simulation will be discussed in more detail in Section 4.4.

4.3.6 Discussion of Test Limitations

While Section 4.2 introduces the simulation as an equivalent to the system for lunar application, this validation campaign serves as a terrestrial confirmation. This introduces discrepancies in the materials assumed in the simulation and used in the validation campaign. On the other hand, the simulation accepts some simplifications that must be accounted for in the validation.

Some materials used in these tests are not applicable in the lunar context. The sawtooth conveyor in the validation tests is made of 3D-printed PLA, not aluminium, as calculated in the simulation. Quartz sand and glass beads were used as granular simulants for lunar regolith. Surface roughness and distinct layer lines in the 3D-printed parts introduce complex collision mechanics not present in machined aluminium surfaces. Consequently, the collision mechanics used in the simulation, and as a result, the calculated limit velocity v_{limit} and simplified restitution behaviour cannot be generally applied for these tests.

The simulation considers only a single particle size, introducing potential inconsistencies due to discrepancies between the idealised simulation and the imperfect granular test material. The particle size distribution of the quartz sand used in Series 1 and 2 can be seen in Figure 4.15 [115]. The sizes range from 125 µm to 500 µm. The glass beads

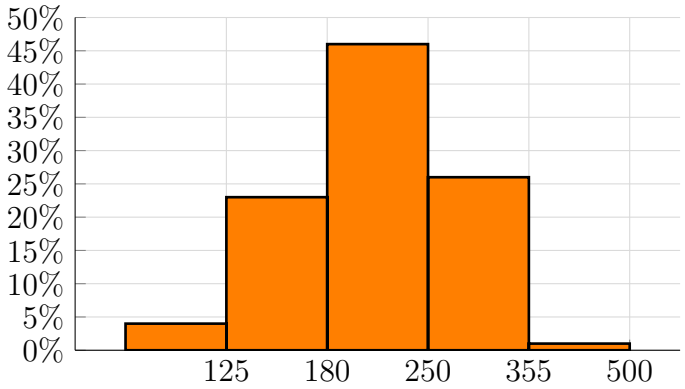

Figure 4.15: Particle size distribution of WF-34 quartz sand

used in Series 3 exhibit a more homogeneous particle-size distribution. While the exact distribution of the glass beads is unknown, their sizes range from 100 µm to 200 µm. This tighter particle-size distribution more closely resembles the single-particle size simulated in Section 4.2. Additionally, the small particle sizes improve the comparison between the test and the simulation. Since the drag model used in the simulation inherently exhibits inaccuracies in the examined flow regime (cf. Section 4.1.3), a smaller particle size, and thus a smaller Reynolds number, increases the linear model's accuracy. In the simulation, perfectly spherical particles are assumed. While sphericity measurements for the exact WF-34 quartz sand used are not available, quartz sand generally exhibits a high roundness (e.g. Ottawa sand at 0.7 - 0.8 [90]). However, manufactured glass beads offer almost perfect

sphericity, further increasing the likelihood of validation test and simulation [116]. Note that the manufacturer specifies the roundness of the particles based on "U.S. Standard Screen Size", where 100 µm - 200 µm particles correspond to a mesh size of 70 - 140.

The particle removal operation carries some potential for error: Small particles may be prone to tribo-electric charging and be attracted to the shield or other parts, influencing the test result. Additionally, pressurised air may bleed to the blocked teeth and disturb or move the particles, despite the shielding. In the results of test 3, most test runs show some discrepancies between the input material mass and the cumulative distributed particle mass measured during the weighing procedure. These discrepancies are attributed to the identified error factors.

Although the simulation's accuracy seems promising for Test 3, this perceived proficiency might mask a more fundamental issue with this validation approach. The values for k_{elastic}, μ_{friction}, and k_{drag} determined in this fitment optimiser might only produce a high accuracy simulation for these specific boundary conditions, but not lead to a generally valuable digital twin of the conveyor. This effect is known as "overfitting" in machine learning [117, p. 56]. Another possible challenge requiring further investigation lies in the inherent interweaving of the restitution coefficients and empirical drag parameter in this approach of simulation alignment. The coefficients determining restitution may not yield satisfactory results without the drag parameter, rendering the simulation less robust in vacuum scenarios.

An indication of the general applicability of the drag parameter is given by the comparison of the drag force calculated with this linear model using the empirically determined drag parameter to the drag force calculated with the Schiller-Naumann correlation, as can be seen in Figure 4.16. In this graph, the slope of the linear-fit line is defined by k_{drag}. The drag parameter, empirically determined by aligning the simulation with the results of Series 3 of the validation campaign, almost perfectly aligns the linear fit to the Schiller-Naumann force, slightly overrepresenting the force. It is to be noted that the Schiller-Naumann correlation calculates the drag force purely on the basis of the Reynolds number and is independent of any application-specific parameters. The high degree of correlation between the two forces provides a strong physical justification for the validation approach taken in this study, virtually eliminating any doubt about overfitting, at least regarding the drag parameter k_{drag}, as well as the dependence of the restitution parameters on the drag parameter. Tests performed under vacuum would help further alleviate concerns about the inappropriate interweaving of parameters. However, overfitting might still occur in the remaining parameters k_{elastic} and μ_{friction}. A similar validation test to the one performed in this section is proposed for the optimised sawtooth conveyor. While the test would also be performed under the same environmental conditions, the geometric and motion parameters of the optimised conveyor will likely differ significantly. Inves-

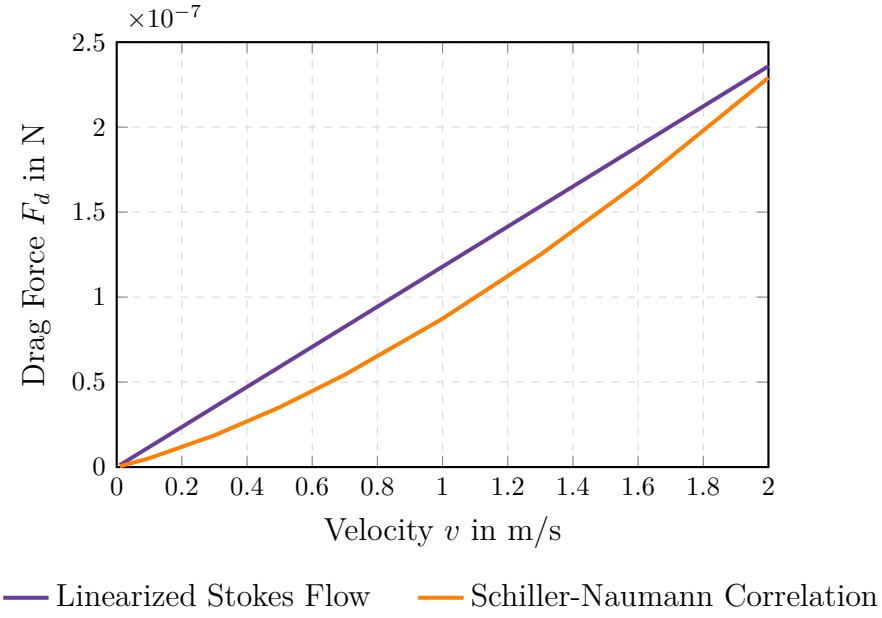

Figure 4.16: Linear drag force with empirical parameter k_{drag} compared to Schiller-Naumann drag force

tigating the similarity between the simulation results and the optimised validation test using the coefficients established in this section will inform the general applicability of the simulation.

4.4 Simplifications and Limitations

The particles in the simulation are considered to be spherical. This assumption influences the considerations of restitution and atmospheric drag. The effects of this simplification are apparent from the high correlation with the near-spherical glass beads used in Section 4.3, particularly regarding their atmospheric drag. The restitution model introduced in Section 4.1.2 was simplified only to apply to spherical particles in Equation (4.14). Furthermore, the particles in this simulation are assumed not to accumulate any rotational momentum. This simplification would no longer be sufficiently accurate with the implementation of non-spherical particles; Impact offset from the centre of mass may convert a significant fraction of the translational kinetic energy into rotational energy. Currently, these effects are approximated by randomising particle launch velocities and angles.

The drag calculation is simplified to a linear representation, as reasoned in Section 4.1.3. While this assumption aligns closely with established approximations such as the Schiller-Naumann Correlation (cf. Section 4.3.6), it still represents a linear fit to non-linear behaviour. This simulation's limitation to a single particle size further influences the drag calculation. The effect of this simplification became apparent in the comparison between validation tests with the morphologically more diverse quartz sand and the more uniform

glass beads: the simulation reproduced the behaviour of the uniform material much more closely than that of the diverse sand. Incorporating a particle-size distribution into the simulation would improve its adaptability to lunar regolith. For simulating the final concept under lunar environmental conditions, these considerations are inherently obsolete.

Particle interactions are not implemented in this simulation due to their intense computational overhead. Consideration of particle interactions is likely not feasible for an optimisation-ready simulation. As discussed in Section 4.1.1, the material used in the simulation is approximated as cohesionless. For a higher fidelity simulation of lunar regolith, this simplification must be addressed. Currently, the regolith is assumed to be fully uncompressed. This assumption is sufficiently accurate for this simulation. In Section 4.1.2, the non-elastic behaviour of regolith-like particles is introduced. In contrast to metallic particles, materials that are present in lunar regolith do not deform plastically when exceeding elastic deformation, but instead shatter. While the kinetic energy lost to this process is taken into consideration, the possible splitting of particles is not.

The simulation examines particle behaviour two-dimensionally. The sawtooth profile in the full concept is prismatic along the normal to the simulation plane. A two-dimensional simulation is thus considered a sufficient approximation. In real-world testing, transverse motion of particles is generated by collisions with uneven surfaces and side walls, as well as by particle collisions, neither of which is accounted for in this simulation. Since both the actuation force and gravity are acting in the simulation plane, the net particle movement is also assumed to be congruent with the simulation plane, with transverse particle motion considered minimal. The simulation represents the particle flow in the conveyor's centre plane. The boundary effects of the lateral walls are assumed not to propagate into the central bulk transport zone.

5. System Optimisation

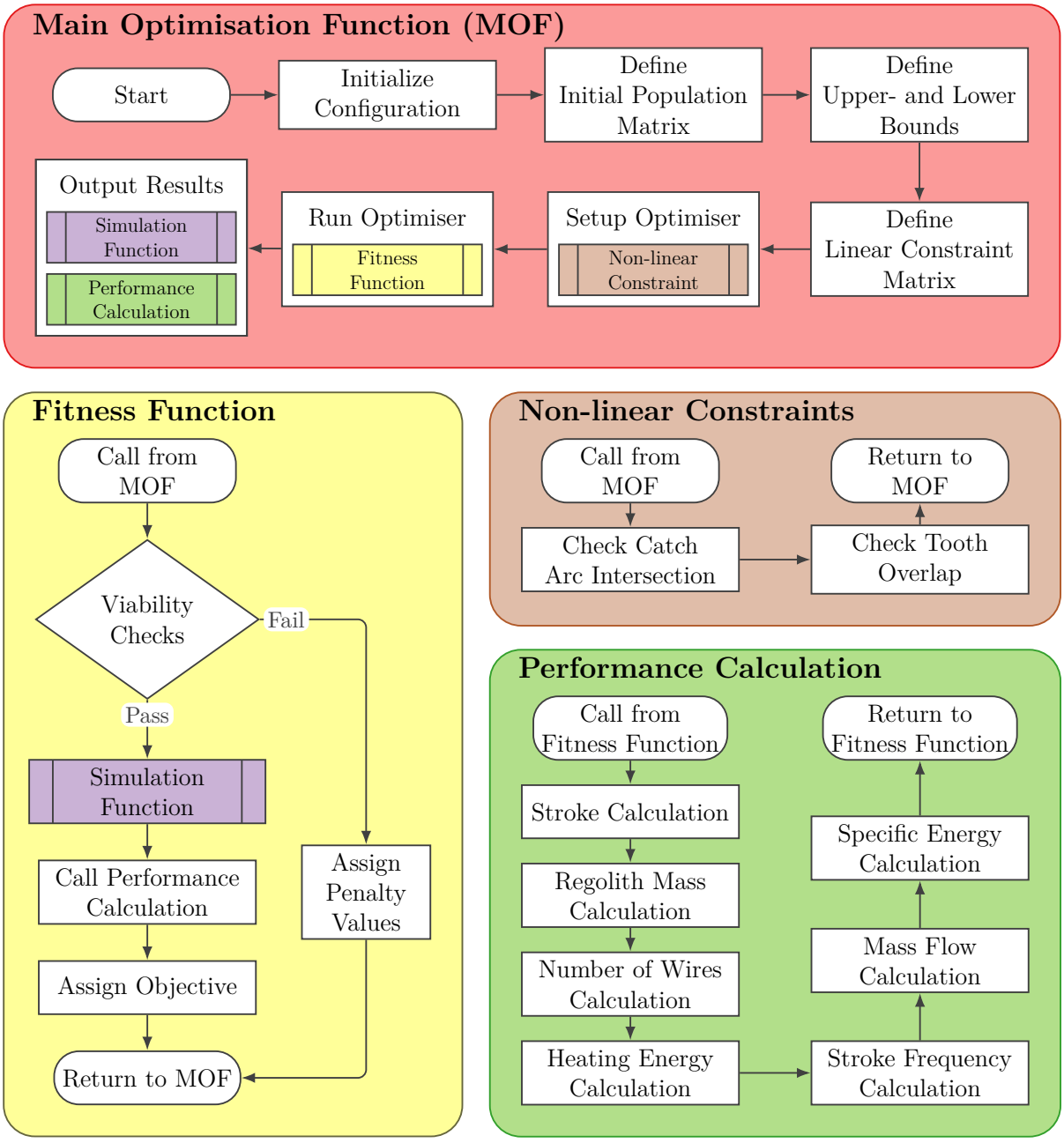

Figure 5.1: Flowchart of the Optimiser and Adapted Calculation Function

The system simulation is utilised to maximise the performance of the sawtooth conveyor concept. This optimiser aims to tweak specific geometric and motion parameters (optimisation parameters) to find a configuration that best meets the optimisation objectives. This chapter begins with the optimisation objectives in Section 5.1, then explains the design space defined by the optimisation parameters and their constraints in Section 5.2. Section 5.3 discusses the fitness function, which converts the results from the system

simulation into objectives interpretable by the optimising algorithm. This section also includes foundations on multi-objective optimisation and measures taken to enhance the optimiser's performance. The optimiser is characterised in Section 5.4, where repeatability, sensitivity to varying input coefficients and dependency on the conveyor angle are examined. The chapter concludes with the selection of final solutions in Section 5.5 and the subsequent inspection of these solutions in comparison to the regolith transport-and-dosing mechanism used by Team BREMEN in the SRC and the initial configuration of the sawtooth conveyor concept, introduced in Section 3.4.1.

5.1 Optimisation Objectives

In the initial energy estimation (cf. Section 3.4.3), both mass flow and specific energy consumption were high, particularly relative to the competing Concept 6. Additionally, the inherent limitation of SMA-actuation in the low stroke frequency must be addressed. This optimiser is employed to address the limitations identified during concept development. Geometric and kinematic parameters are identified to simultaneously reduce the specific energy consumption (and mass flow) and ensure a low stroke frequency.

For this, a multi-objective optimiser with the inherent capability of jointly investigating two objectives is used. This optimisation uses MATLAB 's `gamultiobj` solver. This solver minimises target values. The stroke frequency f_{stroke} and specific energy W_{spec} are calculated for every individual of this optimisation and defined as optimisation objectives. The exact implementation of the optimisation objectives is discussed in Appendix D.6.

5.2 Design Space and Constraints

The genetic algorithm modifies eight specific features to optimise the sawtooth geometry and kinematics. The values for restitution and atmospheric drag that were determined in Section 4.3.4 are not further modified in this optimisation. The influence of these parameters on the optimisation results is evaluated in Section 5.4.2. The geometric parameters of the sawtooth profile were defined in Section 4.2.2. These include the tooth pitch l_c, the tooth length l_a, the tooth height l_b, the catch radius r, the intersection angle between the catch arc and the base ω and the launch angle δ. The motion parameters of launch velocity v_0 and conveyor acceleration a_{conv} shape the regolith fill area (cf. Section 4.2.3). Additionally, acceleration plays an important role in calculating specific energy. These features are restricted by strict upper and lower limits to ensure manufacturability, summarised in Table 5.1.

Table 5.1: Upper and lower bounds of optimisation parameters

	l_c in mm	l_a in mm	l_b in mm	r in mm	ω in °	δ in °	v_0 in m/s	a_{conv} in m/s^2
Upper Bound	5	3	2	2	0	0	0.5	20
Lower Bound	150	150	150	150	120	45	2	80

In addition to these strict bounds, the optimisation parameters are restricted by both linear and non-linear constraint equations, preventing the optimiser from evaluating geometrically impossible configurations. Linear constraints can directly be implemented in the `gamultiobj` solver, preventing the evaluation of an individual with a parameter set (or chromosome) that violates these constraints. These constraints are set with a constraint matrix:

$$\begin{bmatrix} 0 & -1 & 1 & 0 & 0 & 0 & 0 & 0 \\ -1 & 1 & 0 & 0 & 0 & 0 & 0 & 0 \\ 0 & -1 & 0 & 1 & 0 & 0 & 0 & 0 \\ 0 & 0 & 1 & -1 & 0 & 0 & 0 & 0 \\ 0 & 0 & 0 & 0 & 0 & 0 & 0 & 0 \\ 0 & 0 & 0 & 0 & 0 & 0 & 0 & 0 \\ 0 & 0 & 0 & 0 & 0 & 0 & 0 & 0 \\ 0 & 0 & 0 & 0 & 0 & 0 & 0 & 0 \end{bmatrix} \begin{bmatrix} l_c \\ l_a \\ l_b \\ r \\ \omega \\ \delta_{\text{offset}} \\ v_0 \\ a_{\text{conv}} \end{bmatrix} \leq \begin{bmatrix} 0 \\ 0 \\ 0 \\ 0 \\ 0 \\ 0 \\ 0 \\ 0 \end{bmatrix} \tag{5.1}$$

Converting the constraints entailed in this matrix to linear constraint equations results in a continuous dimensional chain for l_c, l_a, l_b, and r:

$$l_b \leq r \leq l_a \leq l_c \tag{5.2}$$

The relation between l_b and r still permits geometrically impossible cases in which the diameter of the catch arc is large enough to intersect with both p_2 and the conveyor base. Too large radii could result in a severe "undercut" of the tooth ramp by the catch arc, which is not desired. The relation between l_a and l_c reduces the overlapping of teeth by keeping the ramp length strictly smaller than the tooth pitch. However, specific combinations of r and the catch angle ω can still result in the overlapping of the catch arc with the ramp of the next tooth. Non-linear constraints catch this and other cases.

Non-linear constraints cannot be implemented in a genetic algorithm as linear constraints can. While the non-linear constraints provide a framework for further detection of invalid features, these cases are not caught before the individual is evaluated in the simulation. Still, they do impose a gradient penalty on the evaluated configuration based on the magnitude of its constraint violation. This provides an incentive for the optimiser to find eligible solutions. Since these non-linear parameters do not prevent the individual

from being evaluated, they should be avoided and replaced by linear constraints wherever possible; however, some illegal cases can only be caught this way.

The non-linear constraints function is called for each individual by passing the chromosome as an argument. The constraint values are passed back for use in the genetic algorithm. Any individual whose constraint value exceeds the value defined by a constraint tolerance is determined as infeasible. Without any specific instructions, the `gamultiobj` solver applies the software's standard constraint tolerance of 1×10^{-3}. Among infeasible individuals, the individual with the lower constraint value is preferred. Between feasible individuals, that is, individuals for which the constraint value lies below the constraint tolerance, the individual with the better objective function value is preferred, even if its constraint value is higher [118]. This follows the common genetic algorithm constraint handling method first proposed by Deb in [119].

From the geometric parameters contained in the chromosome, the coordinates of p_2^{local} and p_3^{local}, as well as the x-coordinate of p_4^{local}, are calculated. The x and y components of p_3^{local} are defined in Equation (4.26) and Equation (4.24), respectively. x_4^{local} is defined in Equation (4.27). In the original definition of p_2^{local}, its global coordinates were used. These values are calculated within the simulation function and are therefore not available in the context of the non-linear constraints. The coordinates of p_2^{local} are instead calculated with:

$$\begin{bmatrix} x_2^{\text{local}} \\ y_2^{\text{local}} \end{bmatrix} = l_a \begin{bmatrix} \cos(\phi) \\ \sin(\phi) \end{bmatrix} \tag{5.3}$$

The tooth angle ϕ is derived from the ratio of the tooth height l_b to the tooth length l_a, as established in Equation (4.23). These local coordinates are used to ensure viable catch geometry and prevent tooth overlap. For large values of the catch angle ω in combination with a relatively small catch radius r, the circle encompassing p_3 might not intersect with p_2. The constraint value for this first investigation is calculated with:

$$c_1 = |y_2 - y_3| - r \tag{5.4}$$

For a radius that is larger than the vertical distance between the catch arc's centre and p_2, this results in a value of $c_1 < 0$. If the difference between the vertical distance and the radius rose, the constraint value would increase, providing an incentive towards acceptable values. For all $c_1 < 1 \times 10^{-3}$, the magnitude of c_1 is irrelevant, thus no incentive is given towards larger radii in the case of a viable geometry. The second constraint is investigated only if the first investigation confirmed an eligible geometry. Otherwise, the second constraint value is set to a high penalty value of $c_2 = 1 \times 10^6$, since the incentive for improvement is already given by c_1.

The second constraint ensures geometry viability by verifying that the local x-coordinate of p_4 does not exceed the tooth pitch l_c, therefore penalising interference between subsequent teeth:

$$c_2 = x_4^{local} - l_c \tag{5.5}$$

For all $l_c > x_4^{local}$, this function results in a negative constraint value c_2. Similarly, the third constraint detects non-feasible geometry in which the catch arc extends back beyond the start of the tooth with:

$$c_3 = -x_4^{local} \tag{5.6}$$

This equation penalises negative values for x_4^{local}.

5.3 Implementation and Computation

This section first discusses incorporating the simulation function into the optimisation via the fitness function. Subsequently, the concept of multi-objective optimisation is elaborated on, and this section concludes with measures to improve the optimiser's performance.

5.3.1 Fitness Function

The optimisation algorithm calls the fitness function for each individual. It acts as a wrapper that translates the results from the simulation function and the performance calculation into objective values for optimisation. Additionally, it runs viability checks on the parameters passed to the fitness function to prevent values that would cause errors in the simulation function, thereby preventing premature termination of the optimisation. The non-linear constraints provide an incentive for the optimiser to improve the faulty parameters, while the viability checks subsequently prevent the simulation function from being executed with fatal or non-feasible parameters.

These cases are handled by the non-linear constraint function; this implementation does not prevent the simulation from running with faulty parameters. This task is performed by the viability checks. Here, high penalty values are applied to the optimisation objectives for faulty parameters, and the execution of the simulation is prevented:

$$\begin{bmatrix} q_{\text{obj},1} \\ q_{\text{obj},2} \end{bmatrix} = 1 \times 10^6 \quad \text{if} \quad \begin{cases} |y_2^{\text{local}} - y_3^{\text{local}}| & > r \\ x_4^{\text{local}} & > l_c \\ x_4^{\text{local}} & < 0 \end{cases} \tag{5.7}$$

In addition to rejecting cases already deemed faulty by the non-linear constraints, the viability checks also investigate two additional cases for which calculating an incentive gradient within the scope of the non-linear constraints is not feasible. A geometry in which the catch arc intersects the tooth ramp not only at p_2, but also between p_1 and p_2 is still possible with the established constraints. A line intersecting a circle results in two intersection points t_1 and t_2, unless the line is tangential to the circle, in which case both points are identical. The projection of the circle's centre on the ramp section is calculated with the dot product of its coordinates with the unit normal vector of the ramp:

$$p_{\text{proj}} = x_3^{\text{local}} \cos\phi + y_3^{\text{local}} \sin\phi \tag{5.8}$$

where $\cos\phi$ and $\sin\phi$ are the components of the ramp's unit normal vector. The scalar p_{proj} represents the position of the projection point along the ramp. For the secant of a circle, p_{proj} lies exactly halfway between t_1 and t_2, resulting in:

$$t_2 = 2\,p_{\text{proj}} - t_1 \tag{5.9}$$

with t_1 defined by the position along the ramp with: $t_2 = \sqrt{x_2^2 + x_3^2}$. If the position of the second intersection lies between the start of the ramp (0) and the end of the ramp (t_1), the geometry is considered invalid, resulting in the optimisation objective receiving the penalty value, analogous to Equation (5.7). In the case of a catch arc that is exactly tangent to the ramp, a tolerance of 1×10^{-5} leads to t_1 being determined as outside the interval between p_1 and p_2, thus not triggering the viability check.

The accelerated AOR is calculated as part of the viability checks to prevent cases in which the regolith AOR under acceleration would cause the material to spill into the next tooth. While these cases would not violate physical constraints, the simulation is not adapted to handling such configurations. This check is performed by identifying if the angle formed by the regolith surface exceeds the conveyor angle, in which case it is flagged as invalid and penalised in accordance with Equation (5.7). The calculation of the regolith surface's angle is performed as presented in Section 4.2.3.

After the viability checks, the simulation function (as described in Section 4.2) is called from within the fitness function. After execution, the simulation function returns the average particle distance d_{avg} (cf. Equation (4.57)) and the cross-sectional area of the regolith fill to the fitness function. Since the regolith fill area is defined as a polygon in Section 4.2.3, its cross-sectional area A_{regolith} is trivially determined with MATLAB 's function `polyarea()`.

These values are used in the subsequently called performance calculation function to determine key performance values of mass flow $\dot{m}$, specific energy W_{spec}, stroke length l_{stroke}, number of required actuation wires n_{wire} and stroke frequency f_{stroke}. These performance

values are used in the result analysis to compare different configurations. The calculations performed in the performance calculation are based on the energy estimation discussed in 3.4.3. While the basic procedure is identical, some specific changes are necessary due to the changed context of the calculations. In Section 3.4.3, the regolith mass used in the kinetic and potential energy was based on the mass of sand in an individual tooth, as determined in the POC-tests. The varying tooth sizes in the optimisation necessitate the derivation of the regolith mass from the regolith fill area (cf. Section 4.2.3) with:

$$m_{\text{regolith}} = A_{\text{regolith}}\, n_{\text{teeth}}\, l_{\text{width}}\, \rho_{\text{regolith,min}} \tag{5.10}$$

The number of teeth n_{teeth} is not part of the optimisation parameters. It is set at 100 to ensure no particle flight path exceeds the simulated conveyor length, which would interfere with the results. The conveyor width l_{width} and density of loose regolith $\rho_{\text{regolith,min}}$ are defined in Section 3.4.3. In Section 3.4.3, the acceleration and stroke were also derived from the POC-tests. In the new optimisation context, acceleration is encoded in the individual's chromosome. The stroke is calculated as a function of the acceleration and the particle launch velocity (also part of the chromosome) with $l_{\text{stroke}} = v_0^2/2a$. The number of wires n_{wire} is calculated as introduced in Equation (3.6).

The stroke frequency is calculated as the inverse of the sum of the time required for the stroke t_{stroke} and the cooldown-time t_{cool} of the SMA-wire below its martensitic finish temperature M_f (cf. Section 3.1):

$$f_{\text{stroke}} = \frac{1}{t_{\text{stroke}} + t_{\text{cool}}} \tag{5.11}$$

The stroke time is the sum of the time required for the upstroke t_{up} and the time required for the downstroke t_{down}. For the upstroke, t_{stroke} simply follows from the launch velocity v_0 and the (constant, cf. Section 3.4.3) acceleration a with:

$$t_{\text{up}} = \frac{v_0}{a} \tag{5.12}$$

For the downstroke time, an estimated downstroke velocity v_d is taken from the POC-tests. There, the actuator showed an average downstroke velocity of $v_d \approx 0.05\,\text{m/s}$, as apparent from Figure 3.11. The downstroke time t_{down} is thus calculated with the stroke distance l_{stroke}:

$$t_{\text{down}} = \frac{l_{\text{stroke}}}{v_d} \tag{5.13}$$

To determine an accurate value for t_{down}, further tests incorporating SMA-actuators and compliant flexure bearings must be performed. These tests are beyond the scope of this study. The cooldown time t_{cool} as a component of the stroke frequency f_{stroke} is derived

from the heat loss rate Q_{rad}, as defined in Equation (3.22), and the change in stored thermal energy $\dot{E}_{\text{st}}$ with $Q_{\text{rad}} = -\dot{E}_{\text{st}}$ [120, p. 255]:

$$\epsilon_{\text{wire}} \cdot \sigma \cdot (T_{\text{hot}}^4 - T_{\infty}^4) \cdot A_{\text{surface}} = -\rho_{\text{wire}} V_{\text{wire}} c_{\text{p,wire}} \frac{dT}{dt} \tag{5.14}$$

The values of specific heat capacity $c_{\text{p,wire}}$, wire surface area A_{surface}, Stefan-Boltzmann-Constant σ, and wire emissivity ϵ_{wire} were introduced in Equation (3.7). The wire density ρ_{wire} was introduced in Equation (3.8). V_{wire} is the volume of the cylindrical wire. For this estimation, the ambient temperature is assumed to be T_{∞} =0 K for simplicity. Simplifying the equation by cancelling out the wire length and π, and integrating from $t_0 = 0$ to $t_1 = t_{\text{cool}}$ results in:

$$t_{\text{cool}} = \frac{\rho_{\text{wire}} d_{\text{wire}} c_{\text{p,wire}}}{12\,\sigma\,\epsilon_{\text{wire}}} \left(\frac{1}{T_{\text{low}}^3} - \frac{1}{T_{\text{high}}^3} \right) \tag{5.15}$$

The limit temperatures T_{low} (equivalent to M_f) and T_{high} (equivalent to A_f) are estimated at 333 K and 363 K, respectively [121].

The calculation of mass flow in this performance calculation also differs from that in the preliminary energy estimation. While the mass flow was initially based on a measurement from the POC-tests, the method used here incorporates the simulated particle distance:

$$\dot{m} = m_{\text{regolith}} \frac{d_{\text{avg}}}{l_{\text{conv}}} f_{\text{stroke}} \tag{5.16}$$

The ratio of the average particle distance d_{avg} and the conveyor length l_{conv} describes the ratio of the total regolith mass that leaves the conveyor in each stroke. Multiplication with the total regolith mass m_{regolith} and the stroke frequency f_{stroke} yields the average mass flow $\dot{m}$. The subsequent calculation of the specific energy W_{spec} is done with Equation (3.10).

The fitness function concludes with the definition of optimisation objectives. The first objective is assigned the stroke frequency f_{stroke}. The second objective is the specific energy W_{spec}. The stroke frequency is capped at $f_{\text{limit}} = 2$ Hz. If the calculated stroke frequency exceeds this limit value, a dynamic penalty is calculated for both objectives with the penalty weights $w_{\text{pen,1}} = 1000$ and $w_{\text{pen,2}} = 1000000$, respectively:

$$q_{\text{obj,1}} = -f_{\text{limit}} + (f_{\text{stroke}} - f_{\text{stroke}})\, w_{\text{pen,1}} \tag{5.17}$$

$$q_{\text{obj,2}} = W_{\text{spec}} + (f_{\text{stroke}} - f_{\text{stroke}})\, w_{\text{pen,2}} \tag{5.18}$$

The different penalty weights allow for the different magnitudes of the objective values. Incorporating dynamic penalties aids the optimiser in converting toward eligible configurations by incorporating a gradient toward lower stroke frequencies.

5.3.2 Multi-Objective Optimization

In this study, multi-objective optimisation is employed to optimise two objectives simultaneously. This significantly differs from the approach taken in Section 4.3.4. In both approaches, multiple variables were tweaked as part of the chromosomes; however, while the fitment optimiser aimed to improve on a single metric of SSE, the optimiser discussed in this section aims to minimise both stroke frequency f_{stroke} and specific energy W_{spec}. There can thus be no single configuration that can be seen as an optimal solution. While the specific energy might be minimal for one configuration, the configuration with the minimal stroke frequency might entail an entirely different geometry. Each configuration in which neither of the two optimisation objectives can be improved upon without compromising the other objective is thus considered an optimal solution. These specific results are called "Pareto-optimal solutions". The set of all Pareto-optimal solutions forms the Pareto front [122, pp. 10ff.].

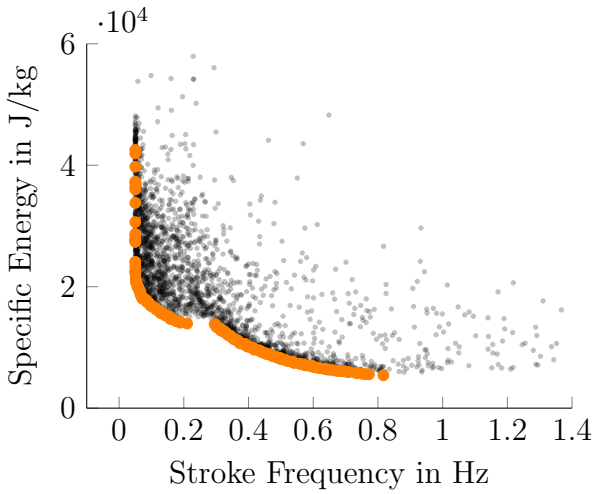

Figure 5.2: Pareto front in the objective space

Figure 5.2 shows the results of a subset of the simulations performed in an optimisation run as a point cloud. The Pareto front is depicted by orange points on the origin-ward boundary of the point cloud. In this illustration, a Pareto-optimal solution is identified by having no dominating points in the axial directions towards lower values of W_{spec} and f_{stroke}. All Pareto-optimal solutions are optimal results. However, to find the best solution for a specific application, one option must be chosen from the Pareto front. The solutions on the Pareto front range from a full focus on the objective of specific energy, while neglecting the stroke frequency (the lower right end of the Pareto front) to the inverse of a full optimisation of the stroke frequency while neglecting the specific energy (top left of the Pareto front).

5.3.3 Optimizer Performance Enhancement

MATLAB is an interpreted language [123]. In an interpreted language, the source code is executed directly, line by line. An alternative to interpreted languages is the ahead-of-time compilation. In compiled languages, source code is initially translated from the source language into a target language. Usually, this target language is machine code, which is directly interpreted by the computer's Central Processing Unit (CPU). The translated code generated by the compiler generally offers a significant performance advantage over the interpreter language. An interpreter can, however, provide better diagnostics, due to its behaviour of executing the commands sequentially [124]. The performance benefits of compilers become increasingly apparent when using nested `for`-loops. The interpreter must evaluate every command of the program separately, independent of its previous appearances. The execution time of a MATLAB script scales approximately with the number of executed commands [123]. The compiler, on the other hand, is much more efficient at executing a high number of statements, such as in nested `for`-loops [123].

In the system simulation, the examination of particle behaviour incorporates several levels of loops, resulting in 1×10^6 total iterations:

```
Simulation Root
└─ Iterating Bounces (n_bounce = 100)
   └─ Iterating Particles (n_launch = 100)
      └─ Iterating Teeth (n_teeth = 100)
         └─ Intersection Calculation
```

This architecture leads to significant performance disadvantages for the MATLAB implementation compared to a compiled-language implementation, such as with `C++`. Using MATLAB 's `Coder`, MATLAB source code is compiled into `C++`-code, a compiled language. In this optimisation, the simulation code, including the main calculation function and all subordinate functions, is compiled. The optimiser is not converted due to the converter's limited capabilities and thus runs directly in MATLAB. The compiled simulation function is subsequently called from within the optimiser. This compilation reduces optimisation time by a factor of approximately two orders of magnitude.

The optimisation utilises parallelisation to distribute the evaluation of individuals to all available CPU cores, as per MATLAB 's Parallel Computing Toolbox. This significantly improves performance further. Standard MATLAB operations perform single-threaded execution, processing individuals sequentially. In the case of the hardware, the optimisations were performed on, parallelisation allows for the leveraging of the full hardware capacity of eight cores.

5.4 Optimiser Characterisation

In this section, statistical analyses are performed on the optimisation results before the resulting optimisation parameters are discussed. The statistical analyses include a repeatability study, an analysis of sensitivity to the empirical parameters determined in Section 4.3.4, and an investigation of the effects of the conveyor angle on the optimisation results. Unless noted otherwise, all optimisation runs assumed a conveyor angle of 35°.

5.4.1 Repeatability Study

A repeatability study is conducted with optimisations under terrestrial and lunar environmental conditions. For each study, 45 optimisation runs with identical initial conditions are evaluated. The optimisation runs are performed with a population of 500. The runs terminate once the change in average Pareto spread across generations is less than the function tolerance of 1×10^{-4}. The Pareto spread is the distance between individual solutions on the Pareto front.

To evaluate the repeatability of optimisation runs, runs are compared based on the solution closest to the target mass flow. This ensures the optimisation runs are compared at similar operating points. The target value of 48 kg/h, as defined in Section 2.4.1, is reached in neither lunar nor terrestrial conditions. The lunar optimisations consistently resulted in mass flows exceeding the target, whereas the terrestrial optimisations found solutions at lower mass flows. For this reason, different target values are chosen for evaluating the repeatability of the optimisation runs under lunar and terrestrial conditions. Lunar runs are evaluated based on the solution closest to the target value 79.2 kg/h (0.022 kg/s), and terrestrial runs target 79.2 kg/h (0.008 kg/s). These values are chosen as the most extreme round values reachable by the respective optimisation runs.

Figure 5.3 illustrates the optimisation objectives of stroke frequency and specific energy and their repeatability across all evaluated optimisation runs at the defined target mass flows. The shaded areas represent the 25th to 75th percentiles, i.e., the central 50% of the data. The thick horizontal line shows the median of the data set. The horizontal lines outside the shaded area denote the samples within 1.5 × the shaded area. Outliers are marked with

+ symbols. The points show the individual results of the repeatability study. A factor of 1/10 is applied to the terrestrial specific energy to enable comparison with the lunar value in this illustration. Investigating the Coefficient of Variation (CV) allows comparison of repeatability with respect to stroke frequency and specific energy. It is calculated as a fraction of the standard deviation and the mean. The stroke frequency is highly repeatable

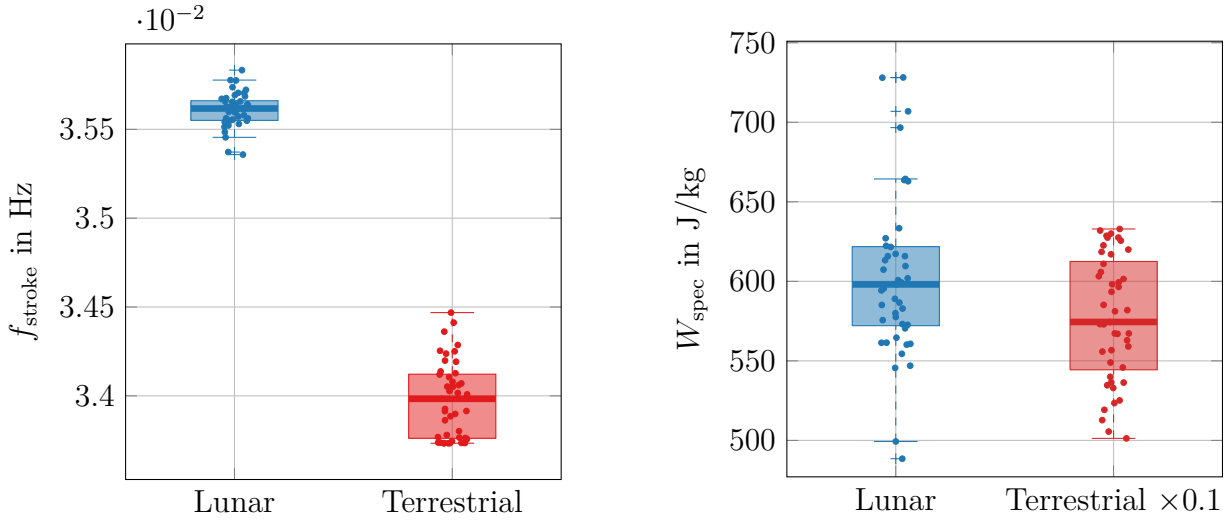

Figure 5.3: Optimisation reliability

under both lunar and terrestrial conditions at an CV of 0.275 % and 0.210 % respectively. The specific energy is both less repeatable and shows a significantly higher difference between the two conditions. Here, the CV under lunar conditions equates to 6.297 %, the terrestrial counterpart 2.297 %. This noise, due to repeatability, will be taken into account in further analyses investigating the influence of varying parameters.

5.4.2 Sensitivity Analysis

The optimisations are based on the empirical coefficients determined by the fitness optimiser using the validation campaign results, as described in Section 4.3.4. Here, the influence of changes in these coefficients on the optimisation results is determined. For each environmental condition, both k_{elastic} and μ_{friction} are investigated, in a range of $\pm 10\,\%$ of their original values. For the terrestrial conditions, the atmospheric drag parameter k_{drag} is varied in the same range. Here, optimisation runs are performed for the boundary values and the original value. Additionally, intermediate values of $\pm 5\,\%$ are investigated under lunar environmental conditions. For clarity, the illustrations in this analysis are shown only for lunar environmental conditions, with the full data, including terrestrial values, appended in Appendix C.2. Figure 5.4 shows the deviation from the norm value for both optimisation objectives as a percentage for all investigated empirical coefficients. The colours for the graphs are chosen to best represent the full range of values and are not comparable between frequency and specific energy graphs. Similar to the repeatability study, stroke frequency is much more stable than specific energy. The highest deviation of f_{stroke} is found at the maximum $k_{\text{elastic,1.1}}$ and an increased $\mu_{\text{friction,1.05}}$. The resultant stroke frequency is 5.15 % lower than the norm. Notably, the modified stroke frequency results tend to increase with lower values of k_{elastic}. An inverse effect is apparent in the specific energy; It increases with greater values of k_{elastic}. The variances in f_{stroke} pale in

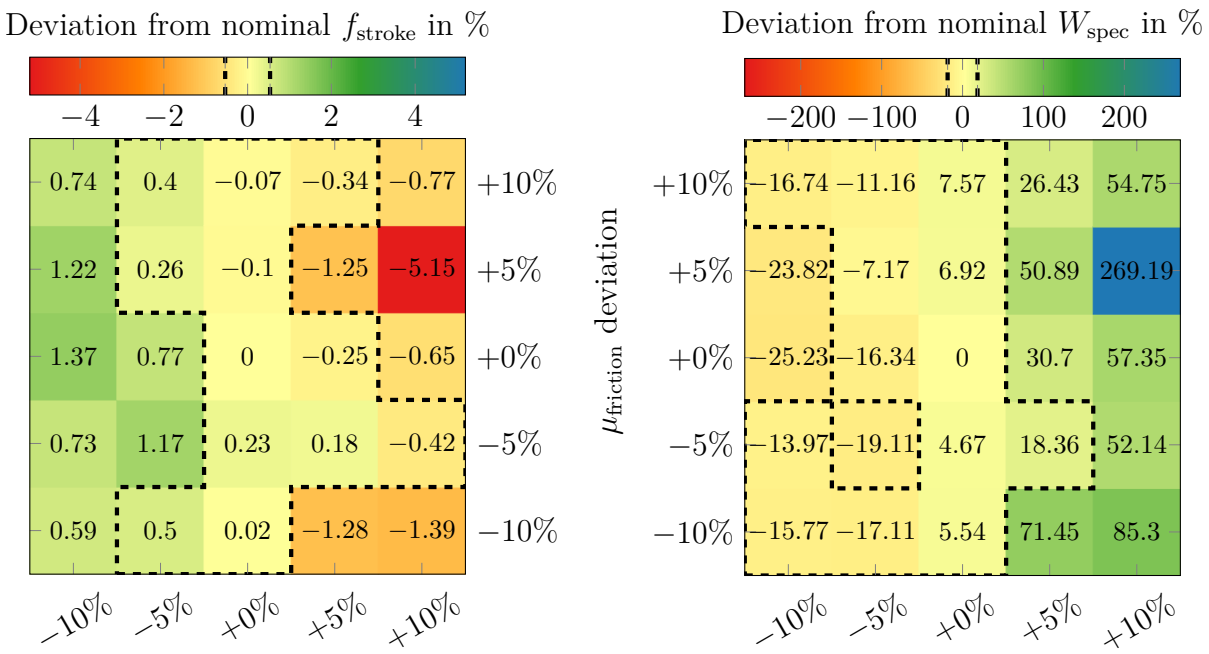

(a) Stroke Frequency

(b) Specific Energy

Figure 5.4: sensitivity of optimisation objectives to variance in empirical input values

comparison to the influence of varying empirical coefficients on the specific energy W_{spec}. Here, input deviations of 10 % lead to differences in the result of up to 269.19 %. The heat maps in Figure 5.4 show significant outliers at $k_{\text{elastic},1.1}$ and $\mu_{\text{friction},1.05}$ for both stroke frequency and specific energy. In this investigation, only a single optimisation run was performed for each coefficient combination. This, and the selection of only a single result from the full Pareto front, contribute to the limitation that these results do not reflect the optimiser's actual behaviour. The 2σ confidence interval for the repeatability is shown on the colour bar above each respective heat map. Results that fall within the confidence interval are marked with a dashed border. When expressed as a percentage of the nominal value, the interval for the stroke frequency is at ± 0.536 %, for the specific energy at ± 18.473 %. The deviations caused by variations in the coefficient μ_{friction} are significantly smaller than the confidence interval in the case that k_{elastic} remains unchanged. Variation of μ_{friction} in the investigated interval causes deviation far exceeding the confidence interval for both objectives.

5.4.3 Conveyor Angle Analysis

The optimisation for both environmental conditions was performed across conveyor angles ranging from 1° to 40°. For each data point, one optimisation run was performed. Options regarding population and function tolerance are the same as those used for the repeatability analysis. The influence of the conveyor angle is illustrated in Figure 5.5. The

shaded areas show the 2σ confidence interval for repeatability, used to evaluate the significance of the conveyor angle's effect. In most cases, no clear correlation between conveyor

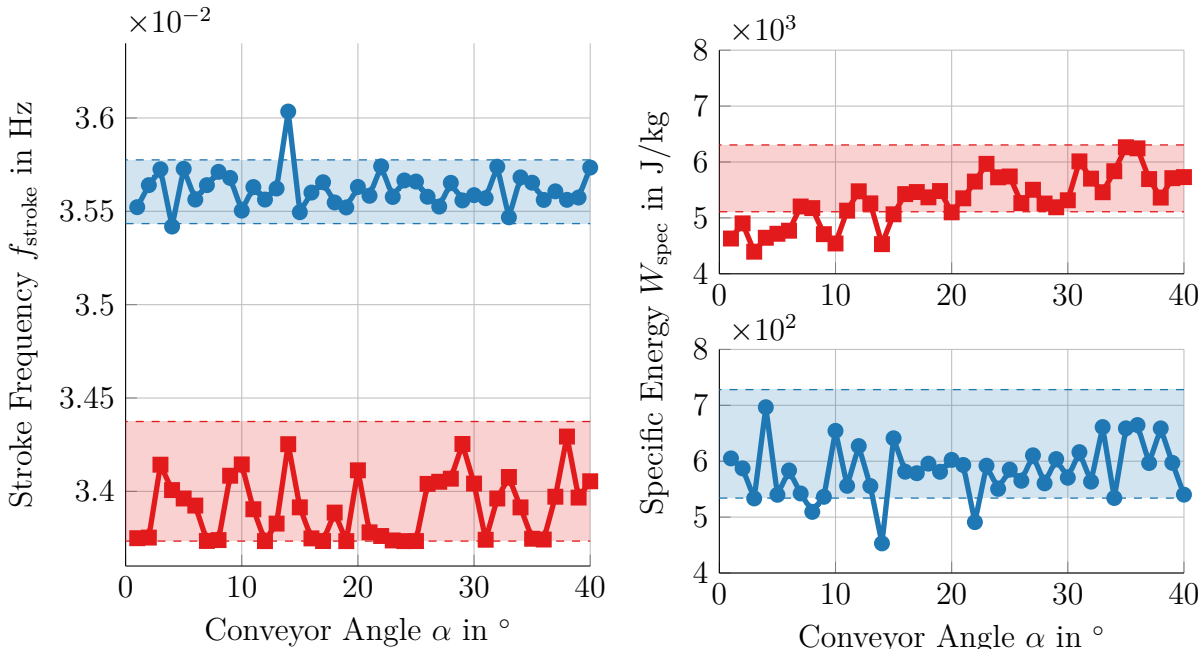

Figure 5.5: Optimisation conveyor angle dependence under lunar conditions (blue) and terrestrial conditions (red)

angles and solution value is apparent. The results from this analysis mostly fall within the confidence interval dictated by the repeatability. The optimisation runs under lunar environmental conditions show some outliers outside the confidence interval. The specific energy under terrestrial environmental conditions shows a clear upward trend with increasing conveyor angle. The source of this effect is immediately apparent. As discussed in Section 5.3.1, the specific energy includes the change in potential energy of the sledge and the loaded material. At higher conveyor angles, the change in potential energy is greater for equal stroke length, consequently leading to a higher specific energy. The same effect applies to the specific energy under lunar environmental conditions. However, due to the lower gravitational acceleration, the magnitude of potential energy, and thus its change, is much lower, negligible in relation to the change in kinetic energy.

5.5 Solution Selection

The optimisation runs discussed in Section 5.4 were performed with a population size of 500 and a function tolerance of 1×10^{-4}. For determining a final solution, one high-fidelity optimisation was performed for each terrestrial and lunar environmental condition. This run featured a population size of 1000 and a function tolerance of 1×10^{-6}. Figure 5.6 shows the solutions of the repeatability runs, the high-fidelity runs, and depicts the Pareto-optimal results of this combined dataset (black line, with markings), as well

as the Pareto-front of the high-fidelity optimisations (coloured line). These high-fidelity

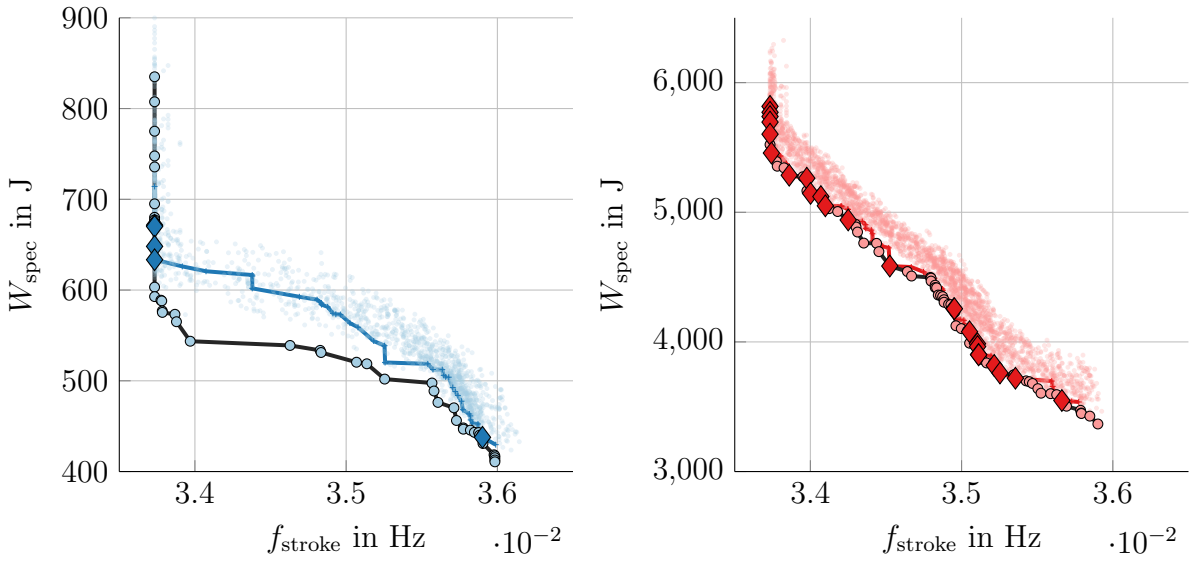

Figure 5.6: Pareto-optimal results from repeatability study and high-fidelity runs under lunar conditions (left) and terrestrial conditions (right)

runs did, however, only best the results from previous optimisations in a small number of cases. Under terrestrial environmental conditions, the Pareto front of the high-fidelity runs closely aligns with the ultimate Pareto front of the complete dataset. The diamond markings in both graphs depict the results of the high-fidelity optimisations that lie on the ultimate Pareto front. Conversely, the high-fidelity results reached the ultimate Pareto front under lunar environmental conditions only at the extreme frequencies. For further examinations, the ultimate Pareto front is used, as it contains the overall best results.

As introduced in Section 5.3.2, a single result must be selected from the Pareto front. Conventionally, a trade-off between the two objectives is taken, defining the relative weight of the objectives. A single entry is subsequently chosen that best fits this trade-off.

The stroke frequencies of the solutions found across the optimisation runs range from $3.373 \times 10^{-2}\,\text{Hz}$ to $3.598 \times 10^{-2}\,\text{Hz}$ under lunar environmental conditions and from $3.373 \times 10^{-2}\,\text{Hz}$ to $3.590 \times 10^{-2}\,\text{Hz}$ under terrestrial environmental conditions. While a low stroke frequency is necessary for a feasible configuration, due to the SMA-actuators' limitations, the minimal frequency difference in the results yields no significant preference between solutions. Consequently, solutions are chosen based on the specific energy W_{spec} and mass flow $\dot{m}$, as these were identified in Section 3.5 as Concept 4's primary disadvantages relative to Concept 6.

Three solutions for the following targets are considered for the final application, stemming from these conceptual limitations:

A. Solution closest to target mass flow of 48 kg/h

B. Solution with the highest mass flow

C. Solution with the lowest specific energy

Table 5.2 shows the performance parameters of the three final solutions. The source of the solution is noted in the last column. Under terrestrial environmental conditions, solutions

Table 5.2: Performance metrics of the final solutions

Metric	f_{stroke} in Hz$\times 10^{-2}$	W_{spec} in J/kg	$\dot{m}$ in kg/h	l_{stroke} in mm	n_{wire} –	d_{avg} in mm	Source –
Lunar environmental conditions:							
A	3.585	443.22	46.116	15.67	23	148.46	Rep_01
B	3.397	543.62	273.024	90.18	24	701.53	Rep_28
C	3.598	410.71	70.272	11.00	35	167.63	Rep_28
Terrestrial environmental conditions:							
A	3.386	5285.77	33.12	94.62	25	101.75	HF
B	3.386	5285.77	33.12	94.62	25	101.75	HF
C	3.590	3366.94	16.92	14.39	52	67.36	Rep_26

A and *B* are identical; the solution with the highest mass flow also exhibits the mass flow closest to the target, since no solution exceeded the target value. Conversely, solution *A* under lunar environmental conditions is the solution out of the Pareto front with the lowest mass flow. Solution *B* exhibits the highest mass flow by a significant margin; however, its stroke length of 90.18 mm dictates an actuation wire length of 1803.6 mm, given a contraction ratio of 5 %, as assumed in Section 3.4.3. That exceeds the length of the sledge of $l_{\text{total}} = 1.3054$ m, as defined in Equation (3.1). Accommodating this actuator wire would likely lead to additional complications. Solution *C* requires an actuator length of 220 mm. This configuration outperforms solution *A* in both specific energy and mass flow, with a minimal increase in stroke frequency, and is thus chosen as the final solution. Solution *C* is chosen for future tests under terrestrial environmental conditions for the same reason of a more feasible actuator length. Performance and geometrical parameters of all solutions in the ultimate Pareto front are appended in Appendix C.4. Table 5.3 shows the optimisation parameters for the final solution for each environmental condition.

Table 5.3: Optimisation parameters of the final solutions

Metric	l_c in mm	l_a in mm	l_b in mm	r in mm	γ in °	δ in °	v_0 in m/s	a in m/s^2
Lunar environmental conditions:								
C	47.35	46.90	32.18	43.49	94.44	11.96	0.84	32.05
Terrestrial environmental conditions:								
C	47.38	45.88	34.38	36.91	62.84	17.55	1.30	58.59

5.6 Final Configurations

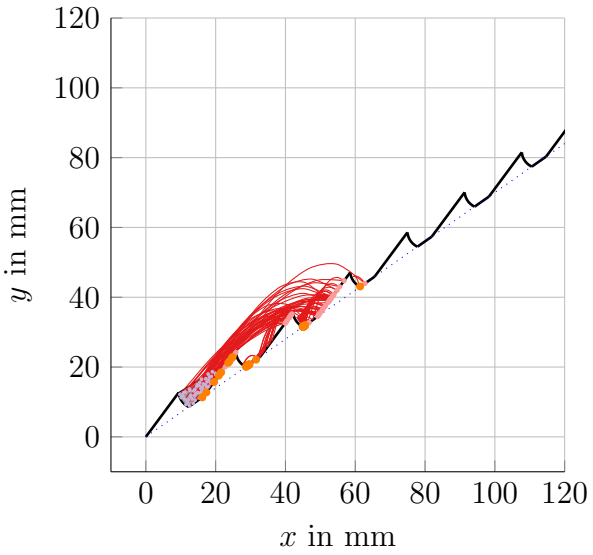

(a) POC configuration for terrestrial conditions

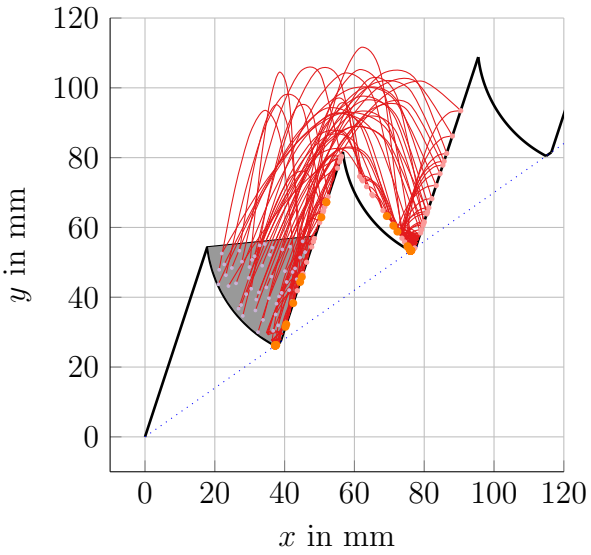

(b) Optimised configuration under terrestrial conditions

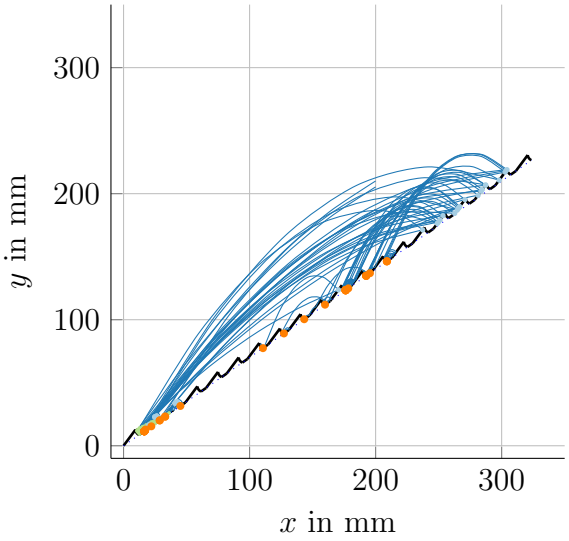

(c) POC configuration for lunar conditions

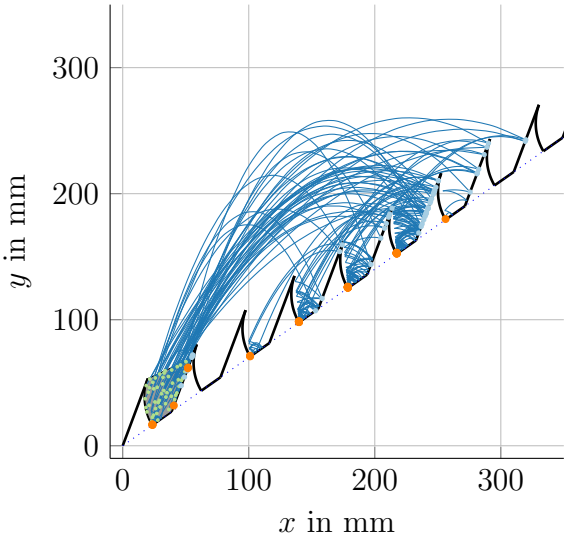

(d) Optimised configuration under lunar conditions

Figure 5.7: Particle trajectories and sawtooth geometries: Optimised configurations vs. POC baseline. Terrestrial results are scaled for clarity.

Figure 5.7 shows the particle trajectories for the optimised configurations in comparison to the initial configuration used in the POC-tests. Figure 5.7c displays the application of the POC geometric and motion parameters under reduced lunar gravity and absence of atmosphere. The graphs depicting the terrestrial environmental conditions, Figure 5.7a and Figure 5.7b, are scaled relative to the lunar graphs to improve clarity. The scale between configurations under the same environmental conditions is equal. While the exact geometry varies, the optimised geometries exhibit a significantly larger tooth size, independent of the environment. The initial particle flight distances (distance to first collision)

appear not to have increased significantly in the optimised configurations. Under lunar environmental conditions, the initial particle flight distances in the optimised solution (cf. Figure 5.7d) are generally lower than in the initial graph. However, in the optimisation, the final particle distance is used as the metric, that is, the locations the particles end up at after termination of the bounce loop. This distance is generally higher for the optimised configurations. Additionally, the significantly larger teeth in the optimised solutions increase the mass flow by moving more material per conveyor stroke. The optimised solution exhibits more aggressive overhangs (high γ) in the teeth's catch sections. This is assumed to help prevent particle backflow.

Table 5.4: Performance comparison of the initial and optimised sawtooth conveyor configuration and equivalent conveyor belt

Mechanism	W_{spec} in J/kg	$\dot{m}$ in kg/h	P_{avg} in W
SRC conveyor belt	74	48	1
POC terrestrial configuration	31690.9	0.62	5.458
Optimised terrestrial configuration	3366.94	16.92	15.825

Table 5.4 compares the key performance metrics of specific energy W_{spec}, mass flow $\dot{m}$ and average continuous power draw P_{avg}. Values are given for the regolith dosing and transport mechanism used by Team BREMEN in the SRC, the initial terrestrial configuration of the sawtooth conveyor, as used in the POC tests, and the optimised configuration of the sawtooth conveyor for application under terrestrial environmental conditions. The values for the POC-configuration differ significantly from the preliminary energy estimation in Section 3.4.3. In the initial estimation, the values were based on measurements from the POC-tests and scaled to fit the full concept. Additionally, the frequency estimate was based solely on the required mass flow. The values in Table 5.4 are instead based on the simulation results, obtained using the same calculation as the optimiser's performance calculation function (cf. Section 5.3.1), to improve comparability between the results.

The conveyor belt significantly outperforms the sawtooth conveyors across all examined metrics. Substantial improvements, however, can be examined by comparing the initial sawtooth conveyor with the optimised configuration. Both the specific energy and the mass flow of the final solution improve on the initial values by an order of magnitude. The average continuous power draw P_{avg} is higher in the final solution by a factor of 3. However, this is to be set against the significantly higher mass flow achieved by the final design. Table 5.5 explores the compliance of the final sawtooth conveyor configuration under lunar environmental conditions with the requirements set in Section 2.4.

The final lunar configuration of the sawtooth conveyor is fully compliant with the feed rate, improving on the minimum requirement by an order of magnitude. It is also fully compliant with the requirements regarding conveyor slope and transport distances, as

Table 5.5: compliance of the final concept with the system requirements

Requirement	**Target Value**	**Optimised Result**	**Status**
Performance			
Feed Rate	>6 kg/h	70.272 kg/h	Compliant
Material Loss	Minimal	N/A	N/A
System Mass (m)	<17 kg	N/A	N/A
Power Consumption (P)	<5 W	8.017 W	Non-Compliant
Dust Generation	Minimal	N/A	N/A
Horizontal Distance (d_h)	0.6 m to 1.0 m	1 m	Compliant
Vertical Distance (d_v)	0.386 m to 0.643 m	0.643 m	Compliant
Conveyor Slope (θ)	up to 40°	up to 40°	Compliant
Flow Continuity	Continuous	N/A	N/A
Environmental Conditions	—	—	Compliant
Geometric Constraints	—	—	Compliant
RAMS	—	—	N/A
Architecture	—	—	Compliant

shown in Section 5.4.3. The architectural, geometric and environmental constraints have been explored in the concept evaluation in Section 3.3. The sawtooth conveyor concept is considered compliant with these requirements. Compliance with the requirements for material loss, dust generation, flow continuity, and RAMS cannot be directly inferred from the simulation results. Material loss and dust generation must be controlled with shielding, as discussed in Section 3.3.1. With these adaptations, material loss and dust generation are assumed to be reducible to a sufficiently low level. The flow continuity has not been examined in detail in this study. This must be evaluated as part of further tests with the full concept. Evaluation of system mass and RAMS requirements requires further system design. The final concept is not compliant with the power consumption requirement. Under lunar conditions, the simulation indicates a continuous average power consumption of 8.017 W, exceeding the maximum requirement of 5 W. In the optimiser, the sledge mass is conservatively estimated to be equivalent to that of an aluminium plate 5 mm thick. Reducing the sledge's mass would significantly lower the continuous power draw. The requirement is thus considered to be achievable with further development.

6. Conclusion and Outlook

Lunar dust is one of the largest inhibitors to sustained lunar surface operations. To address this danger, this study successfully adapted the concept of IDM into a functional lunar regolith transport mechanism for application in an ISRU production chain using Compliant Mechanisms. Conventional transport mechanisms incorporating sliding tribological pairs inherently pose a high susceptibility to this highly abrasive material. These components are replaced by compliant mechanisms, inherently circumventing the risk of mechanical seizure and increased wear.

The development process began with the theoretical synthesis and evaluation of six transport system concepts, against requirements in the fields of performance, RAMS, environmental conditions and architectural compatibility. The sawtooth conveyor emerged from this concept evaluation as the frontrunner. Its conceptually high flow continuity and compatibility with existing beneficiation architecture set this concept apart from its competitors. While Concept 6 was not chosen for further development in this study due to its integration problems with existing ISRU production infrastructure, it is likely highly applicable to long-distance lunar regolith transport due to its high modularity and low energy consumption. Further development of this wave chain concept is recommended for this application.

Actuation of the sawtooth mechanism requires coping with the extreme lunar environmental conditions. Shape memory alloys were selected over amplified piezoelectric actuators for their significantly higher volumetric energy density. This immense energy density outweighs the cooling-limited stroke frequency due to the lunar vacuum. To ensure precise, friction-free parallel motion of the conveyor sledge, the mechanism is guided by Single Parallelogram Flexure Bearing. The compliant guides have a secondary function: applying the bias force required to extend the SMA wires after actuation. These compliant mechanisms proved advantageous over their more complex counterparts in Double Parallelogram Flexure Bearing due to their simplicity.

For in-depth evaluation and further development, a custom two-dimensional system simulation was programmed and benchmarked against validation tests under terrestrial environmental conditions. Empirical parameters were determined with a fitment optimiser to align the simulation to the real-world test results. The validation campaign substantiated the accuracy of the system simulation while also exposing limitations in reproducing complex particles.

Based on this validated simulation tool, a multi-objective genetic algorithm was employed to maximise the performance of the sawtooth conveyor. The optimiser tweaked geometric and kinematic variables to minimise specific energy and stroke frequencies in both lunar and terrestrial environmental conditions. Transport slopes in the range of 1° to 40° were examined. The optimiser produced configurations that successfully tackled the entire application range.

This study demonstrated that pairing compliant mechanisms with SMA-actuators in the novel sawtooth conveyor concept yields a highly capable lunar regolith transport solution that relies on Implicit Dust Mitigation techniques, ensuring reliable long-term operation for future lunar ISRU infrastructure.

6.1 Outlook

This section provides an outlook on future work recommended based on this study. It is split into further development of the system design, improvements and extensions to the simulation and optimisation, proposed tests, and additional developments not considered in this study.

6.1.1 System Design

In this study, the system design was only discussed preliminarily as a final concept definition Section 3.5. For further work on the sawtooth conveyor concept, an in-depth design is required. The system simulation and optimisation provide a strong framework for the elaboration of other design aspects. The actuation system was preliminarily determined to utilise SMA-actuators. In further development, the actuation system is to be designed in conjunction with the compliant flexure mechanism to examine their symbiosis. An analytical simulation of the compliant mechanism is proposed to identify design parameters that meet the requirements for stroke length and SMA bias force, as derived from the simulation and optimisation in **??**.

In the simulation and optimisation, the mass of the sledge was assumed to be equivalent to that of an aluminium sheet 5 mm thick. The sledge mass is an important parameter for determining the system's efficiency. A high mass in motion is likely detrimental to the mechanism's lifespan as well. A highly weight-optimised sledge design is thus advantageous. This weight optimisation may, for example, be accomplished through material selection and topology optimisation.

A complete design of the interfaces between multiple conveyor modules, as well as the beneficiation, is required. The interface to the beneficiation mechanism may be adapted

from the approach taken by Team BREMEN in the SRC. Here, a passive chute sufficed. A sufficiently steep component helps prevent clogging of the interface with lunar regolith. Vibrational agitation of the material eliminated powder bridging. The inherent agitation produced by the sledge's movement would likely ensure continuous powder flow.

As discussed in Section 3.5, piezoelectric actuators were disregarded in this study in favour of SMA-actuators for their significantly lower volume-specific energy. Adaptation of the simulation to implement piezoelectric actuators might provide interesting in-depth insights into the application of the two actuation principles in this specific concept. As opposed to SMA-actuation, utilising piezoelectric actuators would allow for low-stroke actuation at very high frequencies. The resulting increase in flow continuity might, in some cases, outweigh the lower volume and complexity of SMA-actuators.

Dust shielding is paramount for this concept, preventing both material losses and contamination of nearby hardware. The exact implementation of dust shielding must be discussed. Both direct attachment to the sledge and a static solution covering the whole system exhibit significant advantages and disadvantages. The decision between the concepts is outside the scope of this study and should be evaluated in future work.

6.1.2 Simulation and Optimisation

The simplifications and limitations of the simulation and optimisation were discussed in Section 4.4. This section details possible improvements to these limitations. It is assumed that further development of the simulation will prioritise the application under lunar environmental conditions, precluding the need for a comprehensive atmospheric drag model.

As discussed in Section 4.4, the simulation assumes perfectly spherical particles, with effects on atmospheric drag and coefficients of restitution. Wedel et al. primarily discussed the development of a general restitution model for non-spherical particles [102]. From this work, the simplified solution for spherical particles was used. For future implementation of non-spherical particles, the more advanced model might be used. This would, however, require more in-depth investigation of the particle morphology and dynamics. While the assumption of spherical particles also influences atmospheric drag, further simulations would likely focus on the lunar application, thereby negating the need for a higher-fidelity drag model.

A more comprehensive simulation of particles of different sizes is recommended to improve the simulation's adaptability to lunar regolith. Following the approach used in this study to synthesise restitution coefficients, a validation test campaign across a variety of particle sizes is proposed. Restitution coefficients for various particle sizes may be interpolated from the empirically derived values obtained in this validation campaign.

The simulation does not consider any cohesive effects in the simulated material. Further investigation of these effects is recommended for future development. In lunar regolith, a variety of effects, including particle interlocking under material compression, electrostatic forces, and van der Waals forces, occur. When not investigating particle collisions, however, the computational overhead introduced by considering these attractive forces would likely preclude their implementation for further optimisation. A highly comprehensive DEM simulation is instead proposed for a select few configurations resulting from the system optimisation.

In the multi-objective optimisation performed as part of this study, geometric parameters of the initial sawtooth geometry are varied. The shape of the sawtooth profile is, however, dictated by the initial geometry. Entirely different geometries not investigated here might prove more performant than the initially proposed. Further simulation and optimisation shall consider other geometries, possibly permitting greater freedom in the geometry construction for the optimiser. In the optimiser characterisation, more optimisation runs are required for in-depth analysis of sensitivity effects and dependency on the conveyor angles. Notably, the extreme outliers in the sensitivity analysis shall be examined further. The optimiser did not find the global optimum. The repeatability runs performed for both environmental conditions showed a large spread in results. This effect is, however, less pronounced under terrestrial conditions; the high-fidelity run produced solutions better than the vast majority of results from the repeatability runs. Convergence to a global optimum might be aided by varying the mutation and crossover parameters, or by using even higher population and generation counts than those used in the high-fidelity runs.

The optimisation includes preliminary calculations of energy and stroke frequency. While sufficiently accurate for comparing different configurations, the quantitative determination of both values requires further insight from testing with the full concept, including SMA-actuation and compliant guides, across different configurations. The constraints of this study did not allow for analysis of the optimiser's behaviour. More in-depth investigations on preferences in the optimisation parameters might reveal foundational rules for high-performance configurations.

6.1.3 Testing

In the scope of this study, POC-tests and a validation campaign for the system simulation were performed. In this section, additional tests are proposed.

While the applicability of the underlying simulation has been corroborated by tests conducted under terrestrial environmental conditions, the optimiser itself has not been tested under such conditions. A validation campaign is thus proposed for configurations identified by the optimiser as advantageous to the initial concept. This will both validate the opti-

miser's ability to produce geometries and motion parameters superior to the initial values and alleviate concerns about possible overfitting of the fitment optimiser, as discussed in Section 4.3.6. This validation campaign could be coupled with test runs performed under vacuum conditions to investigate the corresponding simulations. In Section 3.4.1, tests were performed at inclinations of 15° and 38°. Slope angles ranging from close to the full required range were investigated in the optimisation. These angles shall be examined empirically, especially the boundary values of 0° and 40°. These extreme values may inhibit conveyance: at very low inclinations, the accumulation of material in the tooth catches, which ensures consistent agitation across strokes, is not guaranteed. Conversely, performance is assumed to be inhibited by chaotic particle bounces off the conveyor, causing particle backsliding.

The regolith transport-and-dosing mechanism developed by Team BREMEN for the SRC extracted material from a depot, which was filled in bulk loads by the excavation rover. In this application, the transport mechanism is, in part, constantly covered by a large amount of regolith. The inclusion of such a depot would be beneficial for the flexible application of the sawtooth conveyor. Tests with a simple bunker component, as utilised in the SRC, are to be performed using this concept. Should these tests prove unsuccessful, developing alternative depot variants is recommended, possibly leveraging the sawtooth conveyor concept's inherent percussive agitation. Validation tests with lunar regolith simulants are likely not adding much at the current state of the simulation, given its limitations in particle morphology. Upgrading the simulation as discussed in Section 6.1.2 should precede any more comprehensive testing.

Neither the actuation method nor the compliant guide system has been investigated beyond the concept stage. Following their in-depth design, tests of both components are recommended. Integrated system tests are then to be conducted in terrestrial lunar-analogue facilities. The focus of these tests shall be on evaluating the long-duration applicability of the proposed concept and investigating problems caused by lunar regolith. The dust production in these tests is to be measured to investigate the system's influence on surrounding hardware.

6.1.4 Additional Development

The sawtooth conveyor, as well as the other concept conceived in Section 3.2, bears possibilities for further development beyond the applications discussed in this study.

Technical exchange with the German Aerospace Center (DLR) Institute of Space Research indicated that the sawtooth conveyor concept is highly compatible with in-situ characterisation methods. Particularly, the inclusion of Laser-induced Breakdown Spectroscopy (LIBS) was discussed in this context. For an accurate LIBS-measurement to

be taken of a granular material, the surface of the test-subject must be prepared. This preparation is performed by slightly compressing the material. Implementation of the sawtooth conveyor concept would require the mechanism to halt between strokes, allowing a separate mechanism to compress a small area of regolith within each tooth. The area requiring preparation is minimal, with the spots created by the LIBS measurement approximately 400 µm in size, allowing measurement within a single tooth. Following compression, the measurement is performed before the transport cycle can continue. The transport mechanism must not be adapted to accommodate these measurements, though additional hardware is required for sample preparation.

As discussed in Section 2.2.2, some terrestrial transport concepts can additionally be used for excavation. This secondary application is to be investigated for the sawtooth conveyor concept. The tests performed to ensure compatibility with a regolith depot (cf. Section 6.1.3) are expected to yield results that are valuable to this research question. Initial penetration of the surface is assumed to be the greatest inhibitor to this application. Abrading material from existing walls is expected to work well, with the sawtooth profile acting like a saw. In the SRC, this procedure of first creating a deep hole, which is subsequently laterally expanded, proved to be an efficient way of gathering material.

Further development of Concepts 1 and especially Concept 6 is recommended. Both concepts are considered viable for lunar regolith transport, with Concept 6 expected to be the best-performing among the examined concepts for long-range transport. All initially discarded concepts for regolith transport are to be reevaluated for excavation.

In this study, a system for horizontal and inclined transport of lunar regolith was developed. The sawtooth conveyor concept may, however, also be applicable for vertical transport. For this, the sawtooth profile is arranged around the inner walls of a vertically oscillating tube. The particles' ballistic trajectories would transport them from one side of the tube to the other. Adaptation of the system simulation (cf. Chapter 4) to represent a cross-section of this vertical conveyor is recommended to investigate the feasibility of this concept.

Bibliography

[1] National Aeronautics and Space Administration, "FACT SHEET: NASA Unveils Transformative Initiatives to Achieve America's National Space Policy," NASA Office of Communications, mar 2026.

[2] Deep Space Exploration Laboratory, "International Lunar Research Station (ILRS)," China National Space Administration (CNSA), Tech. Rep., may 2023.

[3] National Aeronautics and Space Administration, "Moon Base User's Guide: Architecture Resources," NASA Headquarters, Washington, DC, Tech. Rep. NP-2026-04-6806-HQ, apr 2026. [Online]. Available: www.nasa.gov/architecture

[4] A. Owens, W. Cirillo, C. Stromgren, J. Cho, C. Lynch, and J. M. Vega, "Integrated logistics and supportability challenges of sustained human lunar exploration," in *51st International Conference on Environmental Systems*, April 2022. [Online]. Available: https://ntrs.nasa.gov/citations/20220006045

[5] G. H. Heiken, D. T. Vaniman, and B. M. French, *Lunar Sourcebook, A User's Guide to the Moon*. Cambridge, UK: Cambridge University Press, 1991.

[6] P. Gläser, A. Sanin, J.-P. Williams, I. Mitrofanov, and J. Oberst, "Temperatures near the lunar poles and their correlation with hydrogen predicted by lend," *Journal of Geophysical Research: Planets*, vol. 126, no. 9, p. e2020JE006598, 2021. [Online]. Available: https://agupubs.onlinelibrary.wiley.com/doi/abs/10.1029/2020JE006598

[7] L. Kiewiet, M. Heitkamp, C. Kalis, and P. Zabel, "Design investigation of lunar water extraction," 04 2023.

[8] European Space Agency and European Space Resources Innovation Centre, "Rulebook: Second Space Resources Challenge," European Space Agency, Tech. Rep., 07 2025, document distributed to teams participating in the field test.

[9] Z. Zhao, M. Yüksel, K. M. Kulkarni, R. Dominguez, S. Fälker, T. Gumbold, A. Bresser, A. Suresh, P. Zabel, M. Rejon Lopez, S. Reershemius, and M. Meder, "Beneficiation of regolith and mobile excavation (Team BREMEN)," in *18th Symposium on Advanced Space Technologies in Robotics and Automation (ASTRA-2025)*. Zenodo, Oktober 2025. [Online]. Available: https://elib.dlr.de/221989/

[10] J. Kleinhenz and J. Sanders, "ISRU evaluation of Artemis campaign sites: Considerations and methodology," in *Proceedings of the Lunar Surface Science*

Workshop (LSSW). NASA Technical Reports Server (NTRS), April 2023, document ID: 20230004302. [Online]. Available: https://ntrs.nasa.gov/citations/20230004302

[11] D. Bussey, J. McGovern, P. Spudis, C. Neish, H. Noda, Y. Ishihara, and S.-A. Sørensen, "Illumination conditions of the south pole of the moon derived using kaguya topography," *Icarus*, vol. 208, no. 2, pp. 558–564, 2010. [Online]. Available: https://www.sciencedirect.com/science/article/pii/S0019103510001375

[12] J. S. Levine, "Perturbing the mass and composition of the lunar atmosphere during the Artemis surface missions," in *Report of the Science Definition Team for Artemis*, 2011. [Online]. Available: https://www.lpi.usra.edu/announcements/artemis/whitepapers/2011.pdf

[13] R. Hsieh, "Cold welding in space: Limitations and opportunities," *National High School Journal of Science*, February 2026. [Online]. Available: https://nhsjs.com/wp-content/uploads/2026/02/Cold-Welding-in-Space-Limitations-and-Opportunities.pdf

[14] European Cooperation for Space Standardization, *ECSS-Q-ST-70-02C: Thermal vacuum outgassing test for the screening of space materials*, ECSS Executive Secretariat, Noordwijk, The Netherlands, November 2008. [Online]. Available: https://ecss.nl/standard/ecss-q-st-70-02c-thermal-vacuum-outgassing-test-for-the-screening-of-space-materials/

[15] M. G. Kivelson and C. T. Russel, *Introduction to Space Physics*. Cambridge University Press, 1995.

[16] K. L. Ryder and M. J. Campola, "The lunar radiation environment," May 2022. [Online]. Available: https://ntrs.nasa.gov/citations/20220007070

[17] B. A. Stein, "LDEF materials overview," in *LDEF: 69 Months in Space. Part 3: Second Post-Retrieval Symposium*. Hampton, VA, United States: NASA Langley Research Center, April 1993, document ID: 19930019066. [Online]. Available: https://ntrs.nasa.gov/citations/19930019066

[18] D. A. Yahalomi, M. T. Scoggins, N. Anderson, M. Driker, K. Onuma, K. T. Awotwi, J. M. Donovan, and P. Sathianathan, "Micrometeoroid impact rate analysis for an artemis-era lunar base," 2025. [Online]. Available: https://arxiv.org/abs/2511.04740

[19] D. A. Kring, "Parameters of lunar soils," Lunar Exploration Initiative, Technical Briefing, 2006, accessed: April 25, 2026. [Online]. Available: https://www.lpi.usra.edu/science/kring/lunar_exploration/briefings/lunar_soil_physical_properties.pdf

[20] J. Connolly and W. Carrier, "An engineering guide to lunar geotechnical properties," 03 2023, pp. 1–9.

[21] R. M. Nedderman, *Statics and Kinematics of Granular Materials*. Cambridge University Press, 1992.

[22] W. D. C. III, "Geotechnical properties of lunar soil," September 2005. [Online]. Available: https://www.lpi.usra.edu/lunar/surface/carrier_lunar_soils.pdf

[23] V. S. Engelschiøn, S. R. Eriksson, A. Cowley, M. Fateri, A. Meurisse, U. Kueppers, and M. Sperl, "Eac-1a: A novel large-volume lunar regolith simulant," *Scientific Reports*, vol. 10, no. 1, p. 5473, 2020. [Online]. Available: https://doi.org/10.1038/s41598-020-62312-4

[24] R. V. Morris, "Surface exposure indices of lunar soils: A comparative FMR study," *Proceedings of the Lunar Science Conference*, vol. 7, pp. 315–335, 1976.

[25] National Aeronautics and Space Administration, "Apollo 17 technical crew debriefing," Manned Spacecraft Center, Houston, Texas, Tech. Rep. MSC-07631, January 1973.

[26] J. R. Gaier, "The effects of lunar dust on eva systems during the apollo missions," National Aeronautics and Space Administration, Glenn Research Center, Cleveland, Ohio, Tech. Rep. NASA/TM—2005-213610, March 2005.

[27] National Aeronautics and Space Administration, "Apollo 11 mission report," Manned Spacecraft Center, Houston, Texas, Tech. Rep. MSC-00171, November 1969.

[28] ——, "Apollo 12 mission report," Lyndon B. Johnson Space Center, Houston, Texas, Tech. Rep. MSC-01855, March 1970.

[29] Trelleborg Slovenija d.o.o., *Conveyor Belts: Catalogue US Version 4.02025*, Trelleborg Seals and Profiles, Kranj, Slovenia, 2025. [Online]. Available: https://www.trelleborg.com/en/seals-and-profiles/products-and-solutions/conveyor-belts/conveyor-belts-brochure

[30] T. Annakulov, M. Dostonbek, and E. Kamoljon, "Application of belt conveyors and determination of the main parameters of mobile complexes for the transportation of overburden rocks of the angren coal mine," *International Journal of Emerging Trends in Engineering Research*, pp. 383–389, 04 2021.

[31] European Space Agency, "Esa-esric space resources challenge field test: DSC_6364," Official ESA Space Resources Challenge Website, 2025, image showing robotic platform equipped with a conveyor-based regolith transport system. [Online]. Available: https://src.esa.int/wp-content/uploads/2025/11/DSC_6364-scaled.jpg

[32] C. Bourdarie, C. Conway, F. Ghaffari, O. Milian, J. Chaussard, C. Lesenne, F. Terranova, M. R. López, and N. Veronese, "Over the dusty moon - how to transport lunar soil," Technical De-Briefing Slides, Cologne, Germany, 2023. [Online]. Available: https://downloads.ctfassets.net/5pl1svt61ugb/2MALDS7xeYbpVhRjUSuSE6/9e645f9b68508e77fd29c9842e84f7a5/002_Spaceship_EAC_Folien.pdf

[33] P. Kulinowski, "Prototype of a conveyor system for the transport of lunar regolith," in *Selected Proceedings of the 6th Space Resources Conference*, A. Kołodziejczyk, J. Pyrkosz-Pacyna, K. Grabowski, K. Malinowska, and O. Sergijenko, Eds. Cham: Springer Nature Switzerland, 2024, pp. 153–170.

[34] S. Salihler, "Space resources handling systems for lunar, martian, and space missions," in *Space Resources Roundtable*, Golden, Colorado, USA, Jun. 2024. [Online]. Available: https://isruinfo.com/public/index.php?page=srr_24#SRR_24_1

[35] European Space Agency, "Esa-esric space resources challenge field test: DSC_7266," Official ESA Space Resources Challenge Website, 2025, image showing robotic platform equipped with a screw-type excavator. [Online]. Available: https://src.esa.int/wp-content/uploads/2025/11/DSC_7266-scaled.jpg

[36] ——, "Esa-esric space resources challenge field test: DSC_0661," Official ESA Space Resources Challenge Website, 2025, image showing robotic platform equipped with a screw-type excavator. [Online]. Available: https://src.esa.int/wp-content/uploads/2025/11/DSC_0661-scaled.jpg

[37] ——, "Esa-esric space resources challenge field test: R.BARBOSA-LUNA-CHALLENGE-T-AM-scaled," Official ESA Space Resources Challenge Website, 2025, image showing robotic platform equipped with a screw-type excavator. [Online]. Available: https://src.esa.int/wp-content/uploads/2025/11/R.BARBOSA-LUNA-CHALLENGE-T-AM-scaled.jpg

[38] A. Olson, J. Mantovani, B. Kemmerer, and J. Gleeson, "Vertical regolith transport system for lunar and mars isru applications," in *Space Resources Roundtable*, Golden, Colorado, USA, Jun. 2022. [Online]. Available: https://isruinfo.com/public/index.php?page=srr_22

[39] Webster Industries, *Vibrating Conveyors*, IPCD Inc., technical Product Brochure. [Online]. Available: http://www.ipcd-inc.com/wp-content/uploads/2016/09/vibrating_conveyors.pdf

[40] H. Kawamoto, "Vibration transport of lunar regolith for in situ resource utilization using piezoelectric actuators with displacement-amplifying mechanism," *Journal of Aerospace Engineering*, vol. 33, no. 3, May 2020.

[41] H. Kawamoto, K. Nogami, and Y. Kadono, "Vibration conveyance of lunar regolith in lunar environment," *Acta Astronautica*, vol. 197, 05 2022.

[42] B. Kemmerer, "Development of the vertical lunar regolith conveyor (VLRC) technology," in *Proceedings of the 75th International Astronautical Congress (IAC)*, ser. IAC-24, no. IAC-24,A3,IP,188,x86197. Milan, Italy: International Astronautical Federation (IAF), October 2024.

[43] D. G. Schrunk, B. L. Sharpe, B. L. Cooper, and M. Thangavelu, *The Moon: Resources, Future Development and Settlement*, second edition ed. Chichester, UK: Praxis Publishing Ltd, 2008.

[44] A. Taschner, "Development of a conveying system for the moon," Master's thesis, Montanuniversität Leoben, Leoben, Austria, August 2021.

[45] K. Birkeland, "Vibratory conveyer," Norway Patent US754 637A, March, 1904. [Online]. Available: https://patents.google.com/patent/US754637A/en

[46] B. C. Eimer and L. A. Taylor, "Lunar regolith, soil, and dust mass mover on the moon," in *38th Lunar and Planetary Science Conference*, ser. LPI Contribution No. 1662. Lunar and Planetary Institute, 2007. [Online]. Available: https://www.lpi.usra.edu/meetings/lpsc2007/pdf/1662.pdf

[47] D. Budzyń, H. Zare-Behtash, A. Cowley, and A. Cammarano, "Implicit lunar dust mitigation technology: Compliant mechanisms," *Acta Astronautica*, vol. 203, pp. 146–156, 2023. [Online]. Available: https://www.sciencedirect.com/science/article/pii/S0094576522006506

[48] C. Calle, C. Buhler, M. Johansen, M. Hogue, and S. Snyder, "Active dust control and mitigation technology for lunar and martian exploration," *Acta Astronautica*, vol. 69, no. 11, pp. 1082–1088, 2011. [Online]. Available: https://www.sciencedirect.com/science/article/pii/S0094576511001883

[49] V. Dananjaya, S. Holmes, R. Simons, P. Kingshott, and N. V Salim, "A review of materials and structures for passive lunar dust mitigation and anticontamination in space and extreme environment applications," *Advanced Composites and Hybrid Materials*, vol. 9, no. 2, p. 189, 2026. [Online]. Available: https://doi.org/10.1007/s42114-026-01725-7

[50] N. Air and S. Museum, "Tongs, long," inventory Number: A19750112000, Accessed: April 26, 2026. [Online]. Available: https://airandspace.si.edu/collection-objects/tongs-long/nasm_A19750112000

[51] J. H. Allton, "Catalog of apollo lunar surface geological sampling tools and containers," Lockheed Engineering and Sciences Company, Houston,

Texas, Tech. Rep. JSC-23454 / LESC-26676, March 1989. [Online]. Available: https://www.lpi.usra.edu/captem/lsac/alltonLunarToolCatalog.pdf

[52] J. W. Carson and G. Y. Wang, "An introduction to flexure design," in *Proceedings of the 47th Aerospace Mechanisms Symposium*. NASA Langley Research Center, 2024, pp. 413–428. [Online]. Available: https://www.esmats.eu/amspapers/pastpapers/pdfs/2024/carson.pdf

[53] X. Pei and J. Yu, "Adlif: a new large-displacement beam-based flexure joint," *Mechanical Sciences*, vol. 2, no. 2, pp. 183–188, 2011. [Online]. Available: https://ms.copernicus.org/articles/2/183/2011/

[54] Thorlabs, Inc., *Amplified Piezoelectric Actuator, 150 V, 2.5 mm Displacement*, 2026, accessed: April 20, 2026. [Online]. Available: https://media.thorlabs.com/globalassets/items/a/ap/apf/apfh720/ctn014508-s01.pdf?v=0116103012

[55] European Space Agency and European Space Resources Innovation Centre, "Extract of the Proposal Evaluation Report," European Space Agency, Tech. Rep., 01 2026, document distributed to teams participating in the field test.

[56] ECSS Secretariat, *Glossary of terms*, European Cooperation for Space Standardization, Noordwijk, The Netherlands, October 2012.

[57] ——, *Space Product Assurance: Availability Analysis*, European Cooperation for Space Standardization, Noordwijk, The Netherlands, July 2008.

[58] D. C. Lagoudas, Ed., *Shape Memory Alloys: Modeling and Engineering Applications*. New York, NY: Springer Science & Business Media, 2008.

[59] Ingpuls Smart Materials and Engineering, "Charakterisierung zyklierter Aktordraht [Characterization of cycled actuator wire]," German Aerospace Center, Institute of Space Systems (DLR), Bremen, Germany, Internal Characterization Report, September 2022, unpublished internal data.

[60] J. H. Lienhard, IV and J. H. Lienhard, V, *A Heat Transfer Textbook*, 4th ed. Mineola, NY: Dover Publications, Dec. 2017. [Online]. Available: https://ahtt.mit.edu

[61] T. Wildi, *Electrical Machines, Drives, and Power Systems*, 6th ed. Harlow: Pearson Education Limited, 2014.

[62] I. Boldea, *Linear Electric Machines, Drives, and MAGLEVs Handbook*, 2nd ed. Boca Raton: CRC Press, 2023.

[63] LinMot, *Produktkatalog Industrielle Linearmotoren*, 24th ed., Spreitenbach, Schweiz, accessed: 2026-04-20. [Online]. Available: https://www.linmot.com/fileadmin//user_upload/Downloads/databooks/LinMot_Datenbuch_d_recent.pdf

[64] H. Janocha, *Actuators: Basics and Applications*, 01 2004.

[65] Cedrat Technologies, *Piezoelectric Actuators: Product and Warranty Information*, Cedrat Technologies, Meylan, France, July 2016, version 6.10. [Online]. Available: https://cedrat-technologies.com/wp-content/uploads/2023/07/inst_man_actuator_v6.1.pdf

[66] X. Jiang, W. B. Cook, and W. S. Hackenberger, "Cryogenic piezoelectric actuators," in *SPIE Proceedings*, vol. 7439. SPIE, 2009, p. 74390Z. [Online]. Available: https://doi.org/10.1117/12.826341

[67] C. Belly, F. Barillot, and F. Dubois, "Piezoelectric actuators and future motors for cryogenic applications in space," in *Proceedings of the 43rd Aerospace Mechanisms Symposium*. NASA Ames Research Center, May 2016, pp. 135–142. [Online]. Available: https://esmats.eu/amspapers/pastpapers/pdfs/2016/belly.pdf

[68] F. Claeyssen, R. Le Letty, F. Barillot, N. Lhermet, and G. Rajeev, "Amplified piezoelectric actuators for air & space applications," in *Proceedings of Aero India 2003*, Bangalore, India, 2003. [Online]. Available: https://metrology-spb.ru/upload-files/CEDRAT_TECHNOLOGIES/English_articles_PDF/Aero_India_2003_Piezo_actuators_air_space.pdf

[69] RNA Automation, *Product Information: RNA Step Feeder STS*, Rhein-Nadel Automation GmbH, 2021, available at: https://www.rnaautomation.com/wp-content/uploads/2021/06/Product-Information-RNA-Step-Feeder-STS-1.pdf (Accessed: April 9, 2026).

[70] T. Tanno, G. Ueki, K. Kikyodani, F. Ito, and T. Nakamura, "Development of a peristaltic mixing conveyor with a radial independently deformable closing mechanism," *IFAC-PapersOnLine*, vol. 59, no. 17, pp. 179–184, 2025, 10th IFAC Symposium on Mechatronic Systems MECHATRONICS 2025. [Online]. Available: https://www.sciencedirect.com/science/article/pii/S2405896325015538

[71] J. E. Huber, N. A. Fleck, and M. F. Ashby, "The selection of mechanical actuators based on performance indices," *Proceedings of the Royal Society A: Mathematical, Physical and Engineering Sciences*, vol. 453, no. 1965, pp. 2185–2205, 10 1997. [Online]. Available: https://doi.org/10.1098/rspa.1997.0117

[72] H. H. Oehmen, "Theory of vibrating conveyors," *Bulk Solids Handling*, vol. 1, no. 2, pp. 245–254, 1981.

[73] P. Seefeldt, "Development and qualification of deployable membranes for space applications," Ph.D. dissertation, Universität Bremen, April 2018. [Online]. Available: https://elib.dlr.de/121938/

[74] K. Matsumoto, M. Suzuki, S.-i. Nishida, and S. Wakabayashi, "Wear of materials in lunar dust environment," vol. 11, 2009. [Online]. Available: http://esmat.esa.int/Materials_News/ISME09/pdf/3-Ground/S3%20-%20Matsumoto.pdf

[75] E. Grossman and I. Gouzman, "Space environment effects on polymers in low earth orbit," *Nuclear Instruments and Methods in Physics Research Section B: Beam Interactions with Materials and Atoms*, vol. 208, pp. 48–57, 2003, ionizing Radiation and Polymers. [Online]. Available: https://www.sciencedirect.com/science/article/pii/S0168583X03006402

[76] Goodfellow, *Kapton® HN Polyimide Film*, Goodfellow Cambridge Ltd., technical Data Sheet, Accessed: April 21, 2026. [Online]. Available: https://www.goodfellow.com

[77] Smiths Metal Centres, *PTFE (Polytetrafluoroethylene) Technical Datasheet*, 2023, technical Datasheet, Accessed: April 21, 2026. [Online]. Available: https://www.smithmetal.com

[78] Specialty Silicone Products, Inc., *SSP2575: Low Outgas, Low Temperature Silicone*, Specialty Silicone Products, Inc., Oct. 2021, technical Data Sheet, Accessed: April 21, 2026. [Online]. Available: https://sspinc.com/wp-content/uploads/2025/02/SSP2575-October-2021.pdf

[79] The Rubber Company, *FFKM Perfluoroelastomer Seals Datasheet*, The Rubber Company, Aug. 2023, technical Data Sheet, Accessed: April 21, 2026. [Online]. Available: https://therubbercompany.com/wp-content/uploads/2023/08/FFKM-Perfluoroelastomer-Seals-Datasheet.pdf

[80] Curbell Plastics, *RTV630*, Curbell Plastics, Nov. 2015, technical Data Sheet, Accessed: April 27, 2026. [Online]. Available: https://www.curbellplastics.com/wp-content/uploads/2022/11/RTV630-Data-Sheet.pdf

[81] M. Laffranchi, N. G. Tsagarakis, F. Cannella, and D. G. Caldwell, "Antagonistic and series elastic actuators: a comparative analysis on the energy consumption," in *Proceedings of the 2009 IEEE/RSJ International Conference on Intelligent Robots and Systems*, ser. IROS'09. IEEE Press, 2009, p. 5678–5684.

[82] K. Schneider, "Experimental characterization of SMA actuator wire," Internal Research Data, DLR Institute of Space Systems, 2025, unpublished test results.

[83] Dynalloy, Inc., *Technical Characteristics of Flexinol Actuator Wires*, Dynalloy, Inc., document No. TCF1140. [Online]. Available: https://cdn.sparkfun.com/datasheets/Components/General/TCF1140.pdf

[84] K. Sasaki, "Push-pull device design and SMA wire characteristics analysis," DLR Institute of Space Systems, Internal Working Paper, 2023, unpublished internal calculations.

[85] T. C. da Silva and E. da Silva, "Emissivity measurements on shape memory alloys," in *Proceedings of the 13th Quantitative InfraRed Thermography Conference (QIRT 2016)*, Gdańsk, Poland, July 2016. [Online]. Available: https://www.ndt.net/article/qirt2016/papers/018.pdf

[86] S. Awtar, A. H. Slocum, and E. Sevincer, "Characteristics of beam-based flexure modules," *J. Mech. Des. N. Y.*, vol. 129, no. 6, pp. 625–639, Jun. 2007.

[87] H. M. Beakawi Al-Hashemi and O. S. Baghabra Al-Amoudi, "A review on the angle of repose of granular materials," *Powder Technology*, vol. 330, pp. 397–417, 2018. [Online]. Available: https://www.sciencedirect.com/science/article/pii/S0032591018301153

[88] C. I. Calle and C. R. Buhler, "Measurement of the Angle of Repose of Apollo 14 Lunar Sample 14163," in *The Impact of Lunar Dust on Human Exploration*, ser. LPI Contributions, vol. 2141, Feb. 2020, p. 5030.

[89] W. D. Carrier, III, J. K. Mitchell, and A. Mahmood, "The relative density of lunar soil," *Lunar and Planetary Science Conference Proceedings*, vol. 4, p. 2403, Jan. 1973.

[90] L. Li and M. Iskander, "Use of machine learning for classification of sand particles," *Acta Geotechnica*, vol. 17, no. 10, pp. 4739–4759, 2022. [Online]. Available: https://doi.org/10.1007/s11440-021-01443-y

[91] H. Heywood, "Particle size and shape distribution for lunar fines sample 12057,72," *Lunar and Planetary Science Conference Proceedings*, vol. 2, p. 1989, Jan. 1971.

[92] ASTM C778-21, "Standard specification for standard sand," ASTM International, West Conshohocken, PA, Tech. Rep., 2021. [Online]. Available: https://www.astm.org/c0778-21.html

[93] G.-C. Cho, J. Dodds, and J. Santamarina, "Particle shape effects on packing density, stiffness, and strength: Natural and crushed sands," *Journal of Geotechnical and Geoenvironmental Engineering*, vol. 132, pp. 591–602, 05 2006.

[94] T. Pöschel and T. Schwager, *Computational granular dynamics: Models and algorithms*. Springer Berlin Heidelberg, 2005.

[95] I. Yardeny, D. Portnikov, and H. Kalman, "Experimental investigation of the coefficient of restitution of particles colliding with surfaces in air and water,"

Advanced Powder Technology, vol. 31, no. 9, pp. 3747–3759, 2020. [Online]. Available: https://www.sciencedirect.com/science/article/pii/S0921883120303563

[96] D. S. McKay, J. L. Carter, W. W. Boles, C. C. Allen, and J. H. Allton, "JSC-1: A New Lunar Regolith Simulant," in *Lunar and Planetary Science Conference*, ser. Lunar and Planetary Science Conference, Mar. 1993, p. 963.

[97] ASM Aerospace Specification Metals Inc. and MatWeb, "Material property data: Aluminum 6061-t6; 6061-t651," 2026, accessed: March 26, 2026. [Online]. Available: https://asm.matweb.com/search/specificmaterial.asp?bassnum=ma6061t6

[98] MatWeb, "Material property data: Basalt," 2026, accessed: March 29, 2026. [Online]. Available: https://www.matweb.com/search/DataSheet.aspx?MatGUID=9642fc0c6767406592332016 27b67b73

[99] H. Gercek, "Poisson's ratio values for rocks," *International Journal of Rock Mechanics and Mining Sciences*, vol. 44, no. 1, pp. 1–13, 2006. [Online]. Available: https://www.sciencedirect.com/science/article/pii/S136516090600075X

[100] K. L. Johnson, *Contact Mechanics*. Cambridge University Press, 1985.

[101] G. R. McDowell and M. D. Bolton, "On the micromechanics of crushable aggregates," *Géotechnique*, vol. 48, no. 5, pp. 667–679, 10 1998. [Online]. Available: https://doi.org/10.1680/geot.1998.48.5.667

[102] J. Wedel, M. Hriberšek, P. Steinmann, and J. Ravnik, "Coefficient of tangential restitution for non-spherical particles," *Powder Technology*, vol. 437, p. 119526, 2024. [Online]. Available: https://www.sciencedirect.com/science/article/pii/S0032591024001682

[103] R. Clift, J. R. Grace, and M. E. Weber, *Bubbles, Drops, and Particles*. New York: Academic Press, 1978.

[104] "Standard Atmosphere," International Organization for Standardization, Geneva, Switzerland, Standard, may 1975.

[105] J. Taylor, *Classical Mechanics*, ser. G - Reference,Information and Interdisciplinary Subjects Series. University Science Books, 2003. [Online]. Available: https://books.google.de/books?id=P1kCtNr-pJsC

[106] M. Pharr, W. Jakob, and G. Humphreys, in *Physically Based Rendering (Third Edition)*, third edition ed., M. Pharr, W. Jakob, and G. Humphreys, Eds. Boston: Morgan Kaufmann, 2017, pp. 401–504. [Online]. Available: https://www.sciencedirect.com/science/article/pii/B9780128006450500075

[107] J. B. Wanscher and M. V. Sørensen, "Drawing a random number," 2006.

[108] B. R. Munson, *Fundamentals of fluid mechanics*. Sixth edition. Hoboken, NJ : John Wiley & Sons, Inc., [2009], 2009. [Online]. Available: https://search.library.wisc.edu/catalog/9910120918002121

[109] A. P. Arya, *Introduction to classical mechanics / Atam P. Arya.* Boston: Allyn and Bacon, 1990.

[110] G. K. Batchelor, *An Introduction to Fluid Dynamics*. Cambridge University Press, 1967. [Online]. Available: https://www.cambridge.org/core/books/an-introduction-to-fluid-dynamics/18AA1576B9C579CE25621E80F9266993

[111] D. E. Goldberg, *Genetic Algorithms in Search, Optimization, and Machine Learning*. New York: Addison-Wesley, 1989.

[112] E. Oberg, F. D. Jones, H. L. Horton, and H. H. Ryffel, *Machinery's Handbook*, 32nd ed., C. J. McCauley and R. M. Heald, Eds. South Norwalk, CT, USA: Industrial Press, 2024.

[113] The MathWorks, Inc., *Global Optimization Toolbox User's Guide: Genetic Algorithm Options*, Natick, MA, USA, 2026, accessed: April 4, 2026. [Online]. Available: https://uk.mathworks.com/help/gads/genetic-algorithm-options.html

[114] ——, *Global Optimization Toolbox: ga (Genetic Algorithm) Function Reference*, Natick, MA, USA, 2026, accessed: April 4, 2026. [Online]. Available: https://uk.mathworks.com/help/gads/ga.html

[115] Quarzwerke GmbH, "Stoffdaten: Quarzsand weferlingen wf 32, wf 33, wf 34," Quarzwerke GmbH, Frechen, Germany, Tech. Rep., 2018, datasheet 1106, www.Quarzwerke.com.

[116] Potters Industries LLC, "MIL-PRF 9954D GLASS BEADS," 2022, accessed: 2026-04-10. [Online]. Available: https://assets.allredi-us.com/documents/potters---glass-beads-MIL-PRF---brochure.pdf

[117] A. Smola and S. V. N. Vishwanathan, *An Introduction to Machine Learning*. Cambridge University Press, 2008. [Online]. Available: https://api.semanticscholar.org/CorpusID:149734561

[118] The MathWorks, Inc., *Global Optimization Toolbox, Multiobjective Optimization: gamultiobj Algorithm*, Natick, MA, USA, 2026, accessed: April 22, 2026. [Online]. Available: https://uk.mathworks.com/help/gads/gamultiobj-algorithm.html

[119] K. Deb, "An efficient constraint handling method for genetic algorithms," *Computer Methods in Applied Mechanics and Engineering*, vol. 186, no. 2, pp. 311–338, 2000. [Online]. Available: https://www.sciencedirect.com/science/article/pii/S0045782599003898

[120] T. L. Bergman, A. S. Lavine, F. P. Incropera, and D. P. DeWitt, *Fundamentals of heat and mass transfer, eigth edition enhanced EPUB*, 8th ed. Nashville, TN: John Wiley & Sons, Nov. 2016.

[121] Fort Wayne Metals, *0.25 mm Nitinol Actuator Wire Datasheet*, Fort Wayne Metals, 2024, accessed: 2026-05-01. [Online]. Available: https://fwmetals.com/media/tm0lsfqa/0-25-mm-actuator-data-sheet.pdf

[122] K. M. Miettinen, *Nonlinear Multiobjective Optimization*. Norwell, Massachusetts, USA: Kluwer Academic Publishers, 1999.

[123] C. Moler, "Performance of the matlab compiler," *MathWorks Technical Articles*, 1996. [Online]. Available: https://uk.mathworks.com/content/dam/mathworks/tag-team/Objects/p/77493_Spr96Cleve.pdf

[124] A. V. Aho, M. S. Lam, R. Sethi, and J. D. Ullman, *Compilers: Principles, Techniques, and Tools (2nd Edition)*, August 2007.

A. Evaluation Matrix

Table A.1: Concept Evaluation Table (c: conformance score, W = weighted conformance score, $w_{max} = 110$

No.	Requirement	w	C1		C2		C3		C4		C5		C6	
			c	W	c	W	c	W	c	W	c	W	c	W
1	**Performance**			**1**		**9**		**18**		**13**		**−2**		**10**
1.1	Feed Rate	3	–	–	–	–	–	–	–	–	–	–	–	–
1.2	Material Loss	2	−1	−2	1	2	2	4	1	2	1	2	−1	−2
1.3	Mass	3	–	–	–	–	–	–	–	–	–	–	–	–
1.4	Power	2	–	–	–	–	–	–	–	–	–	–	–	–
1.5	Dust Generation	2	−1	−2	1	2	2	4	−1	−2	−1	−2	1	2
1.6	*Transportation Direction*													
1.6.1	Horiz. Transportation Dist. (per module)	2	2	4	2	4	2	4	2	4	2	4	2	4
1.6.2	Vert. Transportation Dist. (per module)	2	2	4	2	4	2	4	2	4	−2	−4	2	4
1.6.3	Slope	2	−1	−2	−1	−2	2	4	2	4	−2	−4	2	4
1.7	Flow Continuity	1	−1	−1	−1	−1	−2	−2	1	1	2	2	−2	−2
2	**RAMS**			**6**		**−11**		**−13**		**8**		**8**		**3**
2.1	Reliability	3	1	3	−1	−3	−1	−3	1	3	1	3	1	3
2.2	Availability	3	1	3	−2	−6	−2	−6	1	3	1	3	0	0
2.3	Maintainability	2	0	0	−1	−2	−2	−4	1	2	1	2	0	0
3	**Environmental Conditions**			**18**		**−5**		**−3**		**22**		**30**		**29**
3.1	Ambient Pressure (Vacuum)	3	0	0	−1	−3	−2	−6	0	0	2	6	1	3
3.2	Temperature Range	3	0	0	−1	−3	−2	−6	0	0	2	6	0	0
3.3	Radiation Resilience	3	2	6	−1	−3	−2	−6	2	6	2	6	2	6
3.4	*Flexibility to Input Material*													
3.4.1	Particle Sizes	2	1	2	1	2	2	4	1	2	−1	−2	2	4
3.4.2	Composition	2	2	4	1	2	1	2	1	2	1	2	2	4
3.5	Gravitational Acceleration	3	1	3	0	0	2	6	2	6	2	6	2	6
3.6	Dust Resilience	3	1	3	0	0	1	3	2	6	2	6	2	6
5	**System Architecture**			**14**		**8**		**12**		**12**		**12**		**8**
5.1	Interface to Beneficiation	2	1	2	1	2	2	4	1	2	1	2	−1	−2
5.2	Modularity	2	2	4	−1	−2	1	2	1	2	1	2	1	2
5.3	Scalability	2	1	2	1	2	0	0	1	2	1	2	2	4
5.4	*Geometric Constraints*													

Table A.1 – Continued from previous page

No.	Requirement	w	C 1		C 2		C 3		C 4		C 5		C 6	
			c	W	c	W	c	W	c	W	c	W	c	W
5.4.1	Length	1	2	2	2	2	2	2	2	2	2	2	2	2
5.4.2	Height	1	2	2	2	2	2	2	2	2	2	2	0	0
5.4.3	Width	1	2	2	2	2	2	2	2	2	2	2	2	2
Total Score (weighted)				**39**		**1**		**14**		**55**		**48**		**50**
Total Score (unweighted)				12		−1		6		20		15		16
Relative Score (weighted)				35.5 %		0.9 %		12.7 %		50.0 %		43.6 %		45.5 %

Conformance scale: $c =$ 2 full conformity; $c =$ 1 good conformity; $c =$ 0 partial conformity; $c = -1$ limited conformity; $c = -2$ no conformity.
–: requirement not assessed. Bold W values in category rows are the weighted subtotals for that category. Relative score = $W_{\text{total}}/w_{\text{max}}$.

B. Validation Test Raw Data

Table B.1: Extended raw data for Validation Test 1 (Motion profile from POC tests, Quartz sand)

Run	**Mass Tooth 1 [g]**	**Mass Tooth 2 [g]**	**Mass Tooth 3 [g]**	**Mass Tooth 4 [g]**	**Total Mass [g]**
1	0.50	0.70	0.50	0.30	2.00
2	1.00	0.80	0.50	0.20	2.50
3	0.50	0.80	0.30	0.20	1.80
4	0.70	0.70	0.50	0.20	2.10
5	0.50	0.70	0.30	0.20	1.70
6	0.70	0.70	0.50	0.20	2.10
7	0.50	0.80	0.60	0.20	2.10
8	0.70	0.60	0.50	0.10	1.90
9	0.50	0.60	0.60	0.10	1.80
10	0.50	0.50	0.70	0.20	1.90
μ	**0.61**	**0.69**	**0.50**	**0.19**	**1.99**
σ	**0.16**	**0.10**	**0.12**	**0.06**	**0.22**

Table B.2: Extended raw data for Validation Test 2 (Delayed Downstroke, Quartz sand)

Run	**Mass Tooth 1 [g]**	**Mass Tooth 2 [g]**	**Mass Tooth 3 [g]**	**Mass Tooth 4 [g]**	**Total Mass [g]**
1	0.60	0.80	0.40	0.10	1.90
2	0.70	0.50	0.60	0.10	1.90
3	0.50	0.70	0.60	0.10	1.90
4	0.40	0.70	0.30	0.30	1.70
5	0.70	0.50	0.60	0.10	1.90
6	0.70	0.40	0.50	0.30	1.90
7	0.50	0.70	0.50	0.40	2.10
8	1.00	0.40	0.60	0.10	2.10
9	0.80	0.40	0.60	0.10	1.90
10	1.10	0.40	0.50	0.10	2.10
μ	**0.70**	**0.55**	**0.52**	**0.17**	**1.94**
σ	**0.22**	**0.15**	**0.10**	**0.12**	**0.13**

Table B.3: Extended raw data for Validation Test 3 (Delayed Downstroke, Glass beads)

Run	**Mass Tooth 1 [g]**	**Mass Tooth 2 [g]**	**Mass Tooth 3 [g]**	**Mass Tooth 4 [g]**	**Total Mass [g]**	**Input Mass [g]**	**Retrieved Fraction**
1	0.94	0.49	0.41	0.05	1.89	2.00	0.945
2	0.94	0.59	0.33	0.07	1.93	1.96	0.985
3	0.86	0.64	0.46	0.06	2.02	2.06	0.981
4	0.68	0.69	0.50	0.08	1.95	2.00	0.975
5	0.82	0.68	0.35	0.07	1.92	2.00	0.960
6	0.73	0.73	0.38	0.08	1.92	1.97	0.975
7	0.85	0.68	0.45	0.07	2.05	2.02	1.015
8	0.71	0.74	0.40	0.05	1.90	2.01	0.945
9	0.92	0.68	0.36	0.10	2.06	2.06	1.000
10	0.85	0.65	0.43	0.06	1.99	2.01	0.990
μ	**0.83**	**0.66**	**0.41**	**0.07**	**1.96**	**2.01**	**0.977**
σ	**0.10**	**0.07**	**0.06**	**0.02**	**0.06**	**0.03**	**0.022**

C. Optimisation Results

C.1 Repeatability Study

Table C.1: Mean, standard deviation, and coefficient of variation of optimised design parameters across 45 independent runs per environment. ω is converted from radians to degrees.

	Lunar			Terrestrial		
Parameter	Mean	Std	CoV (%)	Mean	Std	CoV (%)
l_c in mm	47.82	0.48	1.00	48.84	0.80	1.63
l_a in mm	46.21	0.62	1.35	46.63	0.87	1.86
l_b in mm	30.05	0.80	2.66	32.65	0.88	2.70
r in mm	37.27	1.27	3.40	36.47	0.85	2.33
ω in $^\circ$	91.51	1.17	1.28	83.49	3.14	3.76
δ in $^\circ$	11.04	0.47	4.26	13.01	0.85	6.53
v_0 in m/s	0.85	0.05	5.34	1.98	0.02	1.26
a in m/s^2	27.80	8.45	30.4	20.40	0.38	1.85
f_{stroke} in Hz	0.036	9.9×10^{-5}	0.275	0.034	7.2×10^{-5}	0.21
l_{stroke} in mm	13.97	3.46	24.7	96.34	3.00	3.11
d_{avg} in mm	152.3	13.8	9.07	106.0	3.3	3.14
n_{wire}	28.93	8.61	29.8	23.78	0.64	2.67

C.2 Sensitivity Analysis

Table C.2: Sensitivity study results for lunar conditions ($g = 1.625$ m/s^2, $\alpha = 35$ř, AOR $= 58$ř, $\mu_{\text{drag}} = 0$) across the 5×5 parameter grid ($\mu_{\text{fric}} \in [0.0954, 0.1166]$, $k_{\text{elastic}} \in [0.7848, 0.9592]$). Each row gives the Pareto-optimal solution closest to the lunar target mass flow $\dot{m} = 0.022$ kg/s. $\bar{d}$: average particle transport distance per stroke; n_{w}: number of SMA actuator wires required.

μ_{fric}	k_{elastic}	$\dot{m}$ (kg/h)	W_{spec} (J/kg)	f_{stroke} (Hz)	stroke (m)	$\bar{d}$ (m)	n_{w}
0.0954	0.7848	80.04	478.7	0.0358	0.0184	0.2027	25
0.0954	0.8284	79.56	471.1	0.0357	0.0195	0.2053	23
0.0954	0.8720	82.61	599.9	0.0356	0.0259	0.2206	23
0.0954	0.9156	80.79	974.5	0.0351	0.0437	0.2255	22
0.0954	0.9592	77.10	1053.2	0.0351	0.0451	0.2045	22
0.1007	0.7848	82.49	489.0	0.0358	0.0166	0.2179	29
0.1007	0.8284	78.99	459.7	0.0360	0.0111	0.1955	39
0.1007	0.8720	81.10	594.9	0.0356	0.0232	0.2140	25
0.1007	0.9156	76.72	672.7	0.0356	0.0239	0.2072	26
0.1007	0.9592	79.58	864.7	0.0354	0.0320	0.2167	26
0.1060	0.7848	80.04	425.0	0.0361	0.0086	0.1990	47
0.1060	0.8284	79.15	475.5	0.0358	0.0161	0.1898	28
0.1060	0.8720	79.96	568.4	0.0356	0.0261	0.2140	21
0.1060	0.9156	75.53	742.9	0.0355	0.0295	0.2032	23
0.1060	0.9592	77.65	894.3	0.0353	0.0351	0.2136	24
0.1113	0.7848	79.60	433.0	0.0360	0.0105	0.1966	39
0.1113	0.8284	78.41	527.6	0.0357	0.0226	0.2041	22
0.1113	0.8720	82.26	607.7	0.0355	0.0274	0.2185	22
0.1113	0.9156	86.52	857.6	0.0351	0.0431	0.2422	21
0.1113	0.9592	78.78	2098.4	0.0337	0.1000	0.2337	21
0.1166	0.7848	75.38	473.2	0.0358	0.0164	0.1844	26
0.1166	0.8284	78.99	505.0	0.0357	0.0208	0.2065	23
0.1166	0.8720	80.72	611.4	0.0355	0.0270	0.2161	22
0.1166	0.9156	77.78	718.6	0.0354	0.0307	0.2136	22
0.1166	0.9592	71.79	879.5	0.0353	0.0365	0.1974	21

Table C.3: Sensitivity study results for terrestrial conditions ($g = 9.81$ m/s^2, $\alpha = 35$ř, AOR $= 34$ř) across the $3 \times 3 \times 3$ parameter grid ($\mu_{\text{fric}} \in [0.0954, 0.1166]$, $k_{\text{elastic}} \in [0.7848, 0.9592]$, $\mu_{\text{drag}} \in [4.895, 5.983]$). Each row gives the Pareto-optimal solution closest to the terrestrial target mass flow $\dot{m} = 0.008$ kg/s. $\bar{d}$: average particle transport distance per stroke; n_{w}: number of SMA actuator wires required.

μ_{fric}	k_{elastic}	μ_{drag}	$\dot{m}$ (kg/h)	W_{spec} (J/kg)	f_{stroke} (Hz)	stroke (m)	$\bar{d}$ (m)	n_{w}
0.0954	0.7848	4.8951	28.77	5748	0.0337	0.1000	0.1196	21
0.0954	0.7848	5.4390	28.79	5453	0.0341	0.0859	0.0999	23
0.0954	0.7848	5.9829	28.84	6278	0.0337	0.1000	0.0994	23
0.0954	0.8720	4.8951	28.86	5251	0.0341	0.0827	0.0996	23
0.0954	0.8720	5.4390	28.46	5590	0.0341	0.0832	0.0970	24
0.0954	0.8720	5.9829	29.05	5677	0.0341	0.0828	0.0941	25
0.0954	0.9592	4.8951	28.91	6258	0.0338	0.0954	0.0989	24
0.0954	0.9592	5.4390	28.64	6158	0.0338	0.0972	0.1011	23
0.0954	0.9592	5.9829	28.77	6565	0.0337	0.0999	0.0955	24
0.1060	0.7848	4.8951	28.81	5908	0.0338	0.0981	0.1104	22
0.1060	0.7848	5.4390	28.83	5596	0.0340	0.0884	0.1014	23
0.1060	0.7848	5.9829	28.64	5382	0.0341	0.0842	0.0980	23
0.1060	0.8720	4.8951	28.88	5168	0.0343	0.0778	0.0970	24
0.1060	0.8720	5.4390	28.50	5637	0.0340	0.0880	0.0998	23
0.1060	0.8720	5.9829	28.44	6144	0.0338	0.0962	0.0991	23
0.1060	0.9592	4.8951	28.95	6250	0.0337	0.0999	0.1077	23
0.1060	0.9592	5.4390	28.71	5352	0.0341	0.0839	0.1071	23
0.1060	0.9592	5.9829	27.40	6044	0.0338	0.0953	0.1047	22
0.1166	0.7848	4.8951	28.78	5740	0.0341	0.0866	0.0995	24
0.1166	0.7848	5.4390	28.79	6242	0.0338	0.0992	0.1019	23
0.1166	0.7848	5.9829	28.82	6253	0.0337	0.0995	0.1007	23
0.1166	0.8720	4.8951	28.84	5994	0.0337	0.0998	0.1136	22
0.1166	0.8720	5.4390	28.76	5978	0.0339	0.0946	0.1000	23
0.1166	0.8720	5.9829	29.19	6470	0.0337	0.0999	0.0962	24
0.1166	0.9592	4.8951	28.83	5333	0.0341	0.0839	0.1042	23
0.1166	0.9592	5.4390	28.72	5574	0.0340	0.0876	0.1028	23
0.1166	0.9592	5.9829	28.04	5844	0.0340	0.0898	0.1053	23

C.3 Conveyor Angle Analysis

Table C.4: Pareto Optimal Results for Lunar Mission Analysis (Alpha Sweep)

f_{stroke}	W_{spec} (J)	l_c	l_a	l_b	r	ω	δ	v_0	a	$\dot{m}$	l_{stroke}	n_{wire}	d_{avg}	Source
0.036	605.017	47.552	46.480	29.440	36.114	1.599	10.681	1.082	21.060	0.022	0.028	21	0.215	1
0.036	587.190	47.803	46.192	30.465	38.287	1.607	10.976	1.033	22.757	0.021	0.023	23	0.204	2
0.036	533.419	47.385	45.718	29.717	37.924	1.625	11.255	0.978	23.574	0.021	0.020	24	0.198	3
0.035	696.570	48.261	46.252	30.055	36.304	1.579	11.025	1.155	21.013	0.022	0.032	21	0.214	4
0.036	539.921	47.275	44.522	28.823	36.707	1.622	10.883	1.008	25.098	0.022	0.020	25	0.212	5
0.036	583.524	48.532	46.429	29.847	36.743	1.599	10.641	1.050	21.014	0.022	0.026	21	0.212	6
0.036	542.283	48.572	46.800	29.650	36.687	1.602	11.300	1.013	21.925	0.022	0.023	22	0.214	7
0.036	509.345	48.755	47.531	30.841	38.319	1.598	11.146	0.964	22.397	0.022	0.021	23	0.203	8
0.036	536.300	47.523	46.839	31.040	40.652	1.631	11.249	0.981	21.912	0.022	0.022	23	0.197	9
0.036	654.310	47.934	45.598	28.982	37.139	1.624	11.011	1.121	22.025	0.022	0.029	22	0.224	10
0.036	555.947	47.436	45.611	29.488	36.553	1.603	11.220	1.009	21.455	0.022	0.024	22	0.206	11
0.036	627.071	47.564	45.601	30.860	39.050	1.604	10.360	1.074	21.947	0.022	0.026	23	0.204	12
0.036	555.498	47.372	45.471	29.901	37.968	1.616	10.766	1.014	21.395	0.022	0.024	22	0.207	13
0.036	453.020	49.231	48.095	32.699	41.327	1.605	12.122	0.864	40.215	0.021	0.009	44	0.180	14
0.035	640.995	47.573	45.578	28.863	35.632	1.604	9.708	1.098	20.942	0.022	0.029	21	0.217	15
0.036	581.187	48.712	45.873	29.874	36.507	1.590	10.970	1.011	20.611	0.022	0.025	22	0.208	16
0.036	578.547	48.610	47.040	30.165	37.354	1.602	10.557	1.042	23.700	0.022	0.023	24	0.213	17
0.036	595.631	47.263	46.569	29.668	37.281	1.615	10.907	1.047	20.454	0.022	0.027	21	0.210	18
0.036	581.056	47.361	46.152	30.236	36.017	1.566	10.743	1.060	20.215	0.023	0.028	21	0.219	19
0.036	602.323	48.541	45.579	29.043	36.199	1.609	10.601	1.065	23.789	0.022	0.024	24	0.219	20
0.036	593.281	47.545	45.435	29.982	36.337	1.576	10.671	1.039	21.154	0.022	0.025	22	0.206	21
0.036	491.046	47.597	45.749	29.047	36.551	1.613	10.866	0.920	21.564	0.020	0.020	22	0.197	22
0.036	591.968	47.276	45.610	29.097	36.412	1.611	11.086	1.053	21.536	0.022	0.026	22	0.215	23
0.036	550.505	47.611	45.991	29.320	36.631	1.611	11.233	0.997	22.149	0.022	0.022	23	0.207	24
0.036	584.999	47.253	46.315	29.963	37.114	1.597	10.887	1.027	23.210	0.022	0.023	24	0.206	25
0.036	564.990	47.316	45.710	29.789	36.889	1.599	11.277	1.062	21.924	0.024	0.026	23	0.229	26
0.036	610.509	48.087	45.280	29.739	36.300	1.583	10.514	1.067	20.601	0.022	0.028	21	0.216	27
0.036	560.427	49.314	47.191	30.437	37.860	1.605	11.088	0.998	21.744	0.022	0.023	23	0.202	28
0.036	603.846	47.033	45.804	29.722	37.399	1.610	10.918	1.057	21.125	0.022	0.026	22	0.214	29
0.036	570.413	48.390	45.541	29.602	38.409	1.637	11.223	1.036	21.173	0.023	0.025	22	0.217	30
0.036	616.205	47.320	45.388	29.246	37.492	1.621	10.547	1.052	21.310	0.021	0.026	22	0.209	31
0.036	563.449	47.582	46.506	29.692	36.413	1.598	10.691	1.013	25.820	0.022	0.020	27	0.211	32
0.035	661.079	48.176	45.626	28.730	36.597	1.630	10.107	1.110	20.637	0.022	0.030	21	0.223	33
0.036	534.211	48.324	46.248	29.912	36.183	1.573	11.228	0.988	22.352	0.022	0.022	23	0.213	34

Table C.4 – Continued from previous page

f_{stroke}	W_{spec} (J)	l_c	l_a	l_b	r	ω	δ	v_0	a	$\dot{m}$	l_{stroke}	n_{wire}	d_{avg}	Source
0.036	658.804	47.295	44.524	28.339	35.966	1.622	11.108	1.059	24.384	0.020	0.023	25	0.200	35
0.036	664.665	47.426	46.255	29.744	36.038	1.586	10.881	1.104	23.041	0.022	0.026	24	0.211	36
0.036	596.733	47.400	45.055	28.482	36.044	1.622	11.220	1.049	22.303	0.022	0.025	23	0.216	37
0.036	658.689	47.536	46.185	29.845	38.198	1.622	11.004	1.092	22.592	0.022	0.026	24	0.210	38
0.036	597.050	48.241	45.621	29.127	36.691	1.618	10.694	1.051	21.375	0.022	0.026	22	0.219	39
0.036	540.158	47.431	46.497	30.551	39.035	1.616	11.268	0.984	24.245	0.022	0.020	26	0.206	40

Table C.5: Pareto Optimal Results for Terrestrial Mission Analysis (Alpha Sweep)

f_{stroke}	W_{spec} (J)	l_c	l_a	l_b	r	ω	δ	v_0	a	$\dot{m}$	l_{stroke}	n_{wire}	d_{avg}	Source
0.034	4630.636	48.056	45.342	31.193	37.524	1.442	11.923	2.000	20.126	0.008	0.099	17	0.112	1
0.034	4901.805	48.347	46.288	31.357	36.486	1.502	12.142	2.000	20.155	0.008	0.099	18	0.103	2
0.034	4395.284	49.160	45.682	32.143	37.582	1.496	14.389	1.832	20.294	0.008	0.083	19	0.094	3
0.034	4644.263	47.569	45.085	32.661	36.319	1.443	12.400	1.884	20.072	0.008	0.088	19	0.094	4
0.034	4715.898	49.697	48.447	33.739	36.757	1.385	12.691	1.910	20.198	0.008	0.090	19	0.099	5
0.034	4770.333	49.326	46.206	31.868	35.788	1.463	12.477	1.930	20.264	0.008	0.092	19	0.100	6
0.034	5203.543	48.989	45.604	32.804	36.538	1.426	11.472	2.000	20.001	0.008	0.100	19	0.099	7
0.034	5174.465	49.272	46.419	31.495	37.232	1.514	11.000	1.999	20.026	0.008	0.100	19	0.102	8
0.034	4708.680	48.986	48.258	34.044	37.485	1.389	14.263	1.879	20.707	0.008	0.085	20	0.098	9
0.034	4542.495	49.191	46.375	32.195	36.373	1.488	12.411	1.831	20.289	0.008	0.083	20	0.096	10
0.034	5129.337	47.327	46.081	32.071	37.152	1.492	12.983	1.931	20.106	0.008	0.093	20	0.096	11
0.034	5475.571	48.917	45.666	31.759	36.394	1.456	12.345	2.000	20.000	0.008	0.100	20	0.103	12
0.034	5259.530	47.409	45.878	32.072	35.907	1.389	14.723	1.994	20.696	0.008	0.096	20	0.104	13
0.034	4529.981	49.281	45.978	33.028	36.575	1.451	13.899	1.776	20.195	0.008	0.078	21	0.092	14
0.034	5063.971	47.556	45.534	32.191	36.231	1.396	14.677	1.928	20.129	0.008	0.092	20	0.101	15
0.034	5425.228	49.046	45.477	32.748	36.415	1.368	12.486	1.999	20.105	0.008	0.099	20	0.104	16
0.034	5462.127	49.130	45.597	30.795	37.281	1.486	12.227	2.000	20.003	0.008	0.100	20	0.108	17
0.034	5367.491	49.320	47.447	32.006	36.632	1.495	12.201	1.947	20.260	0.008	0.094	21	0.099	18
0.034	5480.053	48.413	46.964	30.729	37.650	1.537	12.979	2.000	20.000	0.008	0.100	20	0.107	19
0.034	5099.305	47.353	45.900	31.715	35.568	1.437	12.843	1.905	21.572	0.008	0.084	22	0.102	20
0.034	5349.836	48.951	46.278	31.906	39.312	1.407	12.324	1.998	20.361	0.008	0.098	20	0.113	21
0.034	5649.561	49.633	46.358	32.168	38.190	1.438	12.573	1.997	20.173	0.008	0.099	21	0.105	22
0.034	5966.438	47.857	47.167	31.908	36.050	1.499	13.593	2.000	20.030	0.008	0.100	22	0.101	23
0.034	5725.472	48.675	45.283	30.825	35.975	1.501	12.053	2.000	20.000	0.008	0.100	21	0.104	24
0.034	5740.415	48.795	46.045	31.615	38.832	1.508	10.964	2.000	20.002	0.008	0.100	21	0.105	25
0.034	5265.078	49.184	47.066	33.188	37.383	1.431	13.023	1.869	20.070	0.008	0.087	22	0.098	26
0.034	5502.962	49.384	45.940	32.475	35.545	1.462	13.316	1.886	20.551	0.008	0.087	23	0.093	27
0.034	5256.731	49.572	47.034	32.566	37.613	1.435	13.484	1.865	20.266	0.008	0.086	22	0.099	28
0.034	5189.573	49.475	47.169	34.205	36.908	1.377	14.478	1.808	20.915	0.008	0.078	24	0.094	29
0.034	5315.227	47.337	46.593	32.949	36.515	1.337	13.158	1.896	20.672	0.008	0.087	22	0.106	30
0.034	6010.656	48.132	44.609	31.034	35.197	1.489	10.828	2.000	20.053	0.008	0.100	22	0.103	31
0.034	5702.329	49.165	45.808	32.563	36.740	1.413	12.500	1.937	20.769	0.008	0.090	23	0.102	32
0.034	5458.874	49.334	47.414	33.205	37.160	1.392	12.801	1.887	20.818	0.008	0.086	23	0.101	33
0.034	5834.954	49.301	45.798	32.779	35.559	1.373	12.493	1.943	20.446	0.008	0.092	23	0.101	34

Table C.5 – Continued from previous page

f_{stroke}	W_{spec} (J)	l_c	l_a	l_b	r	ω	δ	v_0	a	$\dot{m}$	l_{stroke}	n_{wire}	d_{avg}	Source
0.034	6263.462	48.867	44.646	31.033	37.824	1.554	11.167	1.999	20.095	0.008	0.099	23	0.099	35
0.034	6244.084	47.939	46.613	33.052	36.592	1.423	12.450	2.000	20.072	0.008	0.100	23	0.102	36
0.034	5694.143	47.787	45.750	32.370	37.089	1.397	13.179	1.944	20.989	0.008	0.090	23	0.108	37
0.034	5362.894	49.222	47.551	35.194	38.548	1.362	14.314	1.803	21.229	0.008	0.077	25	0.092	38
0.034	5710.485	49.420	48.158	32.684	37.326	1.395	12.475	1.926	20.583	0.008	0.090	23	0.107	39
0.034	5729.184	49.530	47.224	31.848	36.710	1.516	13.052	1.864	20.114	0.008	0.086	24	0.096	40

C.4 Ultimate Pareto-optimal Solutions

Table C.6: Pareto Optimal Results for Lunar Mission Analysis

f_{stroke}	W_{spec} (J)	l_c	l_a	l_b	r	ω	δ	v_0	a	$\dot{m}$	l_{stroke}	n_{wire}	d_{avg}	Source
0.034	835.014	48.851	45.980	31.800	36.386	1.518	10.708	2.000	20.000	0.053	0.100	22	0.508	Rep_016
0.034	807.459	48.851	45.980	31.801	36.386	1.518	10.708	2.000	20.000	0.056	0.100	22	0.538	Rep_016
0.034	775.037	46.518	42.308	24.894	32.521	1.647	10.525	2.000	20.000	0.051	0.100	19	0.630	Rep_001
0.034	747.764	48.665	45.751	29.918	35.550	1.564	10.566	2.000	20.000	0.053	0.100	21	0.542	Rep_013
0.034	735.654	48.578	46.139	29.702	36.792	1.596	10.634	2.000	20.000	0.055	0.100	21	0.572	Rep_021
0.034	695.011	48.578	46.139	29.702	36.793	1.596	10.634	2.000	20.000	0.055	0.100	21	0.567	Rep_021
0.034	680.123	48.578	46.139	29.703	36.793	1.595	10.634	2.000	20.000	0.062	0.100	21	0.639	Rep_021
0.034	677.309	48.578	46.138	29.702	36.791	1.596	10.634	2.000	20.000	0.064	0.100	21	0.658	Rep_021
0.034	673.740	48.578	46.139	29.703	36.795	1.596	10.634	2.000	20.000	0.058	0.100	21	0.600	Rep_021
0.034	671.529	47.927	45.582	30.129	36.224	1.572	10.656	2.000	20.000	0.055	0.100	21	0.567	HF
0.034	670.090	47.927	45.582	30.129	36.224	1.572	10.656	2.000	20.000	0.061	0.100	21	0.629	HF
0.034	648.110	47.927	45.582	30.129	36.224	1.572	10.656	2.000	20.000	0.050	0.100	21	0.513	HF
0.034	633.415	47.927	45.581	30.129	36.223	1.572	10.656	2.000	20.000	0.059	0.100	21	0.611	HF
0.034	603.233	48.652	45.846	29.848	39.579	1.645	10.805	2.000	20.000	0.066	0.100	21	0.670	Rep_028
0.034	592.784	48.644	45.763	29.834	39.005	1.637	10.801	2.000	20.001	0.064	0.100	21	0.650	Rep_028
0.034	588.799	47.510	46.001	30.386	40.422	1.647	10.809	2.000	20.348	0.066	0.098	22	0.644	Rep_028
0.034	588.044	48.659	46.495	30.725	40.659	1.648	10.882	1.994	20.292	0.066	0.098	22	0.646	Rep_028
0.034	576.950	47.452	47.005	30.678	41.010	1.648	10.810	2.000	20.429	0.071	0.098	22	0.688	Rep_028
0.034	575.372	47.451	47.005	30.678	41.010	1.647	10.810	1.999	20.429	0.075	0.098	22	0.732	Rep_028
0.034	573.292	47.477	47.058	31.288	41.500	1.648	10.816	1.999	21.167	0.075	0.094	23	0.709	Rep_028
0.034	565.115	47.403	46.770	31.042	41.172	1.647	10.953	1.990	21.069	0.073	0.094	23	0.693	Rep_028
0.034	543.618	47.617	47.290	31.775	42.461	1.647	10.841	1.987	21.897	0.076	0.090	24	0.702	Rep_028
0.035	538.958	47.390	47.157	31.830	42.526	1.648	10.966	1.838	26.712	0.064	0.063	29	0.582	Rep_028
0.035	533.539	47.302	45.701	29.557	38.545	1.642	11.323	1.549	21.858	0.044	0.055	23	0.424	Rep_039
0.035	531.188	47.345	46.982	32.130	43.044	1.647	11.281	1.589	23.068	0.051	0.055	26	0.454	Rep_028
0.035	520.472	47.542	46.998	31.248	41.679	1.646	11.173	1.443	22.923	0.043	0.045	25	0.393	Rep_028
0.035	518.741	47.555	46.614	31.024	38.817	1.604	11.061	1.377	22.198	0.037	0.043	24	0.343	Rep_013
0.035	501.899	47.348	47.184	32.113	43.553	1.647	11.730	1.461	27.797	0.044	0.038	31	0.388	Rep_028
0.036	497.557	47.489	46.820	31.991	42.382	1.635	11.405	1.084	22.485	0.027	0.026	25	0.235	Rep_028
0.036	488.759	47.537	46.713	31.708	42.230	1.644	11.509	1.103	23.668	0.026	0.026	26	0.231	Rep_028
0.036	476.200	47.543	46.896	30.512	37.971	1.604	10.878	1.026	21.387	0.022	0.025	23	0.204	Rep_001
0.036	470.211	48.759	47.303	31.310	38.569	1.592	11.435	0.939	21.336	0.021	0.021	23	0.193	Rep_009
0.036	456.272	47.528	46.770	31.924	42.082	1.635	11.409	0.955	22.672	0.023	0.020	25	0.202	Rep_028

Continued on next page

Table C.6 – Continued from previous page

f_{stroke}	W_{spec} (J)	l_c	l_a	l_b	r	ω	δ	v_0	a	$\dot{m}$	l_{stroke}	n_{wire}	d_{avg}	Source
0.036	448.077	47.428	46.821	32.049	42.528	1.635	11.429	0.914	22.684	0.021	0.018	25	0.179	Rep_028
0.036	446.696	47.428	46.821	32.049	42.528	1.635	11.429	0.914	22.684	0.022	0.018	25	0.189	Rep_028
0.036	445.658	47.521	46.691	30.359	36.684	1.581	11.389	0.848	21.627	0.016	0.017	23	0.151	Rep_035
0.036	443.220	48.532	46.994	30.616	38.566	1.612	10.914	0.826	21.788	0.016	0.016	23	0.148	Rep_001
0.036	442.971	47.520	46.285	29.936	36.299	1.585	11.285	0.819	22.833	0.017	0.015	24	0.162	Rep_030
0.036	440.015	47.583	45.807	30.037	38.503	1.626	11.528	0.861	25.443	0.018	0.015	27	0.166	Rep_019
0.036	439.968	48.539	47.107	31.509	38.330	1.577	11.526	0.841	25.348	0.018	0.014	27	0.160	Rep_022
0.036	437.715	47.354	45.777	29.844	36.580	1.592	11.229	0.811	23.862	0.016	0.014	25	0.153	HF
0.036	430.935	47.585	47.047	31.412	40.512	1.615	11.496	0.829	25.040	0.019	0.014	27	0.171	Rep_028
0.036	418.419	47.350	46.899	32.188	43.681	1.650	11.969	0.847	32.052	0.019	0.011	35	0.166	Rep_028
0.036	417.258	47.346	46.898	32.184	43.687	1.648	11.964	0.840	32.052	0.019	0.011	35	0.160	Rep_028
0.036	415.291	47.349	46.898	32.180	43.691	1.650	11.966	0.840	32.053	0.019	0.011	35	0.162	Rep_028
0.036	412.715	47.346	46.898	32.184	43.687	1.648	11.964	0.840	32.052	0.020	0.011	35	0.168	Rep_028
0.036	410.712	47.346	46.898	32.183	43.687	1.648	11.964	0.840	32.051	0.020	0.011	35	0.168	Rep_028

Table C.7: Pareto Optimal Results for Terrestrial Mission Analysis

f_{stroke}	W_{spec} (J)	l_c	l_a	l_b	r	ω	δ	v_0	a	$\dot{m}$	l_{stroke}	n_{wire}	d_{avg}	Source
0.034	5816.741	49.023	46.285	32.564	35.802	1.344	11.464	2.000	20.000	0.008	0.100	22	0.106	HF
0.034	5771.169	49.023	46.285	32.563	35.802	1.344	11.464	2.000	20.000	0.008	0.100	22	0.104	HF
0.034	5738.536	49.023	46.285	32.563	35.801	1.344	11.464	2.000	20.000	0.008	0.100	22	0.108	HF
0.034	5695.558	49.023	46.285	32.563	35.801	1.344	11.464	2.000	20.000	0.008	0.100	22	0.107	HF
0.034	5602.455	49.023	46.285	32.563	35.801	1.344	11.464	2.000	20.000	0.008	0.100	22	0.109	HF
0.034	5599.469	49.301	45.894	31.414	36.445	1.524	10.872	2.000	20.000	0.008	0.100	23	0.103	Rep_010
0.034	5521.947	48.142	46.653	31.438	36.050	1.524	13.225	2.000	20.000	0.008	0.100	23	0.104	Rep_034
0.034	5459.517	49.095	46.592	33.042	36.740	1.425	12.563	2.000	20.013	0.008	0.100	23	0.104	Rep_016
0.034	5457.113	49.094	46.973	33.225	35.555	1.388	12.891	1.999	20.049	0.009	0.100	23	0.107	HF
0.034	5391.565	49.616	47.366	34.969	36.505	1.325	13.776	1.995	20.256	0.009	0.098	24	0.106	Rep_040
0.034	5355.478	49.424	46.484	34.145	37.237	1.405	14.234	1.984	20.095	0.009	0.098	24	0.099	Rep_011
0.034	5342.939	49.668	47.581	32.555	36.197	1.481	13.496	1.987	20.537	0.009	0.096	24	0.105	Rep_008
0.034	5285.775	49.402	47.428	34.940	35.884	1.389	13.059	1.961	20.320	0.009	0.095	25	0.102	HF
0.034	5273.872	49.605	49.032	33.647	37.754	1.502	12.203	1.906	20.012	0.008	0.091	24	0.093	Rep_027
0.034	5272.120	49.593	49.060	33.696	37.723	1.496	11.937	1.896	20.019	0.009	0.090	24	0.098	Rep_027
0.034	5262.734	49.353	47.447	33.642	35.520	1.395	13.096	1.925	20.647	0.009	0.090	24	0.101	HF
0.034	5165.479	49.274	47.619	34.211	37.278	1.409	14.463	1.910	20.338	0.009	0.090	24	0.102	Rep_023
0.034	5145.676	49.522	47.800	34.052	35.168	1.379	13.227	1.898	20.328	0.008	0.089	24	0.098	HF
0.034	5139.389	49.435	46.756	34.326	36.854	1.352	14.175	1.879	20.536	0.008	0.086	24	0.094	Rep_011
0.034	5120.996	49.511	47.750	33.859	35.288	1.360	13.478	1.868	20.339	0.008	0.086	24	0.095	HF
0.034	5049.984	49.419	48.268	34.110	35.752	1.381	12.421	1.864	20.536	0.008	0.085	24	0.097	HF
0.034	5027.977	49.152	47.971	36.210	38.331	1.317	15.418	1.833	20.132	0.008	0.083	24	0.096	Rep_043
0.034	5005.690	49.674	47.052	34.660	36.646	1.329	13.880	1.832	20.668	0.008	0.081	24	0.096	Rep_011
0.034	4940.767	49.533	47.688	34.118	35.080	1.379	13.197	1.783	20.307	0.008	0.078	24	0.093	HF
0.034	4908.083	49.306	47.741	34.322	36.959	1.280	13.981	1.772	20.567	0.007	0.076	23	0.087	Rep_040
0.034	4886.524	49.490	48.749	33.431	37.459	1.400	13.207	1.747	20.055	0.007	0.076	23	0.092	Rep_027
0.034	4847.596	49.568	47.731	33.061	35.135	1.359	13.718	1.760	20.455	0.007	0.076	23	0.093	Rep_009
0.034	4762.443	49.657	48.843	33.715	35.920	1.291	14.211	1.770	21.146	0.007	0.074	23	0.092	Rep_016
0.034	4760.381	49.494	46.936	33.988	36.413	1.121	15.136	1.728	21.144	0.006	0.071	22	0.081	Rep_011
0.034	4696.327	49.581	46.842	34.281	36.571	1.335	14.155	1.695	20.551	0.007	0.070	24	0.083	Rep_011
0.035	4585.312	49.291	48.016	33.907	35.637	1.294	13.548	1.667	20.737	0.007	0.067	23	0.089	HF
0.035	4542.619	49.295	48.109	33.254	36.217	1.297	12.796	1.640	21.570	0.007	0.062	23	0.090	Rep_035
0.035	4508.207	49.338	47.977	35.298	36.071	1.094	16.756	1.578	20.381	0.006	0.061	22	0.080	Rep_043
0.035	4497.035	49.523	48.305	33.686	36.570	1.276	12.920	1.558	21.592	0.006	0.056	23	0.080	Rep_035

Table C.7 – Continued from previous page

f_{stroke}	W_{spec} (J)	l_c	l_a	l_b	r	ω	δ	v_0	a	$\dot{m}$	l_{stroke}	n_{wire}	d_{avg}	Source
0.035	4491.712	49.481	48.765	34.642	37.495	1.296	14.441	1.521	20.658	0.006	0.056	23	0.079	Rep_040
0.035	4469.274	49.481	48.765	34.642	37.495	1.296	14.441	1.521	20.658	0.006	0.056	23	0.076	Rep_040
0.035	4437.308	49.637	47.434	34.839	38.537	1.161	14.481	1.494	20.337	0.006	0.055	22	0.079	Rep_043
0.035	4419.423	49.396	49.039	35.363	35.693	1.205	15.885	1.498	20.465	0.006	0.055	23	0.077	Rep_012
0.035	4417.007	49.673	48.088	33.837	36.975	1.141	14.603	1.485	20.236	0.006	0.054	21	0.082	Rep_040
0.035	4361.555	49.342	46.622	35.537	37.271	1.076	17.394	1.483	20.345	0.006	0.054	22	0.079	Rep_043
0.035	4358.329	49.545	47.139	35.082	38.217	1.122	16.800	1.474	20.341	0.001	0.053	22	0.011	Rep_043
0.035	4349.537	49.526	47.392	35.048	38.565	1.131	16.577	1.477	20.624	0.006	0.053	22	0.081	Rep_043
0.035	4325.424	49.407	47.314	35.122	37.012	1.100	16.724	1.468	20.499	0.006	0.053	22	0.079	Rep_043
0.035	4305.979	49.504	47.290	35.079	38.154	1.110	16.353	1.478	20.781	0.006	0.053	22	0.079	Rep_043
0.035	4289.729	49.484	47.375	35.227	38.488	1.113	16.782	1.448	20.409	0.006	0.051	22	0.078	Rep_043
0.035	4287.661	49.497	46.756	34.164	36.569	1.128	15.465	1.445	20.567	0.005	0.051	22	0.075	Rep_011
0.035	4256.572	49.123	47.686	34.233	36.160	1.158	14.566	1.440	20.763	0.005	0.050	22	0.075	HF
0.035	4255.815	49.081	47.771	34.916	36.099	1.098	15.381	1.445	20.955	0.005	0.050	22	0.077	HF
0.035	4230.131	49.890	48.343	34.740	38.029	1.095	14.467	1.410	20.018	0.006	0.050	21	0.081	Rep_043
0.035	4124.626	49.949	48.204	35.576	37.346	1.148	14.190	1.406	20.015	0.005	0.049	22	0.071	Rep_012
0.035	4102.777	49.584	47.494	34.916	38.770	1.106	16.289	1.420	20.980	0.006	0.048	22	0.080	Rep_043
0.035	4084.991	49.810	45.711	32.191	37.183	1.193	15.683	1.368	20.177	0.005	0.046	21	0.071	Rep_008
0.035	4078.576	49.007	47.590	35.051	36.107	1.091	15.086	1.387	20.945	0.005	0.046	22	0.071	HF
0.035	3990.192	49.516	47.703	35.230	38.157	1.110	15.971	1.375	20.606	0.005	0.046	22	0.072	Rep_043
0.035	3986.469	49.000	47.593	34.823	36.066	1.092	14.990	1.354	20.918	0.005	0.044	22	0.066	HF
0.035	3963.792	49.000	47.593	34.823	36.067	1.092	14.990	1.354	20.918	0.005	0.044	22	0.076	HF
0.035	3903.213	48.995	47.602	35.077	36.059	1.092	15.197	1.351	20.948	0.005	0.044	22	0.071	HF
0.035	3900.510	48.995	47.601	35.076	36.059	1.091	15.197	1.351	20.948	0.005	0.044	22	0.072	HF
0.035	3864.331	49.462	46.614	33.959	36.472	1.121	15.493	1.339	20.988	0.005	0.043	22	0.068	Rep_011
0.035	3837.924	49.644	46.942	34.084	38.535	1.116	16.128	1.333	21.393	0.005	0.042	22	0.072	Rep_043
0.035	3836.596	49.473	47.173	33.747	36.304	1.110	15.276	1.343	22.640	0.005	0.040	23	0.074	Rep_011
0.035	3818.554	48.963	47.446	34.790	36.248	1.102	15.907	1.327	22.207	0.005	0.040	23	0.073	HF
0.035	3760.250	48.506	47.315	35.343	36.223	1.098	15.619	1.336	23.354	0.001	0.038	24	0.008	HF
0.035	3746.120	48.929	46.563	33.074	36.472	1.143	15.340	1.228	21.808	0.004	0.035	22	0.060	Rep_040
0.035	3746.040	48.929	46.563	33.072	36.472	1.143	15.340	1.228	21.808	0.004	0.035	22	0.059	Rep_040
0.035	3719.814	48.509	46.517	35.376	36.230	1.097	16.173	1.323	25.457	0.005	0.034	26	0.067	HF
0.035	3699.568	47.481	46.735	32.928	36.766	1.104	15.029	1.252	24.766	0.004	0.032	24	0.068	Rep_015
0.035	3693.191	49.480	46.741	33.765	36.464	1.127	15.504	1.330	28.543	0.000	0.031	28	0.007	Rep_011
0.035	3679.450	49.739	45.990	32.554	38.579	1.164	16.625	1.302	28.106	0.005	0.030	27	0.068	Rep_042

Table C.7 – Continued from previous page

f_{stroke}	W_{spec} (J)	l_c	l_a	l_b	r	ω	δ	v_0	a	$\dot{m}$	l_{stroke}	n_{wire}	d_{avg}	Source
0.036	3639.599	47.559	46.349	32.483	36.209	1.078	16.106	1.272	28.096	0.004	0.029	26	0.070	Rep_041
0.036	3604.506	47.561	46.362	32.488	36.255	1.079	16.358	1.283	29.331	0.004	0.028	27	0.071	Rep_041
0.036	3600.846	47.577	46.384	32.439	36.254	1.080	16.924	1.276	31.666	0.004	0.026	29	0.066	Rep_041
0.036	3593.329	49.762	48.527	32.978	35.305	1.075	14.397	1.301	34.868	0.000	0.024	31	0.008	Rep_016
0.036	3548.146	48.538	47.007	34.661	36.371	1.113	16.295	1.332	38.454	0.005	0.023	36	0.073	HF
0.036	3504.272	47.600	45.874	32.333	35.597	1.086	15.254	1.249	35.709	0.004	0.022	32	0.064	Rep_002
0.036	3472.517	49.592	45.918	32.163	39.124	1.194	16.617	1.269	43.551	0.005	0.019	39	0.069	Rep_042
0.036	3451.174	48.810	45.515	32.118	35.476	0.997	16.525	1.271	44.087	0.004	0.018	37	0.077	Rep_037
0.036	3447.901	48.810	45.510	32.118	35.475	0.997	16.524	1.271	44.089	0.004	0.018	37	0.072	Rep_037
0.036	3427.582	49.236	46.270	32.116	36.515	1.171	15.600	1.268	49.379	0.004	0.016	43	0.061	Rep_021
0.036	3366.937	47.376	45.884	34.375	36.916	1.097	17.552	1.299	58.595	0.005	0.014	52	0.067	Rep_026
0.034	835.014	48.851	45.980	31.800	36.386	1.518	10.708	2.000	20.000	0.053	0.100	22	0.508	Rep_016
0.034	807.459	48.851	45.980	31.801	36.386	1.518	10.708	2.000	20.000	0.056	0.100	22	0.538	Rep_016
0.034	775.037	46.518	42.308	24.894	32.521	1.647	10.525	2.000	20.000	0.051	0.100	19	0.630	Rep_001
0.034	747.764	48.665	45.751	29.918	35.550	1.564	10.566	2.000	20.000	0.053	0.100	21	0.542	Rep_013
0.034	735.654	48.578	46.139	29.702	36.792	1.596	10.634	2.000	20.000	0.055	0.100	21	0.572	Rep_021
0.034	695.011	48.578	46.139	29.702	36.793	1.596	10.634	2.000	20.000	0.055	0.100	21	0.567	Rep_021
0.034	680.123	48.578	46.139	29.703	36.793	1.595	10.634	2.000	20.000	0.062	0.100	21	0.639	Rep_021
0.034	677.309	48.578	46.138	29.702	36.791	1.596	10.634	2.000	20.000	0.064	0.100	21	0.658	Rep_021
0.034	673.740	48.578	46.139	29.703	36.795	1.596	10.634	2.000	20.000	0.058	0.100	21	0.600	Rep_021
0.034	671.529	47.927	45.582	30.129	36.224	1.572	10.656	2.000	20.000	0.055	0.100	21	0.567	HF
0.034	670.090	47.927	45.582	30.129	36.224	1.572	10.656	2.000	20.000	0.061	0.100	21	0.629	HF
0.034	648.110	47.927	45.582	30.129	36.224	1.572	10.656	2.000	20.000	0.050	0.100	21	0.513	HF
0.034	633.415	47.927	45.581	30.129	36.223	1.572	10.656	2.000	20.000	0.059	0.100	21	0.611	HF
0.034	603.233	48.652	45.846	29.848	39.579	1.645	10.805	2.000	20.000	0.066	0.100	21	0.670	Rep_028
0.034	592.784	48.644	45.763	29.834	39.005	1.637	10.801	2.000	20.001	0.064	0.100	21	0.650	Rep_028
0.034	588.799	47.510	46.001	30.386	40.422	1.647	10.809	2.000	20.348	0.066	0.098	22	0.644	Rep_028
0.034	588.044	48.659	46.495	30.725	40.659	1.648	10.882	1.994	20.292	0.066	0.098	22	0.646	Rep_028
0.034	576.950	47.452	47.005	30.678	41.010	1.648	10.810	2.000	20.429	0.071	0.098	22	0.688	Rep_028
0.034	575.372	47.451	47.005	30.678	41.010	1.647	10.810	1.999	20.429	0.075	0.098	22	0.732	Rep_028
0.034	573.292	47.477	47.058	31.288	41.500	1.648	10.816	1.999	21.167	0.075	0.094	23	0.709	Rep_028
0.034	565.115	47.403	46.770	31.042	41.172	1.647	10.953	1.990	21.069	0.073	0.094	23	0.693	Rep_028
0.034	543.618	47.617	47.290	31.775	42.461	1.647	10.841	1.987	21.897	0.076	0.090	24	0.702	Rep_028
0.035	538.958	47.390	47.157	31.830	42.526	1.648	10.966	1.838	26.712	0.064	0.063	29	0.582	Rep_028
0.035	533.539	47.302	45.701	29.557	38.545	1.642	11.323	1.549	21.858	0.044	0.055	23	0.424	Rep_039

Table C.7 – Continued from previous page

f_{stroke}	W_{spec} (J)	l_c	l_a	l_b	r	ω	δ	v_0	a	$\dot{m}$	l_{stroke}	n_{wire}	d_{avg}	Source
0.035	531.188	47.345	46.982	32.130	43.044	1.647	11.281	1.589	23.068	0.051	0.055	26	0.454	Rep_028
0.035	520.472	47.542	46.998	31.248	41.679	1.646	11.173	1.443	22.923	0.043	0.045	25	0.393	Rep_028
0.035	518.741	47.555	46.614	31.024	38.817	1.604	11.061	1.377	22.198	0.037	0.043	24	0.343	Rep_013
0.035	501.899	47.348	47.184	32.113	43.553	1.647	11.730	1.461	27.797	0.044	0.038	31	0.388	Rep_028
0.036	497.557	47.489	46.820	31.991	42.382	1.635	11.405	1.084	22.485	0.027	0.026	25	0.235	Rep_028
0.036	488.759	47.537	46.713	31.708	42.230	1.644	11.509	1.103	23.668	0.026	0.026	26	0.231	Rep_028
0.036	476.200	47.543	46.896	30.512	37.971	1.604	10.878	1.026	21.387	0.022	0.025	23	0.204	Rep_001
0.036	470.211	48.759	47.303	31.310	38.569	1.592	11.435	0.939	21.336	0.021	0.021	23	0.193	Rep_009
0.036	456.272	47.528	46.770	31.924	42.082	1.635	11.409	0.955	22.672	0.023	0.020	25	0.202	Rep_028
0.036	448.077	47.428	46.821	32.049	42.528	1.635	11.429	0.914	22.684	0.021	0.018	25	0.179	Rep_028
0.036	446.696	47.428	46.821	32.049	42.528	1.635	11.429	0.914	22.684	0.022	0.018	25	0.189	Rep_028
0.036	445.658	47.521	46.691	30.359	36.684	1.581	11.389	0.848	21.627	0.016	0.017	23	0.151	Rep_035
0.036	443.220	48.532	46.994	30.616	38.566	1.612	10.914	0.826	21.788	0.016	0.016	23	0.148	Rep_001
0.036	442.971	47.520	46.285	29.936	36.299	1.585	11.285	0.819	22.833	0.017	0.015	24	0.162	Rep_030
0.036	440.015	47.583	45.807	30.037	38.503	1.626	11.528	0.861	25.443	0.018	0.015	27	0.166	Rep_019
0.036	439.968	48.539	47.107	31.509	38.330	1.577	11.526	0.841	25.348	0.018	0.014	27	0.160	Rep_022
0.036	437.715	47.354	45.777	29.844	36.580	1.592	11.229	0.811	23.862	0.016	0.014	25	0.153	HF
0.036	430.935	47.585	47.047	31.412	40.512	1.615	11.496	0.829	25.040	0.019	0.014	27	0.171	Rep_028
0.036	418.419	47.350	46.899	32.188	43.681	1.650	11.969	0.847	32.052	0.019	0.011	35	0.166	Rep_028
0.036	417.258	47.346	46.898	32.184	43.687	1.648	11.964	0.840	32.052	0.019	0.011	35	0.160	Rep_028
0.036	415.291	47.349	46.898	32.180	43.691	1.650	11.966	0.840	32.053	0.019	0.011	35	0.162	Rep_028
0.036	412.715	47.346	46.898	32.184	43.687	1.648	11.964	0.840	32.052	0.020	0.011	35	0.168	Rep_028
0.036	410.712	47.346	46.898	32.183	43.687	1.648	11.964	0.840	32.051	0.020	0.011	35	0.168	Rep_028

D. Simulation Code

D.1 Main Calculation Function with Bounce Loop

```
function [avg_dist_m,A_reg_tooth] =
   particle_tracing_parametrization(x,cfg)
    % Design Variable Designation:
    % Note that angles have different designations than used
       in the thesis.
    % l_c    = x(1); in mm
    % l_a    = x(2); in mm
    % l_b    = x(3); in mm
    % r      = x(4); in mm
    % theta = x(5); in rad, omega in this function
    % gamma = x(6); in degree, delta_offset in this function
    % v_0    = x(7); in m/s
    % acc    = x(8); in m/s^2
l_c = x(1);
l_a = x(2);
l_b = x(3);
r   = x(4);
omega=x(5);
delta_offset = x(6);
v0_m= x(7);
acc   = x(8);

%% 1. Initialisations

% Points for regolith fill area geometry [x; y]
p_fill_d    = NaN(2, 1);
p_fill_ramp = NaN(2, 1);
p_fill_base = NaN(2, 1);
p_fill      = NaN(2, 1);

% Bounce state matrices
```

```
% Rows: n_launch particles, Cols: initial trajectory + n_bounce possible iterations
v_l   = NaN(cfg.n_launch, cfg.n_bounce + 1);
delta = NaN(cfg.n_launch, cfg.n_bounce + 1);

%% 2. Calculation Parameters
delta_offset = cfg.initial_delta_offset + delta_offset;  % in degree, launch angle offset from cfg.alpha
l_limit = 0.1;          % in m, minimum average bounce distance below which the bounce loop is terminated

delta_offset_r = deg2rad(delta_offset);
g_mm = cfg.g*1000;      % in mm/s^2

rand_t = 0.90;      % lower bound factor for velocity/angle randomisation
rand_b = 1.10;      % upper bound factor for velocity/angle randomisation

% Initial launch speed pre-allocation
v_l(1:cfg.n_launch,1) = v0_m*1000;     % in mm/s, launch speed

cfg.alpha = deg2rad(35);% in rad, conveyor angle

phi = atan(l_b/l_a);% in rad, tooth ramp angle

% normals to the base section and ramp section
base_normal = [-sin(cfg.alpha),cos(cfg.alpha)];
ramp_normal = [-sin(cfg.alpha + phi),cos(cfg.alpha + phi)];

base = @(x) tan(cfg.alpha)*x;  % conveyor base line equation

%% 3. Profile Construction
% Initialise point arrays for all tooth geometry points
p_1 = zeros(2,cfg.n_teeth);
p_2 = zeros(2,cfg.n_teeth);
p_3 = zeros(2,cfg.n_teeth);
p_4 = zeros(2,cfg.n_teeth);
```

```
63
64 % Tooth start points (p_1) and ramp end points (p_2)
65 for i_teeth = 1:cfg.n_teeth
66     if i_teeth > 1
67         p_1(1,i_teeth) = p_1(1,i_teeth-1) + l_c*cos(cfg.alpha
               );
68         p_1(2,i_teeth) = p_1(2,i_teeth-1) + l_c*sin(cfg.alpha
               );
69     end
70     ramp_length = sqrt(l_a^2 + l_b^2);
71     p_2(1,i_teeth) = p_1(1,i_teeth) + ramp_length*cos(cfg.
          alpha+phi);
72     p_2(2,i_teeth) = p_1(2,i_teeth) + ramp_length*sin(cfg.
          alpha+phi);
73 end
74
75 % Catch arc centre (p_3) and base tangent point (p_4)
76 for i_teeth = 1:cfg.n_teeth
77     x2_loc = l_a; % local x distance between p_1 and p_2 (
          relative to base)
78     y2_loc = l_b; % local y distance between p_1 and p_2
79
80     y3_loc = r * cos(omega);
                                                          % local
           y coordinate of p_3
81
82     x3_loc = x2_loc + sqrt(r^2 - (y2_loc - y3_loc)^2);
                               % local x coordinate of p_3
83
84     x4_loc = x3_loc - r * sin(omega);
                                                % local x
          coordinate of p_4
85     y4_loc = 0;

          % local y coordinate of p_4 (on base)
86
87     p_3(1,i_teeth) = p_1(1,i_teeth) + (x3_loc * cos(cfg.alpha
          ) - y3_loc * sin(cfg.alpha));  % global x of p_3
```

```
88      p_3(2,i_teeth) = p_1(2,i_teeth) + (x3_loc * sin(cfg.alpha
           ) + y3_loc * cos(cfg.alpha));  % global y of p_3
89
90      p_4(1,i_teeth) = p_1(1,i_teeth) + (x4_loc * cos(cfg.alpha
           ) - y4_loc * sin(cfg.alpha));  % global x of p_4
91      p_4(2,i_teeth) = p_1(2,i_teeth) + (x4_loc * sin(cfg.alpha
           ) + y4_loc * cos(cfg.alpha));  % global y of p_4
92  end
93
94  % Catch arc angular bounds (from p_2 to p_4 around p_3)
95  angle_to_p2 = 0.0;
96  angle_to_p4 = 0.0;
97  for i_teeth = 1:cfg.n_teeth
98      angle_to_p2 = atan2(p_2(2,i_teeth) - p_3(2,i_teeth), p_2
           (1,i_teeth) - p_3(1,i_teeth));  % starting angle of
           catch arc (at p_2)
99      angle_to_p4 = atan2(p_4(2,i_teeth) - p_3(2,i_teeth), p_4
           (1,i_teeth) - p_3(1,i_teeth));  % end angle of catch
           arc (at p_4)
100 end
101 if angle_to_p4 < angle_to_p2
102     angle_to_p4 = angle_to_p4 + 2*pi; % wrap angle to ensure
           correct arc direction
103 end
104
105 % Catch surface normal (used for bounce reflection at the arc
    )
106 catch_normal = [(p_2(2,1)-p_4(2,1)),-(p_2(1,1)-p_4(1,1))];
107 catch_normal =catch_normal/ norm(catch_normal);
108
109 %% 4. Regolith Fill Level
110 % Effective gravity under launch acceleration determines fill
     surface angle
111 g_true = [0,-cfg.g];
112 g_acc  = [-acc*cos(cfg.alpha+delta_offset_r),-acc*sin(cfg.
    alpha+delta_offset_r)];
113 g_eff  = g_true + g_acc;
114 beta   = atan2(g_eff(2),g_eff(1))+pi/2;
```

```
115 delta_fill  = beta+deg2rad(cfg.AOR); % in rad, fill surface
    angle including AOR
116
117 % Ramp line of the second tooth (used as upper fill boundary
    reference)
118 a = (p_2(2,2)-p_1(2,2))/(p_2(1,2)-p_1(1,2));
                        % slope of ramp line
119 b = p_1(2,2)-a*p_1(1,2);
                                              % intercept of
    ramp line
120 ramp_2 = @(x) a*x + b;
                                                % ramp line
    equation
121
122 % Fill surface line through p_2 of the first tooth in the
    fill direction
123 p_fill_1 = p_2(:,1);
                                                  % fill
    surface anchor point (p_2 of first tooth)
124 p_fill_d(1) = p_fill_1(1)+cos(delta_fill);
                            % x component of fill direction
    vector
125 p_fill_d(2) = p_fill_1(2)+sin(delta_fill);
                            % y component of fill direction
    vector
126 a = (p_fill_d(2)-p_fill_1(2))/(p_fill_d(1)-p_fill_1(1));
            % slope of fill surface line
127 b = p_fill_1(2)-a*p_fill_1(1);
                                          % intercept of fill
    surface line
128 fill = @(x) a*x + b;
                                                  % fill
    surface line equation
129
130 f_fill_ramp = @(x) fill(x) - ramp_2(x);
131 f_fill_base = @(x) fill(x) - base(x);
132
133 % Intersection of fill surface with tooth ramp (upper
    regolith boundary)
```

```
134 if sign(f_fill_ramp(p_fill_1(1))) ~= sign(f_fill_ramp(p_2
    (1,2)))
135     p_fill_ramp(1) = fzero(f_fill_ramp,[p_fill_1(1)  p_2(1,2)
        ]);  % x coordinate of intersection
136     p_fill_ramp(2) = fill(p_fill_ramp(1));
137 else
138     p_fill_ramp(1) = nan;
139     p_fill_ramp(2) = nan;
140     avg_dist_m = 0;
141     A_reg_tooth = 0;
142     return;
143 end
144
145 % Intersection of fill surface with conveyor base (lateral
    regolith boundary)
146 if sign(f_fill_base(p_fill_1(1))) ~= sign(f_fill_base(p_1(1,
    end)))
147     p_fill_base(1) = fzero(f_fill_base,[p_fill_1(1,1) p_1(1,
        end)]);  % x coordinate of intersection
148     p_fill_base(2) = fill(p_fill_base(1));
                                    % y coordinate of
        intersection
149 else
150     p_fill_base(1) = nan;
151     p_fill_base(2) = nan;
152     avg_dist_m = 0;
153     A_reg_tooth = 0;
154     return;
155 end
156
157 % Select the intersection point closest to the tooth (
    innermost fill boundary)
158 p_fill_x = [p_fill_ramp(1), p_fill_base(1)];
159 p_fill_y = [p_fill_ramp(2), p_fill_base(2)];
160
161 [p_fill(1),index] = min(p_fill_x);
162 p_fill(2) = p_fill_y(index);
163
164 %% 5. Launch Points
```

```
n_grid = 1000;

   % number of grid points along catch arc for regolith
   boundary
beta_grid = linspace(angle_to_p2,angle_to_p4-0.05,n_grid);
                    % angle vector for catch arc grid
delta(1:cfg.n_launch,1) = cfg.alpha+deg2rad(delta_offset);
                    % initial launch angle for all particles

% Compute catch arc boundary points for regolith polygon
p_grid = zeros(2,n_grid);
for n = 1:n_grid
    p_grid(1,n) = p_3(1,1) + r * cos(beta_grid(n));
                                % x-positions of catch arc
       grid
    p_grid(2,n) = p_3(2,1) + r * sin(beta_grid(n));
                                % y-positions of catch arc
       grid
end

% Define regolith polygon boundary; shape depends on whether
   fill surface reaches next tooth
if p_fill(1) > p_1(1,2)
    patch_x = [p_4(1,1) p_1(1,2) p_fill(1) p_grid(1,1:100:end
       )];            % x coordinates of regolith polygon
    patch_y = [p_4(2,1) p_1(2,2) p_fill(2) p_grid(2,1:100:end
       )];            % y coordinates of regolith polygon
else
    patch_x = [p_4(1,1) p_fill(1) p_grid(1,1:100:end)];
                           % x coordinates of regolith
       polygon
    patch_y = [p_4(2,1) p_fill(2) p_grid(2,1:100:end)];
end

% Bounding box for Halton point filtering
bbox_x_min = min(patch_x);
bbox_x_max = max(patch_x);
bbox_y_min = min(patch_y);
bbox_y_max = max(patch_y);
```

```
190
191 % Scale pre-computed Halton sequence to bounding box and
       retain points inside regolith polygon
192 rx_all = bbox_x_min + (bbox_x_max - bbox_x_min) * cfg.pts(:,
       1);
193 ry_all = bbox_y_min + (bbox_y_max - bbox_y_min) * cfg.pts(:,
       2);
194
195 in_idx = inpolygon(rx_all, ry_all, patch_x, patch_y);
196 rx_valid = rx_all(in_idx);
197 ry_valid = ry_all(in_idx);
198
199 % Safety return if the regolith polygon is too small to
       provide enough launch points
200 if length(rx_valid) < cfg.n_launch
201     avg_dist_m = 0;
202     A_reg_tooth = 0;
203     return;
204 end
205
206 % Assign launch positions and angles
207 p_l = zeros(2, cfg.n_launch);
208 p_l(1, :) = rx_valid(1:cfg.n_launch)';
209 p_l(2, :) = ry_valid(1:cfg.n_launch)';
210 delta(1:cfg.n_launch, 1) = cfg.alpha + deg2rad(delta_offset);
       % in rad, global launch angle
211
212 %% 6. Yield Velocity
213 v_yield = yield_velocity();
214
215 %% 7. Bounce Calculation
216 ipoint = NaN(3, cfg.n_launch);
217 for iter_bounce = 1:cfg.n_bounce
218     [delta,v_l] = randomatico(cfg.random_switch,cfg.n_launch,
          rand_b,rand_t,delta,v_l); % apply randomisation to
          launch angle and speed
219
220     % Load current launch state and compute intersections
          with all surfaces
```

```
221     if iter_bounce == 1
222         lpoint = p_l;
223         lvelocity = v_l;
224         langle = delta;
225         p_i_catch_b = intersection_points_mexxing(p_2(:,2:end
                ),p_4(:,2:end),lpoint, g_mm, lvelocity, langle,
                cfg.n_launch, cfg.n_teeth, cfg.mu_drag); % call
                intersection calculation function for catch for
                first iteration
226     else
227         lpoint = ipoint(1:2, :);
228         lvelocity = v_l(:, iter_bounce);
229         langle = delta(:, iter_bounce);
230         p_i_catch_b = intersection_points_mexxing(p_2       ,
                p_4               , lpoint, g_mm, lvelocity,
                langle, cfg.n_launch, cfg.n_teeth, cfg.mu_drag); %
                 call intersection calculation for catch for all
                other iterations
231     end
232     p_i_ramp_b  = intersection_points_mexxing(p_1       , p_2
                      , lpoint, g_mm, lvelocity, langle, cfg.
            n_launch, cfg.n_teeth, cfg.mu_drag); % call
            intersection calculation for ramp for all iterations
233     p_i_base_b  = intersection_points_mexxing(p_1(:,1)  , p_1
            (:,cfg.n_teeth)   , lpoint, g_mm, lvelocity, langle,
            cfg.n_launch, 1       , cfg.mu_drag); % call
            intersection calculation for base for all iterations
234
235     % Select the first surface hit by each particle based on
            travel direction
236     for i = 1:cfg.n_launch
237         x_i = [p_i_ramp_b(1,i), p_i_catch_b(1,i), p_i_base_b
                (1,i)];
238         y_i = [p_i_ramp_b(2,i), p_i_catch_b(2,i), p_i_base_b
                (2,i)];
239
240         vxl = lvelocity(i) * cos(langle(i)); % horizontal
                velocity component
241
```

```
242         if vxl > 0
243             % First hit is the smallest x ahead
244             [ipoint(1,i), index] = min(x_i);
245 
246         else
247 
248             % First hit is the largest x ahead
249             [ipoint(1,i), index] = max(x_i);
250         end
251 
252         % Assign y coordinate and surface identifier (0=base,
                1=ramp, 2=catch)
253         if isnan(ipoint(1,i))
254             ipoint(2,i) = NaN;
255             ipoint(3,i) = NaN;
256         else
257             ipoint(2,i) = y_i(index);
258 
259             if index == 3
260                 ipoint(3,i) = 0; % Base
261             else
262                 ipoint(3,i) = index; % 1 for Ramp, 2 for
                        Catch
263             end
264         end
265     end
266 
267     % Compute impact velocities and apply bounce model
268     ivelocity_comp = zeros(2,cfg.n_launch);
269     t = zeros(cfg.n_launch);
270     for i = 1:cfg.n_launch
271         % If the particle has left the domain, propagate NaN
              to next state
272         if isnan(ipoint(3,i))
273             v_l(i, iter_bounce+1) = NaN;
274             delta(i, iter_bounce+1) = NaN;
275             t(i) = NaN;
276             continue;
277         end
```

```
278
279         % Ballistic flight time and impact velocity: with or
                without aerodynamic drag
280         if cfg.mu_drag < 1e-6
281             t(i) = (ipoint(1,i)-lpoint(1,i)) / (lvelocity(i)
                    * cos(langle(i)));
282
283             ivelocity_comp(1,i) = lvelocity(i) * cos(langle(i
                    ));
284             ivelocity_comp(2,i) = lvelocity(i) * sin(langle(i
                    )) - g_mm * (ipoint(1,i)-lpoint(1,i)) / (
                    lvelocity(i) * cos(langle(i)));
285         else
286             t(i) = -log(1-((ipoint(1,i)-lpoint(1,i))*cfg.
                    mu_drag)/(lvelocity(i)*cos(langle(i))))/cfg.
                    mu_drag;
287
288             ivelocity_comp(1,i) = lvelocity(i)*cos(langle(i))
                     * exp(-cfg.mu_drag*t(i));
289             ivelocity_comp(2,i) = -g_mm/cfg.mu_drag + (
                    lvelocity(i) * sin(langle(i)) + g_mm/cfg.
                    mu_drag)  *  exp(-cfg.mu_drag*t(i));
290         end
291
292         ivelocity_array = ivelocity_comp(:,i);
293
294         % Select surface normal for the hit surface
295         switch ipoint(3,i)
296             case 1
297                 n_vec = ramp_normal.';
298             case 2
299                 n_vec = catch_normal.';
300             case 0
301                 n_vec = base_normal.';
302             otherwise
303                 continue;
304         end
305
```

```
306         % Decompose velocity into normal and tangential
                components
307         v_norm = dot(ivelocity_array, n_vec) * n_vec;
308         v_tang = ivelocity_array - v_norm;
309
310         % Apply plastic correction to restitution coefficient
                for high-speed impacts
311         if v_norm > v_yield
312             k_plastic = cfg.k_elastic*(v_yield/norm(v_norm))
                    ^0.25;
313         else
314             k_plastic = cfg.k_elastic;
315         end
316         k_tang = 1-(cfg.mu_fric*(k_plastic+1))/(3.5/1) * norm
                (v_norm)/norm(v_tang);
317         v_out = k_tang * v_tang - k_plastic * v_norm;
318
319         v_l(i, iter_bounce+1) = norm(v_out);
320         delta(i, iter_bounce+1) = atan2(v_out(2), v_out(1));
321
322         if delta(i, iter_bounce+1) < 0
323             delta(i, iter_bounce+1) = delta(i, iter_bounce+1)
                    + 2*pi;
324         end
325
326     end
327
328     % Terminate early if all particles have left the domain
329     if all(isnan(ipoint(1,:)))
330         break;
331     end
332
333     % Terminate early if average particle displacement falls
            below threshold
334     if mean(abs(lpoint(1,:)-ipoint(1,:)), 'omitnan') <
            l_limit
335         break;
336     end
337 end
```

```
338
339 %% 8. Score Calculation
340 A_reg_tooth = polyarea(patch_x,patch_y); % in mm^2, regolith
       cross-section area per tooth
341
342 % Determine final tooth position of each particle to compute
       transport distance
343 end_dist_m = zeros(cfg.n_launch,1);
344 end_tooth=zeros(cfg.n_launch,1);
345 for i_launch = 1:cfg.n_launch
346     end_tooth(i_launch) = floor((ipoint(1,i_launch) - p_2
          (1,1)) / (p_2(1,2) - p_2(1,1))) + 1;
347     if end_tooth(i_launch) > 1
348         end_dist_m(i_launch) = p_4(1,end_tooth(i_launch));
349     else
350         end_dist_m(i_launch) = 0;
351     end
352 end
353
354 % Sum transport distances across all particles that remained
       in the domain
355 sum_dist = 0;
356 for i_launch = 1:cfg.n_launch
357     if ~isnan(ipoint(1,i_launch))
358         sum_dist = sum_dist + end_dist_m(i_launch);
359     end
360 end
361 avg_dist_m = (sum_dist / double(cfg.n_launch)) / 1000; % in m
       , average particle transport distance per stroke
362
363 end
```

D.2 Intersection Calculation

```
function [p_i] = intersection_points(p_a, p_b, p_l, g_mm, v_l
    , delta, n_launch, n_points, mu_drag)
    %#codegen

    %% 1. Pre-allocation
    possible_x = NaN(n_launch, n_points);
    possible_y = NaN(n_launch, n_points);
    p_i = NaN(3, n_launch);

    %% 2. Intersection Search
    for i_launch = 1:n_launch
        vx = v_l(i_launch) * cos(delta(i_launch)); %
            horizontal velocity component of current particle
        x0 = p_l(1, i_launch); % launch x position
        y0 = p_l(2, i_launch); % launch y position
        d0 = delta(i_launch);  % launch angle, in rad

        for i_points = 1:n_points
            xA = p_a(1, i_points);
            yA = p_a(2, i_points);
            xB = p_b(1, i_points);
            yB = p_b(2, i_points);

            m_s = (yB - yA) / (xB - xA); % slope of the
                current sawtooth segment

            % Clamp search bounds to the segment extent and
                to points ahead of the particle
            x_start = min(xA, xB);
            x_end   = max(xA, xB);

            if vx > 0
                x_start = max(x_start, x0 + 1e-6);
            else
                x_end = min(x_end, x0 - 1e-6);
            end

```

```
34              if x_start >= x_end || abs(vx) < 1e-6
35                  continue;
36              end
37
38              % Further clamp bounds to stay away from the drag
                    asymptote
39              if mu_drag > 1e-6
40                  asymptote_x = x0 + (vx / mu_drag);
41                  if vx > 0
42                      if x_start > (asymptote_x - 1e-3),
                            continue; end
43                      x_end = min(x_end, asymptote_x - 1e-3);
44                  else
45                      if x_end < (asymptote_x + 1e-3), continue
                            ; end
46                      x_start = max(x_start, asymptote_x + 1e
                            -3);
47                  end
48              end
49
50              % Check for a sign change in (trajectory -
                    segment) over the search interval
51              y_diff_start = get_diff(x_start, x0, y0, d0, vx,
                    g_mm, mu_drag, xA, yA, m_s);
52              y_diff_end   = get_diff(x_end,   x0, y0, d0, vx,
                    g_mm, mu_drag, xA, yA, m_s);
53
54              if ~isnan(y_diff_start) && ~isnan(y_diff_end) &&
                    (sign(y_diff_start) ~= sign(y_diff_end))
55
56                  % Locate root using bisection and verify it
                        lies ahead of the particle
57                  x_sol = bisection_solver(x_start, x_end, x0,
                        y0, d0, vx, g_mm, mu_drag, xA, yA, m_s);
58
59                  if (vx >= 0 && x_sol > x0) || (vx < 0 &&
                        x_sol < x0)
60                      if abs(x_sol - x0) > 1e-3
```

```
61                          possible_x(i_launch, i_points) =
                               x_sol;
62                          possible_y(i_launch, i_points) = (m_s
                                * (x_sol - xA) + yA);
63                      end
64                  end
65              end
66          end
67
68          % Select the closest intersection across all segments
69          dist = abs(possible_x(i_launch, :) - x0);
70          [min_dist, best_idx] = min(dist);
71
72          if ~isnan(min_dist)
73              p_i(1, i_launch) = possible_x(i_launch, best_idx)
                   ;
74              p_i(2, i_launch) = possible_y(i_launch, best_idx)
                   ;
75              p_i(3, i_launch) = 1; % surface hit flag
76          end
77      end
78  end
79
80  function diff = get_diff(x_eval, x0, y0, delta, vx, g_mm,
       mu_drag, xA, yA, m_s)
81      % Returns the vertical difference between the particle
           trajectory and the surface segment at x_eval
82      if mu_drag < 1e-6
83          % Vacuum parabola
84          K = g_mm / (2 * vx^2);
85          y_traj = y0 + (x_eval - x0) * tan(delta) - K * (
               x_eval - x0)^2;
86      else
87          % Stokes drag trajectory
88          term1 = tan(delta) + g_mm / (mu_drag * vx);
89          term2 = g_mm / (mu_drag^2);
90          val_log = 1 - (mu_drag * (x_eval - x0)) / vx;
91          % Guard against log(0) near the drag asymptote
92          if val_log < 1e-9
```

```
93              y_traj = -1e10;
94          else
95              y_traj = y0 + term1 * (x_eval - x0) + term2 * log
                    (val_log);
96          end
97      end
98
99      y_slope = m_s * (x_eval - xA) + yA;
100     diff = y_traj - y_slope;
101 end
102
103 function x_sol = bisection_solver(x_low, x_high, x0, y0,
        delta, vx, g_mm, mu_drag, xA, yA, m_s)
104     % Codegen-compatible root finder replacing fzero; fixed
            iteration count ensures deterministic runtime
105     tol = 1e-5;
106     x_sol = x_low;
107     for k = 1:40 % fixed iteration count for codegen
            compatibility
108         x_mid = (x_low + x_high) / 2;
109         f_low = get_diff(x_low, x0, y0, delta, vx, g_mm,
                mu_drag, xA, yA, m_s);
110         f_mid = get_diff(x_mid, x0, y0, delta, vx, g_mm,
                mu_drag, xA, yA, m_s);
111
112         if abs(f_mid) < tol || (x_high - x_low) < tol
113             x_sol = x_mid;
114             return;
115         end
116
117         if sign(f_mid) == sign(f_low)
118             x_low = x_mid;
119         else
120             x_high = x_mid;
121         end
122     end
123     x_sol = (x_low + x_high) / 2;
124 end
```

D.3 Randomisation Function

```
function [delta,v_l] = randomatico(random_switch,n_launch,
   rand_b,rand_t,delta,v_l)
    % Applies independent uniform random scaling to the
       launch angle and speed of each particle.
    % Scale factors are drawn from [rand_t, rand_b] for the
       current bounce iteration only.
    if random_switch == 1
        r = (rand_b-rand_t).*rand(n_launch*2,1) + rand_t; %
           draw 2*n_launch independent scale factors
        for i = 1:n_launch
            delta(i,1) = delta(i,1)*r(i);            % scale
               launch angle
            v_l(i,1) =  v_l(i,1)*r(i+n_launch);     % scale
               launch speed
        end
    end
end
```

D.4 Fitment Optimiser

```
%% 1. Target Definition
clear all;
% Target landing distribution as percentages across tooth positions
% Array length is 21: indices 1-20 correspond to teeth, index 21 is particles that left the conveyor
target_dist = zeros(1, 21);
target_dist(1) = 36.08;
target_dist(2) = 28.35;
target_dist(3) = 26.80;
target_dist(4) = 8.76;

%% 2. Optimisation Setup
n_pop = 500; % population size
problem.solver = 'ga';
problem.fitnessfcn = @(x)optimize_k_objective(x, target_dist);
problem.nvars = 3;
problem.lb = [0.01, 0.01, 0.1]; % lower bounds: [mu_fric, k_elastic, mu_drag]
problem.ub = [1, 1, 15];        % upper bounds: [mu_fric, k_elastic, mu_drag]

problem.options = optimoptions( 'ga', ...
                                'Display'       , 'iter', ...
                                'UseParallel'   , true  , ...
                                'PopulationSize', n_pop   , ...
                                'PlotFcn'       , @gaplotbestf);

% Display active genetic algorithm settings for verification
disp('--- Active Genetic Algorithm Settings ---');
fprintf('Creation Function:  %s\n', char(problem.options.CreationFcn));
fprintf('Mutation Function:  %s\n', char(problem.options.MutationFcn));
```

```
fprintf('Crossover Function: %s\n', char(problem.options.
    CrossoverFcn));
fprintf('Selection Function: %s\n', char(problem.options.
    SelectionFcn));

%% 3. Run Optimiser
disp('Starting Optimization...');
[best_vars,best_error] = ga(problem);

%% 4. Results
disp('--- Optimization Complete ---');
fprintf('Best mu_fric:  %.3f\n', best_vars(1));
fprintf('Best k_elastic: %.3f\n', best_vars(2));
fprintf('Best mu_drag:  %.3f\n', best_vars(3));
fprintf('Final Error (SSE): %.1f\n', best_error);

% Run simulation with optimal parameters and export the
    comparison distribution
final_dist = particle_tracing_slim(best_vars(1), best_vars(2)
    ,best_vars(3));

active_idx = find(final_dist > 0);
active_vals = final_dist(active_idx);
comp_dist = final_dist(1:4);
csvwrite('fitment_optimizer_output_distribution.csv',
    comp_dist);

% Format and display final distribution; index 21 represents
    particles lost off the conveyor
str_headers = join(compose("T%-7d", active_idx), "");
str_values  = join(compose("%-7.1f%%", active_vals), " ");

disp('Final Achieved Distribution:');
disp(str_headers);
disp(str_values);


%% 5. Fitness Function
function error_score = optimize_k_objective(x, target_dist)
```

```
62      %% 1. Simulation
63      k_hor  = x(1);
64      k_vert = x(2);
65      mu_drag = x(3);
66      %gamma_offset = x(4);
67
68      sim_dist = particle_tracing_slim(k_hor, k_vert, mu_drag);
69
70      %% 2. Objective Calculation
71      % Sum of squared errors penalises large deviations
           heavily
72      error_score = sum((sim_dist - target_dist).^2);
73  end
```

D.5 Main Optimisation Function with Non-linear Constraints

```
function wrapper_sawtooth_optimizer(target_folder)
    %% Definition of Constants for use in Fitness Function (
       Simulation and Performance Calculation)
    rng(0,'twister');
    cfg = struct();

    % Material Densities
    cfg.rho_reg       = 890; % in kg/m^3

    % Environmental & Operational Constants
    cfg.g             = 1.625;    % lunar gravitational
       acceleration, in m/s^2
    %cfg.g             = 9.81;    % earth gravitational
       acceleration, in m/s^2
    cfg.alpha         = 35;       % Varied from 1-40 for
       conveyor angle analysis, in degree

    cfg.mu_fric       = 0.106;    % friction coefficient,
       varied for sensitivity analysis
    cfg.k_elastic     = 0.872;    % coefficient for restitution
        calculation, varied for sensitivity analysis
    cfg.mu_drag       = 0;        % lunar drag coefficient
    %cfg.mu_drag       = 5.439;    % terrestrial drag
       coefficient, varied for sensitivity analysis
    cfg.AOR           = 58;        % lunar regolith angle of
       repose, in degree
    %cfg.AOR           = 34;        % quartz sand regolith
       angle of repose, used for terrestrial conditions, in
       degree

    % System Dimensions
    cfg.n_teeth       = 100;      % number of teeth
    cfg.n_launch      = 100;      % number of particles
    cfg.n_bounce      = 100;      % maximum number of simulated
        bounces

```

```
26      % Simulation Parameters
27      cfg.random_switch = true;  % turn on launch angle and
           velocity randomisation
28      cfg.initial_delta_offset = 18.434; % initial launch angle
            offset for simulation
29
30      % pre-define launch point distribution
31      p = haltonset(2, 'Skip', 1);
32      cfg.pts = net(p, 2000);
33
34      % get cooldown time from coolofftime() function
35      cfg.t_cool = coolofftime();
36
37      cfg.v_d = 0.05; % downstroke velocity, in m/s
38
39      % Energy Calculation Constants
40      cfg.rho_alu      = 2700; % in kg/m^3
41      cfg.l_t_sled     = 0.005; % sled thickness, in m
42      cfg.F_sma_single = 10; % force exerted by a single 0.25mm
            sma actuator wire, in N
43      cfg.w_sled       = 0.16; % conveyor width, in m
44      cfg.contraction_ratio = 0.05; % contraction ratio of sma
           actuator wire
45      cfg.delta_T      = 320; % temperature difference in sma
           wires for heating energy calculation, in K
46      cfg.c_wire       = 320; % specific heat capacity of sma
           wires, in J/kgK
47      d_wire           = 0.00025; % sma wire diameter, in m
48      sigma_pull       = 100e6; % stress required for sma wire
           extension (for bias force), in Pa
49      a_wire           = (d_wire/2)^2 * pi;
50      rho_wire         = 6450; % in kg/m^3
51      cfg.m_spec_wire  = a_wire * rho_wire;
52      cfg.F_pull_single = sigma_pull * a_wire;
53
54      % Definition of constants that are given to the mex file
           (simulation function converted to C++ code),
55      % as this requires the correct amount of values to be
           passed
```

```
56      mex_cfg = struct();
57      mex_cfg.rho_reg        = cfg.rho_reg;
58      mex_cfg.rho_cfrp       = cfg.rho_cfrp;
59      mex_cfg.g              = cfg.g;
60      mex_cfg.alpha          = cfg.alpha;
61      mex_cfg.w_conveyor     = cfg.w_conveyor;
62      mex_cfg.n_teeth        = cfg.n_teeth;
63      mex_cfg.n_launch       = cfg.n_launch;
64      mex_cfg.n_bounce       = cfg.n_bounce;
65      mex_cfg.l_conv         = cfg.l_conv;
66      mex_cfg.random_switch  = cfg.random_switch;
67      mex_cfg.AOR_switch     = cfg.AOR_switch;
68      mex_cfg.mu_fric        = cfg.mu_fric;
69      mex_cfg.k_elastic      = cfg.k_elastic;
70      mex_cfg.mu_drag        = cfg.mu_drag;
71      mex_cfg.AOR            = cfg.AOR;
72      mex_cfg.initial_delta_offset = cfg.initial_delta_offset;
73      mex_cfg.pts            = cfg.pts;
74      mex_cfg.t_cool         = cfg.t_cool;
75      mex_cfg.v_d            = cfg.v_d;
76
77      %% Load Initial Population
78      load("Earth_Full_Optimization/legacy optimizer/
           pop1000_gen100/initial_value_earth_pop1000_gen100.mat
           ");
79
80      %% Linear Constraints
81      problem.lb = [5, 3, 2, 2, deg2rad(0), 0, 0.8, 20]; %
           lower bounds of optimisation parameters
82      problem.ub = [50, 50, 50, 50, deg2rad(120), 45, 2, 80]; %
            upper bounds of optimisation parameters
83
84      % linear constraint matrices
85      A = [0, -1, 1, 0, 0, 0, 0, 0; -1, 1, 0, 0, 0, 0, 0, 0; 0,
            -1, 0, 1, 0, 0, 0, 0; 0, 0, 1, -1, 0, 0, 0, 0; 0, 0,
           0, 0, 0, 0, 0, 0; 0, 0, 0, 0, 0, 0, 0, 0; 0, 0, 0, 0,
           0, 0, 0, 0; 0, 0, 0, 0, 0, 0, 0, 0];
86      b = [0; 0; 0; 0; 0; 0; 0; 0];
87
```

```
88      %% Setup Logging inside the Target Folder
89      log_file_path = fullfile(target_folder, '
           All_Evaluations_Log.csv');
90      fileID = fopen(log_file_path, 'w');
91      fprintf(fileID, 'Transport_Score,Stroke_Energy_J\n');
92      fclose(fileID);
93
94      dq = parallel.pool.DataQueue;
95      afterEach(dq, @(data) export_to_csv_local(data,
           log_file_path));
96
97      %% Setup Optimizer
98      problem.solver = 'gamultiobj';
99      problem.fitnessfcn = @(x) optimize_sawtooth_parameters(x,
            cfg, mex_cfg, dq);
100     problem.nvars = 8;
101     problem.nonlcon = @conveyor_nonlinearconstraint;
102     problem.Aineq = A;
103     problem.bineq = b;
104     problem.options = optimoptions('gamultiobj', 'Display', '
           iter', 'UseParallel', true, 'PopulationSize', 500, '
           InitialPopulationMatrix', x, 'FunctionTolerance', 1e
           -4, 'MaxGenerations', 1000, 'PlotFcn', @gaplotpareto);
            %Population size and function tolerance are varied
           for high-fidelity simulation runs
105
106     [x_final, score_final] = gamultiobj(problem); %run
           optimiser
107
108     %% Post-Processing & Exporting
109
110     % Initialise arrays for result export
111     num_results = length(score_final);
112     best_mass_flows = zeros(num_results, 1);
113     avg_dist_all = zeros(num_results, 1);
114     Stroke_all = zeros(num_results, 1);
115     Wire_all = zeros(num_results, 1);
116     Freq_all = zeros(num_results, 1);
117     true_W_spec_all = zeros(num_results, 1);
```

```
118
119     % Calculate results for Pareto-optimal solutions (
            parallel for-loop)
120     parfor i = 1:num_results
121         [avg_dist, A_reg_tooth] =
                particle_tracing_parametrization(x_final(i,:), cfg
                );
122         [temp_m_dot, true_W_spec, S, W, F] =
                performance_calculation(cfg, x_final(i,:),
                avg_dist, A_reg_tooth);
123
124         best_mass_flows(i) = temp_m_dot;
125         avg_dist_all(i) = avg_dist;
126         Stroke_all(i) = S;
127         Wire_all(i) = W;
128         Freq_all(i) = F;
129         true_W_spec_all(i) = true_W_spec;
130     end
131
132     results_table = table(best_mass_flows, true_W_spec_all,
            x_final(:,1), x_final(:,2), x_final(:,3), x_final(:,4)
            , x_final(:,5), x_final(:,6), x_final(:,7), x_final
            (:,8), Freq_all, Stroke_all, avg_dist_all, Wire_all);
            % write all results into one table
133
134     % name table columns:
135     results_table.Properties.VariableNames{'Var3'} = 'l_c';
136     results_table.Properties.VariableNames{'Var4'} = 'l_a';
137     results_table.Properties.VariableNames{'Var5'} = 'l_b';
138     results_table.Properties.VariableNames{'Var6'} = 'r';
139     results_table.Properties.VariableNames{'Var7'} = 'theta';
140     results_table.Properties.VariableNames{'Var8'} = '
            gamma_offset';
141     results_table.Properties.VariableNames{'Var9'} = 'v0_m';
142     results_table.Properties.VariableNames{'Var10'} = '
            a_accel';
143
144     % sort results table by mass flow:
```

```
145     results_table = sortrows(results_table, 'best_mass_flows'
            , 'descend');
146
147     % save results table as .xlsx file for further analysis
148     excel_path = fullfile(target_folder, '
            Sawtooth_Optimization_Results.xlsx');
149     writetable(results_table, excel_path);
150     save(fullfile(target_folder, 'final_workspace.mat'));
151 end
152
153 % export function for export of data for all evaluations
154 % includes: stroke frequency, specific energy, mass flow,
        number of wires
155 function export_to_csv_local(data, path)
156     fileID = fopen(path, 'a');
157     if fileID ~= -1
158         fprintf(fileID, '%.4f, %.4f\n', data(1), data(2));
159         fclose(fileID);
160     end
161 end
162
163 %% Non-linear Constraint Function
164 function [c, ceq] = conveyor_nonlinearconstraint(x)
165     l_c = x(1); l_a = x(2); l_b = x(3); r = x(4); theta = x
            (5);
166     phi = atan(l_b / l_a);
167     x2_loc = l_a; y2_loc = l_b; y3_loc = r * cos(theta);
168     x3_loc = x2_loc+sqrt(r^2- (y2_loc - y3_loc)^2);
169     x4_loc = x3_loc-r*sin(theta);
170     c = zeros(4, 1);
171
172     % Is catch circle radius smaller than distance to p_2?
173     c(1) = abs(y2_loc - y3_loc) - r;
174     if c(1) <= 0
175         ramp_length = sqrt(l_a^2 + l_b^2);
176         p_proj = (x3_loc * cos(phi) + y3_loc * sin(phi));
177         t2 = 2 * p_proj - ramp_length;
178
179         % Does p_4 overlap with the ramp of the next tooth?
```

```
180         c(2) = x4_loc - l_c;
181
182         % Does p_4 overlap with the ramp of this tooth (is it
                smaller than 0)?
183         c(3) = -x4_loc;
184
185         % Does the catch arc intersect the ramp in places
               twice?
186         c(4) = ramp_length - t2;
187     else
188         c(2:4) = 1e6;
189     end
190     ceq = [];
191 end
```

D.6 Fitness Function

```
function obj = optimize_sawtooth_parameters(x, cfg, mex_cfg,
   dq)
    obj = NaN(1, 2);
    % Design Variable Designation:
    % Note that angles have different designations than used
       in the thesis.
    % l_c    = x(1); in mm
    % l_a    = x(2); in mm
    % l_b    = x(3); in mm
    % r      = x(4); in mm
    % theta = x(5); in rad, omega in the thesis
    % gamma = x(6); in degree, delta in the thesis
    % v_0    = x(7); in m/s
    % acc    = x(8); in m/s^2

    %% 1. Run Viability Checks
    phi_check   = atan(x(3) / x(2)); % ramp angle
    y2_loc = x(3);
    y3_loc = x(4) * cos(x(5));
    x2_loc = x(2);
    x3_loc = x2_loc + sqrt(x(4)^2 - (y2_loc - y3_loc)^2);
    x4_loc = x3_loc - x(4)*sin(x(5));

    % penalty values different across viability checks to act
       as exit flags during debugging
    penalty_obj3 = [1000003, 1000003];
    penalty_obj4 = [1000004, 1000004];
    penalty_obj5 = [1000005, 1000005];
    penalty_obj6 = [1000006, 1000006];
    penalty_obj7 = [1000007, 1000007];

    % From Non-linear Constraints:

    % Is catch circle radius smaller than distance to p_2?
    if abs(y2_loc - y3_loc) > x(4)
        obj = penalty_obj3;
        return;
```

```
35      end
36
37      % Does p_4 overlap with the ramp of the next tooth?
38      if x4_loc > x(1)
39          obj = penalty_obj4;
40          return;
41      end
42
43      % Does p_4 overlap with the ramp of this tooth (is it
            smaller than 0)?
44      if x4_loc < 0
45          obj = penalty_obj5;
46          return;
47      end
48
49      % Arc Ramp Intersection Check
50      ramp_length = sqrt(x(2)^2 + x(3)^2);
51      p_proj = (x3_loc * cos(phi_check) + y3_loc * sin(
            phi_check));
52      t2 = 2 * p_proj - ramp_length;
53
54      if t2 > 1e-5 && t2 < (ramp_length - 1e-5)
55          obj = penalty_obj6;
56          return;
57      end
58
59      % Incline/AOR Check
60      alpha_c = deg2rad(cfg.alpha);
61      mu_s_c = tand(cfg.AOR);
62      g_std = 9.81; % in m/s^2
63      delta_off_r = deg2rad(cfg.initial_delta_offset + x(6));
64      delta_check = -atan((x(8)*(cos(alpha_c-delta_off_r)-sin(
            alpha_c-delta_off_r)*mu_s_c)-g_std*mu_s_c) / (x(8)*(
            cos(alpha_c-delta_off_r)*mu_s_c+sin(alpha_c-
            delta_off_r))+g_std));
65
66      if delta_check > alpha_c
67          obj = penalty_obj7;
68          return;
```

```
    end

    %% 2. Call Simulation Function
    [avg_dist_m, A_reg_tooth] =
       particle_tracing_parametrization_mexxing_mex(x,
       mex_cfg);

    %% 3. Call Performance Calculation
    [m_dot,W_spec,~,n_wire,f_op,f_dynamic] =
       performance_calculation(cfg,x,avg_dist_m,A_reg_tooth);

    %% 4. Objective Definition (cutoff at 2 Hz)
    f_limit = 2; % in Hz
    if f_dynamic > 2
        excess_f = f_dynamic - f_limit;
        penalty_weight_1 = 1000;
        obj(1) = -f_limit + (excess_f * penalty_weight_1);

        penalty_weight_2 = 1000000;
        obj(2) = W_spec + (excess_f * penalty_weight_2);
    else
        obj(1) = f_dynamic;
        obj(2) = W_spec;
    end
    %% 5. Logging
    logData = [m_dot, W_spec, f_op, n_wire];
    send(dq, logData);
end
```

D.7 Performance Calculation

```
function [m_dot,W_spec,stroke_m,n_wire,f_op,f_dynamic] =
   performance_calculation(cfg,x,avg_dist_m,A_reg_tooth)
    % Design Variable Designation:
    % Note that angles have different designations than used
       in the thesis.
    % l_c    = x(1); in mm
    % l_a    = x(2); in mm
    % l_b    = x(3); in mm
    % r      = x(4); in mm
    % theta = x(5); in rad, omega in the thesis
    % gamma = x(6); in degree, delta in the thesis
    % v_0    = x(7); in m/s
    % acc    = x(8); in m/s^2
    l_c = x(1);
    v0_m= x(7);
    acc   = x(8);

    % conveyor length for calculations
    l_conv_mm   = 1000; % in mm

    %% 1. Mass and Energy Calculation
    % Stroke Length
    stroke_m    = (v0_m^2) / (2 * acc); % in m

    % Regolith Mass and Total Sledge Mass
    l_conv = l_conv_mm/1000;
    cfg.m_sled = cfg.l_t_sled * cfg.w_sled * l_conv * cfg.
       rho_alu;
    n_teeth_individual = floor(l_conv_mm/l_c);

    V_reg_total_mm3 = (A_reg_tooth * n_teeth_individual) * (
       cfg.w_conveyor * 1000);
    m_reg_total = V_reg_total_mm3 * (cfg.rho_reg * 10^-9); %
       in kg
    m_total = cfg.m_sled + m_reg_total; % in kg

    % SMA Force & Wire Count
```

```
33      F_inertia = m_total * acc; % in N
34      F_gravity = m_total * cfg.g * sind(cfg.alpha); % in N
35      F_needed  = F_inertia + F_gravity; % in N
36      n_wire    = ceil(F_needed / (cfg.F_sma_single - cfg.
            F_pull_single));
37
38      % Wire Heat Energy
39      l_wire_m      = stroke_m / cfg.contraction_ratio; % in m
40      W_stroke_heat = (cfg.delta_T * cfg.c_wire * cfg.
            m_spec_wire * l_wire_m) * n_wire; % in J
41
42      %% 2. Stroke Frequency
43      t_stroke = v0_m/acc + stroke_m/cfg.v_d; % in s
44      f_dynamic = 1/(t_stroke+cfg.t_cool); % in Hz
45      f_op      = min(f_dynamic, cfg.f_max); % in Hz
46
47      %% 3. Optimisation Objectives
48      m_dot = m_reg_total * (avg_dist_m / (l_conv_mm / 1000)) *
            f_op; % in kg/s
49
50      % Result is considered ineligible if mass flow is smaller
            than approximately 0.
51      if m_dot > 1e-9
52          W_spec = (W_stroke_heat * f_op) / m_dot;
53      else
54          W_spec = 1000042;
55          f_dynamic= 2000000;
56      end
57  end
```

D.8 Cooldown Time Calculation

```
function [t_cool] = coolofftime()
    rho_wire = 6450; % sma wire density, in kg/m^3
    r_wire = 0.00025/2; % sma wire radius, in m
    c_p = 320; % sma wire specific heat capacity, in J/kgK
    sigma = 5.6703E-8;% Stefan-Boltzmann constant, in W/m^2K
       ^4
    eps = 0.17;       % approximate average emissivity of
       shape memory alloys
    T_low = 333; % martensitic finish temperature, in K
    T_high = 363; % austenitic finish temperature, in K

    t_cool = (rho_wire * r_wire * c_p)/(6*sigma*eps)*(1/T_low
       ^3 - 1/T_high^3); % cooldown time, in s
end
```